CO_2 Exchanges between the Atmosphere and an Alpine Meadow Ecosystem on the Qinghai-Tibetan Plateau

Tomomichi KATO

A dissertation submitted to the Doctoral Program
in Biological Sciences, the University of Tsukuba
in partial fulfillment of the requirements
for the degree of Doctor of Philosophy in Science

January 2004

Contents

Contents i

Abstract v

List of Tables viii

List of Figures ix

List of Symbols xiv

Chapter 1 General Introduction 1

1.1. Background 1

1.1.1. Global climate change and terrestrial ecosystems 1

1.1.2. Measurement and modeling of carbon dioxide between the atmosphere and terrestrial ecosystems 2

1.1.3. An alpine meadow ecosystem on the Qinghai-Tibetan Plateau, China 4

1.2. Purpose of this study 5

1.3. Composition of the thesis 6

Chapter 2 Site description 8

Chapter 3 Diurnal changes of the CO_2 exchanges 12

3.1. Introduction 12

3.2. Materials and Methods 12

3.2.1. Micrometeorology 13

3.2.2. Eddy covariance method 13

3.2.2.1. Fundaments of the eddy diffusion flux calculations 13

3.2.2.2. Measurement of eddy diffusion fluxes 19

3.2.2.3. Correction of measured turbulent flux data 19

3.2.2.4. Validity of measured flux data 21

3.2.3. Omega factor calculation 25
3.2.4. Bowen ratio calculation 27
3.2.5. Canopy resistance calculation 27
3.2.6. *GPP* and R_e calculations 27
3.2.7. *LAI* and biomass sampling 28
3.3. Results 28
3.3.1. Micrometeorology and vegetation growth 28
3.3.2. Sensible and latent heat fluxes 29
3.3.3. Carbon dioxide flux 30
3.3.4. *GPP* and R_e 31
3.4. Discussion 31
3.4.1. Measurement accuracy of eddy covariance method 31
3.4.2. Environmental controls on the diurnal change of carbon dioxide dynamics 33
3.4.3. Ecosystem carbon assimilation ability 34

Chapter 4 Seasonal changes of the CO2 exchanges 74
4.1. Introduction 74
4.2. Materials and Methods 75
4.2.1. *NEP*, *GPP* and R_e gap-filling methods 76
4.3. Results 77
4.3.1. Micrometeorology 77
4.3.2. Carbon dioxide flux 78
4.3.3. *GPP* and R_e 79
4.3.4. Annual sums of net ecosystem carbon dynamics 81
4.4. Discussion 81
4.4.1. Environmental controls on the seasonal changes of net carbon dioxide exchanges 81
4.4.2. Environmental controls on the seasonal changes of *GPP* and R_e 82
4.4.3. Ecosystem carbon assimilation ability 83

4.4.4. Gap-filling methods and annual carbon dynamics 85

Chapter 5 Model analysis on the relationship between climate perturbations and carbon dynamics: 1981-2000 102

5.1. Introduction 102

5.2. Model description 105

5.2.1. Sim-CYCLE -Basic model- 105

5.2.1.1. Overview of Sim-CYCLE 105

5.2.1.2. Single-leaf processes 107

5.2.1.2. Ecosystem-scale processes 110

5.2.2. Soil thermal profile 117

5.2.2.1. Thermal parameter 119

5.2.3. Water budget 120

5.2.3.1. Rainfall, snow and thawing 121

5.2.3.2. Evaporation and transpiration 121

5.2.3.3. Runoff and Infiltration 126

5.3. Model experiment designs 127

5.4. Results 128

5.4.1. Steady state experiment 128

5.4.2. Transient experiment 129

5.4.3. Model sensitivity analysis 130

5.5. Discussion 131

5.5.1. Model accuracy 131

5.5.2. The Relationship between climate perturbations and ecosystem CO_2 exchanges ... 132

5.5.3. The potential response of the ecosystem CO_2 exchanges against global warming.. 133

Chapter 6 General Discussion 165

6.1. Carbon dioxide assimilation capacity of alpine meadow ecosystem on the Qinghai-Tibetan Plateau 165
6.2. Environmental control on the CO_2 exchange on the different temporal scales 166
6.3. The global warming effects on the ecosystem carbon sequestration 170
6.4. Recommendations for future research 171

Chapter 7 Conclusions 173

Acknowledgement 175
References 177

Abstract

The Qinghai-Tibetan Plateau plays a critical role in regional and global climate change. More than 60% of the surface area of the plateau is covered by grasslands. To reveal the potential contribution of grassland ecosystems to climate change, I examined the CO_2 exchange between the atmosphere and an alpine *Kobresia* meadow (lat 37°29–45′N, long 101°12–23′E, 3250 m a.s.l.) on the northeastern Qinghai-Tibetan Plateau. The ecosystem CO_2 flux was measured continuously using the eddy-covariance method from August 2001 to December 2002. I examined the diurnal and seasonal variations of carbon fluxes and assessed their environmental and biological controls. I further explored the long-term pattern of carbon dynamics in the alpine ecosystem using meteorological and biomass data available for the period from 1981 to 2000 with a simulation model of the carbon cycle in terrestrial ecosystems (Sim-CYCLE).

The major findings from the CO_2 flux measurements were as follows: (1) The daily changes in CO_2 exchange showed CO_2 uptake in the daytime and CO_2 release in the nighttime in summer and small CO_2 release during all the day in winter. In 2002, net ecosystem productivity (*NEP*) during the five months of summer amounted to 138.4 g C m^{-2}. *NEP* during the rest of the year reached -59.9 g C m^{-2} and the winter flux measurements provided very important information to estimate the annual carbon dynamics. The maximum daily CO_2 uptake (3.9 g C m^{-2} day^{-1}) in this site was smaller than that in other grassland ecosystems at almost the same latitude, although the maximum *LAI* was larger. The 78.5 g C m^{-2} yr^{-1} annual *NEP* in 2002 was lower than those of warmer ecosystems, e.g. temperate and tropical grassland ecosystems, and as much as those of other cool ecosystems, e.g. alpine and boreal ecosystems. (2) The CO_2 exchange as influenced by the environmental factors was analyzed on daily and seasonal scales. The increment of photosynthetic photon flux density (*PPFD*) increased the net CO_2 uptake on all temporal scales. The increment of temperature decreased the *NEP* on all temporal scales, which was caused by the enhancement of ecosystem respiration in daily and seasonal changes. The increment of moisture, e.g. soil water content, atmospheric water vapor, did not affect the

daily *NEP* (net CO_2 uptake). The CO_2 efflux in the nighttime was suppressed by soil moisture increase. The patterns of soil water content and CO_2 efflux in the alpine ecosystem seems to be different from that reported for semi-arid grasslands.

Sim-CYCLE model simulation showed the following major findings. (3) The transition experiment for 1981-2000 showed that the annual *NEP* ranged from -70 to +70 g C m^{-2} yr^{-1} over the 20 years. (4) The CO_2 exchange as influenced by the environmental factors was analyzed in the interannual changes. The light increments in the growing season promoted the annual gross primary production (*GPP*) and *NEP*. Increases in temperature decreased the *NEP* on all temporal scales, through enhancement of the heterotrophic respiration in the interannual changes. Increases in precipitation did not affect the *NEP* in the interannual changes. (5) The model sensitivity analysis showed that *GPP*, autotrophic respiration (*AR*), net primary production (*NPP*) and plant biomass responded quickly and the heterotrophic respiration (*HR*), litter and soil biomass responded very slowly to the climate change. Temperature increases of 5 °C increased the *GPP* and those over 7.5 °C decreased the Global Warming by 5 °C advanced the ecosystem photosynthetic activity and the duration of the growing season, and increases the *GPP*. In contrast, warming greater than 7.5 °C may exceed the optimum temperature for photosynthesis and decreased the *GPP*.

This study suggests that (1) the alpine meadow was a CO_2 sink, at least in 2002. The current CO_2 sink strength is comparable with those of many sub-alpine ecosystems reported so far. The very low temperature, which suppressed photosynthetic activity and shortened the duration of the growing season, decreased the net CO_2 uptake. (2) Soil water availability was high in the alpine meadow. The high soil water might reduce the ecosystem respiration, because of the decrement of microbial activity in the well-watered anaerobic conditions. (3) The measured annual CO_2 uptake is close to the fluctuating range derived from model analysis, although CO_2 uptake data may contain estimation errors caused by energy imbalance and gap-filling methods. (4) The interannual relationships between the annual CO_2 exchange and environmental factors did not differ significantly from those of seasonal changes. (5) Long-term global warming will increase the ecosystem carbon uptake. However, extreme warming may

shift this ecosystem to another biome type through invasion of other plant species adaptive to warmer environments.

The primary conclusions are that the alpine meadow has the potential to sequester atmospheric CO_2, but the potential appears to be small, possibly because of the limitation of low temperature. However the data are not enough to judge whether this ecosystem is a CO_2 sink or source on average from the current measurements and model analysis, mainly due to the limited observation data. Multi-year data acquisitions of the CO_2 exchange are therefore required.

List of Tables

Chapter 1

Table 1.1 Global carbon budgets for the 1980s and 1990s 7

Chapter 3

Table 3.1 Instruments and installation height 36

Table 3.2 Different components of carbon exchange fluxes and environmental conditions for the *Kobresia humilis* meadow and other sites at similar latitude 37

Chapter 4

Table 4.1 Monthly meteorological conditions from August 2001 to December 2002 86

Table 4.2 Monthly heat budgets and carbon dynamics from August 2001 to December 2002 87

Table 4.3 Aboveground biomass and leaf area index in 2002 88

Table 4.4 Parameterization of ecosystem respiration and gross primary production regression curves using 15 min averaged data 88

Table 4.5 Ecosystem carbon dynamics 89

Chapter 5

Table 5.1 Site-specific parameters used in Sim-CYCLE running at the Haibei study site. 134

Table 5.2 Comparisons of ecosystem carbon dynamics between Sim-CYCLE estimates and those from other studies 135

Table 5.3 Comparisons of carbon pools and *LAI* between Sim-CYCLE estimates and those from other studies. 137

Table 5.4 Climate and carbon fluxes annual anomalies in the Haibei alpine meadow. 138

List of Figures

Chapter 2

Figure 2.1 Location of the study area 10

Figure 2.2 Map of the observation site 11

Chapter 3

Figure 3.1 A schematic diagram of the flux measurement system 38

Figure 3.2 A view of the experimental site in summer 39

Figure 3.3 A view of the experimental site in winter 40

Figure 3.4 A view of the setting of the instruments -aboveground- 41

Figure 3.5 A view of the setting of the instruments -belowground- 42

Figure 3.6 Time series of x, y, z-axis wind velocities, air temperature, specific humidity and carbon dioxide concentration 43

Figure 3.7 Power spectrum of x, y, z-axis wind velocities, air temperature, specific humidity and carbon dioxide concentration 44

Figure 3.8 Cross spectrum between z-axis wind velocities and air temperature, specific humidity and carbon dioxide concentration 45

Figure 3.9 The wind direction dependent deflection of the 15 min average wind inclination 46

Figure 3.10 Comparisons of 15 min averaged fluxes of corrected sensible heat with uncorrected sensible heat 47

Figure 3.11 Comparisons of 15 min averaged fluxes of corrected latent heat with uncorrected latent heat 48

Figure 3.12 Comparisons of 15 min averaged fluxes of corrected CO_2 with uncorrected CO_2 49

Figure 3.13 Wind direction dependent deflection of the 15 min averaged H, λE and FCO_2 fluxes 50

Figure 3.14 Relationship between aerodynamic stability and dimensionless universal functions under unstable conditions 51
Figure 3.15 Relationship between aerodynamic stability and dimensionless universal functions under near neutral conditions 52
Figure 3.16 Daily energy balance between $H+\lambda E$ and $Rn-G$ 53
Figure 3.17 Seasonal changes of daily energy balance ratio between $H+\lambda E$ and $Rn-G$ 54
Figure 3.18 Daily changes of energy balance ratio between $H+\lambda E$ and $Rn-G$ 55
Figure 3.19 Wind direction dependent of the energy balance ratio 56
Figure 3.20 Energy balance ratio dependent on the friction velocity 57
Figure 3.21 Diurnal changes of hourly averaged air temperature 58
Figure 3.22 Diurnal changes of hourly averaged soil temperature 59
Figure 3.23 Diurnal changes of hourly averaged *PPFD* 60
Figure 3.24 Mean and standard deviation of the aboveground biomass and the leaf area index for the *Koresia humilis* alpine meadow 61
Figure 3.25 Diurnal changes of hourly-averaged H flux for each month of the years 2001 and 2002 62
Figure 3.26 Diurnal changes of hourly-averaged λE flux for each month of the years 2001 and 2002 63
Figure 3.27 Diurnal courses of hourly-means of H, λE and environmental conditions in a sunny week 64
Figure 3.28 Relationship between the hourly-means of soil surface-air temperature difference and sensible heat flux 65
Figure 3.29 Relationship between hourly-means of vapor pressure deficit and latent heat flux 66
Figure 3.30 Diurnal changes of hourly averaged FCO_2 flux 67
Figure 3.31 Relationship between net carbon exchange rate and incident *PPFD* in each month over a growing season 68

Figure 3.32 Diurnal courses of hourly mean CO_2 exchange flux and environmental conditions 69

Figure 3.33 Relationship between hourly-means of the *PPFD* and CO_2 flux 70

Figure 3.34 Diurnal courses of hourly mean gross primary production, and hourly mean ecosystem respiration 71

Figure 3.35 Relationship between gross primary production and irradiant *PPFD*, and ecosystem respiration and soil temperature in July 2002 72

Figure 3.36 Relationship between gross primary production and incident *PPFD*, and *GPP* and evapotranspiration in 2002 73

Chapter 4

Figure 4.1 Seasonal changes in meteorological conditions 91

Figure 4.2 Seasonal changes in daily heat fluxes, moisture and canopy physiological conditions 93

Figure 4.3 Changes in daily net ecosystem production 94

Figure 4.4 Linear regression of daytime accumulated CO_2 uptake flux on incident photosynthetic photon flux density 95

Figure 4.5 Relationship between nighttime CO_2 flux density and nighttime soil temperature 96

Figure 4.6 Relationship between nighttime CO_2 flux density and nighttime soil water content during a dry spell after heavy rainfall 97

Figure 4.7 Ecosystem respiration calculated from light response relationships compared to the values derived from exponential regressions between soil temperature and nighttime fluxes under turbulent conditions 98

Figure 4.8 Seasonal changes in daily mean photosynthetic photon flux density, soil temperature, daily mean gross primary production, ecosystem respiration, ratio between *GPP* and R_e, and daily maximum *GPP* and R_e 99

Figure 4.9 Changes in radiation- and water-use efficiency of gross primary production .. 100

Figure 4.10 *LAI* controls on maximum gross primary production, radiation use efficiency and water use efficiency 101

Chapter 5

Figure 5.1 Schematic diagram of Sim-CYCLE. 139

Figure 5.2 Schematic diagram of single leaf processes in Sim-CYCLE 140

Figure 5.3 Schematic diagram of the Sim-CYCLE calculation processes 141

Figure 5.4 Schematic diagram of soil thermal profile processes in Sim-CYCLE 142

Figure 5.5 Schematic diagram of a one-dimensional description of energy partitioning for a canopy 143

Figure 5.6 Schematic diagram of runoff and infiltration processes in Sim-CYCLE 144

Figure 5.7 Seasonal changes of input climate data in the steady state experiment in temperature, solar radiation, humidity and wind speed. 145

Figure 5.8 Growth of ecosystem carbon fluxes and storages, estimated by Sim-CYCLE equilibrium run 146

Figure 5.9 Schematic diagram of ecosystem carbon dynamics estimated by Sim-CYCLE equilibrium run 147

Figure 5.10 Seasonal patterns of carbon fluxes estimated by Sim-CYCLE equilibrium run 148

Figure 5.11 Seasonal patterns of carbon storages estimated by Sim-CYCLE equilibrium run 149

Figure 5.12 Seasonal patterns of soil thermal profiles, estimated by Sim-CYCLE equilibrium run 150

Figure 5.13 Seasonal patterns of heat budgets estimated by Sim-CYCLE equilibrium run.. 151

Figure 5.14 Seasonal patterns of water budgets estimated by Sim-CYCLE equilibrium run 152

Figure 5.15 Comparisons of the simulated above ground *NPP* of Sim-CYCLE transient run and observed values of other studies 153

Figure 5.16 Yearly changes of ecosystem carbon fluxes and storages estimated by Sim-CYCLE transient run 154
Figure 5.17 Annual climate and anomalies in carbon fluxes 155
Figure 5.18 Relationships between temperature and carbon fluxes anomalies 156
Figure 5.19 Relationships between precipitation and carbon fluxes anomalies 157
Figure 5.20 Relationships between radiation and carbon fluxes anomalies 158
Figure 5.21 Anomalies in monthly climate and carbon flux 159
Figure 5.22 Seasonal changes in the slope of regression between temperature, precipitation, short wave radiation and carbon flux anomalies 160
Figure 5.23 Transitional changes of carbon fluxes 161
Figure 5.24 Transitional changes of carbon storages 162
Figure 5.25 Relationship between prescribed environmental changes and equilibrium carbon fluxes 163
Figure 5.26 Relationship between prescribed environmental changes and equilibrium water, heat fluxes and soil water content 164

List of Symbols

Term	Definition (units)
α	initial slope of light-GPP hyperbolic curves (μmol CO_2 μmol photon^{-1})
ANPP	aboveground net primary production (Mg C ha^{-1} yr^{-1})
AR	autotrophic respiration (Mg C ha^{-1} yr^{-1})
β	Bowen ratio (dimensionless)
C_p	specific heat at constant pressure (J kg^{-1} K^{-1})
D	zero plane displacement (m)
Δ	slope of the saturation vapor pressure versus temperature curve (hPa K^{-1})
E_a	activation energy (J mol^{-1})
EBR	energy balance ratio (dimensionless)
EV	evaporation (mm)
FCO2	CO_2 flux (μmol CO_2 m^{-2} s^{-1})
ϕ	universal function of all kinds of fluctuations (dimensionless)
G	soil heat flux (W m^{-2})
γ	psychrometric constant (hPa °C^{-1})
GPP	gross primary production (μmol CO_2 m^{-2} s^{-1}, g C m^{-2} day^{-1} or Mg C ha^{-1} yr^{-1})
GPP_{max}, GPP_{SAT}	maximum *GPP* and *GPP* at light saturation (μmol m^{-2} s^{-1})
H	sensible heat flux (W m^{-2})
HR	heterotrophic respiration (Mg C ha^{-1} yr^{-1})
k	von Karman's constant (= 0.4)
L	Monin-Obukhov length (m)
LAI	leaf area index (m^2 m^{-2})
λ	latent heat (J kg^{-1})
λE	latent heat flux (W m^{-2})
λE_{eq}	equilibrium evaporation (W m^{-2})
λE_{imp}	imposed evapotranspiration rate (W m^{-2})

NEE	net ecosystem exchange (μmol CO2 m^{-2} s^{-1})
NEP	net ecosystem production (μmol CO2 m^{-2} s^{-1}, g C m^{-2} day^{-1} or Mg C ha^{-1} yr^{-1})
$NEP_{daytime}$, $NEP_{nightitme}$, NEP_{total}	net ecosystem production during daytime, nighttime and all day (g C m^{-2} day^{-1})
NPP	net primary production (μmol CO2 m^{-2} s^{-1}, g C m^{-2} day^{-1} or Mg C ha^{-1} yr^{-1})
PN	penetration (mm)
$PPFD$	photosynthetic photon flux density (μmol photon m^{-2} s^{-1}, mol photon m^{-2} day^{-1})
PR	precipitation (mm)
q_*	friction specific humidity (g kg^{-1})
R	gas constant (8.134 J K^{-1} mol^{-1})
R_{aero}	aerodynamic resistance (s m^{-1})
R_{canopy}	canopy resistance (s m^{-1})
R_e	ecosystem respiration (μmol CO2 m^{-2} s^{-1}, g C m^{-2} day^{-1} or g C m^{-2} yr^{-1})
$R_{e\,max}$	ecosystem respiration (μmol CO2 m^{-2} s^{-1})
$R_{e\,Tref}$	ecosystem respiration rate at T_{ref} (= 283.16 K) (μmol m^{-2} s^{-1})
RH	relative humidity (dimensionless)
R_n	net radiation (W m^{-2})
RO	runoff (mm)
ρ	air density (kg m^{-3})
ρ_{c*}	friction CO2 concentration (ppm)
SWC	soil water content (m^3 m^{-3})
SWC_{up}, SWC_{lw}	soil water content (m^3 m^{-3})
σ_w, σ_T, σ_q, $\sigma_{\rho c}$	standard deviations of vertical element of wind velocity w, air temperature T, specific humidity q, CO2 concentration ρ_c (m s^{-1}, °C, g kg^{-1} and ppm)
T_{air}, T_{soil}, $T_{surface}$	air, soil and soil surface temperature (°C)
TR	transpiration (mm)

TW	thawing snow (mm)
u_*	friction velocity (m s^{-1})
u, v, w	x, y, z-axis wind velocities (m s^{-1})
VPD	vapor pressure deficit (kPa)
WC	stem biomass (Mg C ha^{-1})
WF	foliage biomass (Mg C ha^{-1})
W_{plant}	plant biomass (Mg C ha^{-1})
WR	root biomass (Mg C ha^{-1})
W_{soil}	litter + mineral soil biomass (Mg C ha^{-1})
Ω	decoupling factor (dimensionless)
Z	reference height (m)
Z_0	roughness length of the grassland (m)
ζ	aerodynamic stability (dimensionless)

Chapter 1 General Introduction

1.1. Background

1.1.1. Global climate change and terrestrial ecosystems

The Earth climate system and the functioning of terrestrial ecosystem interact strongly each other. A change in one affects the other and feedback mechanisms occur. These natural interactions are now disturbed by human activities at an unprecedented scale, both in their rate and in their geographical extent. Global climate change is now in progress. Atmospheric CO_2 concentration has increased by nearly 30% since the pre-industrial 1850, when it was about 280 ppm. It is currently 370 ppm and the Earth's surface has been warmed by 0.6 °C during the twentieth century. Climate and terrestrial ecosystems maintain their interactive relationships through CO_2, water cycles and energy flow. Therefore, climate are strongly affected by changes in the productivity of terrestrial ecosystems, and a major integrated process between living organisms and the atmosphere, and land use and feeds back on productivity of terrestrial ecosystems (Roy et al., 2001).

Considering the global CO_2 budget, there are imbalances between the CO_2 efflux by the combustion of the fossil fuel, cement production and land use change, the CO_2 uptake by the ocean known as the "missing sink" (IPCC, 1990). Eight years ago, IPCC (1996) suggested that "missing sink" may be in several forest ecosystems, tropical and boreal forests, but has not concluded. Houghton (2003) has estimated the "residual" terrestrial CO_2 flux to be as much as -2.9 ± 1.1 Pg C yr^{-1} in 1990s (Table 1.1). It was equivalent to one-third of the CO_2 emission by the fossil fuel and land use change (6.3 ± 0.4 and 2.2 ± 0.8 Pg C yr^{-1}, respectively) and as large as the other two major CO_2 sinks; the atmosphere and the ocean (-3.2 ± 0.2 Pg C yr^{-1}, -2.4 ± 0.7 Pg C yr^{-1}, respectively).

The Kyoto Protocol, agreed in Kyoto COP3 Conference (the 3rd Session of the Conference of the Parties to the United Nations Framework Convention on Climate Change) held in Kyoto, Japan, December 1997, has not only set legally-binding greenhouse gas emission objectives for each industrialized country, but also allowed for an international emissions

trading scheme. During the Kyoto commitment period, carbon sinks may be included in emissions trading by allocating credits for the amount of carbon sequestered; increase of carbon stocks due to human induced forest establishment, afforestation and reforestation. However, the CO_2 sequestration functioning of terrestrial ecosystems, including forests, grasslands and deserts etc., has not been understood sufficiently, and is needed further researches using the scientifically correct method are needed to predict the progress of global warming.

1.1.2. Measurement and modeling of carbon dioxide between the atmosphere and terrestrial ecosystems

The "FLUXNET" research network project, including AmeriFlux, CarboEurope (former EUROFLUX), AsiaFlux, KoFlux, OZFlux etc., will provide current understanding of how CO_2, water cycles and energy flow and the productivities of various type ecosystems interact. The FLUXNET is a global network of micrometeorological tower sites that use eddy covariance methods to measure the exchanges of CO_2, water vapor, and energy between terrestrial ecosystems and atmosphere. At present, over 200 tower sites are operating on a long-term and continuous basis. Researchers also collect data on site vegetation, soil, hydrologic, and meteorological characteristics at the tower sites. Valentini et al. (2000) presented data of net ecosystem carbon exchange, collected between 1996 and 1998 from 15 EUROFLUX forest sites, and suggested that many European forest ecosystems act as carbon sinks. Falge et al. (2002) used the FLUXNET database to research the factors that control seasonal changes in gross primary production (*GPP*) and ecosystem respiration (R_e) in a wide range of terrestrial ecosystems. Their results showed that the seasonality of *GPP* was determined by the life-form (e.g. broad leaf or needle leaf), and that of R_e was affected by the climatic types that are characterized usually by temperature. Wilson et al. (2002) presented data of the warm season partitioning between sensible and latent heat flux, and Bowen ratio at 27 FLUXNET sites over 66 site years. Their result showed that the climatic control on Bowen ratio was quantified using the climatological resistance, which is proportional to the ratio of vapor pressure deficit to net

radiation, and in which there were some general differences between vegetation types and climates.

Recently, many integration models that represent carbon, water and energy exchanges between terrestrial ecosystems and the atmosphere have been developed. Based on approaches to estimate photosynthesis (*GPP*) or *NPP*, these models are divided into three categories; Light Use Efficiency (*LUE*) approach, Biochemical approach, and Carbon assimilation approach (Cramer et al., 1999; Arora, 2002). *LUE* approach, e.g. in CASA (Potter et al., 1993), BIOME2 (Haxeltine et al., 1996), GLO-PEM (Goetz et al., 2000), uses satellite data (NDVI) to determine the temporal behavior of the photosynthetic active tissue, and calculates *GPP* or *NPP* as the product of absorbed photosynthetic active radiation (*APAR*) by a conversion efficiency factor ε. These models can be used to examine the effect of climate variability on *NPP*, but the time of interest is limited to that of the satellite archive. The satellite observations provide some biosphere production. Biochemical approach, e.g. in BIOME-BGC (Running and Hunt, 1993), CARAIB (Warnant et al., 1994), DOLY (Woodward et al., 1995), BIOME3 (Haxeltine and Prentice, 1996), HYBRID (Friend et al., 1997), simulates changes in both structure (vegetation distribution and phenology) and function (biogeochemistry) of ecosystems. Generally, equilibrium between climate and vegetation is assumed, but the models can be turned into dynamical global vegetation models (DGVMs). To date, they have been applied to potential vegetation only. This is in contrast to some of models in the other categories which account for land use either explicitly (CARAIB) or implicitly through the use of satellite observations. Carbon assimilation approach, e.g. in FOREST-BGC (Running and Coughlan, 1988), TEM (McGuire et al., 1992), CENTURY (Parton et a., 1993), FBM (Ludeke et al., 1994), PnET-DAY (Aber et al., 1996), Sim-CYCLE (Ito and Oikawa, 2002), simulates the biogeochemical fluxes on the basis of soil and climate characteristics, using either vegetation maps or biogeography models to prescribe vegetation structure. These models simulate phenology either explicitly or implicitly so that the seasonal activity of a canopy can change in response to climate change.

Sim-CYCLE is a mechanistic model, on the basis of the dry-matter production theory established by Monsi and Saeki (1953). The atmosphere-biosphere CO_2 exchange is composed

of physiological processes, such as gross primary production (*GPP*), autotrophic respiration (*AR*), and heterotrophic respiration (*HR*), and then this simulator enables us to estimate the ecosystem carbon budget in a mechanistic way. Terrestrial ecosystems were conceptualized as a five-compartment system: foliage, stem and branch, root, litter, and mineral soil. Sim-CYCLE also contains water, heat and radiation subschemes to estimate physical environment in terrestrial ecosystems. Ito and Oikawa (2000) performed a model analysis of the effect of climatic perturbations from 1970 to 1997 on the carbon budget of terrestrial ecosystems on a global scale, using Sim-CYCLE. During the 28 yr experimental period, global *NEP* ranged from -2.06 Pg C yr^{-1} (source) in 1983 to +2.25 (sink) Pg C yr^{-1} in 1971, being sufficiently large to give rise to anomalies in the atmospheric CO2 concentration from +0.97 to -1.06 ppmv. Regression analyses demonstrated that annual *ΔNEP*s had the highest correlation with the temperature anomaly on a global scale and the responsiveness was primarily attributable to the temperature sensitivities of plant respiration and soil decomposition, and secondarily to the moisture sensitivity of decomposition. They also showed that an *ENSO* event and a volcanic eruption, affected global *ΔNEP*. Thus, the climate dependencies of global terrestrial ecosystems may contain significant implications not only for the present functioning of atmosphere-biosphere carbon exchange, but also for ongoing global warming.

1.1.3. An alpine meadow ecosystem on the Qinghai-Tibetan Plateau, China

On a global basis, grasslands are one of the most widespread vegetation types. Natural grasslands, including tundra, cover 30% of the Earth's surface and contain 452.3 Pg (1/4 of the Earth's total amount) of organic carbon in both biomass and soil (Adams et al., 1990). Scurlock and Hall (1998) reported that temperate and tropical grasslands sequester 0.5 Pg of carbon a year, and suggested that grassland ecosystems might play an important role as a sink of atmospheric carbon. However, most studies of the carbon budget have been conducted only on lowland grassland ecosystems at elevations below 1500 m; studies on alpine grassland ecosystems at elevations above 3000 m are rare.

In alpine meadow ecosystems on the Qinghai–Tibetan Plateau in the western part of China, abundant light and precipitation allow plants to grow efficiently (i.e. sequester carbon) in spite of the restricted growing season. Additionally, low temperature in winter restricts the decomposition of litter. Therefore, this ecosystem might be an annual net sink of atmospheric CO_2. Alpine meadow ecosystems in China cover approximately 63.7×10^4 km^2 and contain 11.3 Pg of carbon in biomass and soil (Ni, 2002). The soil carbon density of this ecosystem (18.2 kg m^{-2}; Ni, 2002) is much higher than that of savanna (5.4 kg m^{-2}; Adams et al., 1990) and temperate grassland (13.0 kg m^{-2}; Adams et al., 1990) and similar to that of tundra (22.0 kg m^{-2}; Adams et al., 1990), where low temperature also limits the growing season. However, tundra is reported to be at risk of changing from a sink to a source of CO_2 with global warming (Oechel et al., 1993). Will the alpine ecosystem on the Qinghai-Tibetan Plateau also be a net carbon source in the warming climate?

1.2. Purpose of this study

IPCC (2001) reported that if the atmospheric CO_2 concentration rises at a rate of 1.0% yr^{-1}, annual averaged temperatures in 2071-2100 on the Qinghai-Tibetan Plateau will become higher of 3.3-8.4°C in summer (June, July and August) and 3.2-10.9°C in winter (December, January and February) than those in 1961-1990. How will the plants and soil microbes react against those great warming and other climate changes? There are no series of fundamental studies on carbon dioxide flux and its dynamics to answer this question.

To fill the regional blanks in knowledge identified by global network of carbon dynamics studies, in this study, the CO_2 exchange between the atmosphere and an alpine meadow ecosystem was measured and simulated at the Haibei station, Chinese Academy of Sciences on the Qinghai–Tibetan Plateau, China, for short and long-term periods. First, a field measurement by the eddy covariance method was conducted to investigate the diurnal and seasonal relationships between the CO_2 flux and environmental factors from August 2001 to December 2002. Second, a model simulation by the Simulation Model of Carbon cYCle in Land Ecosystem (Sim-CYCLE), developed by Ito and Oikawa (2002), has been made to investigate

the interannual relationship between the CO_2 dynamics and climate changes from 1981 to 2000 using the climate data derived at the Haibei meteorological observation field for 20 years. Finally, the differences in the relationships between the CO_2 dynamics and environmental factors on the different temporal period were analyzed and the influences of future climate changes on the CO_2 dynamics were discussed.

The objectives of this study are summarized as follows:

To clarify the daily, seasonal and interannural patterns of CO_2 flux.

To investigate the relationship between CO_2 flux and the environmental factors.

To predict the influences of global warming on the CO_2 flux and dynamics in an alpine meadow ecosystem.

1.3. Composition of the thesis

Chapter 1 introduces the relationship between the global climate change and terrestrial ecosystem, and the global network of flux measurement and model studies to investigate that relationship, and summarizes the objectives of this study. Chapter 2 describes the geographical and vegetation characteristics at the study site. Chapter 3 clarifies the diurnal changes of the CO_2 flux measured by the eddy covariance method and the relationship on the environmental factors in the field study. Chapter 4 clarifies the seasonal changes of the CO_2 flux measured by the eddy covariance method and the relationship on the environmental factors in the field study. Chapter 5 clarifies the interannual changes of the CO_2 dynamics simulated by the Sim-CYCLE and their relationships on the climate changes from 1981-2000 in the model analysis. Chapter 6 summarizes the differences in the ecosystem responses to the environmental changes between the various time scales, and predicts the influences of future climate change. Chapter 7 gives the conclusion of this study.

Table 1.1. Global carbon budgets for the 1980s and 1990s (Pg C yr^{-1}).

	1980s	1990s
Fossil fuel emissions	5.4 ± 0.3	6.3 ± 0.4
Atmospheric increase	3.3 ± 0.1	3.2 ± 0.2
Oceanic uptake	-1.7 ± 0.6	-2.4 ± 0.7
Net terrestrial flux	-0.4 ± 0.7	-0.7 ± 0.8
Land-use change	2.0 ± 0.8	2.2 ± 0.8
Residual 'terrestrial' flux	-2.4 ± 1.1	-2.9 ± 1.1

From Houghton, R.A. (2003).

Chapter 2 Site description

Measurements and estimations of carbon, water vapor and sensible heat fluxes and environmental factors were conducted at the Haibei Alpine Meadow Ecosystem Research Station, Northwest Plateau Institute of Biology, Chinese Academy of Science (lat 37°29–45′N, long 101°12–23′E; 3250 m a.s.l.; Figs. 2.1 and 2.2). The research station is located in a large valley oriented northwest–southeast in northeast Qinghai-Tibetan Plateau, and surrounded on all sides by the Qilian Mountains. The average altitude of the mountains and the valley are 4000 and 2900–3500 m a.s.l.. The Datong River passes from north to the south. The landscape is characterized by large mountain ranges with steep valleys and gorges interspersed with relatively level and wide inter-mountain grassland basins.

The climate at Haibei Station is characterized by low temperature and limited precipitation. The annual average temperature and precipitation for 1981–2000 were –1.7 °C and 561 mm. In the growing season from May to September, the plentiful sunshine and rainfall (80% of annual total rainfall) allow plants to grow effectively, although harmful UV-B radiation is high (Li and Zhou, 1998).

The soil is a clay loam; its average thickness is 65 cm. The surface 5–10 cm horizons, which are classified as Mat Cry-gelic Cambisols according to the Chinese national soil survey classification system (Institute of Soil Science and Chinese Academy of Sciences, 2001), are wet and rich in organic matter.

The plant community is dominated mainly by three major perennial sedges, *Kobresia humilis*, *K. pygmaea* and *K. tibetica* (Cyperaceae), and by one dwarf shrub species, *Potentilla fruticosa* (Rosaceae) (Li and Zhou, 1998). The plants start to grow in May, when the air temperature starts rising, and reach maximum aboveground biomass (342 g d. w. m^{-2}; average for 1980–1993) in July and August, when the air temperature and precipitation are the highest of the year. Their aboveground parts die in October (Li and Zhou, 1998). During the growing season, the plants accumulate photosynthates in belowground storage organs for new shoot

grouth in next spring. This characteristic is a feature of alpine grassland plants (Li and Zhou, 1998).

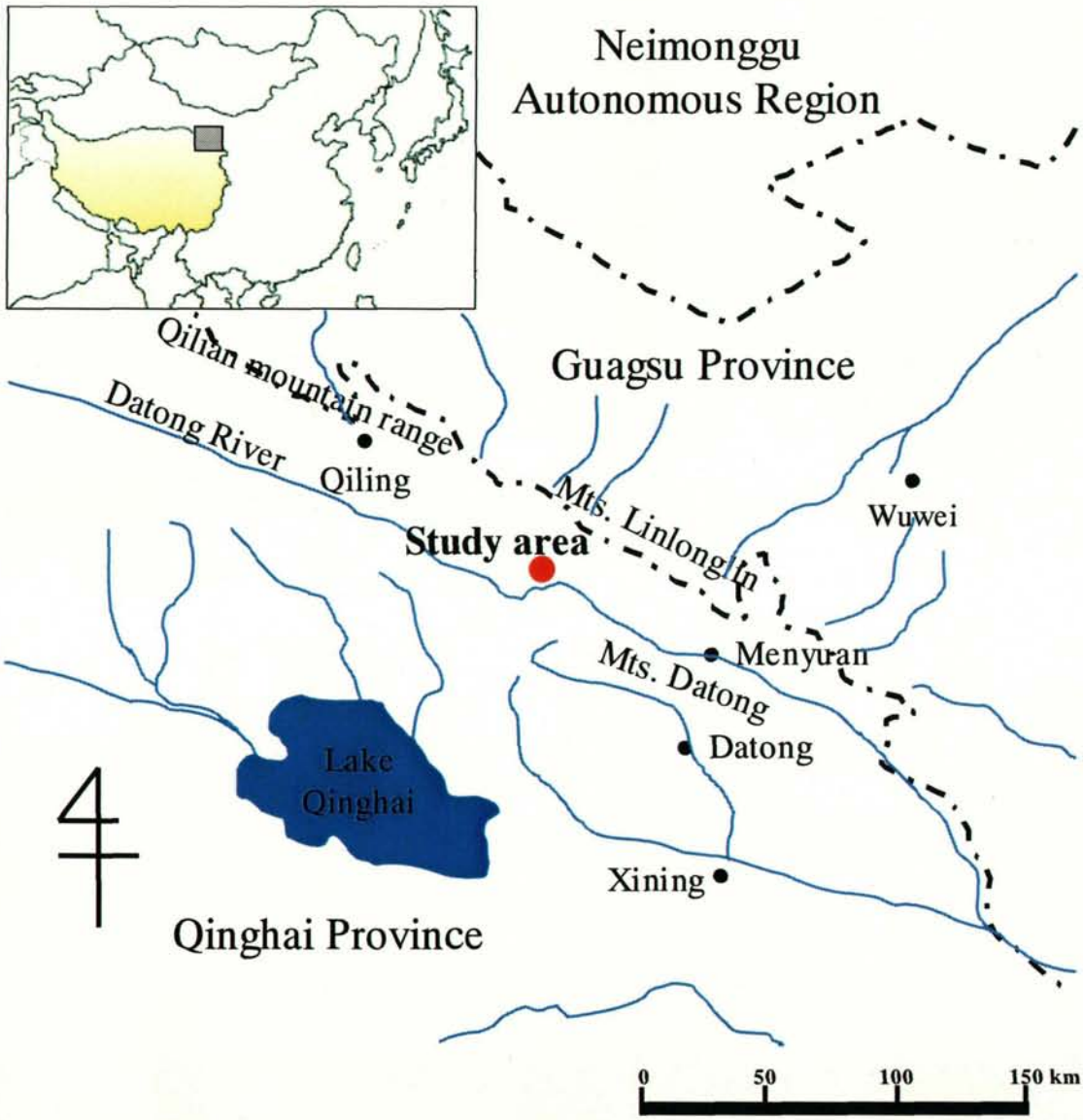

Figure 2.1. Location of the study area

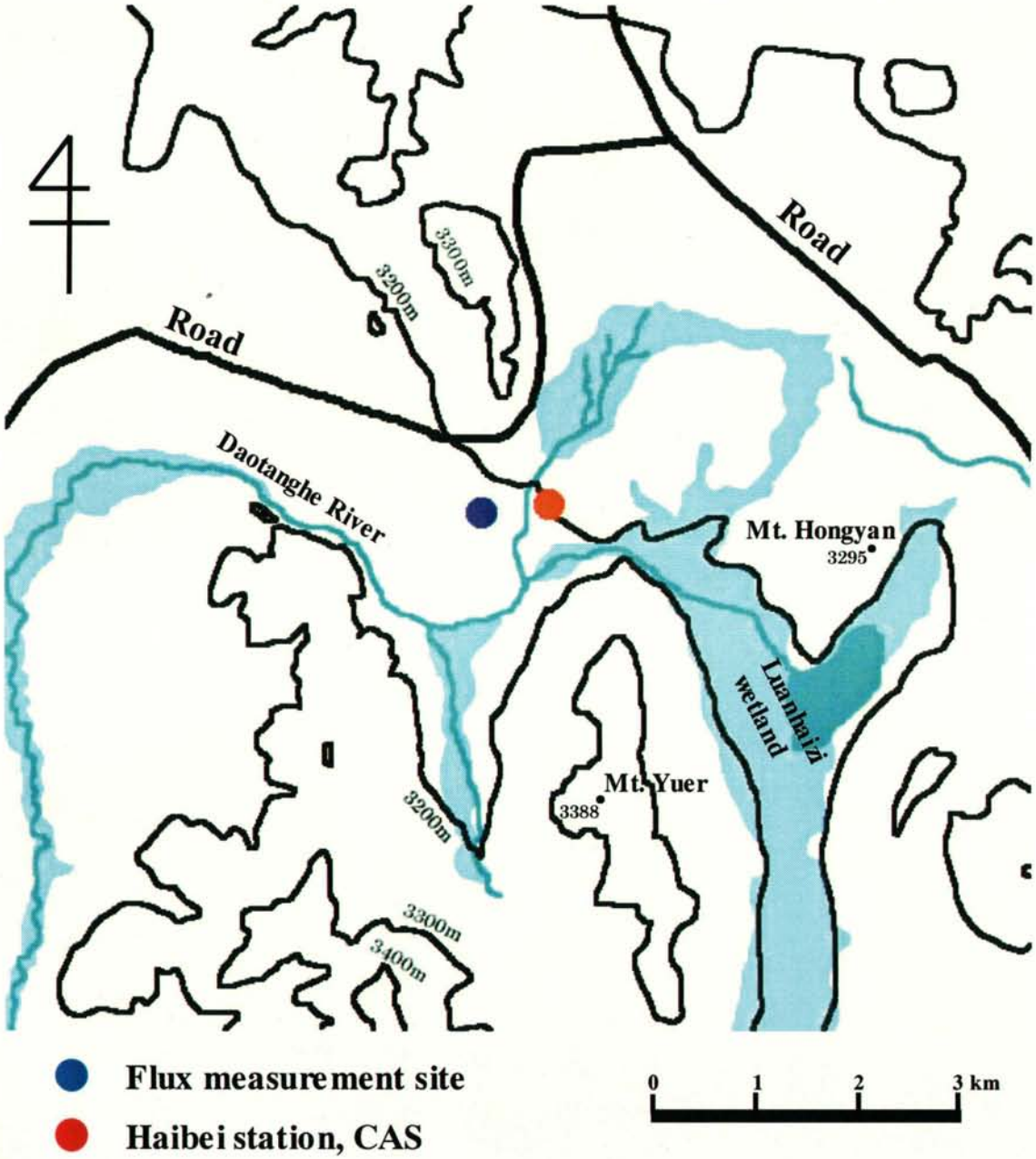

Figure 2.2. Map of the observation site

Chapter 3 Diurnal changes of the CO_2 exchanges

3.1. Introduction

The Qinghai-Tibetan Plateau covers vast area, about 2.5×10^6 km^2 (Zheng et al., 2000), and may contribute significantly to the CO_2, water and energy exchange between the atmosphere and vegetation on a regional or even a global scale. However, in contrast with extensive information obtained in recent years about water and energy exchange (Yasunari, 2001), little evidence is available for understanding CO_2 exchange and its relation to environmental controls in this unique ecosystem.

Eddy covariance method that acquires the fluctuations of wind speed, CO_2 concentration etc. directly, enable us to measure the CO_2 flux without any assumption and has been used widely in various terrestrial ecosystems (Aubinet et al., 2000; Baldocchi et al., 2001; Yamamoto et al., 2001). Net ecosystem exchange (*NEE*) data measured by this method shows that knowledge of leaf and whole plant physiology can be used to interpret whole system variability (e.g. Hollinger et al., 1994; Amthor et al., 1994). Furthermore, Valentini et al. (2000) divided daytime *NEE* data from a global network of tower observations of flux into gross primary production (*GPP*) and ecosystem respiration (R_e) by extrapolating site-specific exponential relationships between nocturnal soil temperature and CO_2 efflux. This approach allows the diurnal pattern and amplitude of *GPP* and R_e to be investigated.

From August 2001 to December 2002, long-term CO_2, water vapor and energy flux measurements using the eddy covariance method were carried out in an alpine meadow on the Qinghai-Tibetan Plateau. Additionally, measured net ecosystem exchanges were divided into *GPP* and R_e. The aims of this chapter are 1) to show the diurnal changes *NEE*, *GPP* and R_e, 2) to clarify the environmental controls on the diurnal changes of the CO_2 fluxes.

3.2. Materials and Methods

3.2.1. Micrometeorology

Micrometeorological measurements were conducted at the winter pasture in the Haibei station of CAS from 9 August to 31 December 2002 (Fig. 2.2). The study site is flat with a fetch of at least 250 m in all directions. Net radiation and photosynthetic photon flux density (*PPFD*) were measured at 1.5 m above the ground with a net radiometer (CNR-1, Kipp & Zonen Inc., Saskatoon, Saskatchewan, Canada; Table 3.1) and a *PPFD* meter (LI-190SB, Li-Cor, Lincoln, NE, USA). Air temperature and humidity were measured at 1.1 and 2.2 m above the ground with a humidity and temperature probe (HMP45C, Vaisala, Helsinki, Finland). Wind speed was measured at 1.1 and 2.2 m above the ground with cup anemometers (034A-L and 014A, R. M. Young Co., Traverse, MI, USA). Soil heat flux was measured at 0.02 m below the ground at three points with heat plates (HFT-3, Campbell Scientific Inc., Logan, UT, USA). Soil temperature was measured at 0.025, 0.05, 0.1, 0.2, 0.3, 0.4, 0.5, 0.6, and 0.7 m below the ground with copper-constantan manufactured thermocouples. Soil water content was measured at 0.05, 0.2, and 0.5 cm with time-domain reflectometry sensors (CS-615, Campbell Scientific Inc.). Soil surface temperature was measured at three points in a 1-m^2 area with thermistor thermometers (107 probe, Campbell Scientific Inc.). Rainfall was measured at 0.7 m above the ground with a tipping bucket (TE525MM, Campbell Scientific Inc.). Fifteen-minute averages of all data were logged by an analog multiplexer (AM416) and a digital micrologger (CR23X, Campbell Scientific Inc.) (Fig. 3.1-3.5).

3.2.2. Eddy covariance method

3.2.2.1. Fundaments of the eddy diffusion flux calculations

1. Definition of the turbulent flow

Figure 3.6 shows the time series of x, y, z-axis wind velocities (u, v, w), air temperature (T_a), specific humidity (q) and carbon dioxide concentration (ρ_c) at the Haibei grassland in winter, 2003 at the frequency of 20 Hz by a sonic anemometer and an open-path Infra-red gas analyzer (the details are in the section 3.2.2.2). Those scalar values were disturbed, and there

seems to be no relationship with each other. This fluctuation is caused by the eddy generation and passage, called as a 'turbulent flow'.

2. Calculation of the turbulent transfer

The vertical turbulent transfer of substance and energy is generated by the turbulent flow and the vertical gradient of substance concentrations and temperatures. The turbulent flux of voluntary substance or energy is represented as follows:

$$Qc = \overline{w(\rho C)} \tag{3.1}$$

$$= \rho\overline{(wC)} \tag{3.2}$$

where Qc is the turbulent flux of substance or energy (kg m^{-2} s^{-1}), w is the vertical transfer velocity of air (m s^{-1}), C is the voluntary substance concentration (kg kg air^{-1}), ρ is the air density (kg m^{-3}). The upper bar means an average. The air density is assumed to be constant in Eq. (3.2). w and C are divided into average and fluctuation components as follows;

$$w = \overline{w} + w' \tag{3.3}$$

$$C = \overline{C} + C' \tag{3.4}$$

where the prime mark means fluctuation value. Eqs. (3.3) and (3.4) are inserted into Eq. (3.2) as follows:

$$Qc = \rho\overline{w}\overline{C} + \rho\overline{w'}\overline{C} + \rho\overline{w}\overline{C'} + \rho\overline{w'C'} \tag{3.5}$$

$$= \rho\overline{w'C'} \tag{3.6}$$

where $\overline{w'}$ and $\overline{C'}$ are zero. $\overline{w}$, the average vertical component of air transfer, is assumed to be zero. When sensible heat (H), latent heat (λE) and carbon dioxide fluxes ($FCO2$) are

calculated, C is assigned for air temperature $T=\overline{T}+T'$ (K), a specific humidity $q=\overline{q}+q'$ (kg kg^{-1}) and atmospheric CO2 concentration $\rho_c=\overline{\rho_c}+\rho_c'$ (mg CO2 m^{-3}), respectively as follows:

$$H = C_p \rho \overline{w'T'} \tag{3.7}$$

$$\lambda E = \lambda \rho \overline{w'q'} \tag{3.8}$$

$$FCO_2 = \overline{w'\rho_c'} \tag{3.9}$$

where ρ is the air density (kg m^{-3}), C_p is the specific heat at constant pressure (J kg^{-1} K^{-1}), λ is the latent heat (J kg^{-1}) as shown in the next:

$$\rho = 100 \times P/(287.1 \times (T_a + 273.16) \times (1 + 0.61 \times q)) \tag{3.10}$$

$$C_p = 1004.7 \tag{3.11}$$

$$\lambda = (2.501 - 0.00237 \times T_s) \times 10^6 \tag{3.12}$$

where P is the air pressure (hPa), T_a is the air temperature (°C), and T_s is the soil surface temperature (°C).

3. Power spectrum of turbulent fluctuation -Verification of turbulent measurement-

To confirm the successful acquisition of turbulent flow across all frequency bands contributing the flux calculation, the power spectrums of each scalar fluctuation should be checked. If acquiring successfully, the spectrum in high frequency band should conform the concept of an inertial sub-range, a part of equilibrium range of turbulent flow (Kaimal, 1988). An equilibrium range is high frequency zone that comprises the local isotropic under which condition the low frequency eddy, caused by the obstruction, is transferred by inertial force and

pressure. The inertial sub-range exist in the frequency range, in which energy does not generate and disappear and energy is only handed off to smaller scale filed, between the energy holding frequency k_0 and the viscidity dispersing frequency k_d. This sub-range usually generated in the atmospheric boundary layer in the condition of high Reynolds number. In this sub-range, the energy spectrum $Fx(\kappa)$, is with no statistically relation to energy holding eddy and viscidity relevant eddy, is determined by energy dissipation rate ε exclusively and described in the dimension analysis as follows:

$$Fx(\kappa) = \alpha \varepsilon^{2/3} \kappa^{-3/5} \tag{3.13}$$

where κ is wave number and α is defined as an absolute constant.

Existence of inertial sub-range in the energy spectrum shows that the eddy covariance measurement instruments acquire the turbulent flow through high frequency zone normally. Although the spectrum theory is usually formulated in wave number space, in the most of turbulent flow measurement, the spectrum is able to be converted into the frequency scale in their spatial scales using the formulation of a Taylor's hypothesis. In the u-spectrum, conversion is described as follows:

$$\kappa = 2\pi f / \overline{u} \tag{3.14}$$

where f is the frequency. The spectrum of frequency $Su(f)$ is defined as follows:

$$\int_0^\infty Fx(\kappa) d\kappa = \sigma_x = \int_0^\infty Su(f) df \tag{3.15}$$

where σ_x is variances of wind speed and substance concentration. Eq. (3.15) is assigned by Eq. (3.14) and differentiated by f as follows:

$$\frac{2\pi}{\overline{u}} Fx\left(\frac{2\pi}{\overline{u}}\right) = Su(f) \tag{3.16}$$

that is:

$$\kappa Fx(\kappa) = fSu(f) \tag{3.17}$$

Next, the similarity function ϕ_ε of the dissipation rate of turbulent movement energy E is defined as follows:

$$\phi_\varepsilon = kz\varepsilon / u_*^{\,3} \tag{3.18}$$

where k is the karman constant (dimensionless), z is height (m), u_* is the friction velocity (m s^{-1}).

The u-spectrum of inertial sub-range is presented in conformity with similarity theory of surface boundary layer as follows:

$$\begin{aligned}\frac{fS_u(f)}{u_*^{\,2}} &= \frac{\alpha_1}{(2\pi)^{2/3}}\left(\frac{\varepsilon^{2/3} z^{2/3}}{u_*^{\,2}}\right)\left(\frac{fz}{u}\right)^{-2/3} \\ &= \frac{\alpha_1}{(2\pi k)^{2/3}} \phi_\varepsilon^{\,2/3}\left(\frac{fz}{u}\right)^{-2/3}\end{aligned} \tag{3.19}$$

where α_1 is uniform value. If the $fz/\overline{u}$ is assumed as a dimensionless frequency n:

$$\frac{fS_u(f)}{u_*^{\,2}\phi_\varepsilon^{\,2/3}} = \frac{\alpha_1}{(2\pi k)^{2/3}} n^{-2/3} \tag{3.20}$$

The spectrum in the inertial sub-range is described by a line with the slope of –2/3 in the logarithmic graph.

Figure 3.7 shows the power spectrum of x, y, z-axis wind velocities (u, v, w), air temperature (T_a), specific humidity (q) and carbon dioxide concentration (C) measured at the Haibei grassland for 12:00-12:15, 13, Aug., 2002. Vertical axes of the figures are normalized with the frequency. The spectrums of each variable are proportional to frequencies in the slope of –2/3 within the inertial sub-range. This confirms that the measurements of turbulent fluctuations are acquired normally in this study.

4. Cross spectrum of turbulent fluctuation -Determination of sampling frequency and calculating period-

All turbulent fluctuation, which contributes to flux calculations, should be acquired between sampling (cut-off) frequency and average time periods, and calculated flux must retain constancy. These frequency and time periods should be determined after checking the cross-spectrum of each fluctuation.

Wyngaard and Cote (1972) present that the cross-spectrum declines in the slope of –7/3 within the inertial sub-range of uw and wT in their empirical equation. In this sub-range which z/L and n are only normalized cross-spectrum, w and T are described in the logarithmic scale as follows:

$$-\frac{fC_{wT}(f)}{u_*^2} \propto G(z/L)n^{-4/3} \tag{3.21}$$

where $G(z/L)$ is determined experimentally as a function of z/L.

Figure 3.8 shows the cross spectrum between z-axis wind velocities (w) and air temperature (T_a), specific humidity (q) and carbon dioxide concentration (C) at the Haibei grassland for 12:00-12:15, 13, Aug., 2002. Vertical axes of the figure are normalized with the frequency. The cross spectrums of each variable are proportional to frequencies in the slope of

–4/3 within the inertial subrange. The cross spectrum between vertical wind w' and air temperature, specific humidity and CO_2 concentration c' showed that co-variance was close to zero when the noise was at frequencies lower than 0.002 Hz (8.3 min per cycle; Fig. 3.8). A period of 15 min was thus enough to avoid the effect of noise. The mean, variance, and covariance values were then calculated and logged for every 15 min.

3.2.2.2. Measurement of eddy diffusion fluxes

Wind speed and sonic virtual temperature were measured at 2.2 m above the ground with a sonic anemometer (CSAT-3, Campbell Scientific Inc.). Carbon dioxide and water vapor concentrations were also measured at the same height with an open-path infra-red gas analyzer (CS-7500, Campbell Scientific Inc.). Wind speed, sonic virtual temperature, and CO_2 and H_2O concentrations were sampled by the digital micrologger at a rate of 10 Hz.

3.2.2.3. Correction of measured turbulent flux data

1. WPL correction

In a CO_2 flux calculation, the air density variation was taken into account in the calculation processing of turbulent flux, as supposed by Webb et al. (1980). CO_2 flux (FCO_2) was given in the next:

$$FCO_2 = \overline{w'\rho_c'} + \overline{w'\rho_q'}\left(\mu\,\overline{\rho_c}/\overline{\rho_a}\right) + \overline{\rho_c}\left(1+\mu\sigma\right)\left(\overline{w'T'}/\overline{T}\right) \tag{3.22}$$

where FCO_2 is the CO_2 flux (mg CO_2 m^{-2} s^{-1}), ρ_q and ρ_a are densities of water vapor and air (kg m^{-3}), μ is the ratio of dry air mass to water vapor mass (kg kg^{-1}), σ is the ratio of $\overline{\rho_q}$ to $\overline{\rho_a}$.

2. Coordinate rotation, trend removing, and water vapor correlation

In this study, flux data correction, e.g. coordinate rotation, trend removing and water vapor correlation, are not enforced to all sampled fluctuation data. However, the influences of un-correction on the calculated flux are examined for 10 days in July, 2002, using fluctuation

data sampled at the frequency of 10 Hz, and implicit estimation error in the flux data are discussed.

Coordinate Rotation Although sonic anemometer is usually settled horizontally, slight inclination of instruments will generate for long-term experiment. The landform, installation mast and instrument body also generate the wind disturbance and bias the horizontal wind (Fig. 3.9) and $\overline{w}$ will not become zero. In that situation, it is necessary to rotate the coordinates of wind vectors by the degrees of blowing up and down angle (ψ).

First, horizontal wind directions are rotated as follows:

$$\theta = \tan^{-1}\left(\frac{U_Y}{U_X}\right) \tag{3.22}$$

$$U = U_X \cos\theta + U_Y \sin\theta \tag{3.23}$$

$$V = -U_X \sin\theta + U_Y \cos\theta \tag{3.24}$$

where θ is the degrees of anticlockwise rotation angle from the center line of anemometer, U_X and U_Y are horizontal and vertical wind velocities in the direction toward the center line of anemometer, U and V are x- and y-axis wind velocities after coordinate rotation. After this coordinate rotation, $\overline{U}$ and $\overline{V}$ become zero.

Second, vertical wind directions are rotated as follows:

$$\psi = \tan^{-1}\left(\frac{\overline{W}}{\overline{U}}\right) \tag{3.25}$$

$$U_c = U\cos\psi + W\sin\psi \tag{3.26}$$

$$W_c = -U\sin\psi + W\cos\psi \tag{3.27}$$

where ψ are the degrees of blowing up and down angle, $\overline{U}$ and $\overline{W}$ are average horizontal and vertical wind velocities, U_c and W_c are x- and z-axis wind velocities after coordinate rotation. After this coordinate rotation, U_c and W_c become zero.

Trend removing Gradual changes of air temperature and humidity in the morning and evening, or instrumental signal drift may bias the averaged data during 15 min average period. In those cases, the differences from the average will be bigger apparently, and this affects the turbulent statistical values, e.g. standard deviation and covariance. Consequently, trend values derived from regression line against time series, are subtracted from the fluctuation data.

Water vapor correction Virtual sonic temperatures derived from sonic anemometer, was affected from the fluctuations of atmospheric water vapor. The water vapor correction is necessary to measure temperature fluctuations and calculate sensible heat flux accurately (Tsukamoto et al., 2001).

$$T = T_0(1 - 0.514q) \tag{3.28}$$

where T is corrected air temperature (°C), and T_0 is uncorrected air temperature (°C).

Figures 3.10, 3.11, 3.12 make comparisons between corrected fluxes and uncorrected fluxes in sensible and latent heat and CO_2 flux calculations. Each regression line slope shows small differences, within 4%, between corrected fluxes and uncorrected fluxes. This indicates that it is unnecessary to apply these three corrections to turbulent fluctuation data.

3.2.2.4. Validity of measured flux data

1. Flux dependent on the wind direction

Figure 3.13 shows the dependence of sensible and latent heat and CO_2 fluxes on the wind direction. The black line in the figure indicates moving average of 100 points. Sensible heat flux H fluctuates between 90 and 270 degrees, and show two minimum peaks in 160 and

260 degrees. This holds in the case of latent heat λE and also hold in the case of CO_2 flux FCO_2 in inverse. It is considered to be due to biased average wind flow, as shown in Figure 3.8, disturbed by installation mast and data logger box settled in the direction of 180 degrees. However, moving average line shows small bias in the measured fluxes, indicating that it is unnecessary to rotate coordination of turbulent fluctuation data.

2. Dimensionless universal function

(1) Monin-Obukhov similarity

According to Monin and Obukhov (1954), in ideal surface boundary layer, i.e. keeping steady state and horizontal homogeneity, all kinds of statistics concerning wind velocity and temperature in the turbulent flow, can be described by momentum τ/ρ, vertical heat flux $H/C_p\rho$ and buoyancy parameter g/T at ground surface, except for height z. This is called "Monin-Obukhov similarity theory".

From the three fundamental quantities mentioned above, dimensional scales of velocity, temperature and length, which describe the statistics of wind velocity and temperature, are drawn as follows:

$$u_* = \left(\frac{\tau}{\rho}\right)^{1/2} = \left(-\overline{u'w'}\right)^{1/2} \tag{3.29}$$

$$T_* \equiv -\frac{H}{C_p \rho u_*} = -\frac{\overline{w'T'}}{u_*} \tag{3.30}$$

$$L = \frac{-u_*^{\,3} T_0}{kg\overline{w'T_0'}} \tag{3.31}$$

where τ is momentum (kg m^{-1} s^{-2}), T_* is friction temperature (K), L is Monin-Obukhov length (m), g is acceleration of gravity (= 9.8 m s^{-2}), and T_0 is temperature near ground surface (°C)

According to Monin-Obukhov similarity theory, the statistics of wind velocity and temperature are described by z/L exclusively as follows:

$$\frac{F}{F_*} = g_F\left(\frac{z}{L}\right) \tag{3.32}$$

where F is the statistics of wind velocity and air temperature near ground surface, F_* is the scales of velocity, temperature and length, and g_F is universal function of F.

(2) Standard deviation of turbulent fluxes σ and dimensionless universal function ϕ

According to Monin-Obukhov similarity theory, the standard deviations of wind velocity, air temperature, specific humidity and CO2 concentration are expressed by z/L exclusively as follows:

$$\frac{\sigma_w}{u_*} = \phi_w\left(\frac{z}{L}\right) \tag{3.33}$$

$$\frac{\sigma_T}{T_*} = \phi_T\left(\frac{z}{L}\right) \tag{3.34}$$

$$\frac{\sigma_q}{q_*} = \phi_q\left(\frac{z}{L}\right) \tag{3.35}$$

$$\frac{\sigma_{\rho_c}}{\rho_{c*}} = \phi_{\rho_c}\left(\frac{z}{L}\right) \tag{3.36}$$

where σ_w, σ_T, σ_q and $\sigma_{\rho c}$ are standard deviations of vertical element of wind velocity w, air temperature T, specific humidity q, CO2 concentration ρ_c, q_* is friction specific humidity ($=E/\lambda\rho u_* = \overline{w'q'}/u_*$), ρ_{c*} is friction CO2 concentration ($=FCO2/u_* = \overline{w'\rho_c'}/u_*$) and ϕ is universal function of all kinds of fluctuations.

(3) ϕ under strongly unstable condition

Strongly unstable condition, under which vertical convection becomes near natural convection state, makes L extremely small; H becomes bigger and u_* becomes near zero. In the case, L is useless scale and universal functions are described by L, which eliminates u_* in itself, as follows:

$$\phi_w = \frac{\sigma_w}{u_*} \approx \left(-\frac{z}{L}\right)^{\frac{1}{3}} \tag{3.37}$$

$$\phi_T = \frac{\sigma_T}{T_*} \approx \left(-\frac{z}{L}\right)^{-\frac{1}{3}} \tag{3.38}$$

$$\phi_q = \frac{\sigma_q}{q_*} \approx \left(-\frac{z}{L}\right)^{-\frac{1}{3}} \tag{3.39}$$

$$\phi_{\rho_c} = \frac{\sigma_{\rho_c}}{\rho_{c*}} \approx \left(-\frac{z}{L}\right)^{-\frac{1}{3}} \tag{3.40}$$

Thus, the dimensionless universal functions are in relation to cube root or minus cube root of stability under strongly unstable condition. These are founded in the field experiments, e.g. Kader and Yaglom (1990), Kaimal and Finnigan (1994) and Ohtaki (1985).

Figure 3.14 shows the relationship between aerodynamic stability and dimensionless universal functions under unstable conditions from 14 Jan. to 31 Dec., 2002. Data show 15 min average values. Universal functions are distributed along the lines with the slopes of 1/3 (σ_w) or −1/3 (σ_T, σ_q, $\sigma_{\rho c}$) against the stability -ζ under unstable condition (-ζ >= 0.2), and this confirms the reasonability of sampling turbulent fluxes in this study.

(4) ϕ under near neutral condition

Figure 3.15 shows the relationship between aerodynamic stability and dimensionless universal functions under near neutral conditions from 14 Jan. to 31 Dec., 2002. Data shows 15 min average values. The geometric means of σ_w/u_* for neutral condition (-0.1 < z/L <0.1) was 1.08 in this study site and is similar to 0.93-1.14 reported by Yaglom (1977) and slightly lower

then 1.2 reported by Ohtaki (1985) for the paddy field, 1.2-1.4 compiled by Pasquille (1974). The σ_T/T_*, σ_q/q_*, and $\sigma_{\rho c}/\rho c_*$ are scattered for neutral condition ($-0.1 < z/L < 0.1$), but and are also distributed around the reported mean values; σ_T/T_*, 2.4 reported by Phelps and Pond (1970) for over water, σ_q/q_*, 2.6 reported by Ohtaki (1985) and 2.3 reported by Phelps and Pond (1970) for over water, $\sigma_{\rho c}/\rho_{c*}$, 3.5 reported by Ohtaki (1985) as a geometric mean (-z/L 0-0.14).

3. Energy imbalance

Historically, energy balance closure has been accepted as an important test of eddy covariance data, and a number of individual sites within the FLUXNET network report energy balance closure as a standard procedure (Wilson, et al, 2002). In this study, the energy balance ratio (*EBR*) between $H+\lambda E$ and $Rn-G$ is also examined.

Figure 3.16 shows the energy balance during 2001 and 2002. The regression coefficients show the surface energy fluxes ($H+\lambda E$) are underestimated by 41 % (2001) and 30 % (2002) relative to estimates of available energy ($Rn-G$). The seasonal changes of *EBR* may be constant for a whole year (Fig. 3.17), but the *EBR* is slightly larger in summer than in winter. The *EBR* shows the apparent diurnal changes in Figure 3.18. During morning and evening transition periods, when the mean value of $Rn-G$ was close to zero, the *EBR* is not especially meaningful. The *EBR* dependence on the wind direction, shown in Fig. 3.19, was lower in near 160° than other directions. The effect of friction velocity on the *EBR* was analyzed separately for daytime and nighttime data using all 15 min data in 2002 (Fig. 3.20). In daytime, when the friction velocity exceeded 0.3 m s^{-1}, the *EBR* might be convergent to near 0.7. In nighttime, there was no obvious trend in the relationship.

3.2.3. Omega factor calculation

The Penman-Montieth model, the most popular evapotranspiration model, uses an electrical analogy to treat vertical water vapor movement in the Soil-Plant-Air-Continuum (SPAC) circulation, and is the one-dimensional model of crop evapotranspiration from a single source. Evapotranspiration from the canopy to atmosphere is obtained as follows:

$$\lambda E = \frac{\Delta(R_n - G) + \rho c_p D / r_a}{\Delta + \gamma(1 + r_c / r_a)} \tag{3.41}$$

in which Δ is the slope of the saturation vapor pressure versus temperature curve (hPa K^{-1}), ρ is the density of air (kg m^{-3}), C_p is the specific heat at constant pressure (J kg^{-1} K^{-1}), D is the vapor pressure deficit (h Pa), r_c is the canopy resistance (s m^{-1}), and r_a is the aerodynamic resistance (s m^{-1}). Jarvis and McNaughton (1986) rewrote the Penman-Monteith model as follows:

$$\lambda E = \Omega \lambda E_{eq} + (1 - \Omega)\lambda E_{imp} \tag{3.42}$$

$$\lambda E_{imp} = \frac{\rho c_p D}{\gamma r_c} \tag{3.43}$$

$$\Omega = \frac{\Delta + \gamma}{\Delta + \gamma(1 + r_c / r_a)} \qquad (0 \le \Omega \le 1) \tag{3.44}$$

where $\lambda Eimp$ is the imposed evapotranspiration rate and Ω is the decoupling factor. When Ω is near 1, the evapotraspiration rate is almost dominated by the available energy. λEeq, the equilibrium evaporation, is defined as the evaporation rate attained by a free surface after it saturates the atmosphere (Penman, 1948). Although this condition is rarely found in the field, comparing measured evaporation with predicted equilibrium evaporation helps diagnose the balance between supply capacity and atmospheric demand for evaporation. Equilibrium evaporation is defined as follows (Jones, 1992):

$$lE_{eq} = \frac{\Delta(R_n - G)}{\Delta + \gamma} \tag{3.45}$$

where lE_{eq} is the equilibrium evaporation (W m^{-2}), Δ is the slope of the relation between saturation vapor pressure and temperature (hPa $°C^{-1}$), R_n is the net radiation (W m^{-2}), G is the soil heat flux (W m^{-2}), and γ is the psychrometric constant (hPa $°C^{-1}$).

3.2.4. Bowen ratio calculation

The Bowen ratio β is defined as follows:

$$\beta = H/\lambda E \tag{3.46}$$

3.2.5. Canopy resistance calculation

Canopy resistance, or diffusion flux resistance, (i.e. the stomatal resistance of a "big leaf") is determined by the physiological activity of the canopy plants in the Penman–Monteith evaporation theory (Monteith, 1972). By transformation of the Penman–Monteith equation, canopy resistance is derived from environmental factors as follows:

$$R_{canopy} = R_{aero}\left[\frac{\Delta(R_n - G - \lambda E) + \rho C_p VPD/R_{aero}}{\gamma \lambda E} - 1\right] \tag{3.47}$$

where R_{canopy} is the canopy resistance (s m^{-1}); R_{aero} is the aerodynamic resistance (=1/ku ln(Z-d/Z_0) (s m^{-1})); k is von Karman's constant (= 0.4); u_* is the friction velocity (m s^{-1}); Z is the reference height (= 2.2 m); d is the zero plane displacement (m) (= 0.63 x canopy height (m)); Z_0 is the roughness length of the grassland (m) (= 0.13 x canopy height (m); Montieth, 1973).

3.2.6. *GPP* and R_e calculations

Ecosystem respiration R_e was measured directly during nighttime periods with strong turbulence (as a *NEE* at a friction velocity $u_* > 0.2$ m s^{-1}), and was extrapolated to other periods by using exponential regressions of measured R_e with soil temperature at a depth of 5 cm with an Arrhenius equation reported by Lloyd and Taylor (1994):

$$R_e = R_{e,T_{ref}} \exp\left[\left(E_a/R\right)\left[\frac{1}{T_{ref}} - \frac{1}{T_K}\right]\right], \quad (3.48)$$

where R_e is nighttime ecosystem respiration rate (μmol CO_2 m^{-2} s^{-1}), $R_{e,Tref}$ is ecosystem respiration rate at T_{ref} (= 283.16 K), and E_a is the activation energy (J mol^{-1}). These two parameters are assigned as the site-specific parameters. R is a gas constant (8.134 J K^{-1} mol^{-1}), and T_K is the soil temperature at a depth of 5 cm T_{soil}. $R_{e,Tref}$ was evaluated for every month. E_a was evaluated from a regression of all R_e data in 2002 against T_{soil} as a constant value throughout the year (81 519 J mol^{-1}).

Values of *GPP* was calculated as the difference between *NEP*, as a negative value of *NEE*, and R_e as follows:

$$GPP = NEP + R_e, \quad (3.49)$$

where *GPP* is ecosystem gross primary production (μmol m^{-2} s^{-1}), and *NEP* is net ecosystem production as CO_2 uptake flux (–*NEE*) (μmol m^{-2} s^{-1}).

3.2.7. LAI and biomass sampling

Aboveground biomass and *LAI* were investigated within a radius of 250 m around the measuring station once in 2001 (20 August) and nine times from May to September in 2002. The aboveground plants were cut at ground levels in five randomly placed 0.5-m^2 quadrates. *LAI* was then measured with an *LAI* meter (LI-3100, Li-Cor). After oven drying for 48 h at 70 °C, the dry matter was weighed on an electric balance.

3.3. Results

3.3.1. Micrometeorology and vegetation growth

Figure 3.21 shows the seasonal changes of monthly averaged diurnal changes of air temperature T_{air}. In summer, July 2002, T_{air} reached a minimum of 5.5 °C at 0600 and a maximum of 16.9 °C at 1500. In winter, January 2002, T_{air} reached a minimum of –24.8 °C at 0900 and a maximum of –8.1 °C at 1700. Thus, this alpine meadow is characterized by a large diurnal amplitude of air temperature variation and extremely low temperature in winter. Figure 3.22 shows the diurnal changes of monthly averaged soil temperature T_{soil} at the depth of –5cm. In summer, July 2002, T_{soil} reached a minimum of 14.0 °C at 0800 and a maximum of 20.7 °C at 1700. In winter, January 2002, T_{soil} reached a minimum of –6.2 °C at 0900 and a maximum of –3.4 °C at 1900. Figure 3.23 shows the seasonal changes of monthly averaged diurnal changes of photosynthetic photon flux density (*PPFD*). In summer, May 2002, *PPFD* reached a maximum of 1660.9 μmol photon m^{-2} s^{-1} at 1200. Thus, this alpine meadow is also characterized by a large amplitude of light intensity.

In 2001, *LAI* and aboveground biomass were 3.1 and 347 g d. w. m^{-2}, respectively, on 20 August (DOY233), which were the annual maximum values. In 2002, the values increased from late May (DOY145); *LAI* reached a maximum of 3.8 on 16 July (DOY197) and then decreased slowly (Fig. 3.24). The aboveground biomass reached a maximum of 283 g d. w. m^{-2} on 30 July (DOY211), remained high during August, and then decreased rapidly in September.

3.3.2. Sensible and latent heat fluxes

To investigate the diurnal courses and amplitudes of sensible H and latent heat fluxes λE, monthly averaged diurnal courses are shown in Figs. 3.25 and 3.26. The amplitudes of H were large in April when plants were beginning to grow and in October when they were dead, but small in January in winter and July when aboveground biomass peaked. On the other hand, the amplitudes of λE were large in July and August when aboveground biomass peaked, but so small from October to March.

To investigate the relationship between these heat fluxes and environmental factors, the diurnal courses of them during a sunny week, 9-15 August 2001 (DOY221-227), were shown in Fig. 3.27. H paralleled the differences between T_{air} and $T_{surface}$, and their relationship was

apparent linear (Fig. 3.28). λE seems to parallel available radiation (Rn-G), however the afternoon λE was bigger than the forenoon λE (Fig. 3.29). The decoupling factor Ω, introduced by Jarvis and MacNaughton (1986), kept nearby constant value during 9:00-16:00 and decreased after 17:00. This presents that high *VPD* lead to high λE in the evening when Rn-G, drove λE in the afternoon, decreased. The Bowen ratio, the ratio of H to λE, decreased gradually in the afternoon. This indicates that in the afternoon λE kept high value and, H decreased with the decreasing T_{air} - $T_{surface}$.

3.3.3. Carbon dioxide flux

The author examined the seasonality of the *FCO2* diurnal course (Fig. 3.30). The minimum *FCO2*, i.e. maximum uptake, was –10.8 μmol m^{-2} s^{-1} at 1300 in August 2001. The maximum *FCO2*, i.e. maximum release, was 4.4 μmol m^{-2} s^{-1} at 0100 in August 2002. The amplitudes of *FCO2* were large in July and August when aboveground biomass peaked. *FCO2* was small in May and June when plants were beginning to grow, and in September when they were dead. In winter, October to April, the *FCO2* was positive even in the daytime. The time courses of *FCO2* were similar for August 2001 and July 2002, but the amplitude of *FCO2* was larger in August 2001 than in August 2002.

FCO2 is plotted against *PPFD* in Fig. 3.31. *FCO2* decreased as *PPFD* increased in any month. During the period from July to August, however, the afternoon *FCO2* was higher than the forenoon *FCO2*, and *FCO2* values in June, July, and August were smaller than those in May and September. Light intensity was similar between August 2001 and August 2002, but the magnitude of *FCO2* was larger in August 2001.

During 9-15 August 2001 (DOY221-227), a sunny week, *FCO2* was positive (i.e. efflux) for several hours after 0000 (midnight, Beijing Standard Time), and then became negative (i.e. uptake flux) at 0800 (Fig. 3.32). *FCO2* decreased to a minimum of –12.4 μmol m^{-2} s^{-1} at 1300 as *PPFD* increased. Then *FCO2* started to increase, becoming positive at 2000. T_{air} reached a minimum of 2.2 °C at 0700 and a maximum of 19.9 °C at 1700. Thus, this alpine meadow is characterized by a large diurnal amplitude of air temperature variation. T_{soil} reached a minimum

of 12.4 °C at 0800 and a maximum of 20.6 °C at 1800. *SWC* ranged between 0.267 and 0.286 because of daytime evapotranspiration and small precipitation on the morning on 12 August 2001. λE paralleled *PPFD*. *VPD* paralleled T_{air} and reached a maximum of 15.4 hPa at 1700. R_{canopy} remained low at 100–140 s m^{-1} in the forenoon, but increased in the afternoon and reached a maximum of 168 s m^{-1} at 1800.

FCO2 is plotted against *PPFD* in Fig. 3.33. In the afternoon, when soil temperature was high, *FCO2* was higher than the forenoon *FCO2*.

3.3.4. *GPP* and R_e

The monthly averaged diurnal courses of *GPP* and R_e are shown in Fig. 3.34. *GPP* shows a maximum value of 15.1 μmol m^{-2} s^{-1} at 1200 in August (Fig. 3.34a). Large *GPP* occurred in July and August, when *LAI* and biomass were maximum, and small *GPP* in May, June, and September. R_e showed a maximum value of 7.0 μmol m^{-2} s^{-1} at 1600 in August (Fig. 3.34b), and increased in the afternoon as soil temperature increased.

The relationships between *GPP* and *PPFD* and between R_e and T_{soil} in July, when plant growth and photosynthesis were maximum, are shown in Figs. 3.35a and 3.35b. As *PPFD* increased, *GPP* increased but showed no significant difference in light response of *GPP* between morning and afternoon. As T_{soil} increased, R_e increased exponentially and also showed no significant difference in response to temperature between morning and afternoon values.

To assess the production efficiency of radiation use (*RUE*) and water use (*WUE*), hourly averaged *GPP*s are plotted against to *PPFD* and evapotranspiration *E* in Fig. 3.36. The *GPP* increased as irradiance *PPFD* increased during growing season, except for October – April. The *GPP* was large in the order August < July < June < September < May < October – April (Fig. 3.36a). The *GPP* increases as *E* increased in the same order.

3.4. Discussion

3.4.1. Measurement accuracy of eddy covariance method

In the spectrum analyses of turbulent fluctuations in wind velocity and other scalars, the power spectrums showed –5/3 power slope (Fig. 3.7) and the cross-spectrums showed –4/3 power slope in the inertial sub-range (Fig. 3.8). The dimensionless universal functions showed –1/3 slope against the atmospheric stability under strongly unstable conditions (Fig. 3.14, 15). These confirm the reasonability of turbulent flux sampling in this study. The estimation errors generated by the absence of coordinate rotation, trend removing and water vapor correction, are very small (Fig. 3.10-12) and this ensures that it is unnecessary to apply these corrections.

However, the energy imbalance, the disagreement between the energy fluxes ($H+\lambda E$) and the available energy ($Rn-G$), existed for whole experimental periods. The regression coefficients show the underestimation of the surface energy fluxes ($H+\lambda E$) of 41% (2001) and 30% (2002) relative to active energy ($Rn-G$) (Fig. 3.16). These slopes of regression lines are lower than the mean of 0.79 presented by Wilson et al. (2002), who compiled the *EBR* data of 22 sites and 50 site-years in FLUXNET, however they are within the range of 0.53 to 0.99 presented by Wilson et al. (2002). The *EBR* is slightly larger in summer than in winter (Fig. 3.17). This may be because total available energy, as the denominator in the *EBR* calculations, was much greater in the peak summer period relative to the winter period (Wilson et al., 2002). During day/night transition periods in morning and evening, since the mean value of $Rn-G$ was close to zero, the *EBR* is not especially meaningful (Fig. 3.18). This pattern of a greater *EBR* in the afternoon relative to the morning was observed in other flux sites (Wilson et al., 2002). The *EBR* shows no significant dependence on the wind direction (Fig. 3.19). This shows that the *EBR* was not influenced by the footprint land cover. The *EBR* shows the convergence to near 0.7 in the daytime, when the friction velocity exceeded 0.3 m s^{-1}, and the dispersion in the nighttime against to the friction velocity (Fig. 3.20). These results show the low *EBR* values were within a range of data from other flux measurement sites (Wilson et al., 2002), and show no obvious trend in the relationship to wind direction and friction velocity. The energy imbalance may be caused by sampling error, instrumental biases and other energy sinks as pointed out by Wilson et al. (2002).

3.4.2. Environmental controls on the diurnal change of carbon dioxide dynamics

One major process may affect the afternoon CO_2 exchange between the land and the atmosphere (*FCO2*; Fig. 3.31): the increasing air and soil temperatures accelerate plant respiration and soil organic matter decomposition, and as a result suppress the net CO_2 uptake flux. In grassland ecosystems with low *LAI*, because of the low interception of sunlight by vegetation, the soil surface temperature could be very high, which will further accelerate the increase of soil CO_2 efflux. This is supposed by the higher values of *FCO2* together with higher soil temperature in the afternoon as shown in Fig. 3.33. In addition, the high *VPD* might cause the closure of stomata and thus suppress CO_2 uptake. Such a stomatal response to increased *VPD* has been observed in a C_3/C_4 prairie grassland (Verma et al., 1992), a black spruce forest (Jarvis et al., 1997), and a jack pine forest (Baldocchi and Vogel, 1997). In the alpine meadow, the increase of R_{canopy} is correlated with the decrease of λE but with the increase of *VPD* (Fig. 3.32). The amplitude of the diurnal *SWC* change was small and may play a very limited role in ecosystem respiration (Fig. 3.32b). Cui et al. (2003) founded out apparent photoinhibition at a high *PPFD*, caused by reduced electron transport rate (*ETR*), founded out in two Asteraceae species at the Haibei alpine meadow. However, the net CO_2 uptake flux was not suppressed in the high *PPFD* over 800-1000 $\mu molm^{-2}s^{-1}$.

Daytime R_e and *GPP* were estimated from the regression relationship between the low nighttime respiration of plant and soil microbiota biomass and soil temperature (Fig. 3.34). Therefore, it is possible that respiration of aboveground plants is enhanced significantly by high soil temperature, or PPFD in the daytime increases R_e more than expected. However, these results provide evidence that respiration by plants biomass and soil microbes greatly decreases the diurnal changes of net CO_2 exchange in alpine meadow ecosystems, as hypothesized above.

R_e increased significantly in the afternoon (Fig. 3.34 and 3.35). In this grassland, because of the small interception of sunshine by plants, the soil surface temperature increased in the mid-afternoon was significantly higher than in the nighttime and early morning, and as a result the CO_2 efflux was noticeably enhanced. *GPP* increased nearly linearly with increasing

PPFD (Fig. 3.35), and there was no suppression of *GPP* flux in the afternoon, as found in net ecosystem flux of CO_2 exchange.

The diurnal course of *GPP* response to the *PPFD* (Fig. 3.36a), showed smaller hysteresis than found in *FCO2* (Fig. 3.31) during the growing season. Furthermore, the diurnal course of *GPP* response against the evapotranspiration (Fig. 3.36b), showed no hysteresis in afternoon, except for July (Fig. 3.36a). This presents that the plant photosynthesis was not suppressed by water loss through leaf stomata. Cui et al. (2002) also showed that photochemical reaction in leaves of two Asteraceae species was aggravated by high leaf temperature at the Haibei alpine meadow. However, the light response of *GPP* was not suppressed in the afternoon with high air and soil temperature.

3.4.3. Ecosystem carbon assimilation ability

The maximum CO_2 uptake flux (minimum *FCO2* value) of study site (–10.8 μmol m^{-2} s^{-1}; Fig. 3.30) was compared with those of other sites at a similar latitude (Table 3.2). The maximum CO_2 uptake flux was two-thirds less than those in an Oklahoma C_3/C_4 prairie (–15.5 μmol m^{-2} s^{-1}; Sims and Bradford, 2001) and a Colorado subalpine conifer forest of subalpine fir and black spruce (–15.5 μmol m^{-2} s^{-1}; 3050 m; Monson et al., 2002). But it was 20 %–40 % less than those in a Kansas C_4 prairie (–25 μmol m^{-2} s^{-1}; Ham and Knapp, 1998), an Oklahoma tall-grass prairie (–31.8 μmol m^{-2} s^{-1}; Suyker and Verma, 2001), and a Japanese C_3/C_4 grassland (–56.7 μmol m^{-2} s^{-1}; Li and Oikawa, 2001).

The maximum CO_2 release flux (maximum *FCO2* value) of study site (4.4 μmol m^{-2} s^{-1}; Fig. 3.30; Table 3.2) was compared similarly. It was 20%–50% less than those in the Colorado subalpine conifer forest (8–9 μmol m^{-2} s^{-1}; Monson et al., 2002), the Kansas C_4 prairie (10 μmol m^{-2} s^{-1}; Ham and Knapp, 1998), the Oklahoma tall-grass prairie (11.4 μmol m^{-2} s^{-1}; Suyker and Verma, 2001), and the Japanese C_3/C_4 grassland (21.6 μmol m^{-2} s^{-1}; Li and Oikawa, 2001).

Thus, this Tibetan alpine meadow ecosystem shows a lower CO_2 uptake and lower release potential than C_4 grasslands, but a similar net CO_2 uptake potential to an alpine conifer forest because of its equal uptake potential and its lower release potential.

The *K. humilis* meadow had relatively high *LAI* (3.1) with relatively low aboveground biomass (ca. 300 g m^{-2}). With a similar *LAI* to study site, the aboveground biomass in an Oklahoma grassland was reported to be as large as 800 g m^{-2}. The lower ratio of aboveground biomass to *LAI* in the *K. humilis* meadow seems to have been due to the low canopy height in the alpine meadow, which resulted from the relatively greater abundance of broad-leaved species and the low height of vegetation. The high *LAI*, on the other hand, seems to contribute to the high belowground biomass in the alpine meadow. The belowground biomass was 6-7 times higher than the aboveground biomass (e.g. 1892 g d. w. m^{-2} on 11 August 2001; unpublished data). This particular allocation pattern of plant biomass may favor high soil carbon storage in the alpine ecosystem.

Although the CO_2 uptake was not high, the daily net ecosystem carbon gain reached a fairly high value during a sunny week in August 2001. One reason may be why the low nighttime temperature (e.g. near freezing air temperature 2.2 °C) limited ecosystem respiration. Another reason is perhaps the low maintenance respiration due to the low aboveground biomass in the alpine meadow (Table 3.2).

Table 3.1. Instruments and installation height

Meteorological elements	Instruments	Height (m)
Wind velocity and air temperature	Sonic anemometer (CSAT/CSI)	2.2
CO_2, H_2O concentration	CO_2/H_2O infrared gas analyzer (CS-7500/CSI)	2.2
Short wave and long wave radiations from the sky and the ground	Radiometer (CNR-1/Kipp & Zonen)	1.5
Air temperatures and humidity	Thermo-hygrometer (HMP45C/Vaisara)	2.2, 1.1
Wind speed	Cup anemometer (034A-L and 014A /R. M. Young)	2.2, 1.1
Soil moisture	TDR sensor (CS615/CSI)	-0.05, -0.2, -0.5
Soil temperature	Thermocouple	-0.025, -0.05, -0.1, -0.2, -0.3, -0.4, -0.5, -0.6, -0.7
Soil surface temperature	Thermistor probe (107/CSI)	0 (3 points)
Soil heat flux	Heat plate (HFT-3/CSI)	-0.02 (3 points)
Precipitation	Tipping bucket rain gage (TE525MM/CSI)	0.5
PPFD	Quantum sensor (LI-190SB/Li-Cor)	1.5
UV-A	Ultra violet radiometer (PD204A/Macam)	1.5
UV-B	Ultra violet radiometer (PD204B/Macam)	1.5

Table 3.2. Different components of carbon exchange fluxes and environmental conditions for the *Kobresia humilis* meadow and other sites at similar latitude.

Site	Latitude, Logitude	Altitude (m a.s.l.)	Maximum *LAI*	Maximum aboveground biomass (g m^{-2})	Minimum *FCO2* (μmol $m^{-2}s^{-1}$)	Maximum *FCO2* (μmol $m^{-2}s^{-1}$)	Maximum NEP_{total} ($gCm^{-2}d^{-1}$)
C_3 alpine meadow[1]	37°37′N 101°18′E	3250	3.8	283	-10.8	4.4	3.9
C_3/C_4 prairie[2]	36°36′N 99°35′W	630	1.5	370	-15.5	---	---
subalpine conifer forest[3]	40°02′N 105°32′W	3050	4.2	---	-15.5	8.0-9.0	1.0
C_4 prairie[4]	39°12′N 96°35′W	324	1.6	414	-25.0	10.0	4.9
C_4 prairie[5]	39°03′N 99°32′W	445	3.2	1100	---	---	6.3
tall-grass prairie[6]	36°56′N 96°41′W	---	2.8	---	-31.8	11.4	8.4
C_3/C_4 grassland[7]	36°06′N 140°06′E	27	5.5	---	-56.7	21.6	---

[1]Qinghai-Tibetan Plateau, China (This study). [2]Oklahoma, USA (Sims and Bradford, 2001). [3]Colorado, USA (Monson et al., 2002). [4]Kansas, USA (Ham and Knapp, 1998). [5]Kansas, USA (Kim et al., 1992). [6]Oklahoma, USA (Suyker and Verma, 2001). [7]Tsukuba, Japan (Li and Oikawa, 2001).

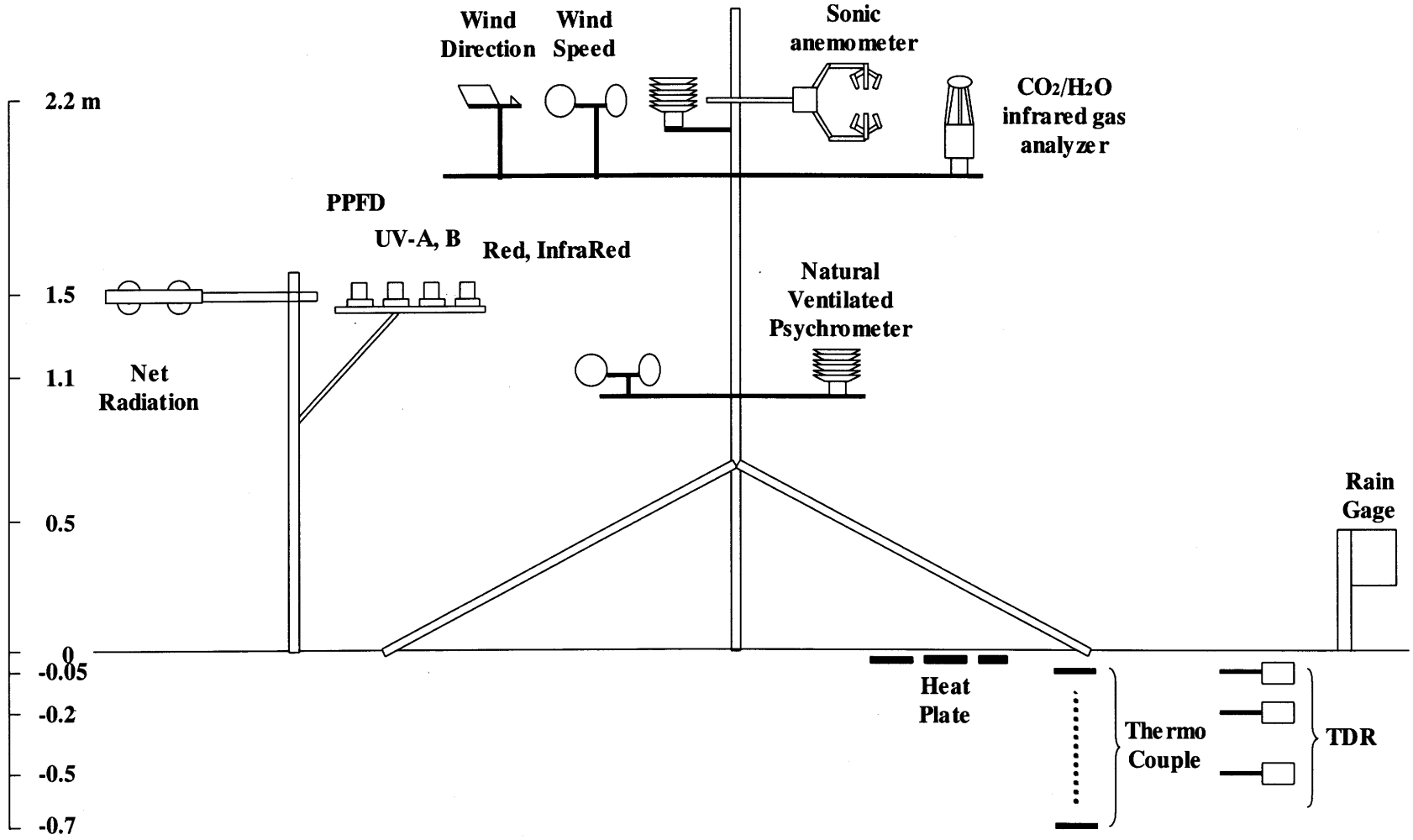

Figure 3.1. A schematic diagram of the flux measurement system

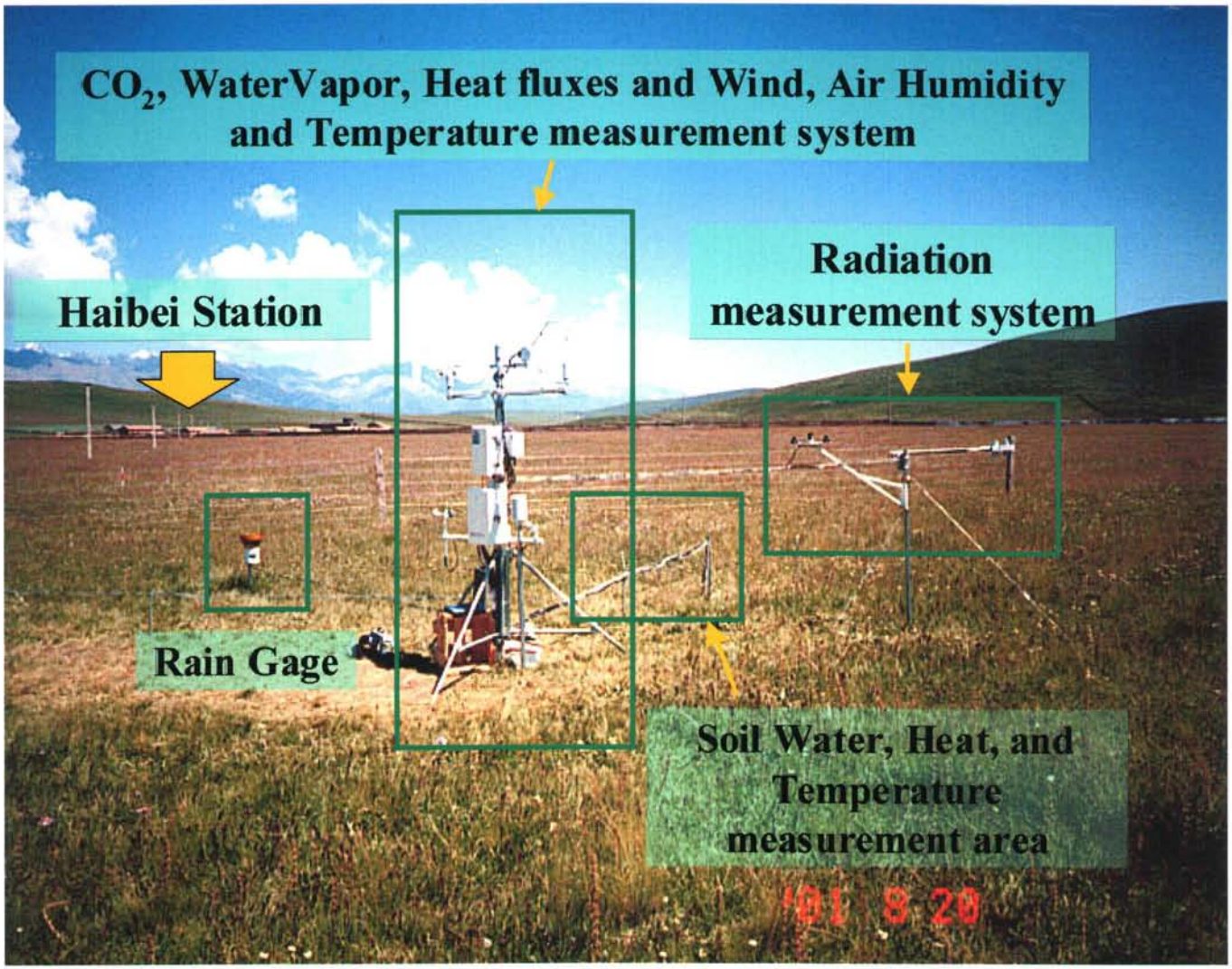

Figure 3.2. A view of the experimental site (summer, 2001)

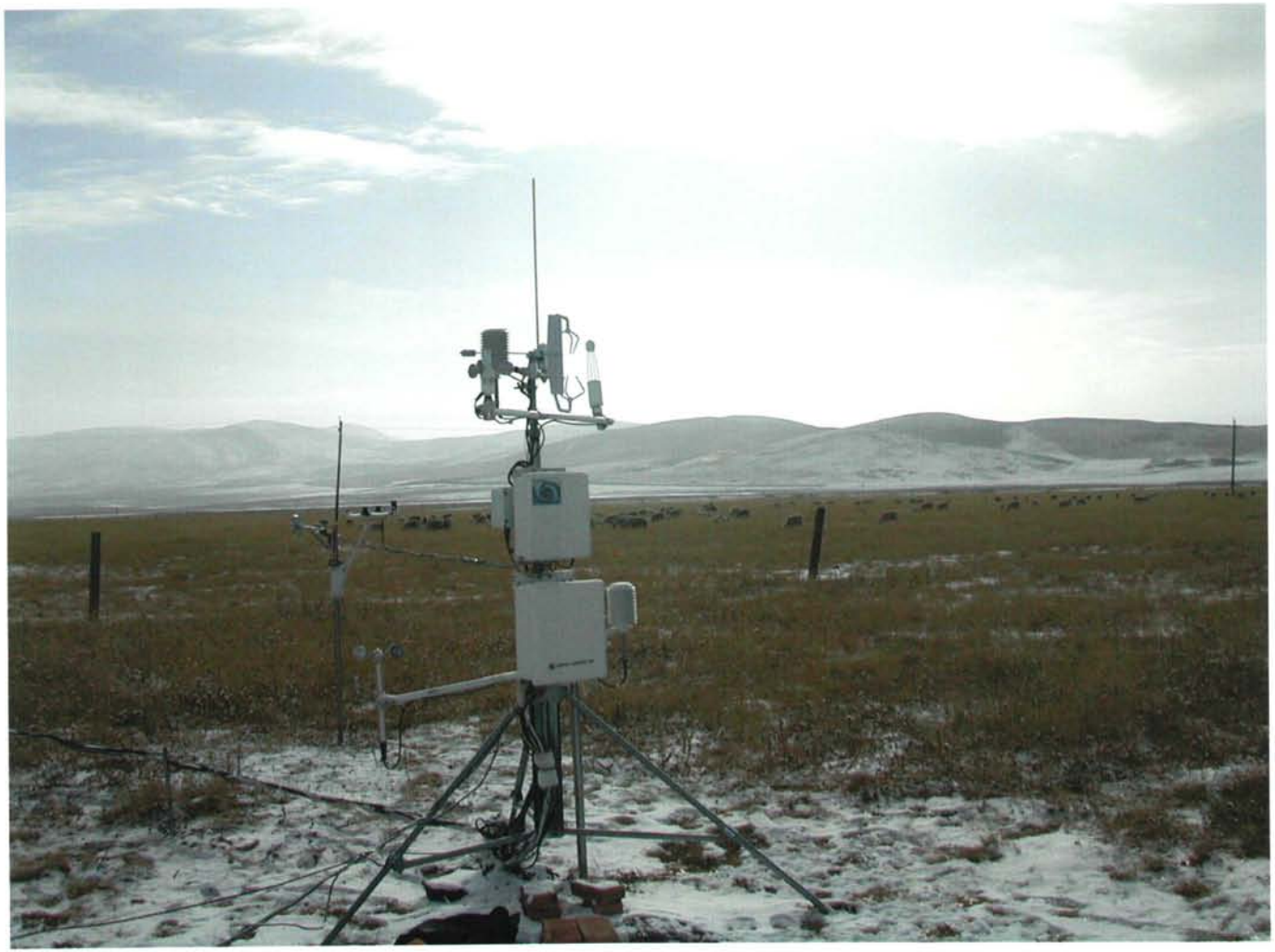

Figure 3.3. A view of the experimental site (winter, 2002)

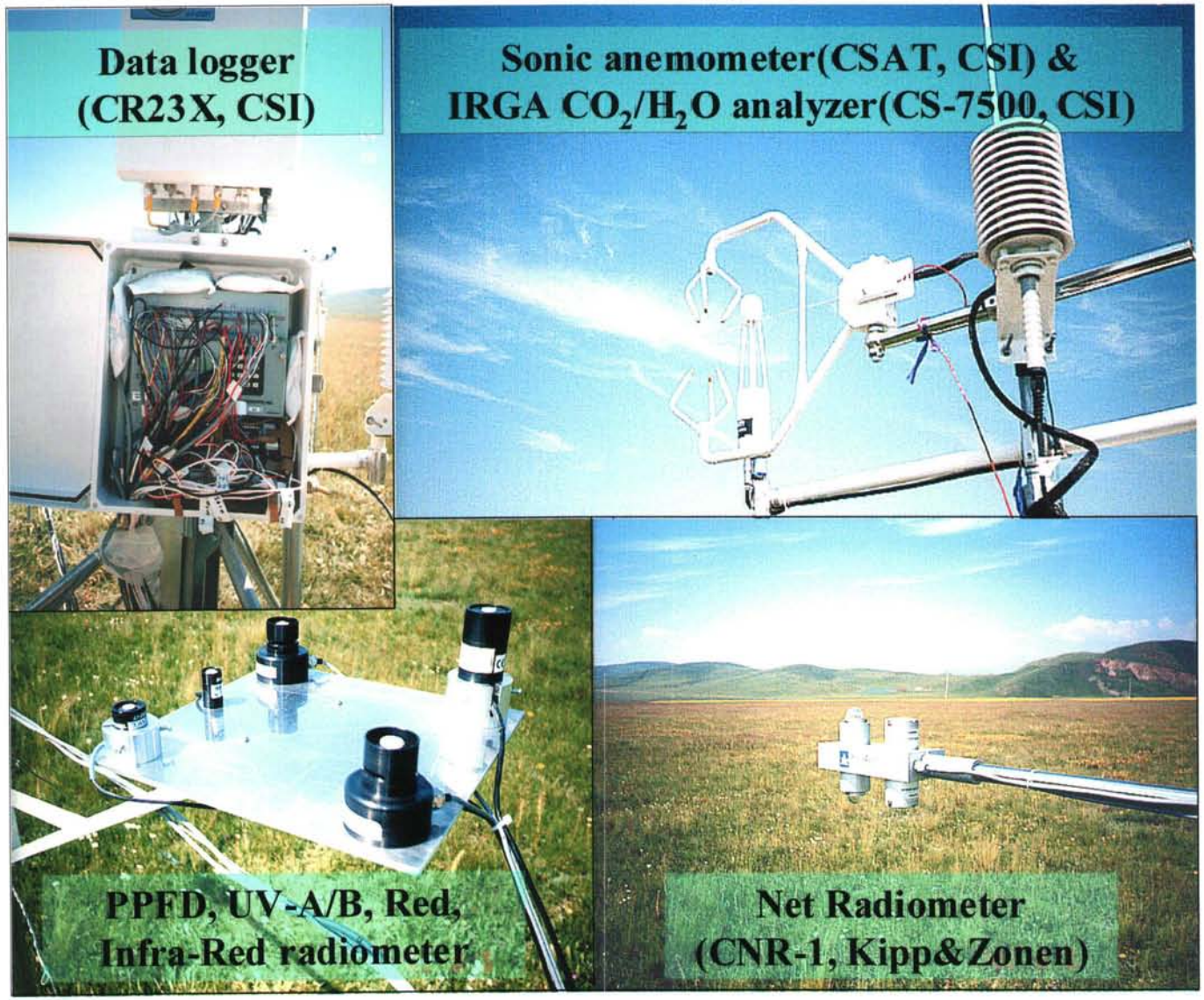

Figure 3.4. A view of the setting of the instruments (aboveground)

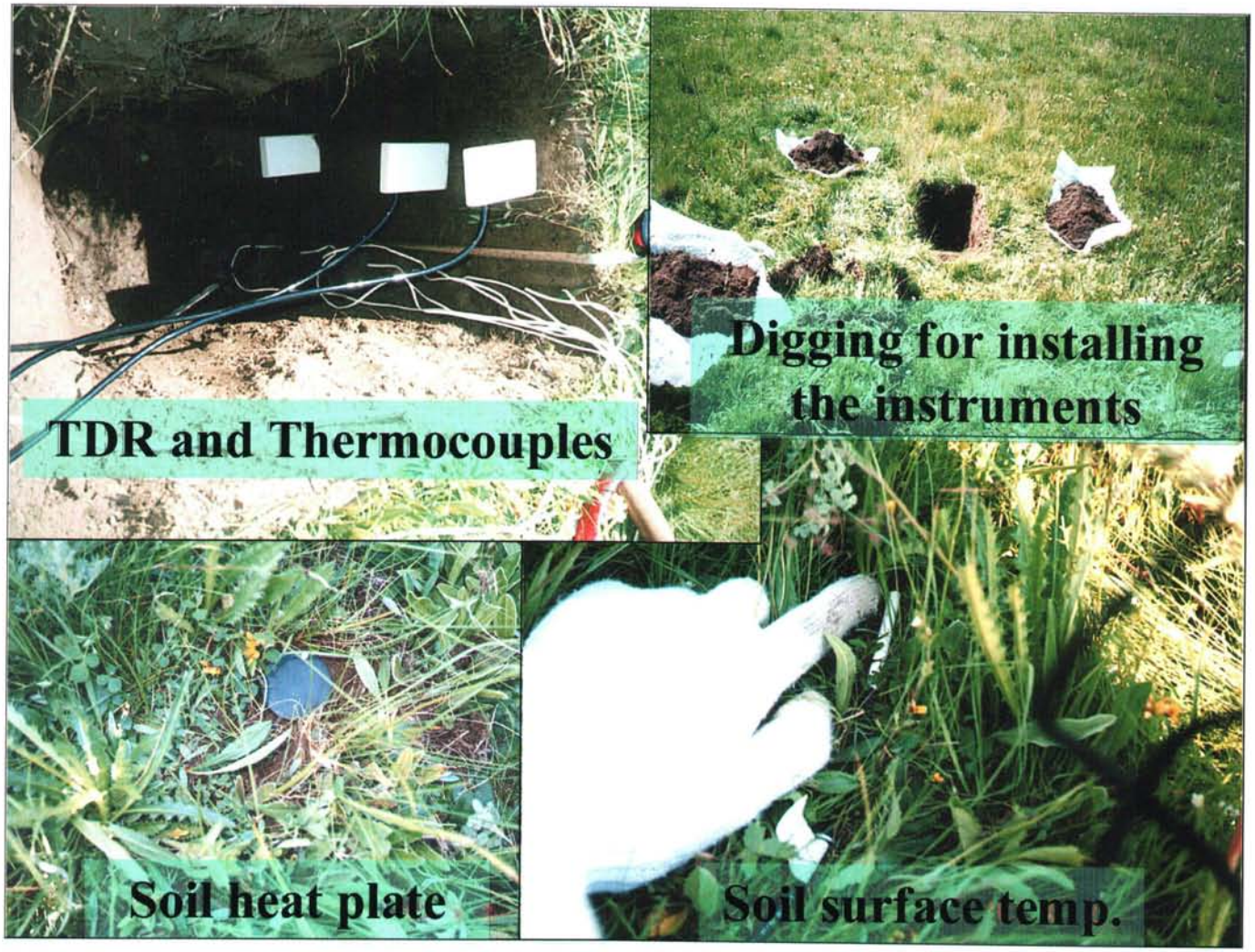

Figure 3.5. A view of the setting of the instruments (belowground)

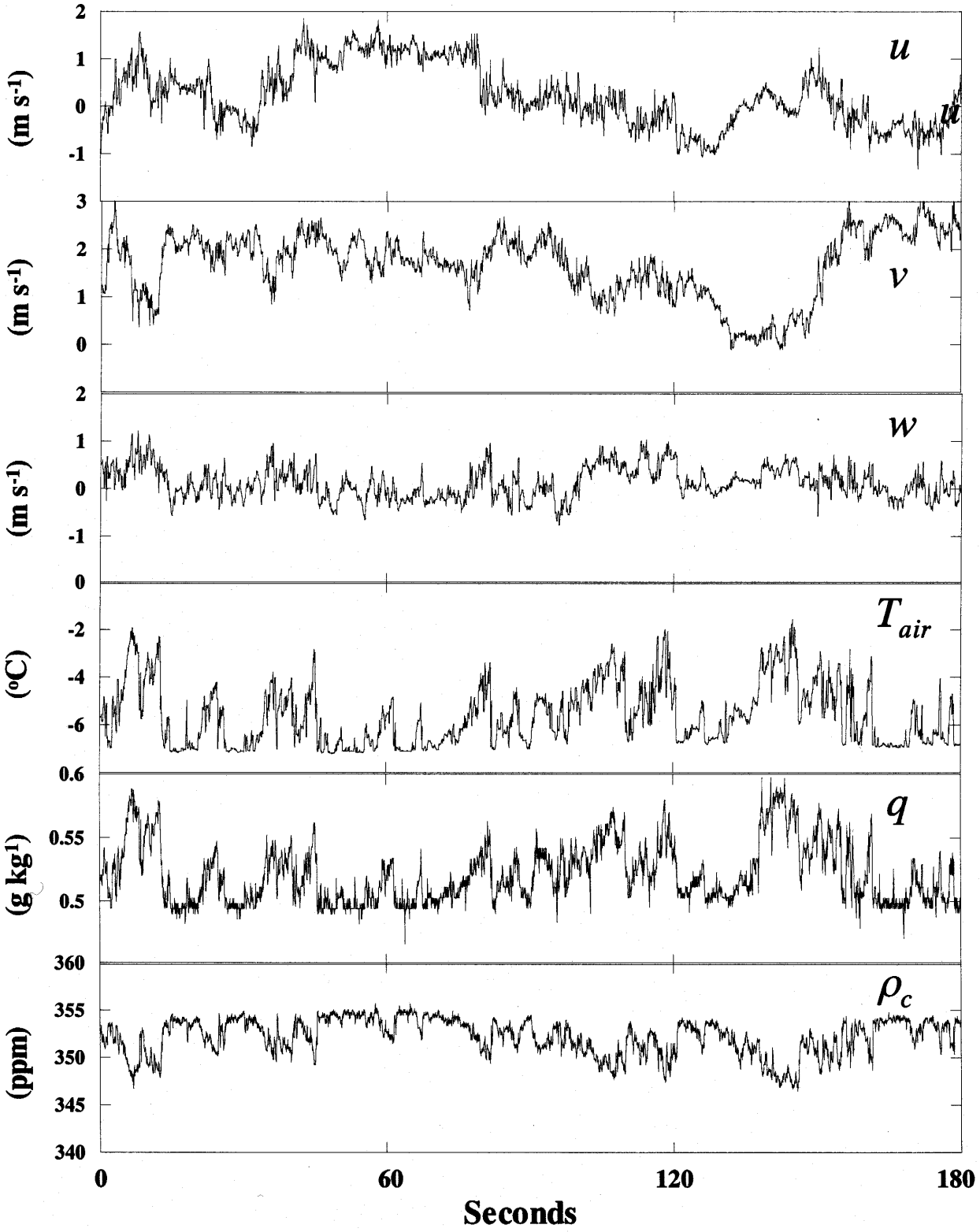

Figure 3.6. Time series of x, y, z-axis wind velocities (u, v, w), air temperature (*Tair*), specific humidity (q) and carbon dioxide concentration (C) at the Haibei meadow, 12:00-12:03, 13 February, 2003. Data show scalar fluctuations measured at the frequency of 20 Hz by a sonic anemometer (CSAT-3, Campbell Scientific Inc., Logan, UT, USA) and an open-path Infra-Red Gas Analyzer (CS-7500, Campbell Scientific Inc.).

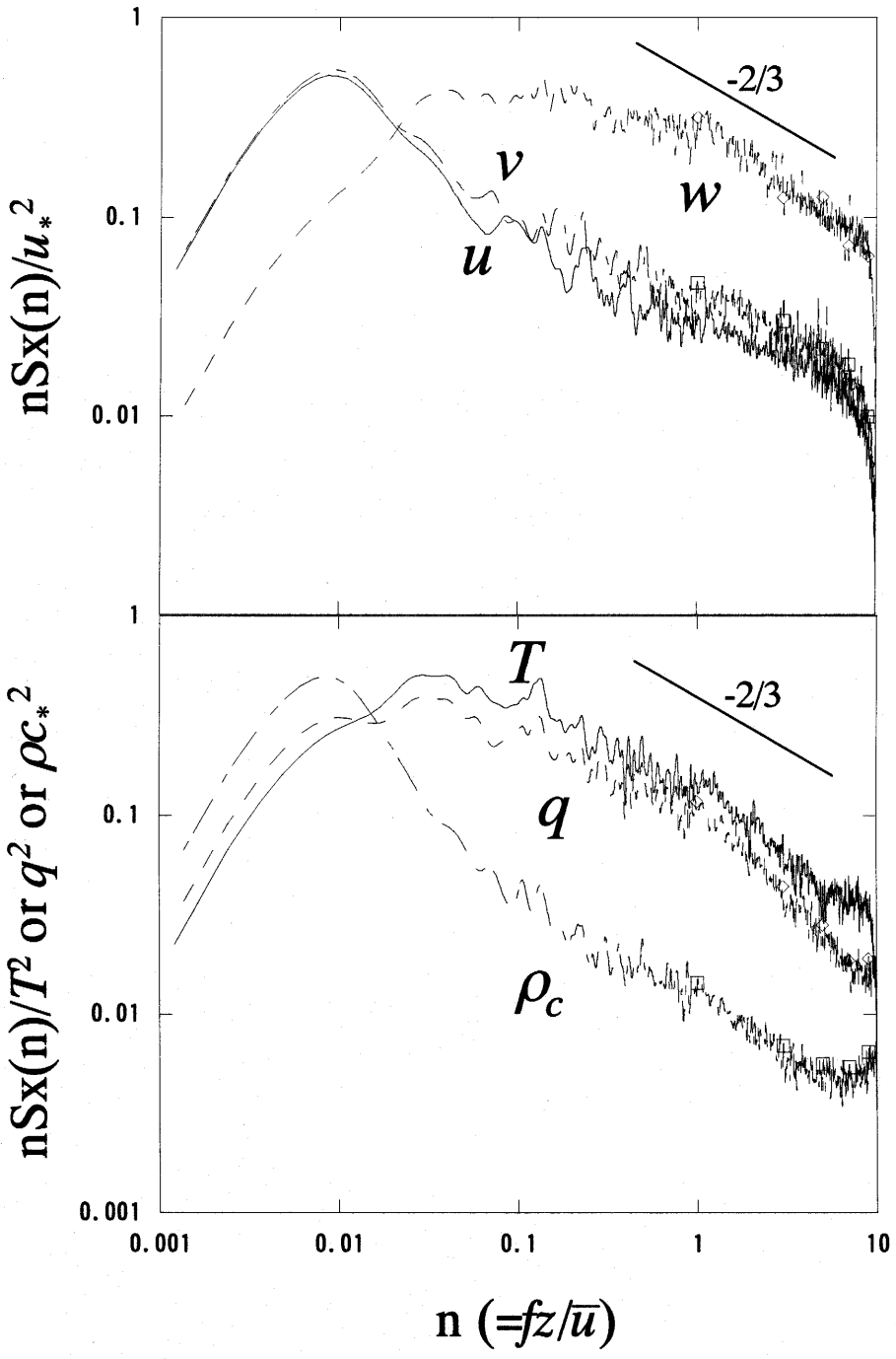

Figure 3.7. Power spectrum of x, y, z-axis wind velocities (u, v, w), air temperature (T_a), specific humidity (q) and carbon dioxide concentration (C) at the Haibei meadow, 12:00-12:15, 13 August, 2002. Vertical axes of the figures are normalized with frequency.

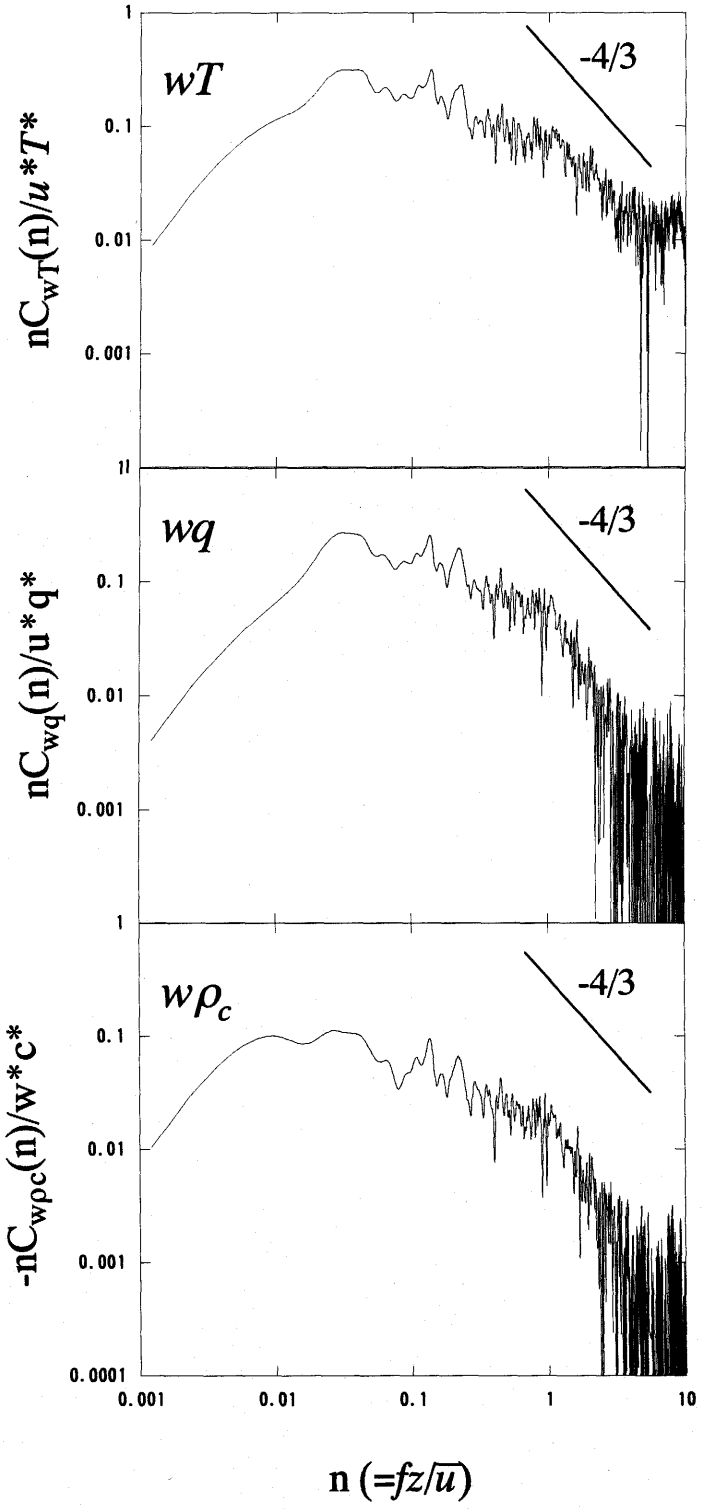

Figure 3.8. Cross spectrum between z-axis wind velocities (w) and air temperature (T_a), specific humidity (q) and carbon dioxide concentration (C) at the Haibei meadow, 12:00-12:15, 13 August, 2002.

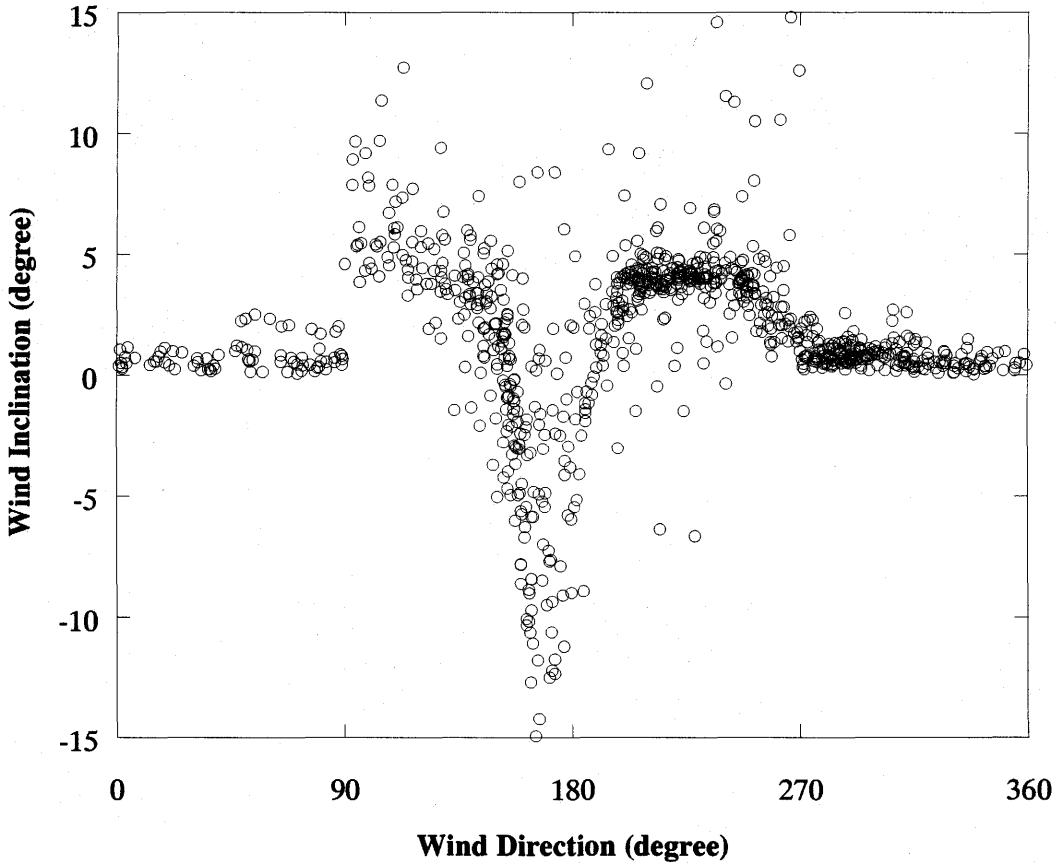

Figure 3.9. The wind direction dependent deflection of the 15 min average wind inclination from 17 July to 26 July 2002. The effect of the tower is clear in between 100 and 270 degrees of wind direction.

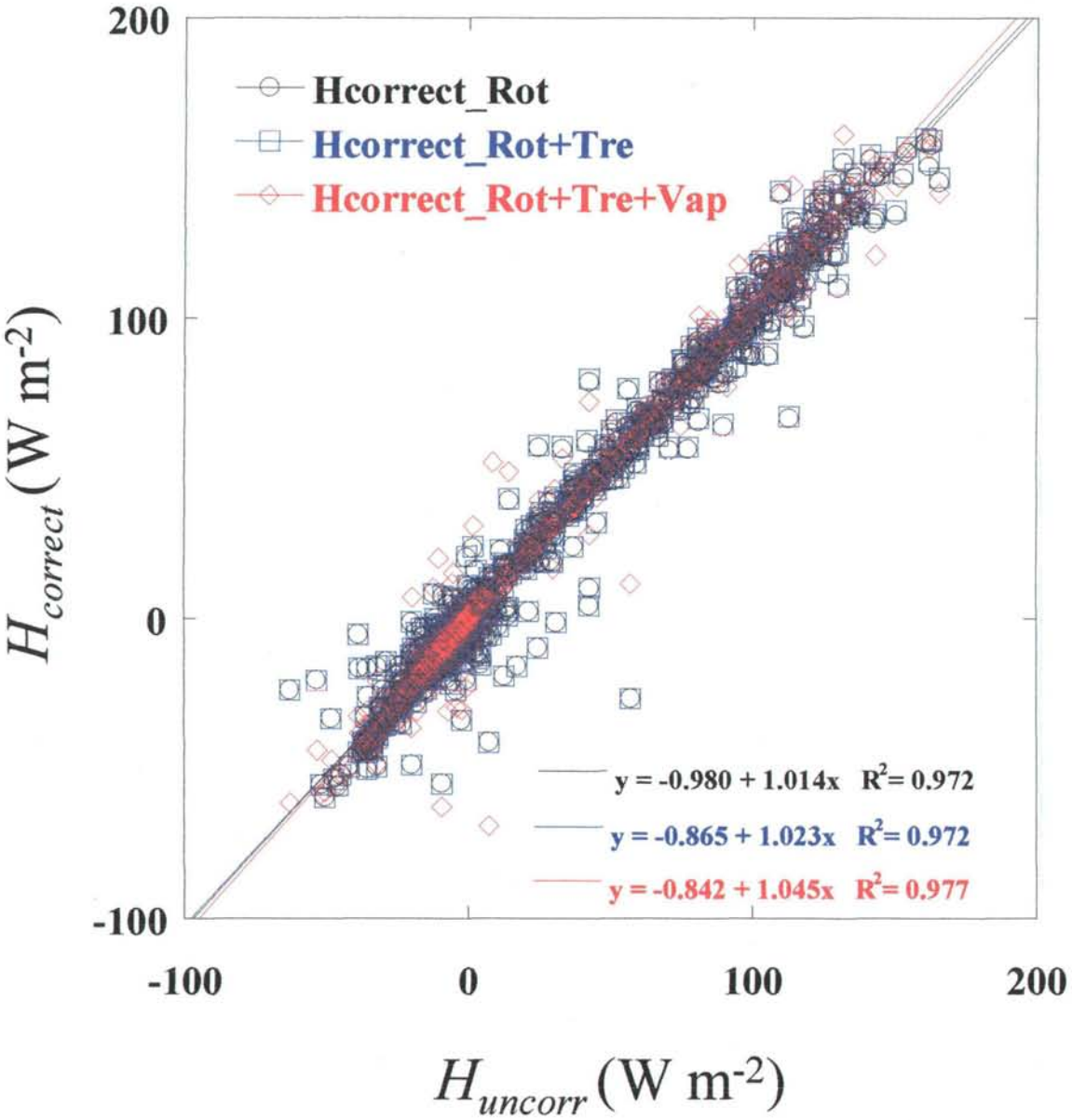

Figure 3.10. Comparisons of 15 min averaged fluxes of corrected sensible heat ($H_{correct}$) with uncorrected sensible heat (H_{uncorr}) measured from 17 July to 26 July, 2002 at the Haibei station. "Rot", "Tre" and "Vap" mean rotation, trend removing and water vapor correction, respectively.

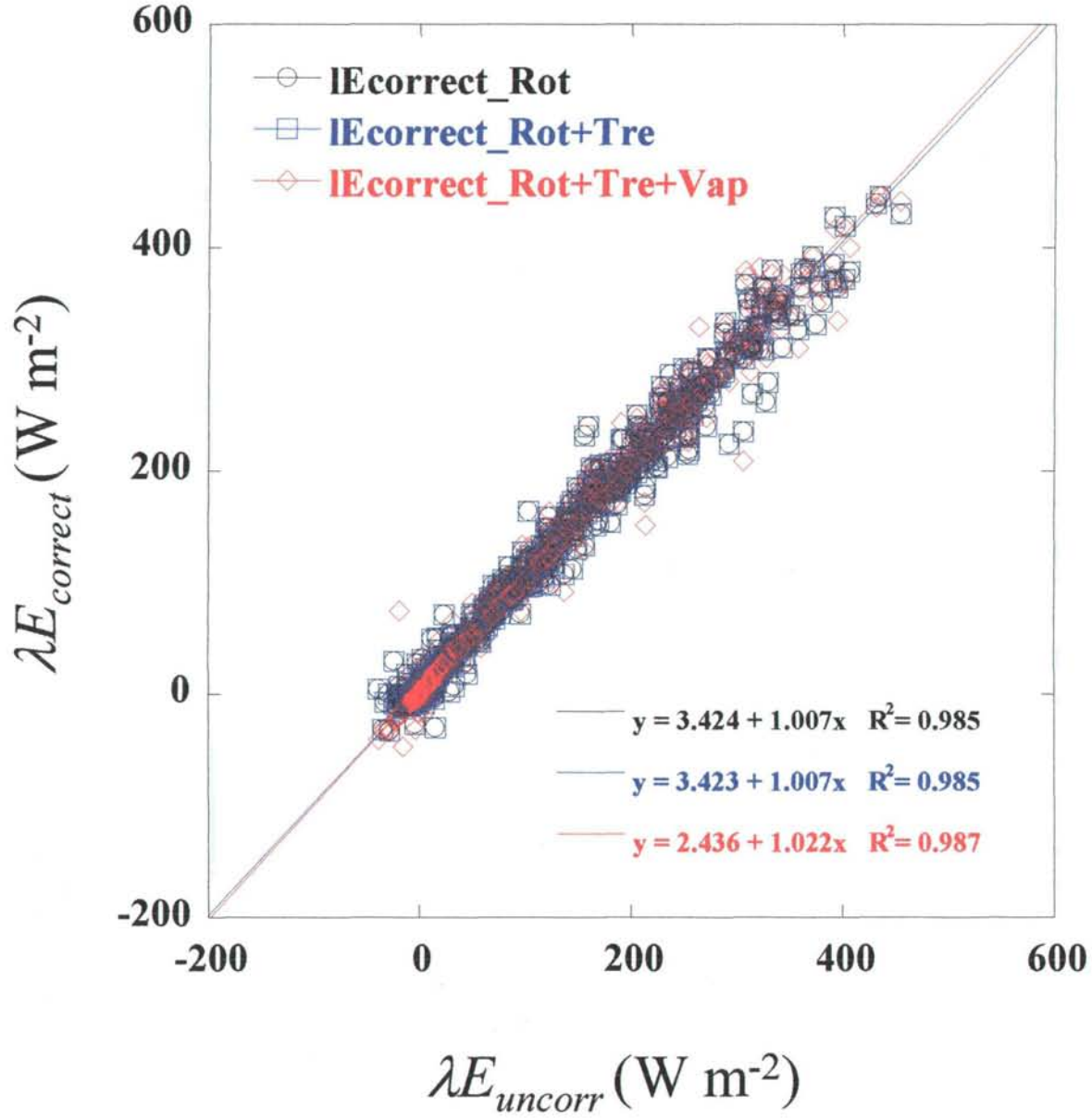

Figure 3.11. Comparisons of 15 min averaged fluxes of corrected latent heat (*λEcorrect*) with uncorrected latent heat (*λEuncorr*) measured from 17 July to 26 July, 2002 at the Haibei station. "Rot", "Tre" and "Vap" mean rotation, trend removing and water vapor correction, respectively.

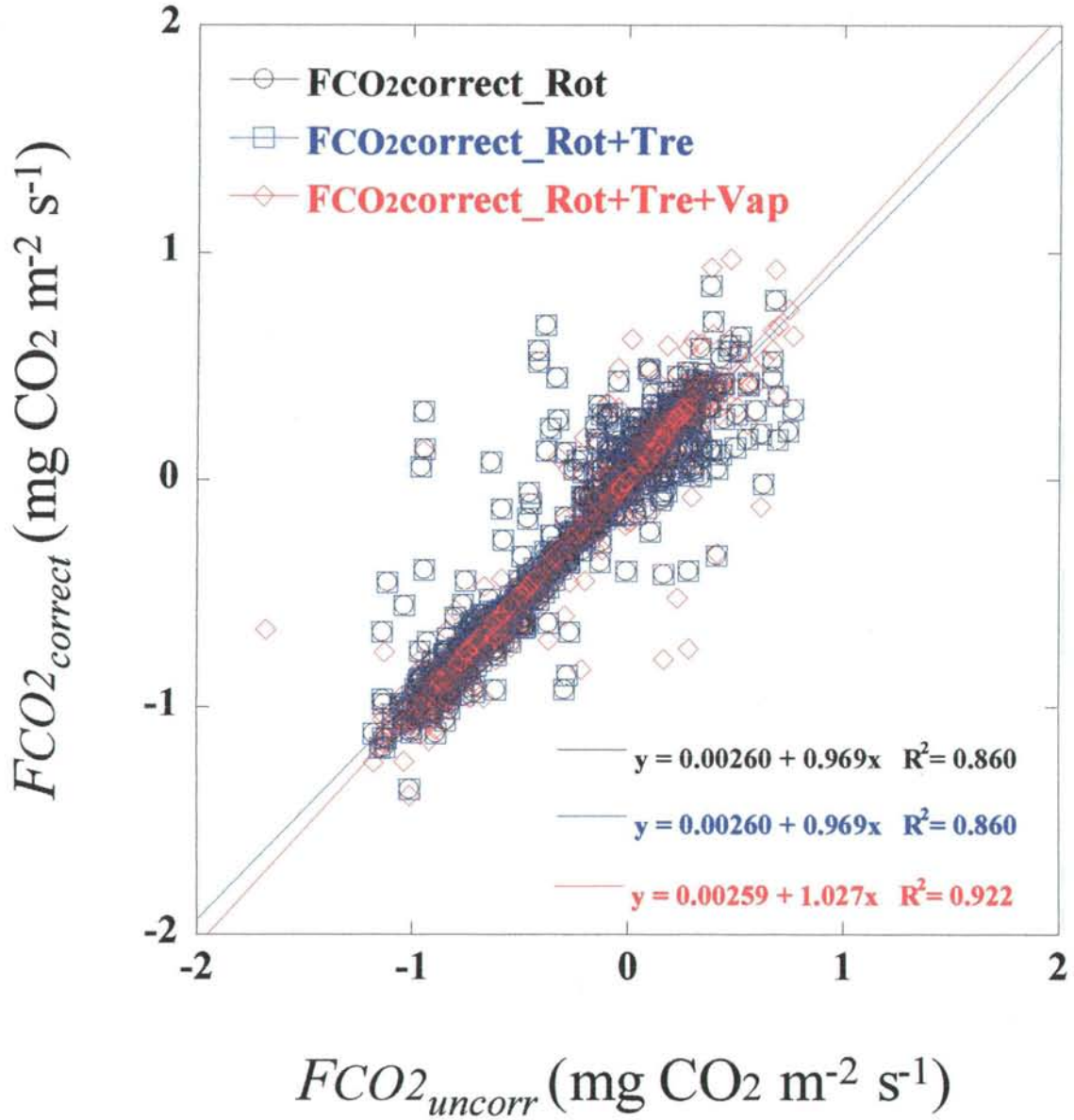

Figure 3.12. Comparisons of 15 min averaged fluxes of corrected CO_2 ($FCO2_{correct}$) with uncorrected CO_2 ($FCO2_{uncorr}$) measured from 17 July to 26 July, 2002 at the Haibei station. "Rot", "Tre" and "Vap" mean rotation, trend removing and water vapor correction, respectively.

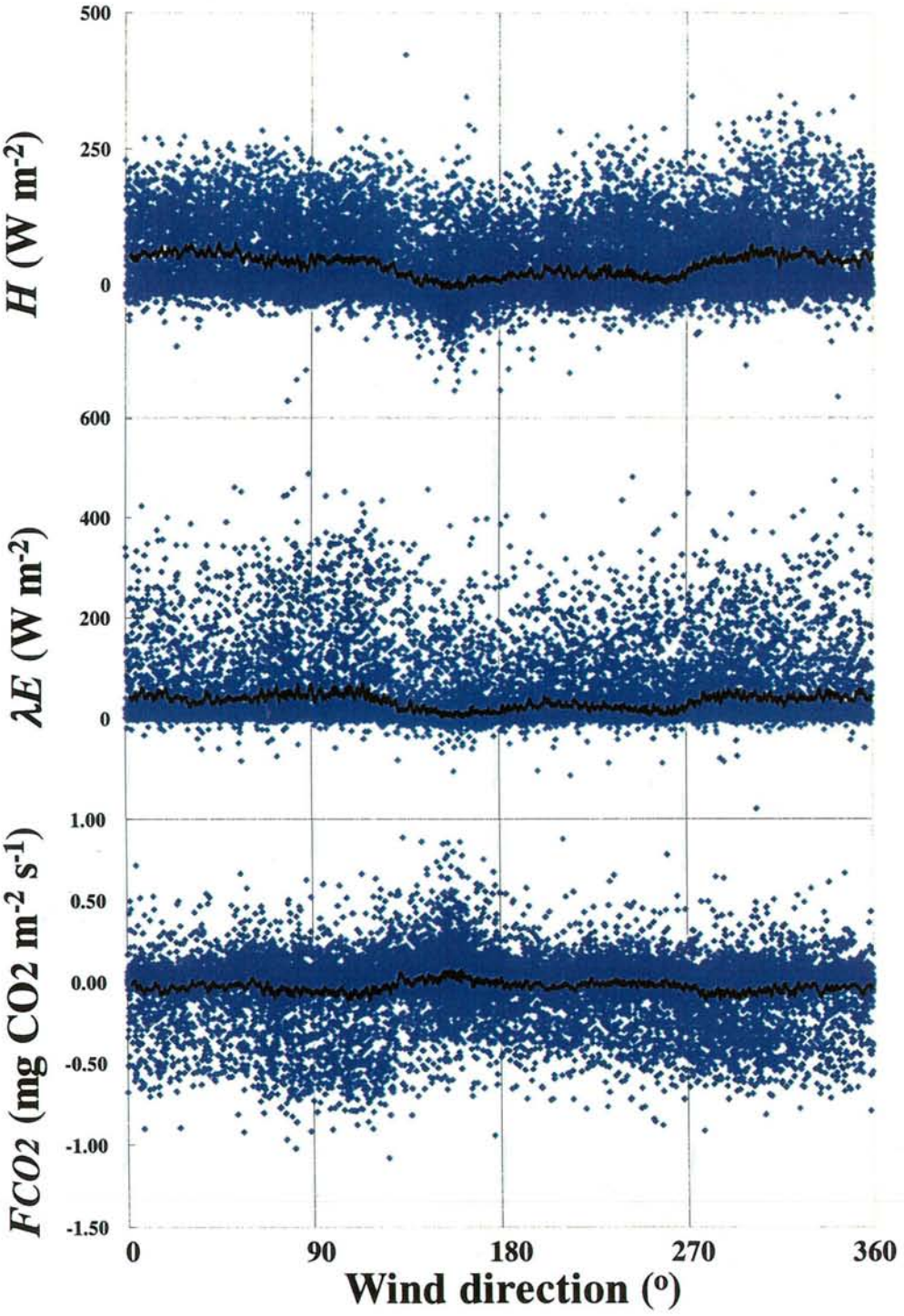

Figure 3.13. Wind direction dependent deflection of the 15 min averaged H, λE and $FCO2$ fluxes from 14 January to 31 December, 2002. Black line shows 100 point moving average.

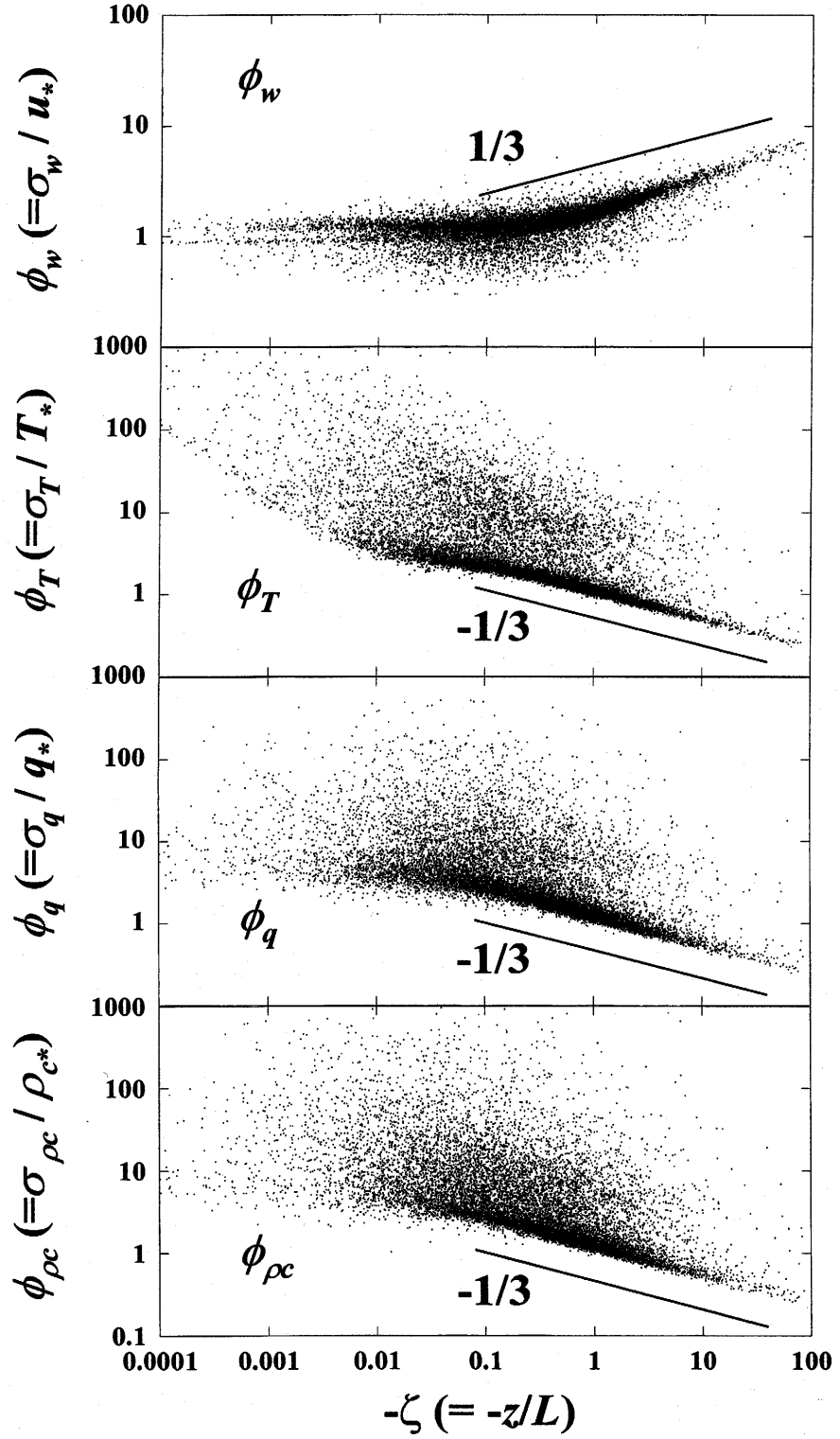

Figure 3.14. Relationship between aerodynamic stability and dimensionless universal functions under unstable conditions from 14 January to 31 December, 2002. Data show 15 min average values.

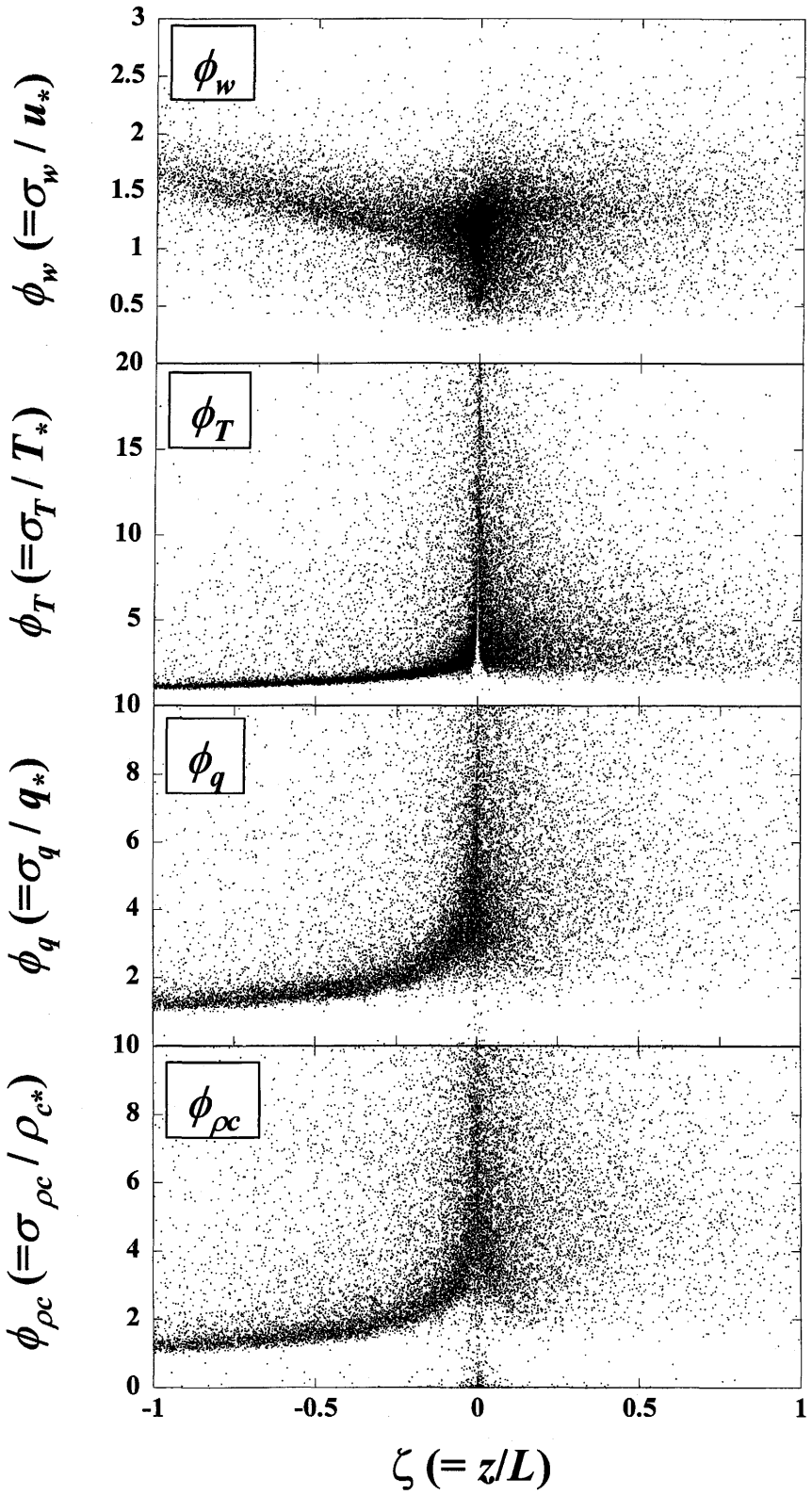

Figure 3.15. Relationship between aerodynamic stability and dimensionless universal functions under near neutral conditions from 14 January to 31 December, 2002. Data show 15 min average values.

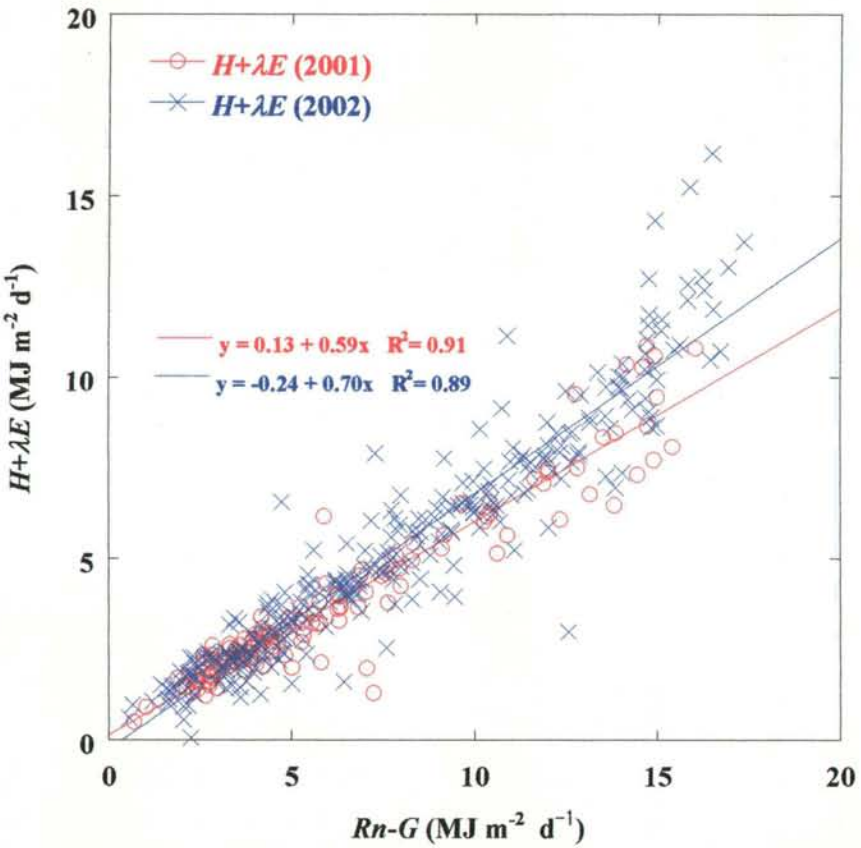

Figure 3.16. Daily energy balance between $H+\lambda E$ and Rn-G in 2001 and 2002.

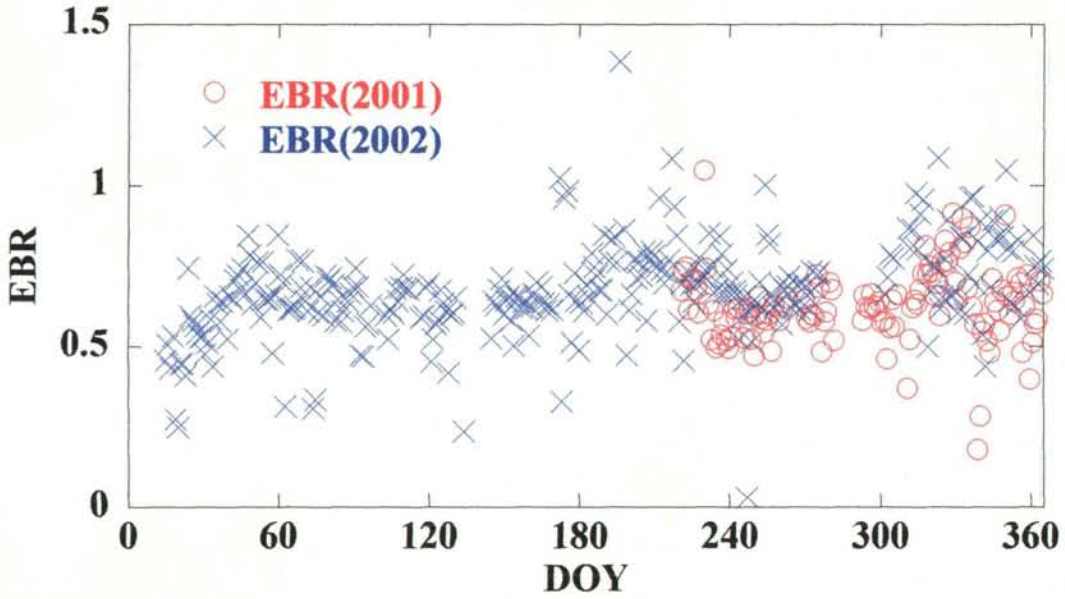

Figure 3.17. Seasonal changes of daily energy balance ratio (*EBR*) between $H+\lambda E$ and $Rn-G$ in 2001 and 2002.

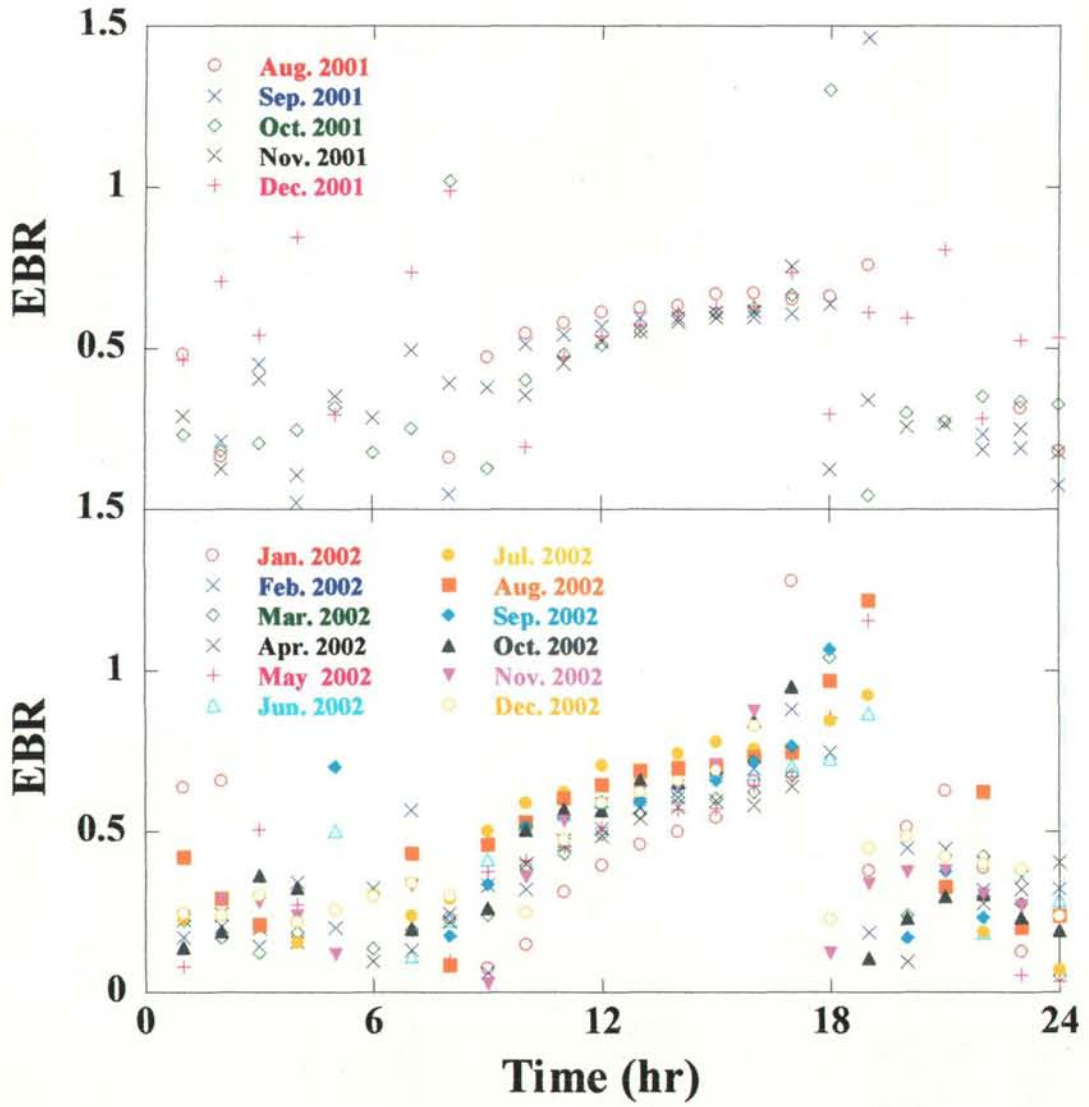

Figure 3.18. Daily changes of energy balance ratio (*EBR*) between $H+\lambda E$ and *Rn-G* in 2001 and 2002. Data shows monthly average values.

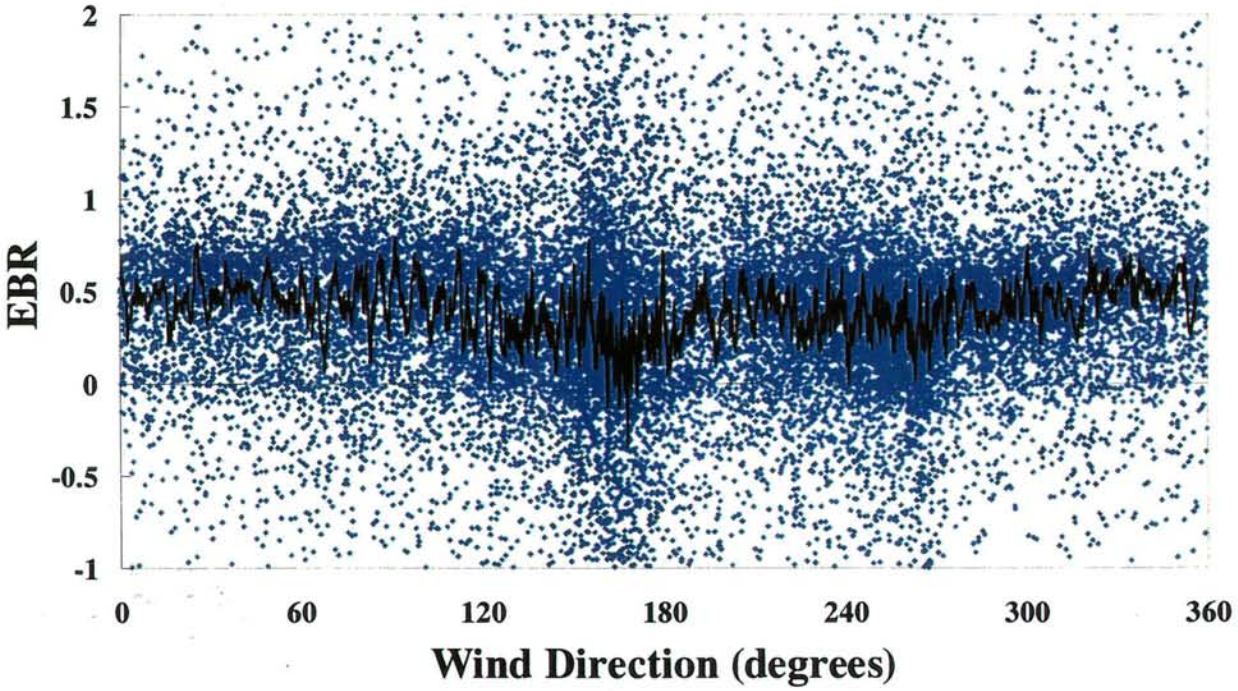

Figure 3.19. Wind direction dependent of the energy balance ratio (*EBR*) from 14 January to 31 December, 2002. Data shows 15 min averages. Black line shows 100-point moving averages.

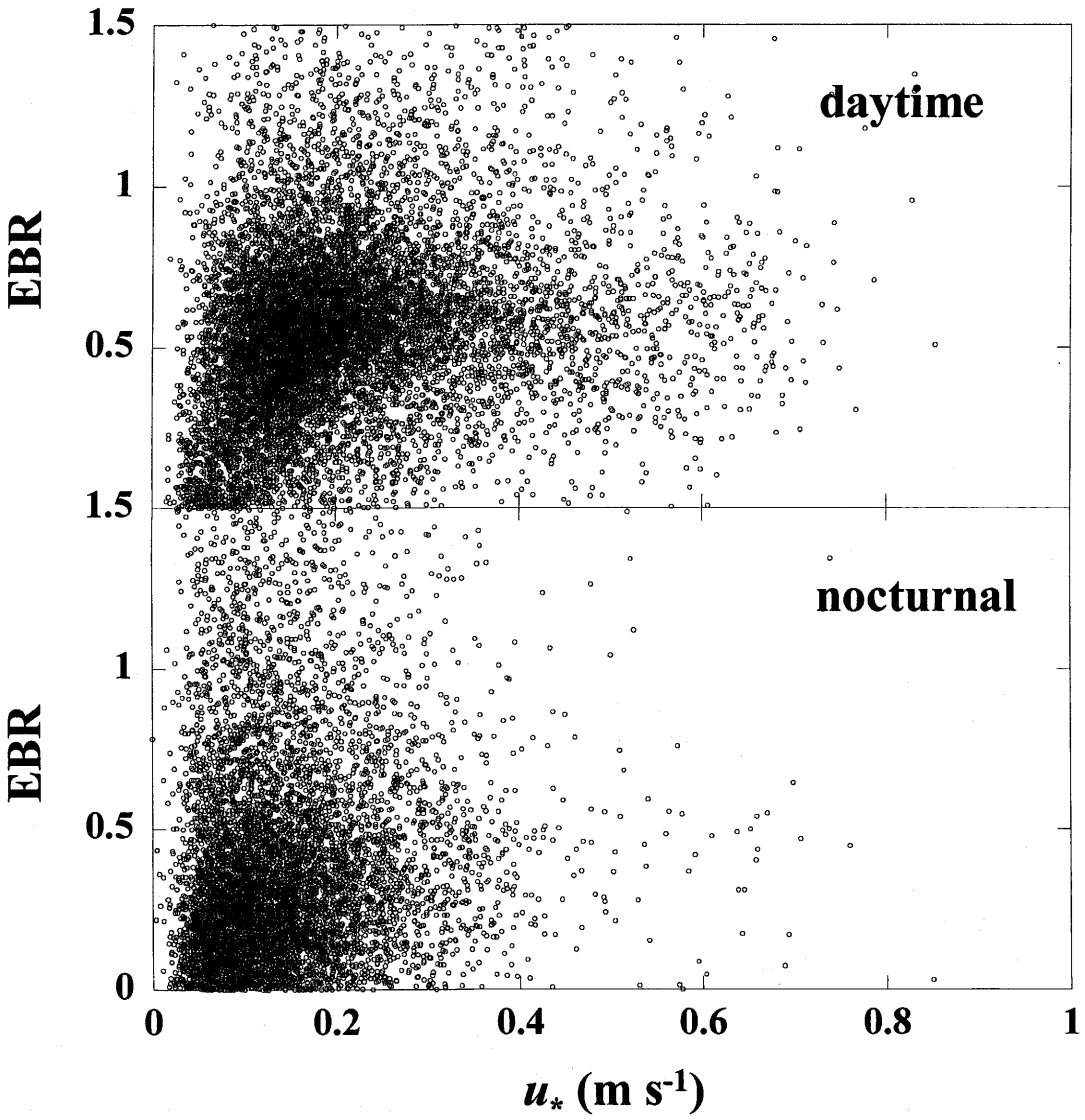

Figure 3.20. Energy balance ratio (*EBR*) dependent on the friction velocity from 14 January to 31 December, 2002. Data show 15 min averages.

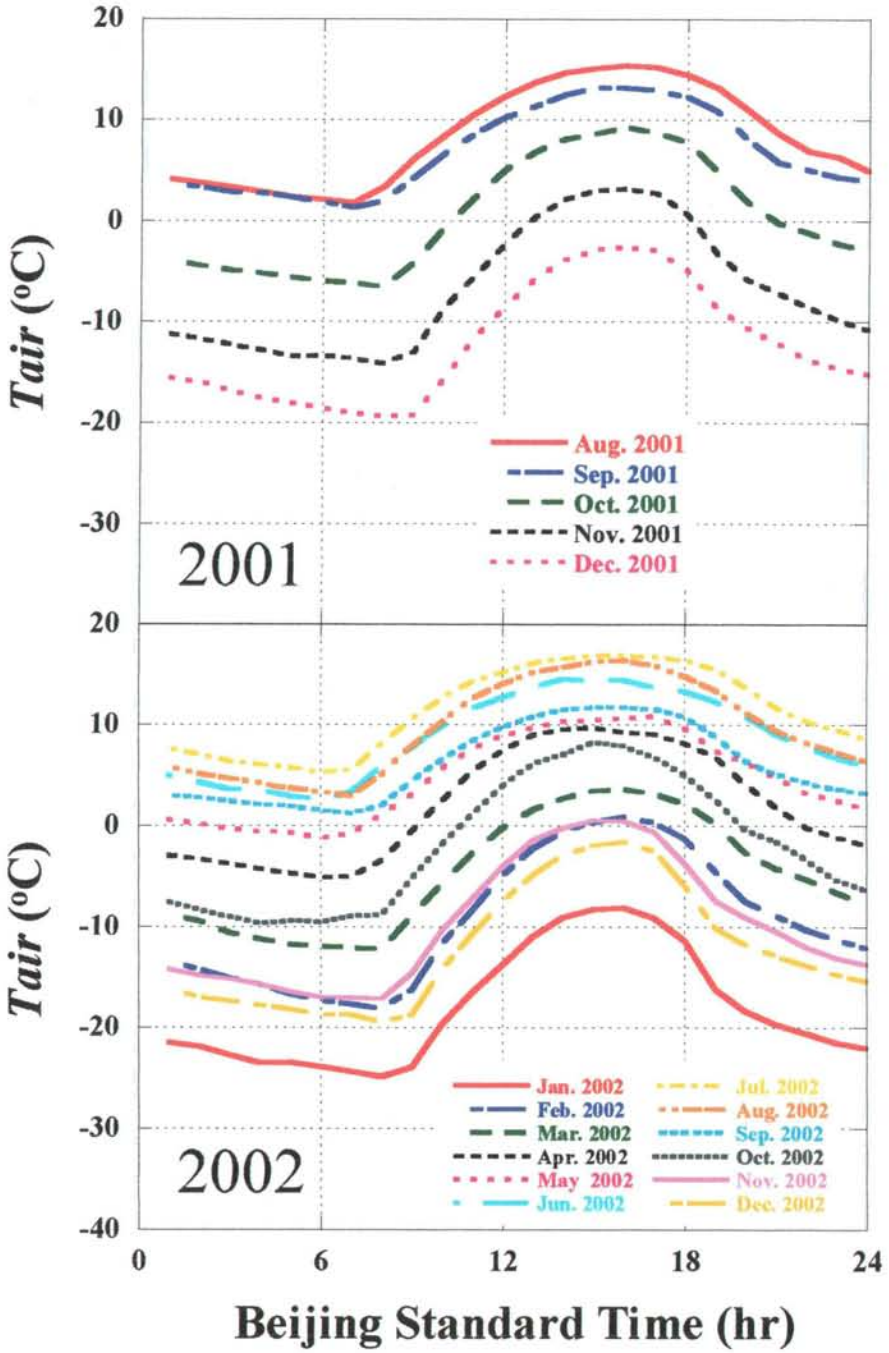

Figure 3.21. Diurnal changes of hourly averaged T_{air} at the Haibei station in 2001 and 2002. Data show monthly averaged values.

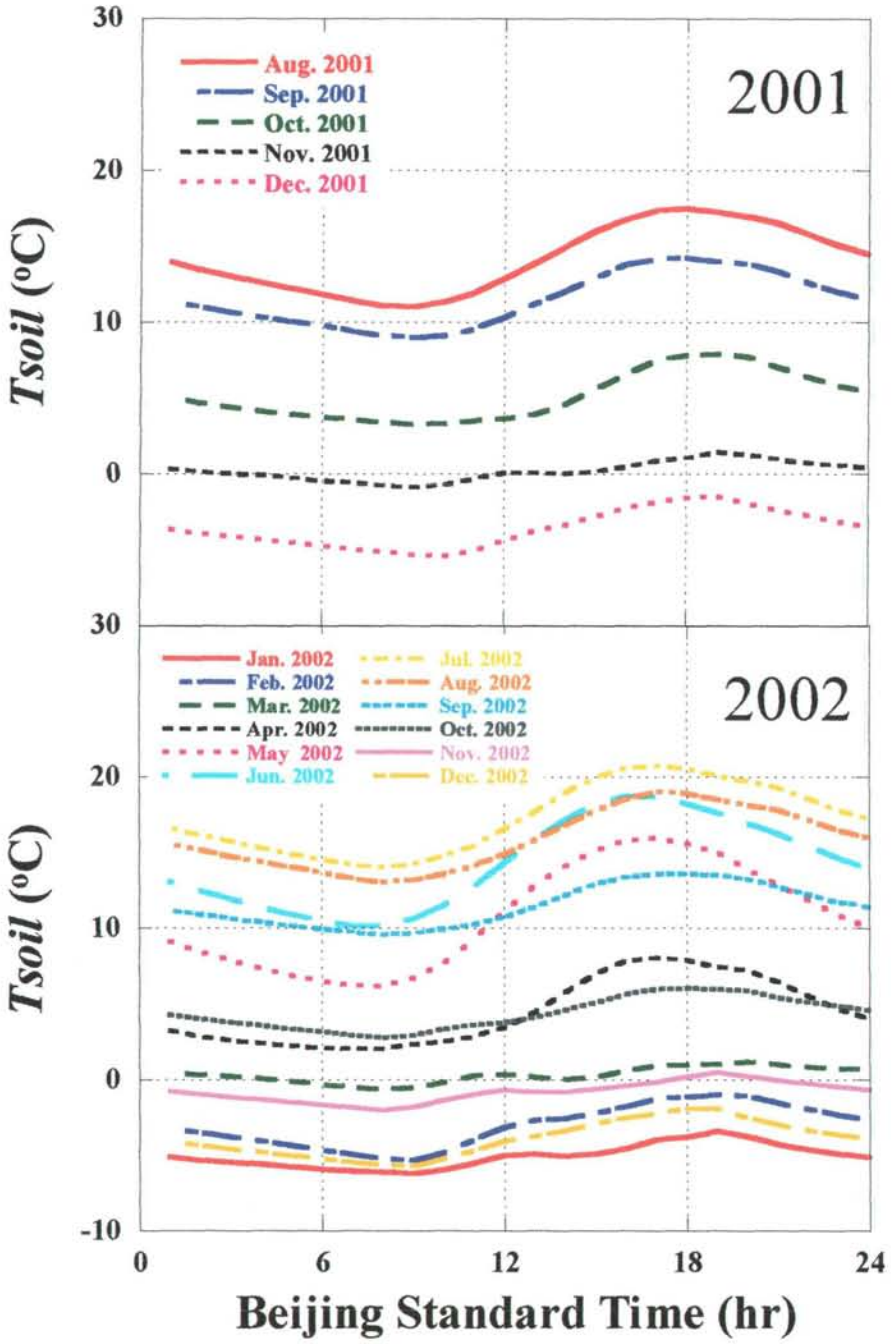

Figure 3.22. Diurnal changes of hourly averaged T_{soil} at Haibei station in 2001 and 2002. Data show monthly averaged values.

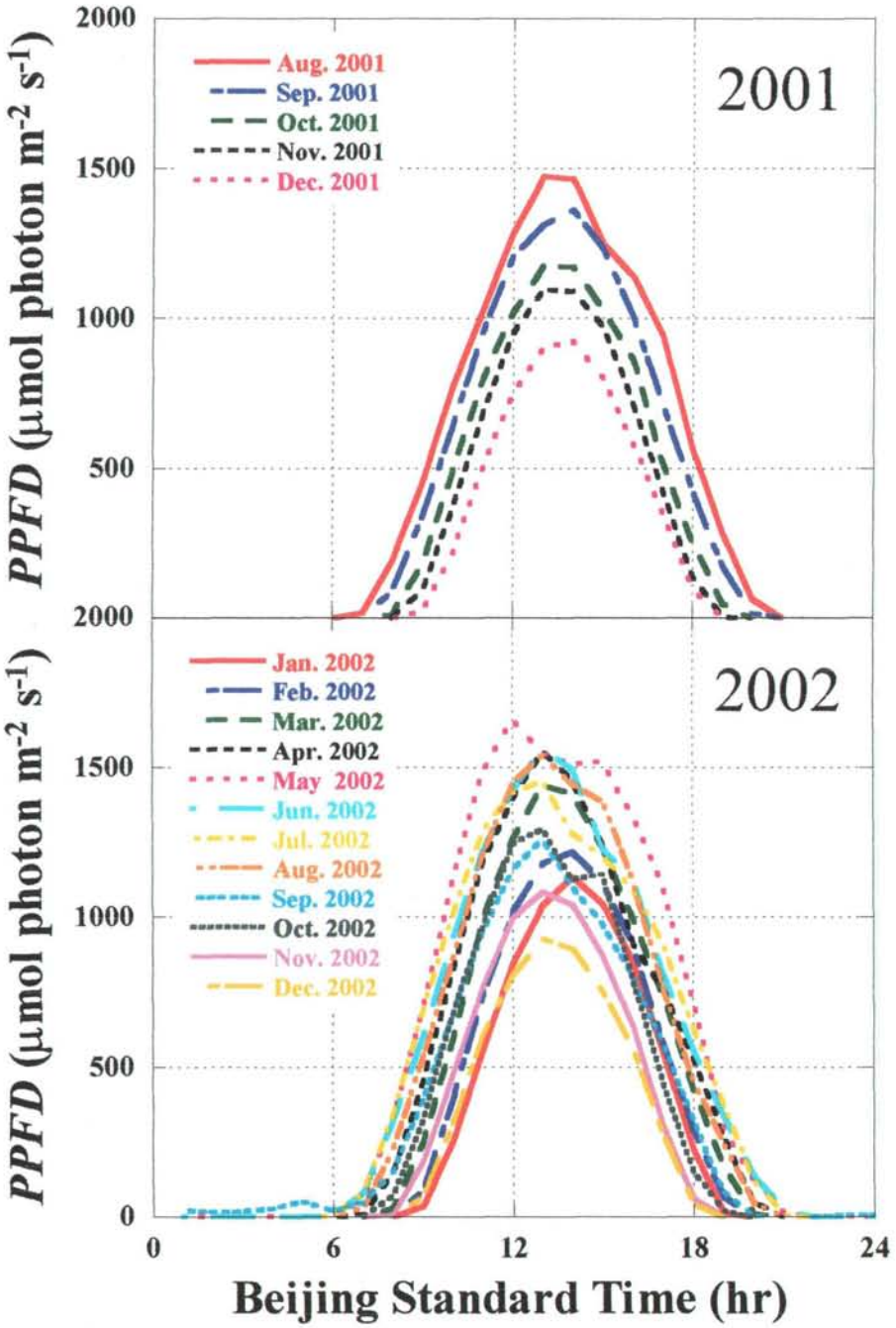

Figure 3.23. Diurnal changes of hourly averaged *PPFD* at the Haibei station in 2001 and 2002. Data show monthly averaged values.

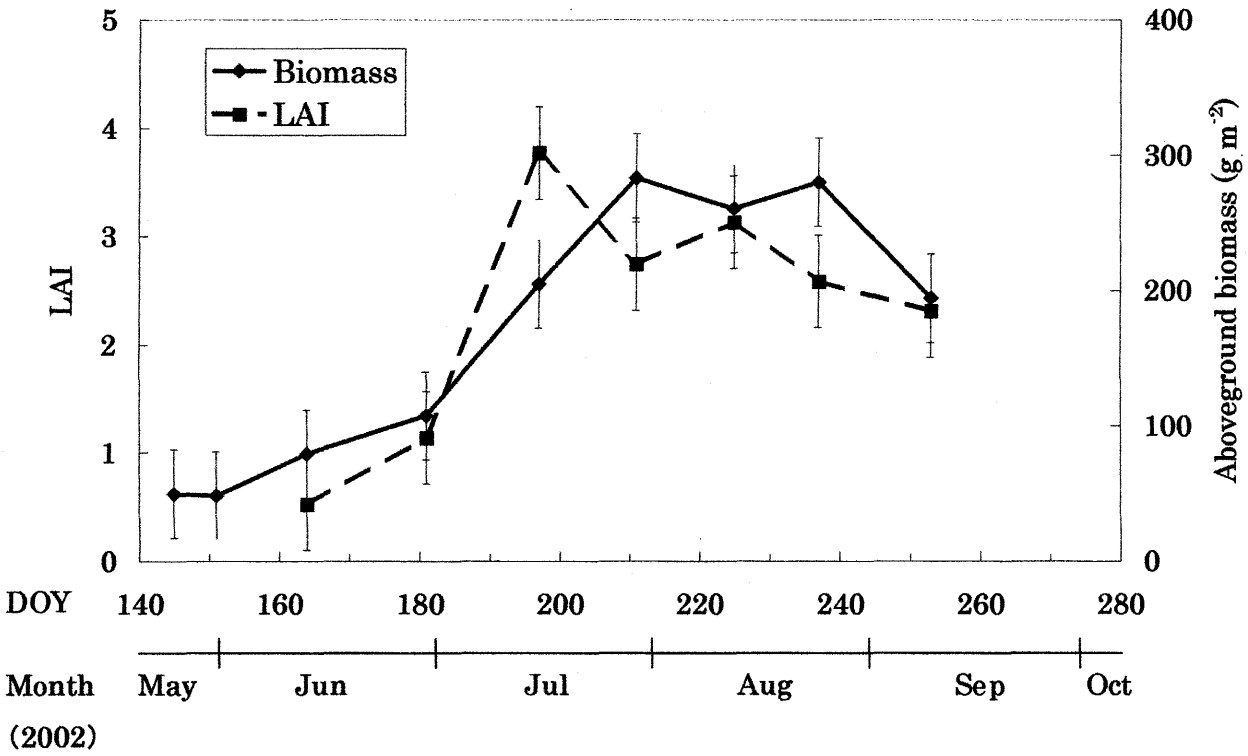

Figure 3.24. Mean and standard deviation (N=5) of the aboveground biomass and the *LAI* (leaf area index) for the *Koresia humilis* alpine meadow in 2002.

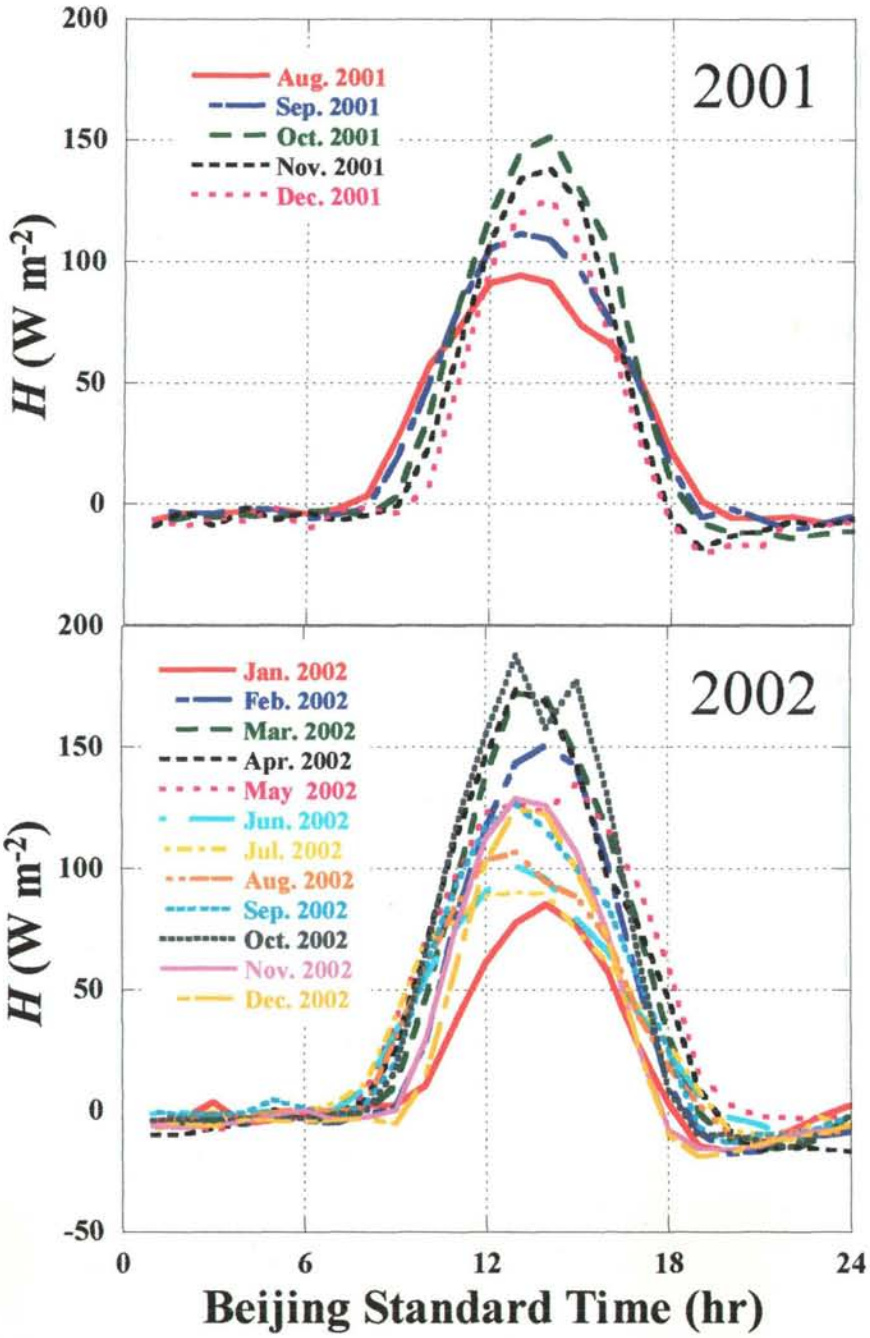

Figure 3.25. Diurnal changes of hourly-averaged H flux at the Haibei station for each month of the years 2001 and 2002, respectively.

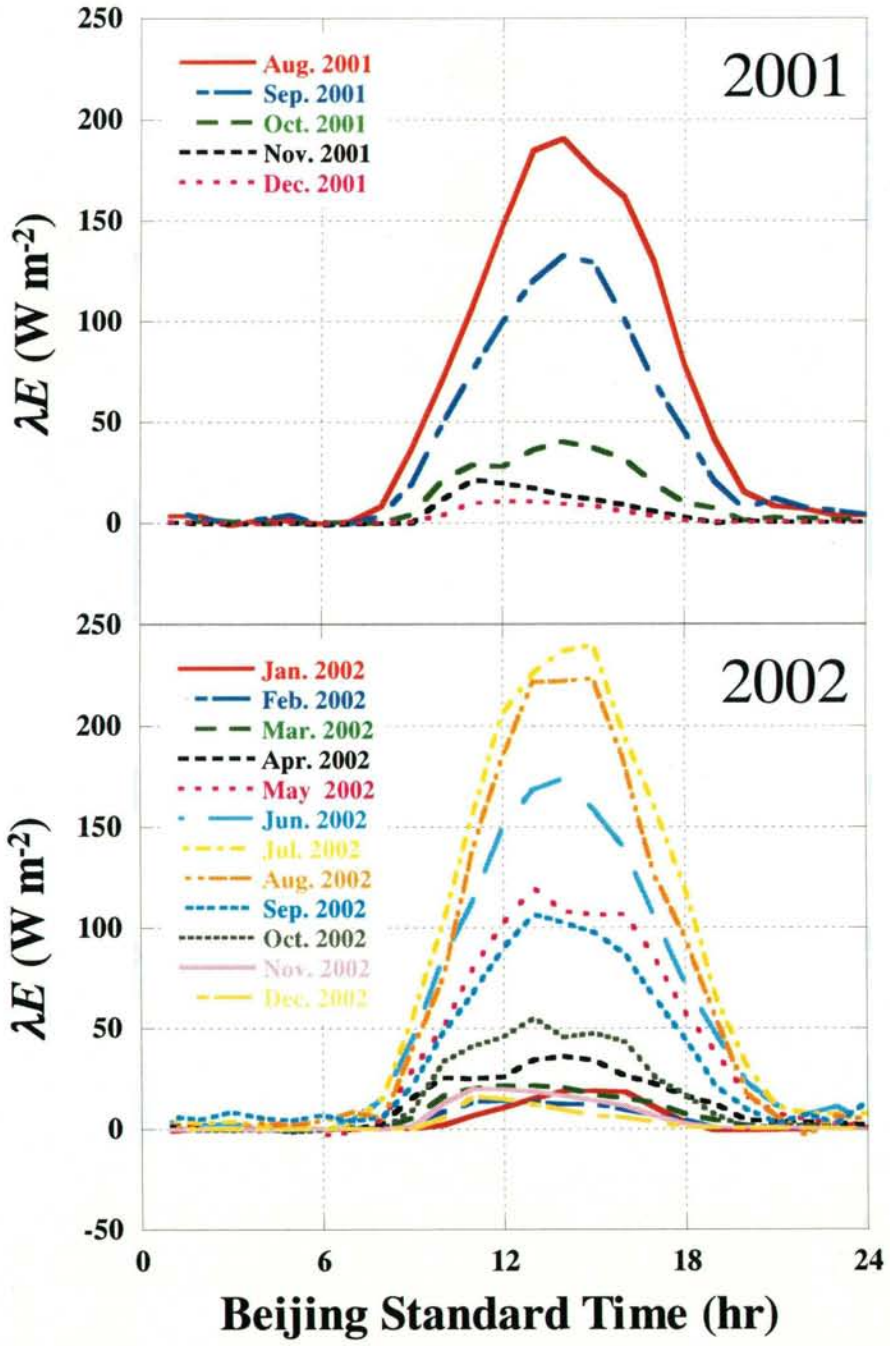

Figure 3.26. Diurnal changes of hourly-averaged λE flux at the Haibei station for each month of the years 2001 and 2002, respectively.

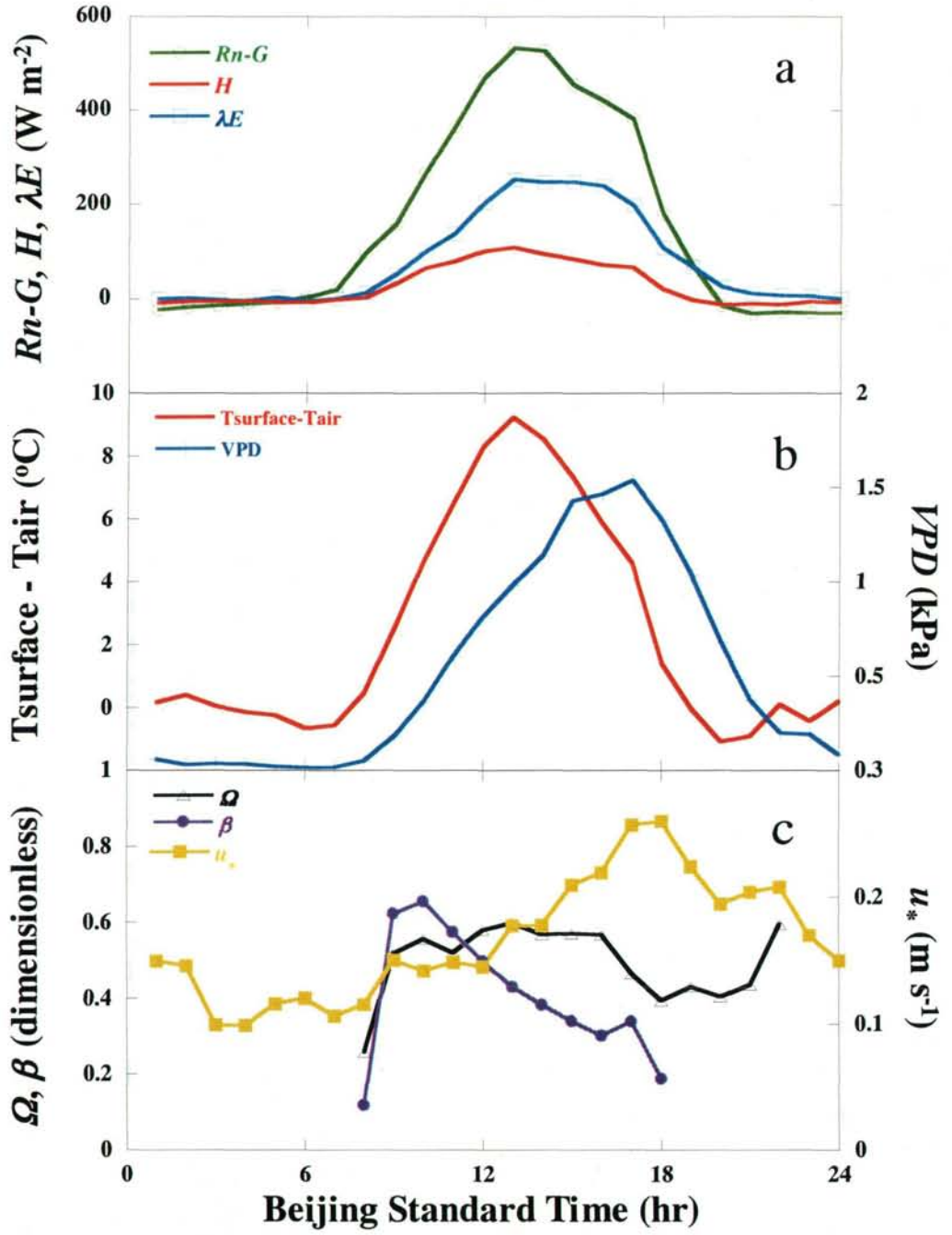

Figure 3.27. Diurnal courses of hourly-means of H, λE and environmental conditions from 9 to 15 August 2001. a) available radiation (Rn-G, ○); sensible heat flux (H, ◇) ; latent heat flux (λE, □); b) the difference between canopy surface temperature and air temperature ($T_{surface}$ - T_{air}, ×); vapor pressure dificit (VPD, +); c) Omega factor (Ω, △); Bowen ratio (β, ●); friction velocity (u_*, ■). The canopy surface temperatures are estimated from the upward long wave radiation data using the Stefan-Boltzmann's law; $Rl = \varepsilon \sigma (T_{surface} + 273.15)^4$, where Rl is the long wave radiation (W m^{-2}), ε is radiation emmisivity (adopted for 0.98), σ is the Stefan-Boltzmann constant = 5.67 x 10^8 W m^{-2} K^{-4}).

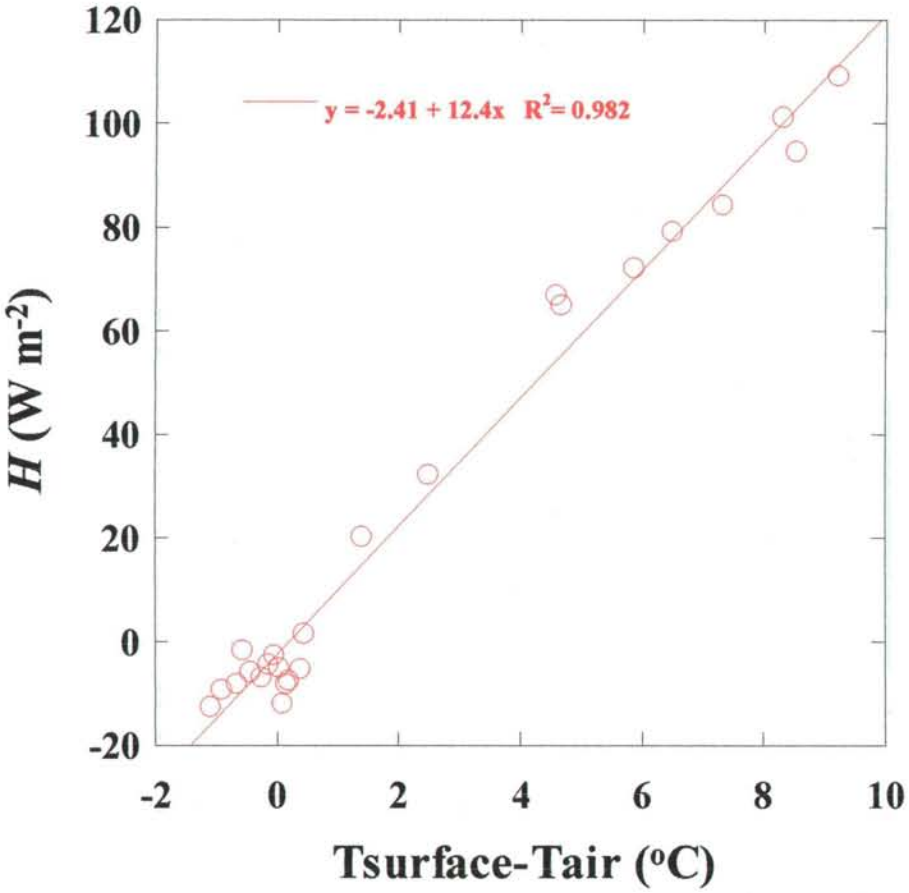

Figure 3.28. Relationship between the hourly-means of soil surface-air temperature difference and sensible heat flux (H) from 9 to 15 August 2001. Data show hourly mean values.

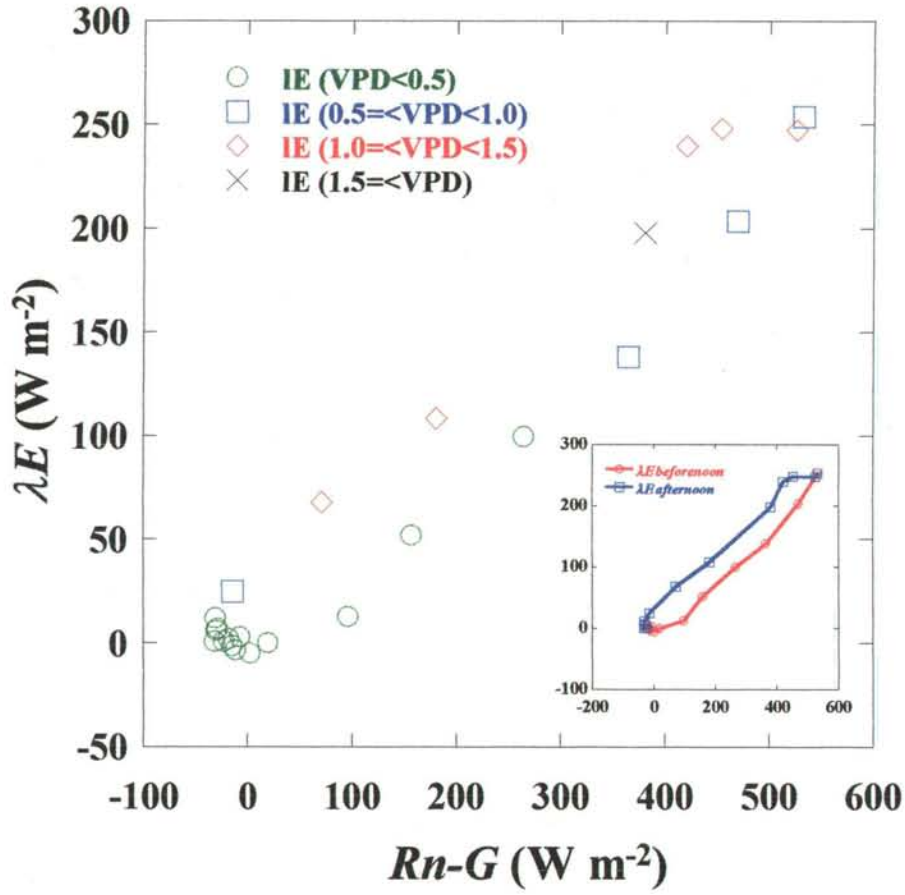

Figure 3.29. Relationship between hourly-means of vapor pressure deficit (*VPD*) and latent heat flux (λE) from 9 to 15 August 2001.

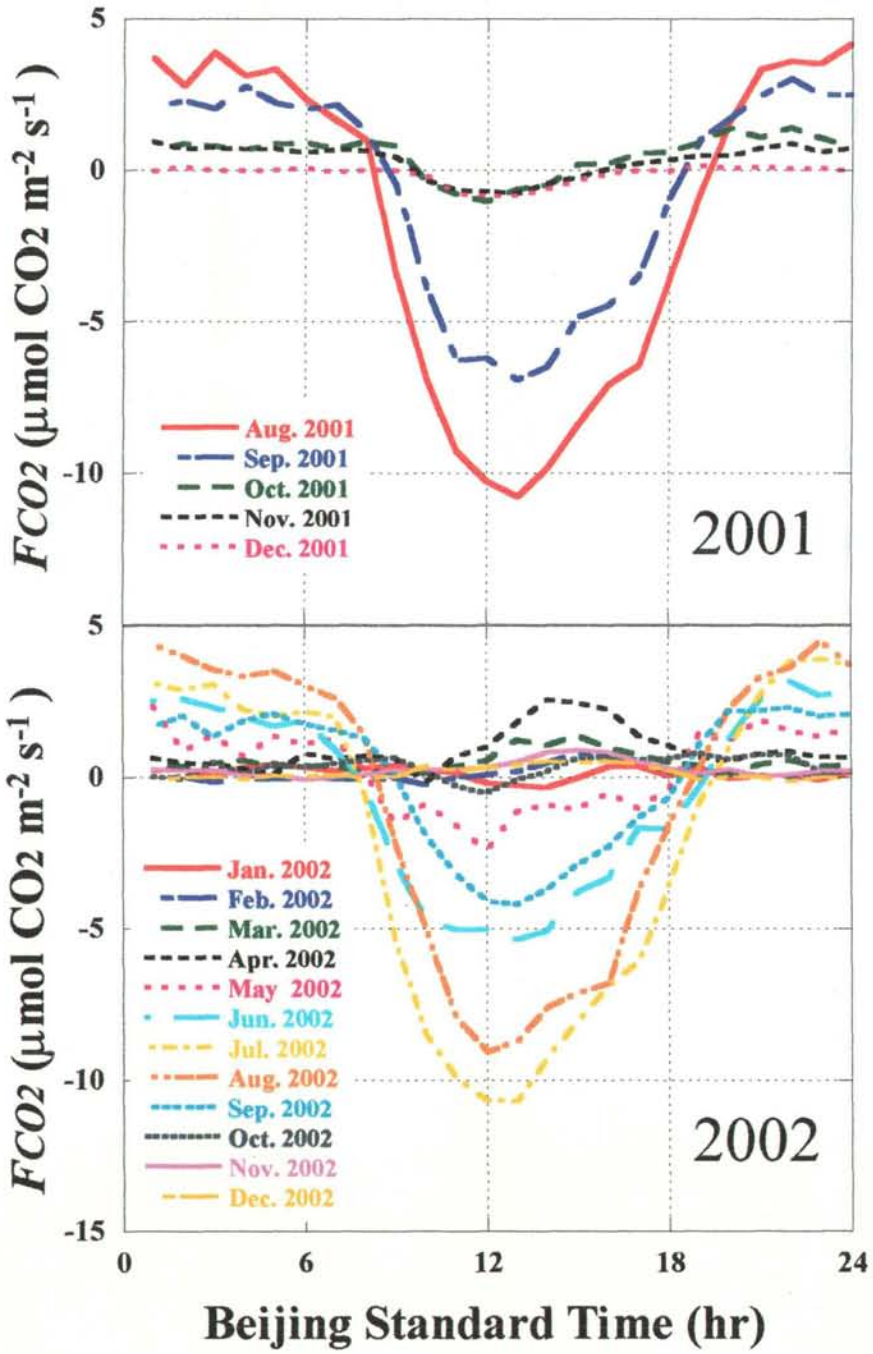

Figure 3.30. Diurnal changes of hourly averaged F_{CO_2} flux at the Haibei station in 2001 and 2002. Data show monthly averaged value.

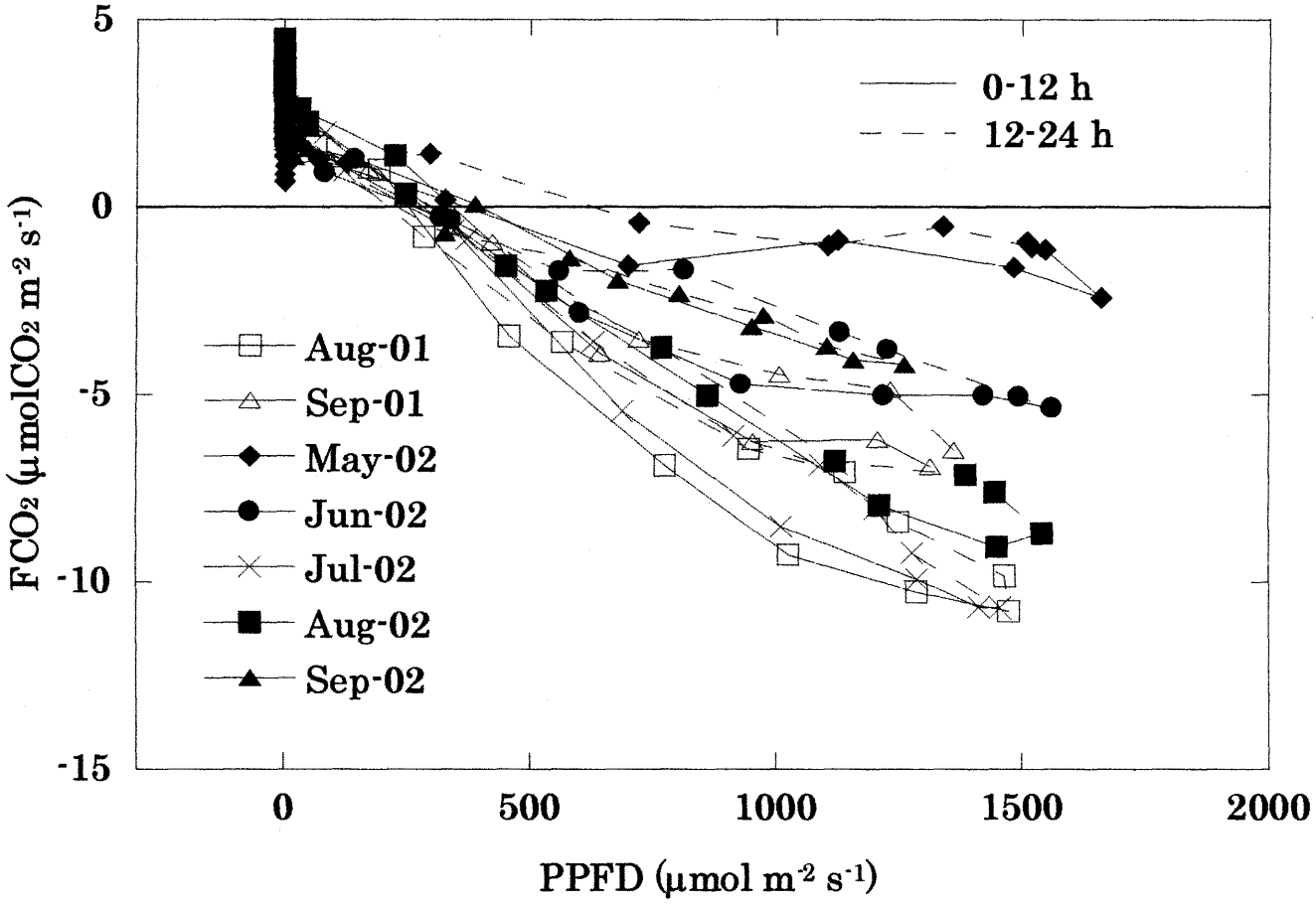

Figure 3.31. Relationship between net carbon exchange rate (F_{CO_2}) and incident *PPFD* (photosynthetic photon flux density) in each month over a growing season: August 2001 (□), September 2001 (△), May 2002 (◆), June 2002 (●), July 2002 (×), August 2002 (■), September 2002 (▲).

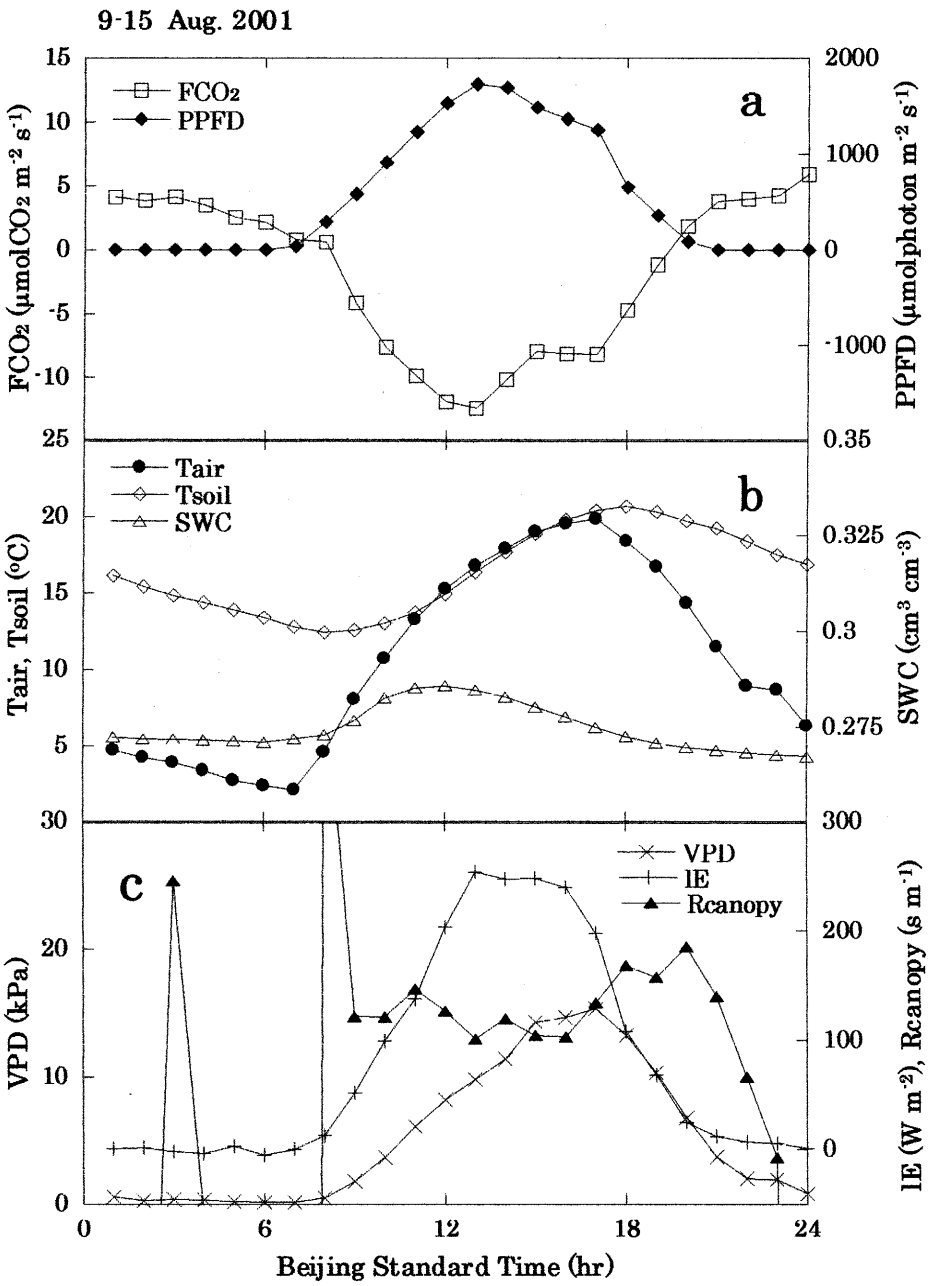

Figure 3.32. Diurnal courses of hourly mean CO_2 exchange flux and environmental conditions on 9-15 August 2001. a) Net carbon exchange rate (F_{CO_2}, □); incident photosynthetic photon flux density ($PPFD$, ◆); b) air temperature (T_{air}, ●); soil temperature (T_{soil}, ◇); soil water content (SWC, △); c) VPD (×), Penman–Monteith canopy resistance (R_{canopy}, ▲), and latent heat flux (λE, +).

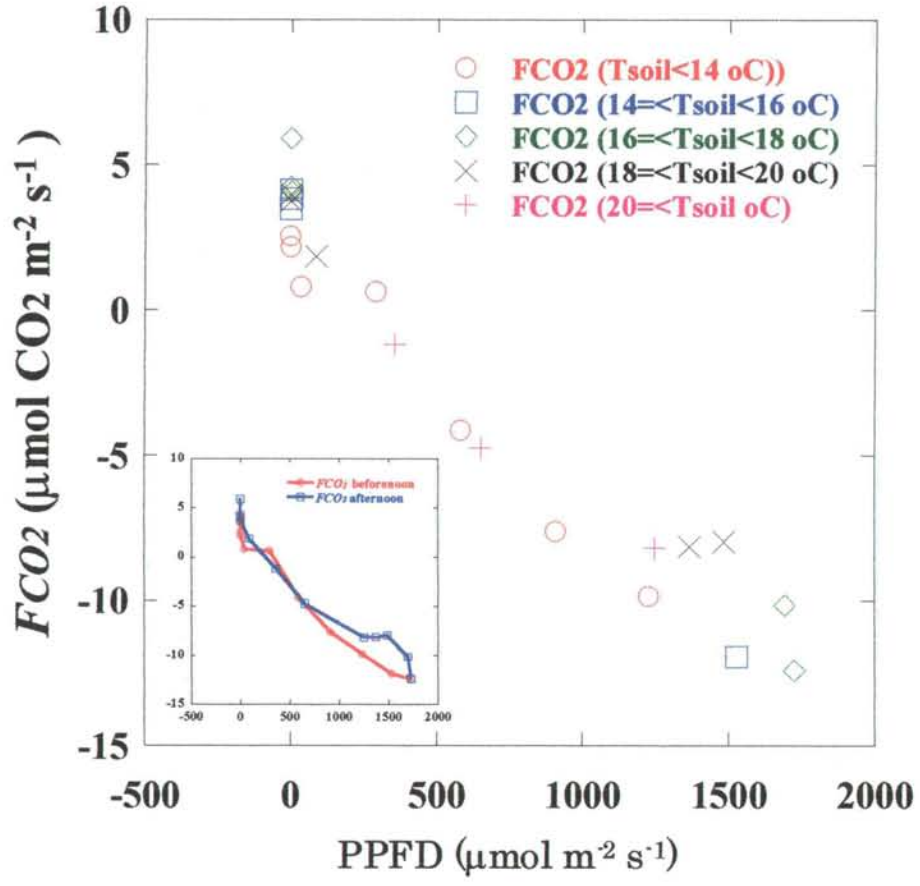

Figure 3.33. Relationship between hourly-means of the *PPFD* and CO_2 flux (F_{CO_2}) from 9 to 15 August 2001.

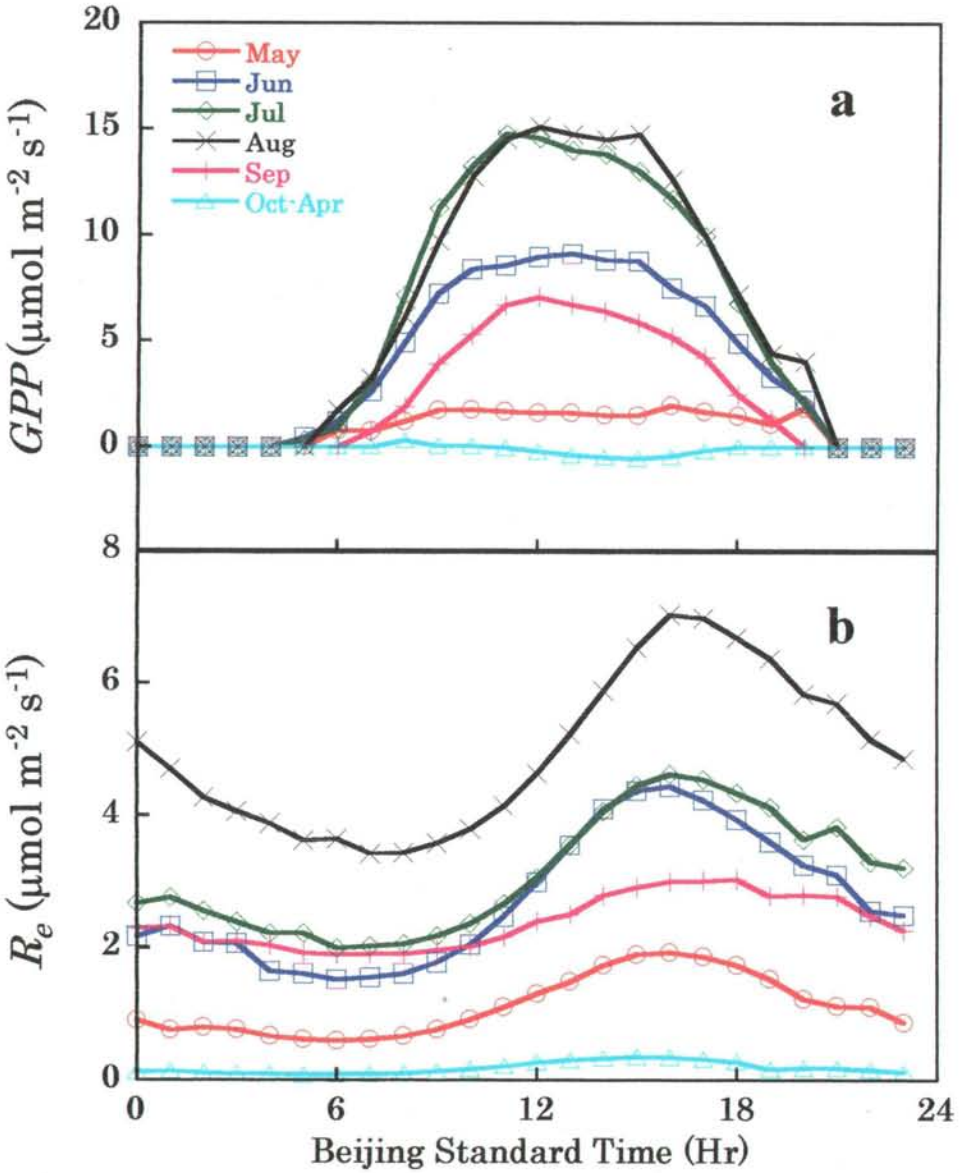

Figure 3.34. Diurnal courses of (a) hourly mean gross primary production (*GPP*), and (b) hourly mean ecosystem respiration (R_e) in 2002 (May ○, June □, July ◇, August ×, September +, October–April △).

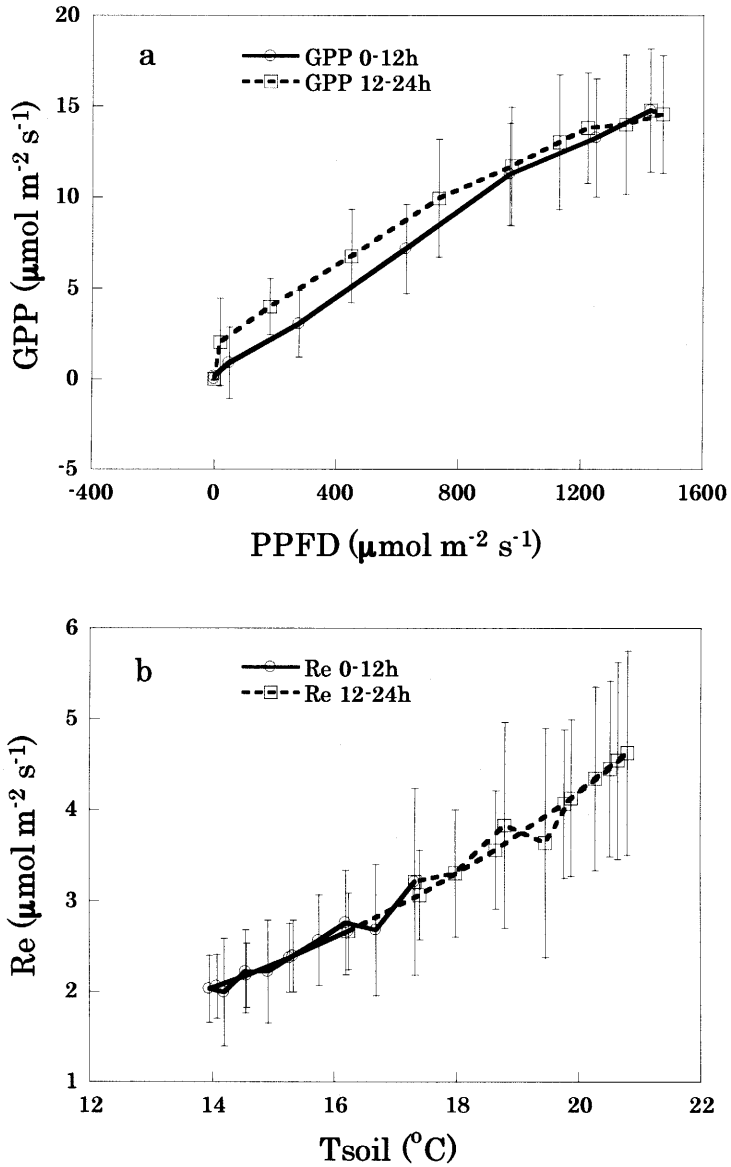

Figure 3.35. Relationship between (a) gross primary production (*GPP*) and irradiant *PPFD* (photosynthetic photon flux density), and (b) ecosystem respiration (R_e) and 5 cm soil temperature (T_{soil}) in July 2002 (0–12 h, ○ with solid lines, 12–24 h □, with broken lines). Data show hourly mean values with standard deviation (n = 30 or 31). The equation for predicting *GPP* from *PPFD* is $y = 0.000292x + 0.18$; $r = 0.612$ (0–12 h), 0.432 (12–24 h); s.e. = 0.0102 (0–12 h), 0.00763 (12–24 h). The equation for predicting R_e from T_{soil} is $y = 0.0174\exp(0.117x)$; $r = 0.594$ (0–12 h), 0.726 (12–24 h); s.e. = 0.000857 (0–12 h), 0.00149 (12–24 h). There is no significant difference between 0-12h and 12-24h in ANOVA of *GPP* and R_e data ($P < 0.0001$).

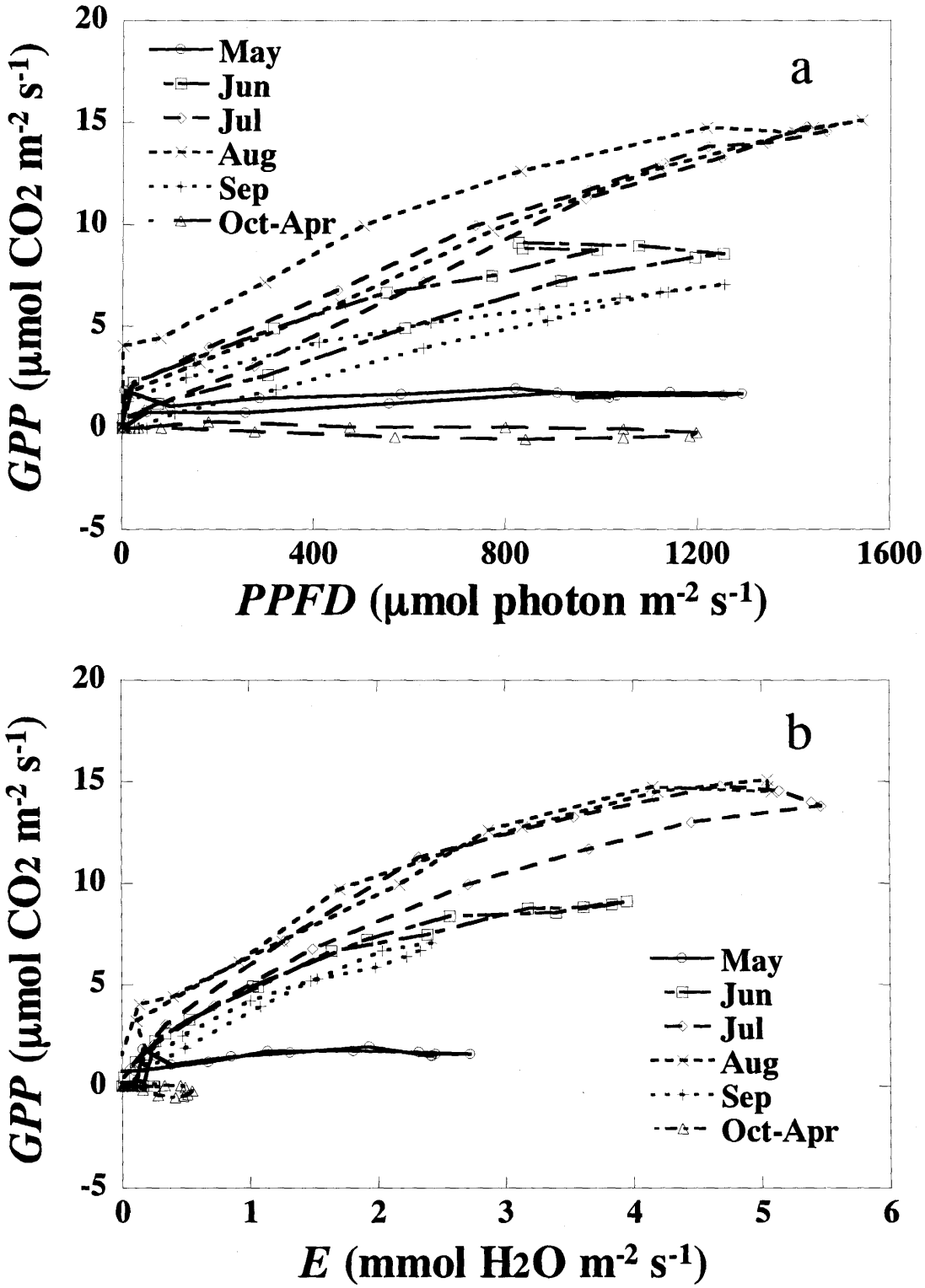

Figure 3.36. Relationship between (a) gross primary production (*GPP*) and incident *PPFD*, and (b) *GPP* and evapotranspiration (*E*) in 2002 (May ○, June □, July ◇, August ×, September +, October–April △).

Chapter 4 Seasonal changes of the CO_2 exchanges

4.1. Introduction

Net ecosystem production (*NEP* = *-NEE*) between the atmosphere and terrestrial ecosystems is influenced by various factors, e.g. temperature, light intensity, soil water content and phenology (Aubinet et al., 2000; Baldocchi et al., 2001; Valentini et al., 2000). Gross primary production (*GPP*), CO_2 uptake by plants via photosynthesis, and ecosystem respiration (R_e), CO_2 efflux by plants and soil microbes via respiration, determine the *NEP*. Seasonal changes in *GPP* are affected mainly by leaf physiological activity, leaf area index (*LAI*), weather, and growing period. R_e is composed of autotrophic respiration (*AR*) and heterotrophic respiration (*HR*), which are controlled by plant and soil microbe activities disparately. *AR* is composed of plant growth and maintenance respiration. *HR* is strongly regulated by soil temperature and moisture (Lloyd and Taylor, 1994; Davidson et al., 1998; Xu and Qi, 2001). Thus, the phase and amplitude of these components determine the seasonal pattern of net CO_2 ecosystem exchange (*NEE*) (Randerson et al., 1999; White et al., 1999; Cramer et al., 1999; Falge et al., 2002). By using the FLUXNET database, Falge et al. (2002) recently studied the factors that control seasonal changes in *GPP* and R_e in a wide range of terrestrial ecosystems. Their result showed that the seasonality of *GPP* was determined by the life-form (e.g. broad leaf or needle leaf), and that of R_e was affected by the climatic types that are characterized usually by temperature. Saigusa et al. (2002) reported that the maximum *GPP* of a cool-temperate deciduous forest, derived from a *PPFD–GPP* regression curve of a rectangular hyperbolic function, was associated with *LAI*, but that light use efficiency as the initial slope of the regression curve did not show clear seasonal changes. Flanagan et al. (2002) found that *GPP* in northern temperate grasslands was strongly related to *LAI* and canopy nitrogen content. Thus, GPP and R_e seems to be affected by plant phenology and climatic seasonality in lowland ecosystems. On the other hand, these relationships in alpine ecosystems are expected to exhibit different patterns from those in lowland ecosystems, even at similar latitudes (Li and Zhou, 1998). Little evidence, however, is available for us to determine the influence of environmental

factors on the seasonal changes in carbon dynamics of alpine ecosystems. Specifically, how do *GPP* and R_e of alpine grassland change seasonally?

From August 2001 to December 2002, long-term CO_2, water vapor and energy flux measurements using the eddy covariance method were carried out in an alpine meadow on the Qinghai-Tibetan Plateau. Additionally, the measured net ecosystem exchanges were attempted to be divided into *GPP* and R_e. The aims of this chapter are 1) to show the seasonal changes of those CO_2 fluxes, *NEP*, *GPP* and R_e, and 2) to clarify the environmental controls on the seasonal changes of those CO_2 dynamics.

4.2. Materials and Methods

CO_2 and H_2O flux were measured by the open-path eddy covariance method from 9 August to 31 December 2002. The study site is flat with a fetch of at least 250 m in all directions. Wind speed and sonic virtual temperature were measured at 2.2 m above the ground with a sonic anemometer (CSAT-3, Campbell Scientific Inc., Logan, UT, USA). Carbon dioxide and water vapor concentrations were also measured at 2.2 m with an open-path Infra-red gas analyzer (CS-7500, Campbell Scientific Inc.). Details are described in subsection 3.2.

Micrometeorological measurements were conducted at the same site. Net radiation and photosynthetic photon flux density (*PPFD*) were measured at 1.5 m above the ground with a net radiometer (CNR-1, Kipp & Zonen Inc., Saskatoon, Saskatchewan, Canada) and a *PPFD* meter (LI-190SB, Li-Cor, Lincoln, NE, USA). Air temperature and humidity were measured at 2.2 m and 1.1 m above the ground with a humidity and temperature probe (HMP45C, Vaisala, Helsinki, Finland). Wind speed was measured at 2.2 m and 1.1 m above the ground with a cup anemometer (034A-L and 014A, R. M. Young Co., Traverse, MI, USA). Soil heat flux was measured at 0.02 m below the ground at three points with heat plates (HFT-3, Campbell Scientific Inc.). Soil temperature was measured at 0.025, 0.05, 0.1, 0.2, 0.3, 0.4, 0.5, 0.6, and 0.7 m below the ground with copper-constantan manufactured thermocouples. Soil water content was measured at 0.05, 0.2, and 0.5 cm with time-domain reflectometry sensors (CS-615, Campbell Scientific Inc.). Soil surface temperature was measured at three points in a 1-m^2 area

with thermistor thermometers (107 probe, Campbell Scientific Inc.). Rainfall was measured at 0.7 m above the ground with a tipping bucket (TE525MM, Campbell Scientific Inc.). Details are described in subsection 3.2.

4.2.1. *NEP*, *GPP* and R_e gap-filling methods

When natural and anthropogenic impacts on the global ecosystem carbon budget are being compared among biome types, phenology, and stress conditions, the calculations usually use annual sum data of net ecosystem exchange (Valentini et al., 2000; Falge et al., 2002). However, Falge et al. (2001) found that the average data coverage during a year was only 65%, owing to system failures or data rejection. They reviewed several methods of gap-filling and applied them to data sets available from the EUROFLUX and AmeriFlux databases. They used mean diurnal variation (MDV), look-up tables (LookUp), and nonlinear regression (Regression) methods, and investigated the impact of different gap-filling methods on the annual sum of *NEP*. In this study, those three methods were also used to fill gaps in order to obtain annual sums of *NEP*. Details of the methods are reported in Falge et al. (2001).

In the MDV method, a missing datum is replaced by the mean for that time period (15 min) from adjacent days. The data windows of 7 and 14 days and two different algorithms of (a) an "independent" window and (b) a "gliding" window were chosen. In (a), for each subsequent period of data, mean diurnal variations are established to fill gaps within that period. In (b), a window of prescribed size around each gap is used to construct mean diurnal variations for gap-filling within that window.

In the LookUp method, look-up tables were created for six bimonthly periods or four seasonal periods ranging from 1 April to 30 May, 1 June to 30 September, 1 October to 30 November, and 1 December to 31 March. For the look-up table, average *NEE*s were compiled for 27 *PPFD* classes × 35 T_{air} (air temperature) classes. *PPFD* classes consisted of 100 μmol m^{-2} s^{-1} intervals from 0 to 2600 μmol m^{-2} s^{-1} with a separate class for *PPFD* class = 0. Similarly, T_{air} classes were defined through 2 °C intervals ranging from –35 to +34 °C.

In the Regression method, regression relationships were established between the *NEP*

component, i.e. R_e and *GPP*, and associated controlling factors (temperature and light) for every month. Missing R_e was extrapolated by using exponential regression equations (Eq. (3.48)) between measured nighttime R_e with strong turbulence ($u_* > 0.2$ m s^{-1}) and soil temperature at a depth of 5 cm. Nighttime eddy covariance flux data under the condition of below the u_* threshold (Aubinet et al., 2000) (0.2 m s^{-1} in this study) were also corrected with the regression equations (Eq. (3.48)); called as "u_*-correction". *GPP* was extrapolated by using rectangular hyperbolic regressions of daytime *GPP* against *PPFD* with Michaelis–Menten type equation (Falge et al., 2001) for every month:

$$GPP = \frac{\alpha\, GPP_{SAT}\, PPFD}{GPP_{SAT} + \alpha\, PPFD}, \tag{4.1}$$

where α is the initial slope of the light–*GPP* curve (μmol CO_2 [μmol photon]$^{-1}$) and is equivalent to the quantum yield. GPP_{SAT} is *GPP* at light saturation (μmol m^{-2} s^{-1}). Those two parameters are assigned as the monthly-specific parameters.

4.3. Results

4.3.1. Micrometeorology

The *PPFD* reached the maximum of 63.9 mol m^{-2} d^{-1} in late June and then decreased gradually (Fig. 4.1a). The daily average air temperature and soil temperature ranged from 2 to 15.5 °C and 6.3 to 19.2 °C, reaching maximum of 15.5 and 19.2 °C in the middle of July, respectively (Fig. 4.1b, c). Rain fell mainly from May to September in both years (Table 4.1). During 7–14 consecutive dry days following the rainy days in 2002 (Fig. 4.1d), the soil water content (*SWC*) decreased gradually from 0.54 cm^3 cm^{-3} (saturation) to 0.2 cm^3 cm^{-3} (Fig. 4.1e), and the vapor pressure deficit (*VPD*) often increased to 5–6 hPa (Fig. 4.1f).

H had two peaks in April and October and λE reached the maximum status in July (Fig. 4.2a, b; Table 4.2). The Bowen ratio (β) showed very high value in winter season and kept low value below 1.0 during the growing season (Fig. 4.2c; Table 4.2). The ratio of actual evaporation (λE) measured by eddy covariance measurement to equilibrium evaporation (λE_{eq}) ranged from 0.8 to 1.0 during the growing season (Fig. 4.2d). This indecates that this ecosystem

has the capacity to produce enough evaporation to meet atmospheric demand, yet remain wet. Omega factor (Ω) ranged from 0.2 to 0.8 during the growing season, and the seasonal pattern was quite similar to that of λE (Fig. 4.2e). R_{canopy} derived from Eq. (3.47) remained low at around 100 s m^{-1} from 23 May (DOY143) to 17 September (DOY260) in 2002 (Fig. 4.2f). This result supposes that the soil moisture was high enough to keep the stomata of canopy plants open. After this period, canopy resistance rose gradually to 300 s m^{-1}. Albedo kept around 0.20 during the growing season, from May to September, and around 0.23 during other period of the year, except occasional snow (Fig. 4.2g; Table 4.2).

4.3.2. Carbon dioxide flux

The seasonal changes of $NEP_{daytime}$, $NEP_{nighttime}$, and NEP_{total}, are the daily integrated values of CO2 uptake flux ($-FCO2$) as net ecosystem production for daytime, nighttime, and the whole day, respectively (Fig. 4.3). In 2002, $NEP_{daytime}$ started to increase from 23 May (DOY143), and reached its maximum status on 30 June (DOY181) and local maximum of 5.4 g C m^{-2} d^{-1} on 7 July (DOY188). $NEP_{daytime}$ started to decrease from 19 August (DOY231) and reached the early summer value on 30 September (DOY273). $NEP_{nighttime}$ showed the opposite change, reaching the minimum of –2.5 g C m^{-2} d^{-1} on 19 August (DOY231). NEP_{total} showed similar changes to those of $NEP_{daytime}$, and peaked at 3.9 g C m^{-2} d^{-1} on 7 July (DOY188). NEP_{total} rarely became negative, but reached the minimum of –1.3 g C m^{-2} d^{-1} on 29 September (DOY272). The cumulative NEP_{total} for the growing season from 23 May to 30 September 2002 was 153.1 g C m^{-2}.

The author performed a linear regression (Fig. 4.4) of $NEP_{daytime}$ (Fig. 4.3) on integrated *PPFD*. The slopes of the regression line showed similar seasonal change pattern to *LAI* (Fig. 3.24; Table 4.3), peaking in July and then decreasing in September 2002.

To investigate the relationship between ecosystem respiration and temperature, the nighttime average *FCO2* was plotted against the nighttime average soil temperature at a depth of 5 cm (Fig. 4.5). The nighttime average *FCO2* increased exponentially as soil temperature increased. However, the nighttime average flux was scattered widely within a narrow range of

soil temperatures in each month. Next, to assess the effect of *SWC* on ecosystem respiration, the nighttime average FCO_2 was plotted against *SWC* for five periods of low *SWC* after heavy rainfall in summer time (Fig. 4.6). The CO_2 efflux increased as *SWC* decreased. CO_2 of at least 0.94 μmol m^{-2} s^{-1} was released even in saturated conditions. In the 2002 periods 23 May-1 June, 11-19 August, and 24-31 August (see Fig. 4.1d, 2nd, 4th, and 5th data sequences), the nighttime average soil temperature increased from 2.8 to 4.2 °C as *SWC* decreased.

4.3.3. *GPP* and R_e

GPP equals to the sum of R_e and *NEP*. The estimation accuracy for *GPP* is thus affected by the estimation error of R_e. Consequently, the estimated R_e was compared to the R_e derived as an offset of the rectangular hyperbolic regression in the light response curves of the FCO_2 (as shown in Suyker and Verma, 2001; eq. (1); Fig. 4.7). The regression line showed a good agreement between two R_es; the slope was 1.08 and offset was 0.06 g C m^{-2} d^{-1}.

Seasonal changes in the monthly parameters of R_e and *GPP* regression curves; R_{10}, α, and GPP_{SAT}, in Eqs. (3.48) and (4.1), are given in Table 4.4. R_{10} reached a maximum status of 2.27, 1.88 μmol m^{-2} s^{-1} in August and September. R_{10} showed negative values in January and February, and that was assumed to be from using the constant parameter in E_a. However, even if daytime R_e calculation has the internal errors, the very small magnitude of R_e in winter don't have so significant influence in annual R_e estimation. α showed abrupt high value in May and reached maximum status in June to August, and kept near zero values in October to April. GPP_{SAT} increased from May and reached maximum status in July and August, and kept near zero values in October to April.

Seasonal changes in the 15-d moving average values of *PPFD* and T_{soil}, which strongly affect *GPP* and R_e, are given in Fig. 4.8a. *PPFD* shows three maximal and three minimal values during the growing season from May to September, which corresponded to three rainfall events: maximums on days of the year (DOY) 181, 207, and 232; minimum on DOY166, 190, and 217. T_{soil} also shows three maximum and three minimum values during the growing season, but those dates lag by 1–13 d in comparison with those of *PPFD*: maximum on DOY189, 213, and 237;

minimum on DOY167, 203, and 230. T_{soil} decreased gradually after the first day of maximum (DOY189).

Seasonal changes in the 15-d moving average values of *GPP* to R_e are given in Fig. 4.8b. *GPP* started to increase on 1 May (DOY121), reaching a first maximum value of 5.90 μmol m^{-2} s^{-1} on 7 July (DOY188), a second maximum of 6.46 μmol m^{-2} s^{-1} on 2 August (DOY214) and a third maximum of 5.71 μmol m^{-2} s^{-1} on 19 August (DOY231). After that day, *GPP* decreased gradually to 1.0 μmol m^{-2} s^{-1} on 28 September (DOY271). R_e started to increase at the beginning of March, reaching a first maximum value of 3.48 μmol m^{-2} s^{-1} on 12 July (DOY193), a second maximum of 5.40 μmol m^{-2} s^{-1} on 8 August (DOY220), and a third maximum of 4.45 μmol m^{-2} s^{-1} on 24 August (DOY236). Thus, the seasonal changes of *GPP* show that the plant growing season ranges from May to September in this alpine meadow ecosystem, but do not correspond perfectly with those of *PPFD*, although the seasonal changes of R_e show a good agreement with those of T_{soil}.

Figure 4.8b also shows the seasonal changes in the ratio of *GPP* and R_e. The ratio remained mostly larger than 1 form May to September. This indicates that this ecosystem was a sink of carbon during the growing season in 2002. The maximum value of the ratio was 2.07 on 24 July (DOY205).

Figure 4.8c shows the seasonal changes in the 15-d moving average values of GPP_{max} and R_{emax}, the maximum values of diurnal *GPP* and R_e change, which are potential values of assimilation and respiration of CO2. GPP_{max} started to increase rapidly on 1 May (DOY121), exceeded 20 μmol m^{-2} s^{-1} for the two months from 2 July (DOY183), and reached a maximum of 23.6 μmol m^{-2} s^{-1} on 31 July (DOY212). After 20 August (DOY232), when *GPP* was 20.4 μmol m^{-2} s^{-1}, *GPP* decreased rapidly to 1.0 μmol m^{-2} s^{-1} on 10 October (DOY283). R_e started to increase on 1 May (DOY121), reaching a first maximum value of 8.10 μmol m^{-2} s^{-1} on 1 July (DOY182) and an annual maximum of 12.0 μmol m^{-2} s^{-1} on 25 August (DOY237), and then decreased rapidly to 1.0 μmol m^{-2} s^{-1} on 25 October (DOY298). Thus, the seasonal changes of GPP_{max} corresponded well with those of *GPP*, although the annual maximum of R_{emax} lagged two weeks behind that of R_e.

The radiation use efficiency (RUE_{GPP}), the ratio between *GPP* and *PPFD* ranged from 10 to 20 mmol CO_2 mol photon^{-1} from June to August, RUE_{GPP} change with plant growth (Fig. 4.9). The water use efficiency (WUE_{GPP}), the ratio between *GPP* and evapotranspiration (*E*) ranged from 2.0 to 4.0 mmol CO_2 mol H_2O^{-1} from June to August, and also changes along with plant growth (Fig. 4.9).

To clarify the effect of *LAI* on CO_2 assimilation potential and resource use efficiency, the relationships between *LAI* and GPP_{max}, RUE_{GPP} and WUE_{GPP} are shown in Fig. 4.10. GPP_{max}, RUE_{GPP}, and WUE_{GPP} tended to increase with the increase of *LAI* increased.

4.3.4. Annual sums of net ecosystem carbon dynamics

Table 4.5 lists annual sums of *GPP*, R_e, and *NEP*, and daily *GPP* and daily *NEP* as the quotient from the division of annual *GPP* and *NEP* by the number of days when $NEP > 0$. Missing data are filled by the Regression method for all parameters, and by the MDV and LookUp methods for *NEP*. Gap-filling methods reduced the proportion of missing data from 33.3% to 4% (Table 4.2). The remaining missing data are almost all in the coldest part of winter, from 1 to 13 January, when there is no biological activity at all, and does not affect annual sums of fluxes. The residue of peak aboveground biomass (134.7 g C m^{-2}: multiplying a peak aboveground dry weight biomass 283 g d.w. m^{-2} by a conversion coefficient to carbon 0.476 (unpublished data)) taken from annual *NEP* (78.5 g C m^{-2} y^{-1}), as annual carbon storage below ground, is –56.2 g C m^{-2} y^{-1}. In the data gap-filled by the Regr. methods without u_*-correction, annual balances of *GPP* and R_e are less than those with u_*-correction.

4.4. Discussion

4.4.1. Environmental controls on the seasonal changes of net carbon dioxide exchanges

The linear regression slopes of $NEP_{daytime}$ against *PPFD* were higher for August 2001 than August 2002 (Fig. 4.4). There are two major processes directly involved in this difference of slope, that is, a higher CO_2 uptake rate and a lower ecosystem respiration could result in a

higher slope. The *LAI* seems the major factor causing the increase of ecosystem CO_2 uptake. As the *LAI* increases, a larger photosynthetic leaf area and thus a higher ecosystem CO_2 uptake would be expected. It is indeed true for low *LAI* values (Larcher 1995). The *LAI* measured on 20 August 2001 was 3.1, which was about 20% higher than the *LAI* of 2.6 obtained on 25 August 2002 (Table 4.3). A detailed assessment of the effects of soil respiration on FCO_2 was beyond the scope of the current work, but it should be further clarified in order to understand the underlying mechanisms for the carbon cycle in the alpine meadow.

The nighttime CO_2 efflux (ecosystem respiration) shows a positive exponential relationship with soil temperature (Fig. 4.5) and an apparent linear relationship with *SWC* (Fig. 4.6). Similar response of nighttime CO_2 flux to SWC has been observed in tundra under near-saturation (Oechel et al., 1998). At this site, an excess of SWC beyond the optimum level (e.g., 0.3) seemed to have greatly affected CO_2 emission. The effect of SWC on CO_2 efflux in the alpine ecosystem seems different from that reported for relatively dry grassland (Hunt et al., 2002), likely because of the different range of *SWC* encountered. However, the decrease of FCO_2 with *SWC* in Fig. 4.6 could be an artifact of changing soil temperatures whose effect was not separated in this analysis, and therefore deserves further investigation.

4.4.2. Environmental controls on the seasonal changes of *GPP* and R_e

The timings of the maximum and minimum daily mean *GPP* synchronized with those of GPP_{max}, an index of potential ecosystem photosynthesis (Figs. 4.8a–c). GPP_{max} is positively related to *LAI* (Fig. 4.10a) as shown in Saigusa et al. (2002) and Flanagan et al. (2002). RUE_{GPP} and WUE_{GPP} also tended to increase as *LAI* increased (Figs. 4.10b, c). These results suggest that *LAI* determines the ecosystem capacity for assimilation and resource requirements.

The timings of the maximum and minimum of the daily mean R_e and R_{emax} synchronized with those of T_{soil}, an environmental factor, when these parameters were maximum (DOY180–230) (Figs. 4.8a–c). R_{emax}, however, increased even though T_{soil} decreased during the same period, as seen in R_{10} (Table 4.4). In general, seasonal changes in respiratory processes are controlled by climate more strongly than by biological factors (Falge et al., 2002). However, at

this study site, R_{emax}, which reached the maximum in autumn, may be associated with above- and below-ground biomass, which reached the maximum at the same time (Kato et al., in press, 2004b; Li and Zhou, 1998).

Seasonal changes of mean *GPP* and R_e were synchronized in the phases, as seen in temperate and Mediterranean ecosystems (Falge et al., 2002) (Fig. 4.8b). In contrast, those of GPP_{max} and R_{emax} were out of phase, as presented in GPP_{SAT} and R_{10} (Table 4.4) and seen in boreal coniferous forests (Falge et al., 2002). That time lag of GPP_{max} and R_{emax} phases is expected to be caused by the differences in the seasonal patterns of biological functions, i.e. LAI, plant and soil biomass, affecting the potential of assimilation and respiration, respectively.

When the GPP/Re ratio was assumed to be conservative in an alpine meadow as suggested in forests (0.47 ± 0.04 s.d.; Waring et al., 1998), the relatively high ratio of GPP/R_e indicates a high contribution of photosynthesis and autotrophic respiration to the carbon dynamics of this ecosystem (Fig. 4.8b). Values of GPP/R_e near 2 in late July correspond to $NEP = R_e$, indicating a low overall contribution of *HR*. This suggests that mainly autotrophic processes govern ecosystem carbon fluxes, as was observed in field crops and at temperate sites (Falge et al., 2002). When *GPP* considerably exceeds R_e like this, the accumulation of litter can reduce free nutrients in the ecosystem. Considering the close link between soil organic matter decomposition and nutrient cycling, this system may show negative feedback in growth and CO2 assimilation or be susceptible to disturbance (Shulze et al., 1999; Amiro, 2001).

4.4.3. Ecosystem carbon assimilation ability

The author compared the maximum NEP_{total} of study site (3.9 g C m^{-2} d^{-1}) with those of other sites at similar latitudes (Table 3.2). The maximum NEP_{total} in the present study was slightly less than that of the Kansas C_4 prairie (6.3 g C m^{-2} d^{-1}, Kim et al., 1992; 4.9 g C m^{-2} d^{-1}, Ham and Knapp, 1998), but 50% less than that of the Oklahoma tall-grass prairie (8.4 g C m^{-2} d^{-1}, Suyker and Verma, 2001). It seems that the alpine meadow ecosystem has a smaller daily CO2 uptake potential than other grassland ecosystems. The daily uptake potential of this site was 4 times that in the Colorado subalpine conifer forest at approximately the same elevation

(1.0 g C m^{-2} d^{-1}; 3050 m; Monson et al., 2002). The low temperature may suppress plant respiration and decomposition of soil organic matter. The small biomass may also an important factor decreasing plant respiration significantly. On the other hand, the short growing season was compensated by the high daily CO_2 uptake potential. Consequently, the alpine ecosystem sequestered a large amount of CO_2 (153 g C m^{-2}) during the growing season in 2002. Although it is still under debate whether or not CO_2 fluxes should be corrected by the magnitude of energy budget closure, the simple correction that compensate the lack proportion of energy balance as presented by Saigusa et al. (2002), was applied: 226 g C m^{-2} in the growing season CO_2 budget.

The author compared the *GPP* of the alpine meadow with those of other ecosystems. The annual *GPP* of 575 g C m^{-2} was lower than those of boreal coniferous forests (723–959 g C m^{-2} y^{-1}) and Colorado subalpine coniferous forest (831 g C m^{-2} y^{-1}; 3050 m) at similar elevations, and much lower than that of tropical forest (3249 g C m^{-2} y^{-1}), but within the range for temperate ecosystems, including forests and grasslands (542–1924 g C m^{-2} y^{-1}; average, 1262 g C m^{-2} y^{-1}; Falge et al., 2002). The daily *GPP* of the study site (3.59 g C m^{-2} d^{-1}, Table 4.5) was similar to those of boreal evergreen forest and Colorado subalpine coniferous forest (4.6 and 4.4 g C m^{-2} d^{-1}, respectively), although slightly lower than those of temperate coniferous forest and C_3 crops and grassland (5.7–6.9 g C m^{-2} d^{-1}). Thus, although the alpine meadow ecosystem has a daily CO_2 assimilation equal to that of a Colorado subalpine forest ecosystem, it has a lower annual *GPP* because of the restriction of the growing period.

The annual *NEP* in our study site (78.5 g C m^{-2} y^{-1}, Table 4.5), which was gap-filled by the Regr. method using the u_*-correction reported by Falge et al. (2002), was close to that of the Colorado subalpine coniferous forest (71 g C m^{-2} y^{-1}), although substantially lower than that of lowland grassland (231.3 g C m^{-2} y^{-1}) and boreal ecosystems (121.4 g C m^{-2} y^{-1}). The daily *NEP* of this site (0.49 g C m^{-2} d^{-1}, Table 4.5) was similar to that of the Colorado subalpine forest (0.38 g C m^{-2} d^{-1}). Although this alpine meadow ecosystem has a lower annual *GPP* than that of the subalpine forest ecosystem, it has a comparable annual *NEP*. It is assumed that not

only low temperature but also small biomass suppresses the ecosystem respiration; as a result, this ecosystem may sequester substantial C.

4.4.4. Gap-filling methods and annual carbon dynamics

Annual *NEP*s differed largely with some gap-filling methods (78.5–149.5 g C m^{-2}; Table 4.5). For the Regression method, which calculates *GPP* and R_e separately, R_e with u_*-correction was higher by 83.1 g C m^{-2} y^{-1} than without u_*-correction. This fact, based on the principle that u_*-correction replaces nighttime eddy covariance fluxes under more stable condition with fluxes under higher turbulence, should be reasonable. The consequent decline in annual *NEP* due to u_*-correction (–35.4 g C m^{-2} y^{-1}) was lower than that observed in other ecosystems (–77.0 g C m^{-2} y^{-1}; Falge et al., 2001). Among the three gap-filling methods, MDV gave the highest annual *NEP*. This fact suggests that environmental factors during gap-periods have potential to be biased by the extreme climate. The differences among the gap-filling methods were smaller than those among various ecosystem types (Falge et al., 2001). It is not able to answer conclusively which method is best. However, when the annual *NEP* estimated from gap-filled data is used to evaluate an ecosystem's capacity for CO2 assimilation or for comparison with other ecosystems, the reduction of errors should be considered.

Table 4.1. Monthly meteorological conditions from August 2001 to December 2002 in Haibei, Qinghai, China.

Year	Month	*PPFD*	T_{air}	T_{soil} 5cm	T_{soil} 50cm	*Prec*	*SWC* 5cm	*SWC* 50cm	*RH*	*VPD*	*Rs*	albedo
		mol photon m^{-2} day^{-1}	°C	°C	°C	mm mon^{-1}	cm^3 cm^{-3}	cm^3 cm^{-3}	Dimensi-onless	kPa	MJ m^{-2} day^{-1}	Dimensi-onless
2001	Aug.	39.4	8.4	14.1	12.4	103.5	0.37	0.39	0.78	0.25	20.5	0.20
	Sep.	32.3	6.7	11.6	10.5	82.5	0.45	0.41	0.78	0.22	16.6	0.20
	Oct.	27.2	0.1	4.9	6.7	7.1	0.39	0.42	0.70	0.21	14.7	0.21
	Nov.	23.4	-6.9	0.1	3.5	2.7	0.24 [a]	0.40	0.60	0.16	12.8	0.24
	Dec.	18.9	-12.3	-3.6	1.6	0.8	0.15 [a]	0.33 [a]	0.55	0.12	10.6	0.25
2002	Jan.	22.5	-18.1	-5.0	-1.0	2.2	0.15 [a]	0.18 [a]	0.72	0.05	12.7	0.45
	Feb.	27.1	-9.4	-3.0	-1.5	0.4	0.16 [a]	0.18 [a]	0.55	0.16	14.8	0.25
	Mar.	34.1	-4.9	0.3	0.1	15.8	0.22 [a]	0.19 [a]	0.55	0.22	18.6	0.26
	Apr.	39.8	1.9	4.4	0.8	19.2	0.39	0.22 [a]	0.59	0.32	19.6	0.24
	May	43.6	3.4	7.9	2.0	68.0	0.51	0.37	0.75	0.20	22.8	0.28
	Jun.	42.6	8.9	14.3	7.8	112.2	0.44	0.47	0.74	0.31	22.8	0.19
	Jul.	43.0	11.4	17.2	13.0	71.4	0.33	0.42	0.74	0.36	22.7	0.20
	Aug.	40.9	9.6	15.8	13.5	92.4	0.37	0.40	0.76	0.30	21.2	0.19
	Sep.	31.3	6.1	11.5	11.2	63.0	0.40	0.41	0.75	0.25	16.4	0.18
	Oct.	29.8	-2.0	4.4	6.8	0.2	0.28	0.40	0.66	0.21	16.0	0.19
	Nov.	23.1	-9.8	-0.8	2.9	5.0	0.17 [a]	0.38	0.63	0.13	12.6	0.32
	Dec.	18.6	-12.0	-3.8	1.2	0.2	0.15 [a]	0.29 [a]	0.59	0.12	10.6	0.24
2002	Ave. [b]	33.0	-1.3	5.2	4.7	---	0.30	0.32	0.67	0.22	17.5	0.25
2002	Sum.	12037.1 [c]	---	---	---	450.0 [d]	---	---	---	---	6405.6 [e]	--

Tair, *Tsoil 5cm*, *Tsoil 50cm*, *SWC 5cm*, *SWC 50cm*, relative humidity (*RH*), *VPD* and albedo show monthly averaged values. *PPFD* and solar radiation (*Rs*) show daily summed values. Precipitation (*Prec*) shows monthly summed value. [a] TDR probes were assumed to indicate no meaningful values for frozen soil moisture. [b] Weighted averages are conducted for days in each month. [c] A unit is in mol photon m^{-2} yr^{-1}. [d] a unit is in mm yr^{-1}. [e] a unit is in MJ m^{-2} yr^{-1}.

Table 4.2. Monthly heat budgets and carbon dynamics from August 2001 to December 2002 in Haibei, Qinghai, China.

Year	Month	H	λE	β	Rn	G	EBR	$FCO2$ [a]	NEP [b]	GPP [b]	R_e [b]	Gap(un-corrected)	Gap (corrected)
		MJ m^{-2} day^{-1}	MJ m^{-2} day^{-1}	Dimensi-onless	MJ m^{-2} day^{-1}	MJ m^{-2} day^{-1}	Dimensi-onless	g C m^{-2} mon^{-1}	g C m^{-2} mon^{-1}	g C m^{-2} mon^{-1}	g C m^{-2} mon^{-1}	%	%
2001	Aug.	2.21	5.19	0.43	11.52	0.08	0.65	-56.9	---	---	---	---	---
	Sep.	2.28	3.24	0.70	8.83	-0.10	0.62	-19.9	---	---	---	---	---
	Oct.	2.59	0.92	2.80	5.49	-0.29	0.61	15.9	---	---	---	---	---
	Nov.	2.17	0.39	5.62	2.74	-1.03	0.68	8.7	---	---	---	---	---
	Dec.	1.72	0.23	7.62	1.78	-1.74	0.55	-4.6	---	---	---	---	---
2002	Jan.	1.32	0.38	3.45	2.11	-1.46	0.48	-1.2	1.5	-0.4	-2.0	50.4	44.2
	Feb.	2.63	0.36	7.35	4.25	-0.37	0.64	1.9	-2.7	-3.1	-0.4	4.0	0.8
	Mar.	3.28	0.64	5.09	6.64	0.40	0.63	8.3	-9.7	-4.8	4.9	13.0	0.0
	Apr.	3.45	1.11	3.10	8.28	0.99	0.63	17.0	-22.7	-6.7	16.0	30.8	0.5
	May	2.89	2.88	1.00	10.48	0.78	0.60	4.1	-9.0	26.6	35.7	44.4	0.0
	Jun.	2.41	5.43	0.44	12.85	1.05	0.66	-36.6	34.4	119.9	85.5	27.1	0.0
	Jul.	2.25	7.03	0.32	12.88	0.59	0.76	-84.6	84.3	184.4	100.1	22.3	0.0
	Aug.	2.30	6.40	0.36	12.04	0.13	0.73	-54.8	30.3	188.3	158.0	29.6	0.0
	Sep.	2.67	3.12	0.86	8.75	-0.09	0.65	-8.9	-1.6	73.0	74.6	12.8	0.0
	Oct.	3.56	1.36	2.62	6.66	-0.24	0.71	2.0	-15.2	5.2	20.4	78.6	0.0
	Nov.	1.97	0.44	4.50	2.19	-0.97	0.76	4.5	-6.8	-5.2	1.6	22.2	0.5
	Dec.	1.77	0.26	6.76	1.60	-1.14	0.74	1.7	-4.3	-2.1	2.3	13.5	0.0
2002	Ave.[c]	2.54	2.43	1.05 [d]	7.37	-0.03	0.67	-12.2	6.1	47.2	41.1	29.2	3.9
2002	Sum.	927.96 [e]	885.79 [e]	---	2689.09 [e]	-11.88 [e]	---	-146.4 [f]	78.5 [f]	575.1 [f]	496.6 [f]	---	---

H, λE, *Rn* and *G* show monthly averaged values. *FCO2*, *NEP*, *GPP* and *Re* show daily summed values. [a] This is not a gap-filled value. [b] These are gap-filled values. [c] Weighted averages are conducted for days in each month. [d] This is the ratio between annual summed *H* and λE. [e] units are in MJ m^{-2} yr^{-1}. [f] units are in g C m^{-2} yr^{-1}.

Table 4.3. Aboveground biomass and leaf area index (*LAI*) in 2002 in Haibei, Qinghai, China.

Date	Aboveground Biomass	*LAI*
	g D.W. m^{-2}	m^2 m^{-2}
25-May	49.7	---
31-May	48.5	---
13-Jun	79.2	0.53
30-Jun	107.5	1.1
16-Jul	205.0	3.8
30-Jul	283.4	2.7
13-Aug	260.6	3.1
25-Aug	280.0	2.6
10-Sep	194.5	2.3

Table 4.4. Parameterization of ecosystem respiration (R_e) and gross primary production (*GPP*) regression curves using 15 min averaged data in 2002.

Month	R_e		*GPP*		
	R_{10} μmol CO_2 m^{-2} s^{-1}	r^2	α x 10^3 μmol CO_2 μmol $photon^{-1}$	GPP_{SAT} μmol CO_2 m^{-2} s^{-1}	r^2
Jan.	-0.75	0.003	0.86	-0.02	0.004
Feb.	-0.03	0.004	0.12	-0.01	0.089
Mar.	0.52	0.007	0.36	-0.02	0.076
Apr.	0.93	0.008	0.12	-0.01	0.120
May	1.31	0.018	139.50	1.54	0.004
Jun.	1.50	0.026	43.99	10.46	0.137
Jul.	1.23	0.006	31.83	20.37	0.489
Aug.	2.27	0.009	48.56	18.29	0.446
Sep.	1.88	0.124	24.47	8.20	0.276
Oct.	1.26	0.440	-2.32	0.10	0.119
Nov.	0.21	0.000	-1.36	-0.88	0.055
Dec.	0.44	0.009	-2.33	-0.22	0.007

The regression follows an Arrenius-type exponential relationship for *Re* (nighttime FCO_2 ($u_* > 0.2$ m s^{-1})): $R_e = R_{10} \exp(E_a/R\ (1/283.15 - 1/(T_{soil} + 273.15)))$, where R_{10} is the respiration rate at the soil temperature of 10 °C (μmol CO_2 m^{-2} s^{-1}), E_a is the active energy (is adopted for only one value for whole year; 81519 J mol^{-1}), R is the gas constant (= 8.134 J K^{-1} mol^{-1}), and a rectangular hyperbolic relationship for *GPP*: $GPP = \alpha \times GPP_{SAT} \times PPFD / (GPP_{SAT} + \alpha \times PPFD)$, where α is quantum yield (dimensionless), and GPP_{SAT} is the saturated *GPP* (μmol CO_2 m^{-2} s^{-1}).

Table 4.5. Ecosystem carbon dynamics in 2002 in Haibei, Qinghai, China.

Method	Specification	Average period	*GPP* (gCm^{-2})	R_e (gCm^{-2})	*NEP* (gCm^{-2})	Days (*NEP*>0) (days)	daily *GPP* (gCm^{-2})	daily *NEP* (gCm^{-2})
Regr.	with u_*-correction	1 month	575.1	496.6	78.5	160	3.59	0.49
	without u_*-correction	1 month	527.4	413.5	113.9	164	3.22	0.69
MDV	independent-window	7 days			147.2			
		14 days			145.2			
	gliding-window	7 days			149.5			
		14 days			141.8			
LookUp	T_{soil}	2 months			122.3			
		Seasonal			96.9			
	T_{air}	2 months			142.3			
		Seasonal			113.8			

"Day (*NEP* > 0)" means the number of days when daily *NEP* > 0 (length of growing season). *GPP*, R_e, and *NEP* mean the periodic sums of gross primary production, ecosystem respiration, and net ecosystem production, respectively. Daily *GPP* and daily *NEP* were calculated by dividing *GPP*, R_e, and *NEP* by the length of the growing season.

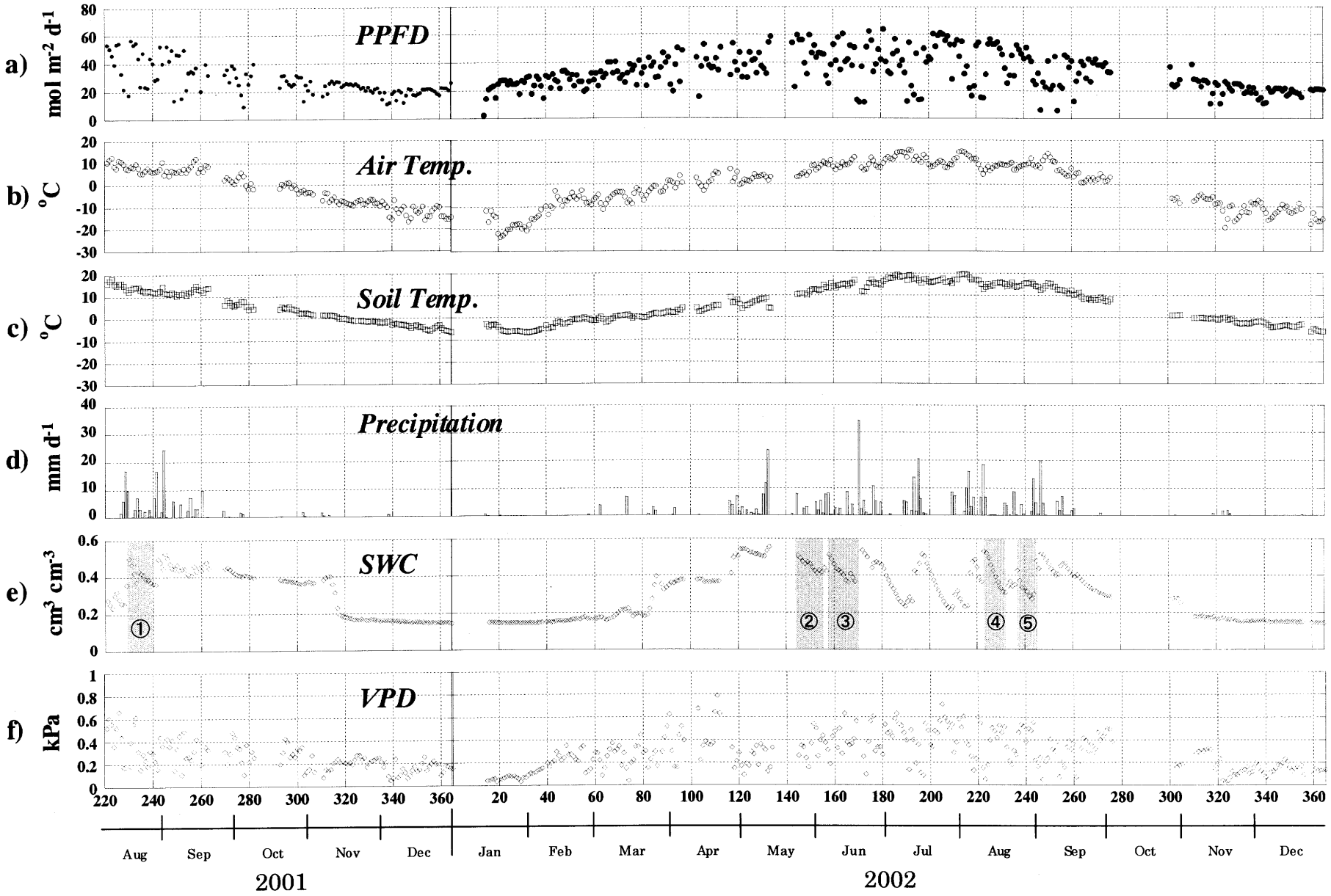
a)
mol m-2 d-1
PPFD
b)
°C
Air Temp.
c)
°C
Soil Temp.
d)
mm d-1
Precipitation
e)
cm3 cm-3
SWC
①
②
③
④
⑤
f)
kPa
VPD
220 240 260 280 300 320 340 360 20 40 60 80 100 120 140 160 180 200 220 240 260 280 300 320 340 360
Aug Sep Oct Nov Dec Jan Feb Mar Apr May Jun Jul Aug Sep Oct Nov Dec
2001
2002

Figure 4.1. Seasonal changes in meteorological conditions in 2001 and 2002 in Haibei, Qinghai, China in 2001 and 2002. a) Photosynthetic photon flux density (*PPFD*); b) air temperature; c) soil temperature at 5-cm depth; d) precipitation; e) soil water content at 5-cm depth (*SWC*) (1, 18–28 Aug 2001; 2, 23 May–1 Jun 2002; 3, 7–18 Jun 2002; 4, 11–19 Aug 2002; 5, 24–31 Aug 2002); f) water vapor pressure deficit (*VPD*). Gray zones (① ~ ⑤) correspond to soil water content (*SWC*) shown in Fig. 4.6.

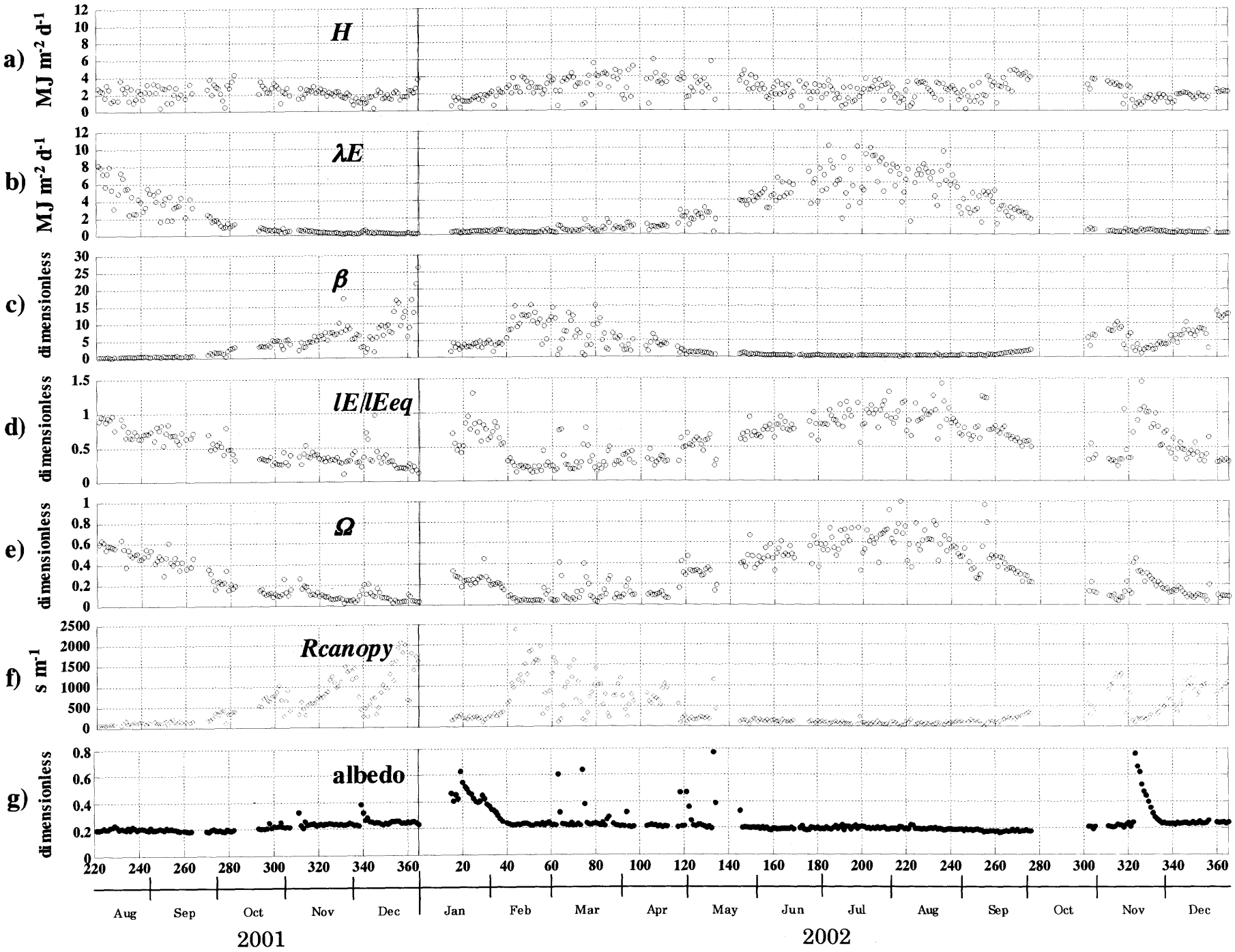
a)
H
MJ m-2 d-1
b)
λE
MJ m-2 d-1
c)
β
dimensionless
d)
lE/lEeq
dimensionless
e)
Ω
dimensionless
f)
Rcanopy
s m-1
g)
albedo
dimensionless
220 240 260 280 300 320 340 360 20 40 60 80 100 120 140 160 180 200 220 240 260 280 300 320 340 360
Aug Sep Oct Nov Dec Jan Feb Mar Apr May Jun Jul Aug Sep Oct Nov Dec
2001
2002

Figure 4.2. Seasonal changes in daily heat fluxes, moisture and canopy physiological conditions in Haibei, Qinghai, China in 2001 and 2002. a) sensible heat flux; b) latent heat flux; c) the Bowen ratio (β); d) the ratio between latent heat flux (λE) and equilibrium evaporation (λE_{eq}); e) omega factor (Ω); f) Penman–Monteith canopy resistance (R_{canopy}) and f) albedo.

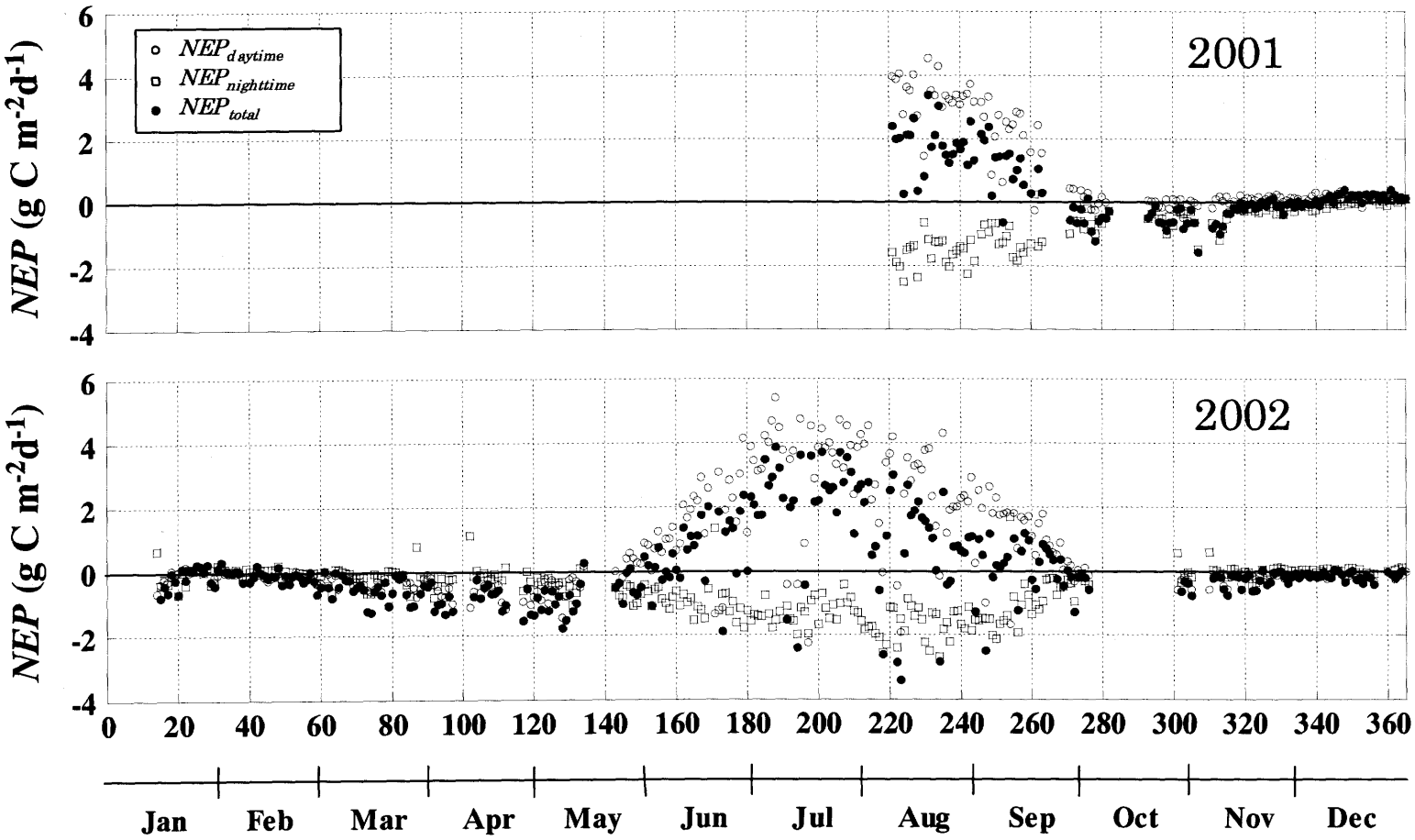

Figure 4.3. Changes in daily net ecosystem production in 2001 (upper graph) and 2002 (lower graph). $NEP_{daytime}$, $NEP_{nighttime}$, and NEP_{total} are the sums of the net CO_2 uptake flux ($-Fco_2$) for daytime, nighttime, and all day, respectively.

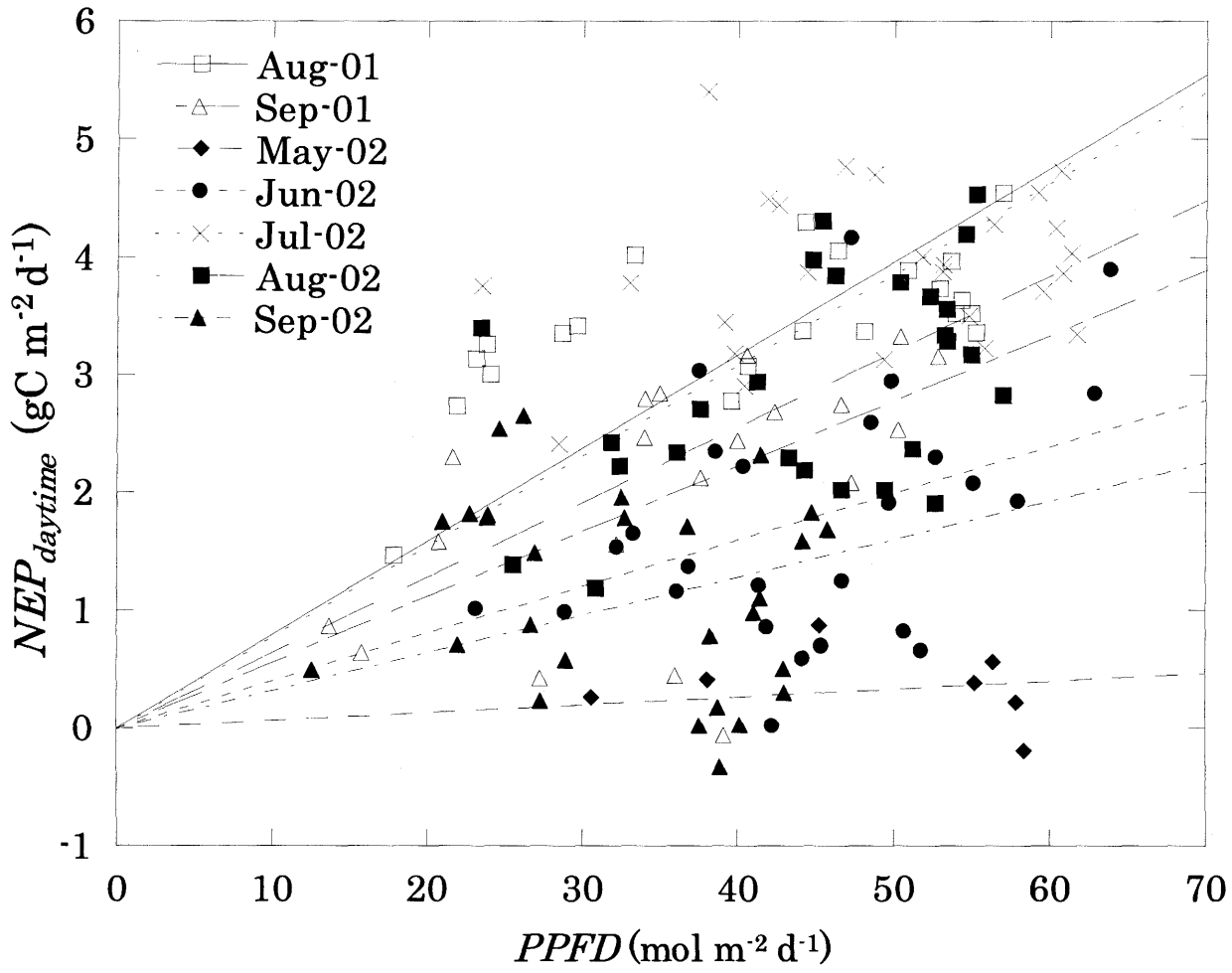

Figure 4.4. Linear regression of daytime accumulated CO_2 uptake flux ($NEP_{daytime}$) on incident photosynthetic photon flux density ($PPFD$). The regression follows a linear relationship: $NEP_{daytime} = a \times PPFD$. Monthly values are presented as follows: Month (symbol, a, r^2). August 2001 (□; 0.0793, 0.418 **), September 2001 (△; 0.0556, 0.324 **), May 2002 (◆; 0.00671, 0.0653 ns), June 2002 (●; 0.0398, 0.170 *), July 2002 (×; 0.0773, 0.0441 ns), August 2002 (■; 0.0641, 0.222 *), and September 2002 (▲; 0.0322, 0.0344 ns). The linear relationships were significant at $p<0.05$ *, $p<0.01$ ** levels of correlation coefficients. ns shows nonsignificant linear relationships.

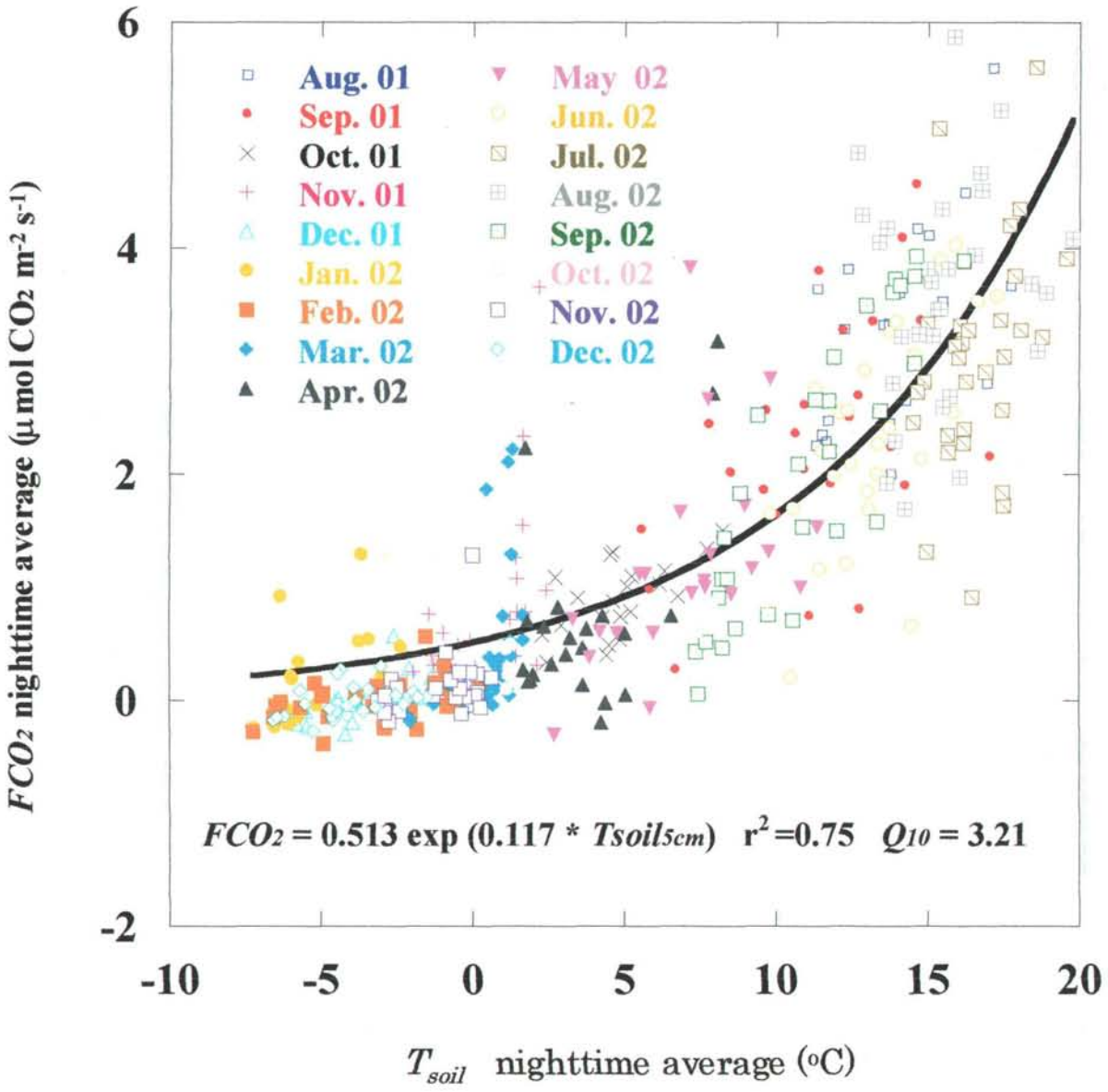

Figure 4.5. Relationship between nighttime CO_2 flux density and nighttime soil temperature at the depth of 5 cm in 2001 and 2002. Data show nighttime averaged values. The exponential relation is described by $FCO_2 = 0.513 \exp(0.117 \times T_{soil})$, $r^2 = 0.75$, $p<0.0001$.

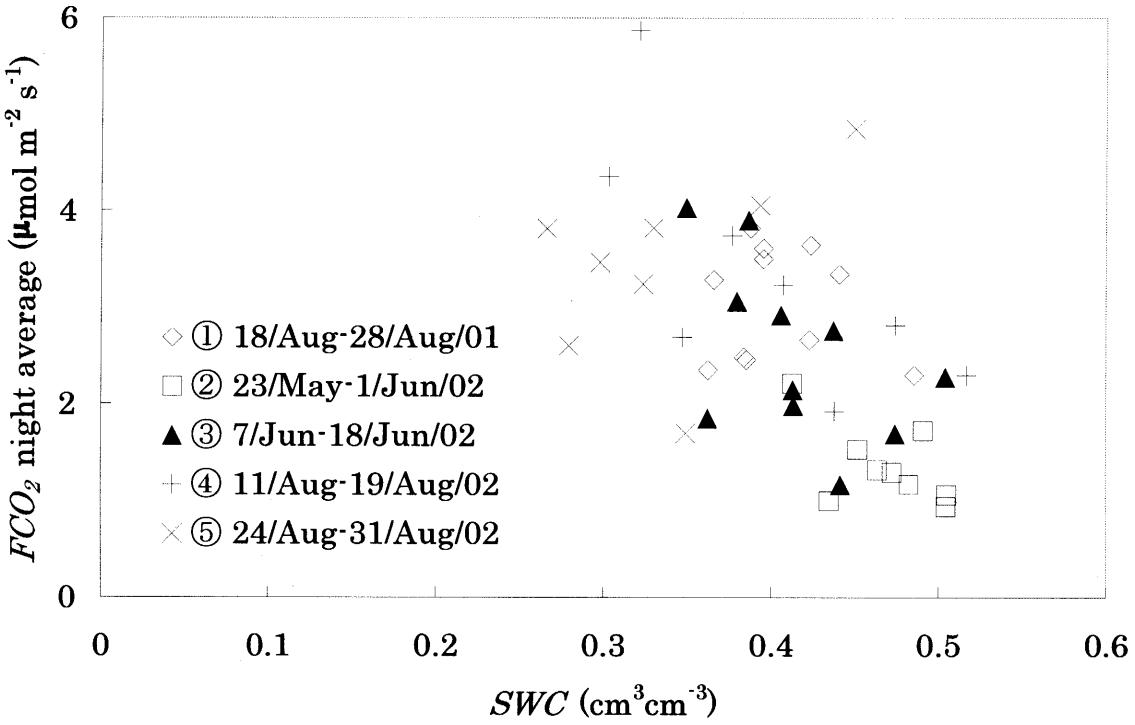

Figure 4.6. Relationship between nighttime CO_2 flux density and nighttime soil water content (*SWC*) during a dry spell after heavy rainfall (1, 18–28 August 2001; 2, 23 May – 1 June 2002; 3, 7–18 June 2002; 4, 11–19 August 2002; 5, 24–31 August 2002). Data show daily mean values. In 2002 during 23 May – 1 June, 11–19 August, and 24–31 August (the 2nd, 4th, and 5th periods, respectively), daily mean nighttime soil temperature rose gradually (first day–last day, °C): 1, 11.7–11.5; 2, 7.5–11.7; 3, 13.5–15.7; 4, 12.9–15.7; 5, 12.6–15.8. The linear relation is described by $FCO_2 = -9.97 \times SWC + 6.77$, $r^2 = 0.345$, $p<0.0001$.

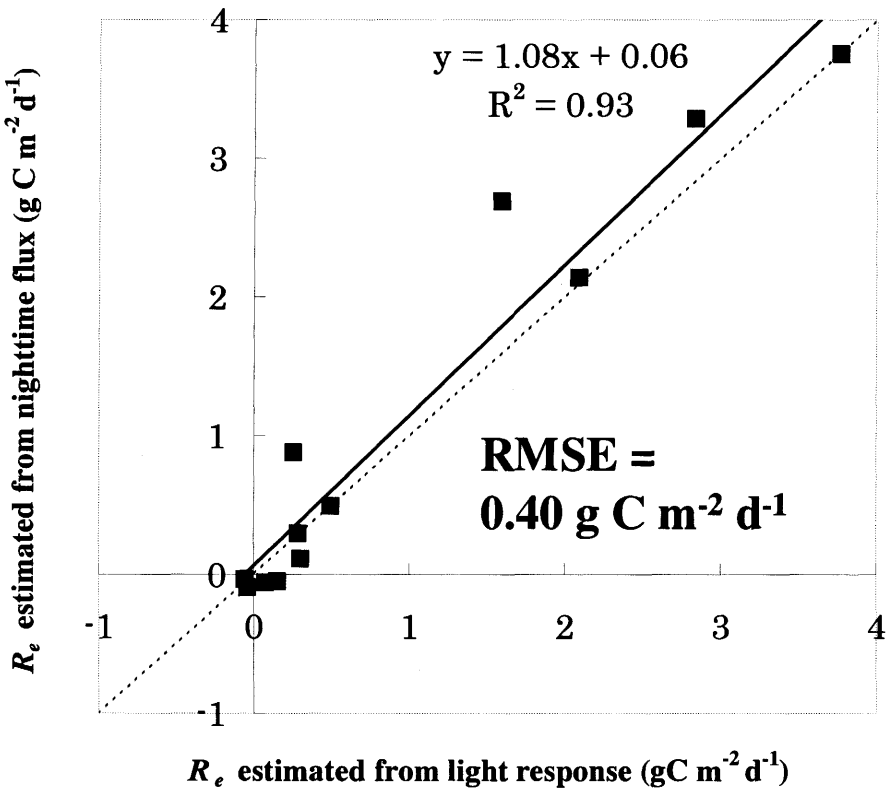

Figure 4.7. Ecosystem respiration (R_e), calculated from light response relationships (Eq. (1) in Suyker and Verma (2001)) compared to the values derived from exponential regressions between soil temperature and nighttime fluxes under turbulent conditions (Eq. (3.48)). Data represent average daily sums of each month on which R_e and *GPP* regression curves are made in 2002.

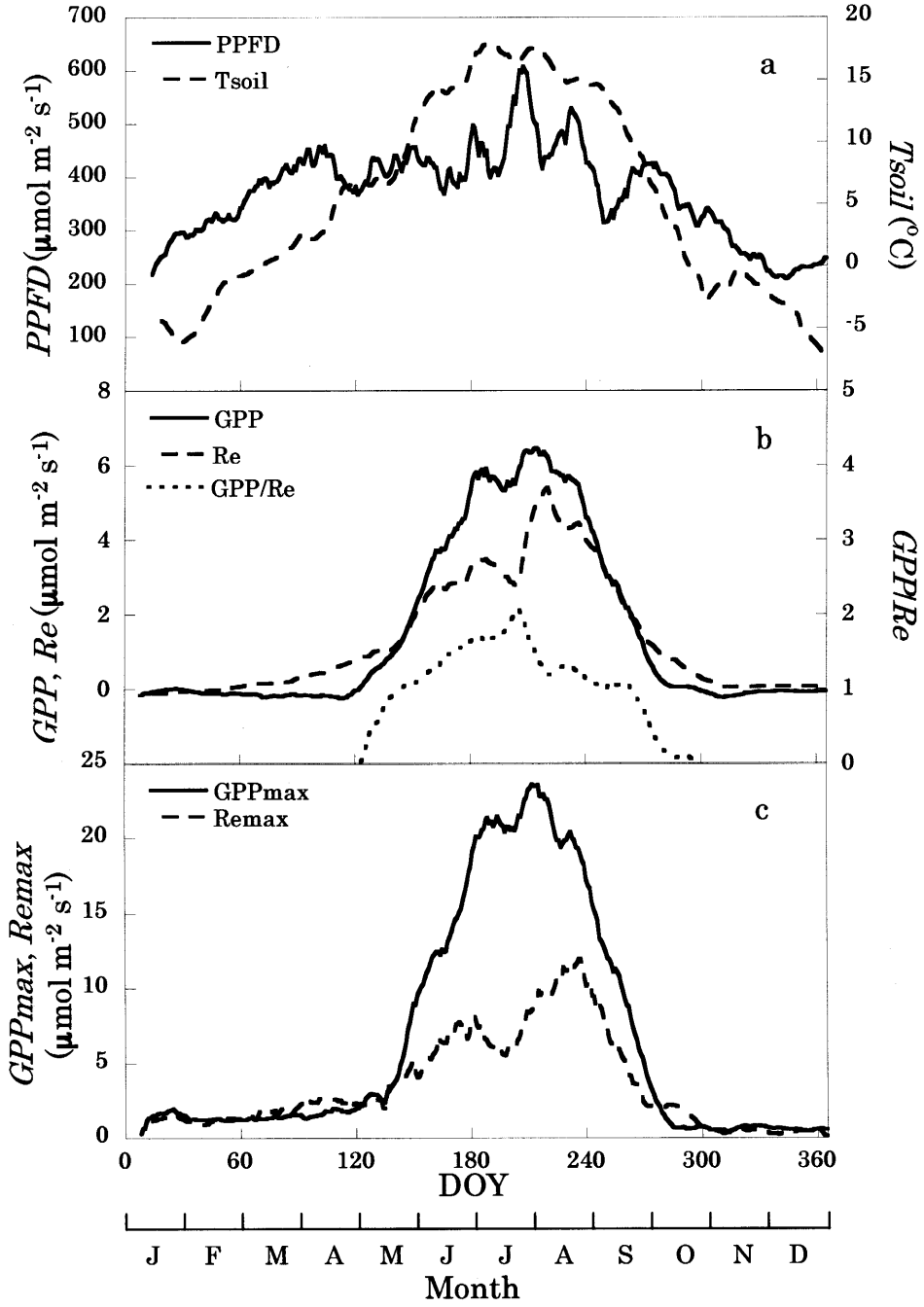

Figure 4.8. Seasonal changes in (a) daily mean photosynthetic photon flux density (*PPFD*; solid lines) and 5 cm soil temperature (T_{soil}; broken lines); (b) daily mean gross primary production (*GPP*; solid lines), ecosystem respiration (R_e; broken lines), and ratio between *GPP* and R_e (dashed lines); and (c) daily maximum *GPP* (solid lines) and R_e (broken lines) in 2002. Data represent the daily means of 15-d moving average GPP/R_e ratio from 14 January to 31 December, 2002.

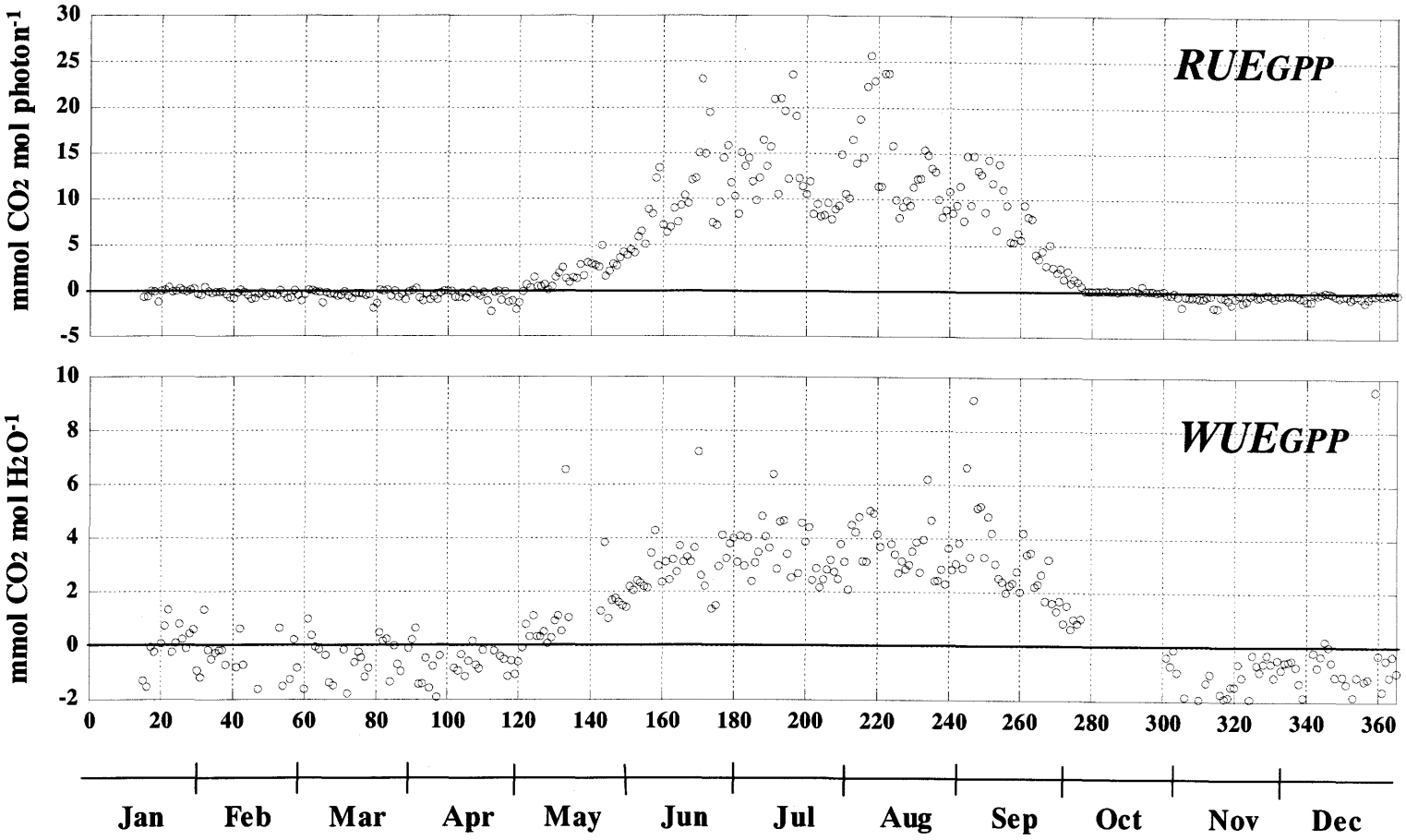

Figure 4.9. Changes in radiation- and water-use efficiency of gross primary production in RUE_{GPP} (upper graph) and WUE_{GPP} (lower graph) in 2002. RUE_{GPP}, WUE_{GPP} are the ratio of the *GPP* to the incident *PPFD* and evapotransipiration, respectively.

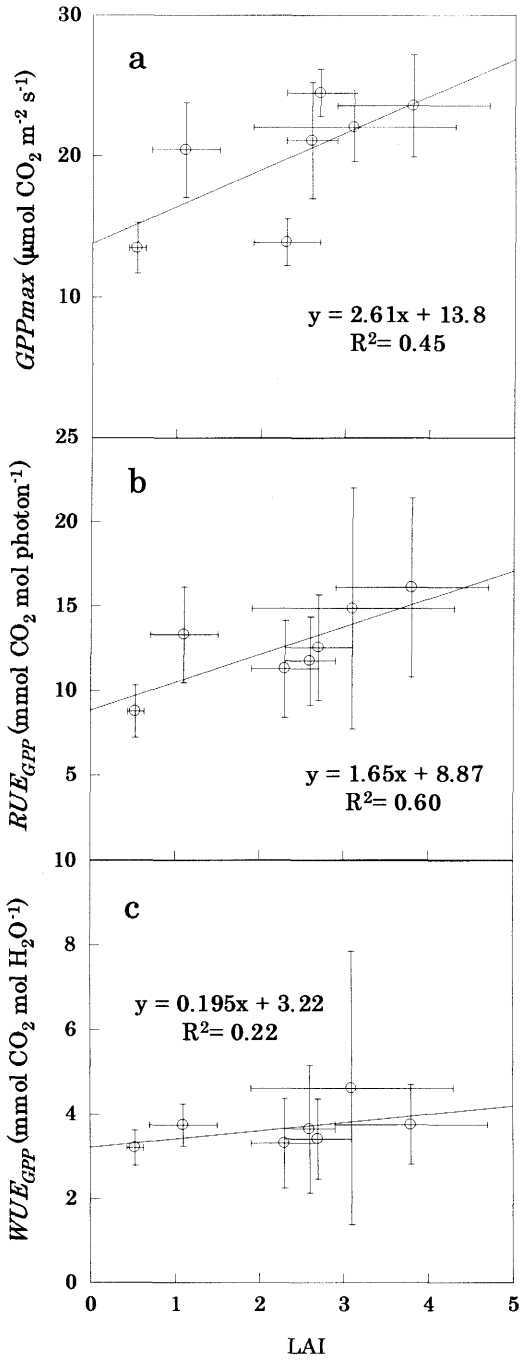

Figure 4.10. *LAI* controls on (a) maximum gross primary production (GPP_{max}), (b) radiation use efficiency (RUE_{GPP}), and (c) water use efficiency (WUE_{GPP}) of *GPP*. Vertical axis data show daily mean value of less than 4 d backward and forward *LAI* sampling day. GPP_{max} data when the *PPFD* was below 1500 μmol m^{-2} s^{-1} were eliminated from the average. Error bars mean standard deviation (horizontal axis: n = 5, vertical axis: n = 7). In the equation for predicting GPP_{max}, RUE_{GPP}, and WUE_{GPP} from *LAI*, standard errors are 1.560, 0.913, 0.177, respectively; P < 0.0001, 0.0001, and 0.05.

Chapter 5 Model analysis on the relationship between climate perturbations and carbon dynamics: 1981-2000

5.1. Introduction

Sim-CYCLE is a mechanistic model, on the basis of the dry-matter production theory established by Monsi and Saeki (1953). The atmosphere-biosphere CO_2 exchange is composed of physiological processes, such as photosynthesis (*GPP*), respiration (*AR*), and decomposition (*HR*), and then this simulator enables us to estimate the ecosystem C budget in a mechanistic way. Plant growth process was retrieved by the Monsi (1960) scheme, and C dynamics including soil organic matter was captured by the Oikawa's (1985) compartment model. Then, terrestrial ecosystems were conceptualized as a five-compartment system: foliage, stem and branch, root, litter, and mineral soil. In addition to *GPP*, *AR*, and *HR*, carbon flows such as litterfall, photosynthate allocation, and humus formation were properly formulated. *GPP* was regulated by a couple of physiological processes at a single-leaf scale (e.g. stomatal conductance and quantum yield), and scaled up to a canopy scale. *AR* consists of two functional components, i.e. maintenance respiration and growth respiration, each of which is regulated by environmental factors independently. The difference between *GPP* and *AR* is termed net primary production *(NPP)*, and the difference between *NPP* and *HR* is termed net ecosystem production *(NEP)*. Sim-CYCLE contains water and radiation subschemes to estimate physical environment in terrestrial ecosystems.

Ito and Oikawa (2000) performed a model analysis of the effect of climatic perturbations from 1970 to 1997 on the carbon budget of terrestrial ecosystems at the global scale, using Sim-CYCLE. During the 28 yr experimental period, global *NEP* ranged from -2.06 Pg C yr^{-1} (source) in 1983 to +2.25 (sink) Pg C yr^{-1} in 1971, being sufficiently large to give rise to anomalies in the atmospheric CO_2 concentration from +0.97 to -1.06 ppmv. Regression analyses demonstrated the following: (1) annual *ΔNEP*s had the highest correlation (r^2 = 0.38) with the temperature anomaly at the global scale; (2) the anomalies in precipitation resulted in a considerable *ΔNEP* in northern high and middle regions; (3) an anomalous global warming by

+1°C brought about a negative *ΔNEP* of -2.7 Pg C yr^{-1}; (4) the responsiveness was primarily attributable to the temperature sensitivities of plant respiration and soil decomposition, and secondarily to the moisture sensitivity of decomposition; and (5) the temperature dependence of *ΔNEP* had a clear seasonality, i.e. most sensitive from July to September (summer in the northern hemisphere) relative to other seasons. In 1983, when an *ENSO* event happened and the tropical zone was anomalously hot (0.4 °C above the long-term mean), the largest negative *ΔNEP* (-2.06 Pg C yr^{-1}) was estimated. On the other hand, in 1971 when global mean temperature was relatively low (0.2°C below the long-term mean), the largest positive *ΔNEP* (+2.25 Pg C yr^{-1}) was estimated. Furthermore, in 1992 when an anomalous cooling during the growing period (0.3°C below the long-term mean) was caused by the Mt. Pinatubo eruption (June 1991), a considerable positive *ΔNEP* (+1.14 Pg C yr^{-1}) was estimated. The climate dependencies of global terrestrial ecosystems analyzed here may contain significant implications not only for the present functioning of atmosphere-biosphere carbon exchange, but also for ongoing global warming.

Frozen soil has a large apparent heat capacity due to the latent energy of freezing and thawing, and act as an impermeable layer because of the large hydraulic conductivity when frozen. Frozen ground, covering mid- to high-latitude regions widely, affects not only the regional scale energy and hydrological condition in those area, but also the continental scale energy and water circulation in the world. A General circulation model (GCM) simulation showed that soil freezing elevates the ground surface temperature in the mid- and high-latitude region in summer (Takata and Kimoto, 2000). The higher temperature over land results from lower evaporation caused by lower surface soil moisture, and the lower surface soil moisture is caused by additional runoff of snowmelt in spring due to the impermeability of frozen soil and low soil liquid water due to the lower evaporation. Thus, soil freezing gives the thermal and hydrological impacts on the climate system, and consequently the carbon dynamics on the ecosystem. In this study, the estimation schemes of soil freezing were adjoined into basic schemes in the Sim-CYCLE newly.

Water budget, e.g. evaporation, transpiration, runoff, infiltration and precipitation, determines the soil water content and plays an important role on the water availability for plants. When ground surfaces are sparsely covered with vegetation, estimation of evaporation and transpiration using the energy transfer model is difficult, because that evaporation from the soil surface beneath the crop canopy can not be negligible in quantity, and it is necessary to treat the vapor flux from the crop fields as the total of soil and plant fluxes, transpiration from leaf stomata, and evaporation from the soil surface. However, the precedent Sim-CYCLE did not take sparse vegetation cover into account. Shuttleworth and Wallace (1985) designed a compartment model (S-W model) to estimate the evaporation from soil and transpiration from crops separately. This model accuracy also was examined by Kato et al. (in press, 2004a) in the sorghum fields, Tottori, Japan, and its availability for sparsely vegetated ground surface was confirmed. This study adopted this compartment model and adjoined into the basic schemes in the Sim-CYCLE as new subschemes. In precedent Sim-CYCLE, the runoff is parameterized by using the Bucket model (Manabe, 1969). This model has the simple calculation schemes that the storage water over a bucket capacity outflows as the runoff, and used widely in the GCM simulation. On the other hand, the Tank model (Sugawara and Maruyama, 1952; Sugawara, 1961), used widely in the flood forecast, has the complex calculation schemes and many parameters to control the runoff from multi-poles installed at the tank sidewall, however, also has a high estimation accuracy. Kondo (1993) developed "a new bucket model", gathering both the simplicity of the Bucket model and the higher accuracy of the Tank model, to calculate the infiltration into the deeper soil layer in the soil surface having the heterogeneity in its soil properties and thickness. This model expresses the runoff in the hyperbolic approximate equation parameterized by precipitation, and applicable for various time scale estimation, from one hour to one month. This study adjoined this new bucket model into the basic schemes in the precedent Sim-CYCLE.

For twenty years, 1981-2000, the monthly carbon fluxes and carbon storages were simulated using the Sim-CYCLE at the Haibei station on the Qinghai-Tibetan Plateau, China. The aims of this chapter are 1) to show the interannual patterns of CO_2 flux, 2) to clarify the

climate controls on the ecosystem carbon dynamics in the alpine meadow ecosystem, and 3) to predict the ecosystem response of the carbon sequestration against the global warming.

5.2. Model description

5.2.1. Sim-CYCLE -Basic model-

5.2.1.1. Overview of Sim-CYCLE

Sim-CYCLE was developed based on the ecosystem-scale model of Oikawa (1985), which has been used to simulate and analyze a tropical rain forest ecosystem (Oikawa, 1986), a temperate broad-leaved evergreen forest (Oikawa, 1998), and grassland (Oikawa, 1993; Alexandrov and Oikawa, 1995). In Sim-CYCLE, terrestrial carbon dynamics is conceptualized as a five-compartment system (Fig. 5.1). A water and radiation subscheme is required, because carbon dynamics is closely coupled with water and radiation budget (Fig. 5.1). Carbon in a given ecosystem (*WE*) is composed of plant biomass (*WP*) and soil organic carbon (*WS*). *WP* is distributed in three compartments: foliage (subscript *F*), stem and branch (subscript *C*), and root (subscript *R*); *WS* is distributed in two compartments: litter (subscript *L*) and mineral soil (subscript *H*):

$$WE = WP + WS \tag{5.1a}$$

$$WP = WP_F + WP_C + WP_R \tag{5.1b}$$

$$WS = WS_L + WS_H \tag{5.1c}$$

Atmosphere–biosphere CO_2 exchange occurs through three major processes: gross primary production *GPP*, autotrophic plant respiration (*AR*), and heterotrophic soil respiration (*HR*). Net primary production (*NPP*), defined as:

$$NPP = GPP - AR \tag{5.2}$$

ecology but also for agronomy and forestry. Net ecosystem production (*NEP*), defined as follows:

$$NEP = NPP - HR \tag{5.3}$$

indicates the carbon balance of the ecosystem during a given period: a net sink or a source. Within a terrestrial ecosystem, carbon is transferred in the form of various organic compounds (largely carbohydrates) through several processes (Fig. 5.1), including translocation of photosynthate (*PT*), litterfall of dead biomass (*LF*), and synthesis of humic mineral soil (*HF*). At this stage, animal processes and lateral transportation of carbon from one ecosystem to another are neglected. The net change in each compartment (Δ) during a given period is given by the following equations:

$$\Delta WP_F = PT_F - ARG_F - LF_F \tag{5.4a}$$

$$\Delta WP_C = PT_C - ARG_C - LF_C \tag{5.4b}$$

$$\Delta WP_R = PT_R - ARG_R - LF_R \tag{5.4c}$$

$$\Delta WS_L = LF - HR_L - HF \tag{5.4d}$$

$$\Delta WS_H = HF - HR_H \tag{5.4e}$$

where photosynthate translocation (*PT*) is the difference between *GPP* and *ARM*. It is apparent that ΔWE is equal to *NEP*. Since in Sim-CYCLE these fluxes are calculated monthly, the seasonal, interannual, and successional behaviors of terrestrial carbon dynamics can be simulated. By carrying out of these simulations, such important quantities as plant biomass, soil carbon storage, leaf area index (*LAI*), *NPP*, and *NEP* can be estimated. The model calculation was launched at the juvenile stage, when initial carbon content was 0.1 Mg C ha^{-1} for each compartment, and repeated for a period sufficiently long to attain the equilibrium state under stationary environmental conditions. The annual *NEP* was used to determine whether the

ecosystem carbon dynamics had sufficiently equilibrated (i.e. climax stage): $NEP < 0.0001$ Mg C ha^{-1} $year^{-1}$.

5.2.1.2. Single-leaf processes

Single-leaf gas exchange is the most fundamental process in plant ecophysiology, which investigates the controls of various environmental factors on stomata, the leaf vents for photosynthesis and transpiration. The controls are described at a physiological scale and extended to a canopy scale (Fig. 5.2). The single-leaf photosynthetic rate (PC) is formulated as a Michaelis-type function of the incident $PPFD$ ($PPFD_{IN}$):

$$PC = \frac{PC_{SAT} \cdot QE \cdot PPFD_{IN}}{PC_{SAT} + QE \cdot PPFD_{IN}} \tag{5.5}$$

where PC_{SAT} is the single-leaf photosynthetic rate under light-saturation, and QE is light-use efficiency, or quantum yield of photosynthesis. PC_{SAT} and QE are complicated functions of temperature, CO_2 level, air humidity, and soil water, and they are different among biome types and between C_3 and C_4 species. They are formulated by using coefficient functions of important environmental factors, in a multiplicative way:

$$QE = QE_0 \cdot F_{QE}(TG) \cdot F_{QE}(CD_{ICL}) \tag{5.6}$$

$$PC_{SAT} = PC_{SAT0} \cdot F_{PC}(TG) \cdot F_{PC}(CD_{ICL}^{'}) \cdot F_{PC}(SW_L) \tag{5.7}$$

where QE_0 and PC_{SAT0} are potential maximum values under optimal conditions, and F_{QE} and F_{PC} denote the coefficient functions for temperature, CO_2, and water conditions, respectively. Before describing these coefficient functions, the author first explains the regulation of single-leaf gas exchange through stomatal conductance (GS). Sim-CYCLE adopts the

semi-empirical model of stomatal conductance described by Ball et al. (1987) and modified by Leuning (1990):

$$GS = \chi_1 + \frac{\chi_2 \cdot PC}{(CD_{ATM} - CD_{CMP})(1 + VPD/\chi_3)} \tag{5.8}$$

where CD_{ATM} is the atmospheric CO_2 concentration, VPD is the vapor pressure deficit, CD_{CMP} is the CO_2 compensation point of photosynthesis, and χ_1, χ_2 and χ_3 are biome-specific parameters. Eq. (5.8) suggests that GS decreases with increasing atmospheric CO_2 concentration, which is the case according to many observations (Morison and Gifford, 1983; Field et al., 1995). Since gas exchange through the leaf cuticle is negligible, the leaf intercellular CO_2 concentration (CD_{ICL}) is defined as follows:

$$CD_{ICL} = CD_{ATM} - \frac{PC}{GS/1.56} \tag{5.9}$$

where 1.56 is a factor to convert GS into CO_2 conductance. CD_{ICL}, rather than CD_{ATM}, is directly related to photosynthetic capacity, although CD_{ICL} tends to change in parallel with the CD_{ATM}. As with the photosynthetic quantum yield QE, Ehleringer and Björkman (1977) showed that C_3 and C_4 species respond to temperature and CO_2 conditions in a disparate manner. Typically, the QE of C_4 species is virtually insensitive to surrounding condition (i.e. $F_{QE}(TG)=F_{QE}(CD_{ICL})=1$), because their CO_2 condensation mechanism eliminates photorespiration. In contrast, the QE of C_3 species depends strongly on temperature (TG) and CO_2 level (CD_{ICL}):

$$F_{QE}(TG) = \frac{52 - TG}{3.5 + 0.75(52 - TG)} \tag{5.10a}$$

$$F_{QE}(CD_{ICL}) = \frac{CD_{ICL}}{90 + 0.6CD_{ICL}} \tag{5.10b}$$

Ehleringer et al. (1997) suggested that the difference in QE between C_3 and C_4 species may be so important that it determines the geographical distribution of these two photosynthetic types. Moreover, it is fully recognized that PC_{SAT} of C_4 species is much higher than that of C_3 species, and that C_4 photosynthesis is vulnerable to low temperatures (Pearcy and Ehleringer, 1984). Sim-CYCLE incorporates such findings into the corresponding coefficient functions. The temperature dependence function of PC_{SAT} is a bell-shaped curve, formulated as follows (Raich et al., 1991):

$$F_{PC}(TG) = \frac{(TG - T_{MAX})(TG - T_{MIN})}{(TG - T_{MAX})(TG - T_{MIN}) - (TG - T_{OPT})^2} \tag{5.11}$$

where T_{MAX}, T_{MIN}, and T_{OPT} are, respectively, the maximum, minimum, and optimum temperatures for photosynthesis. For C_3 plants, T_{OPT} is a function of intercellular CO_2 concentration:

$$T_{OPT} = T_{OPT0} + 0.01 CD_{ICL} \tag{5.12}$$

where T_{OPT0} is the minimum value of T_{OPT} at very low CD_{ICL}. Eqs. (5.9) and (5.12) indicate that increases of atmospheric CO_2 and temperature may be interactive, making a prediction difficult even at the physiological scale, as has been demonstrated by a biochemical model study (Long, 1991). The CO_2 dependence of PC_{SAT} is expressed by a Michaelis-type function:

$$F_{PC}(CD_{ICL}) = \frac{CD_{ICL} - CD_{CMP}}{KM_{CD} + CD_{ICL}} \tag{5.13}$$

where KM_{CD} is a parameter of CO_2 sensitivity. The relationship between CD_{ICL} and PC_{SAT} is strongly affected by temperature, which alters QE and the CO_2 compensation point (CD_{CMP}). At

lower temperatures, an elevated CO_2 concentration would have a small fertilization effect, as observed in tundra species (Tissue and Oechel, 1987). CD_{CMP} differs greatly between C_3 and C_4 species: C_4 species have a very low and constant CD_{CMP} (e.g. 5 ppmv), while C_3 species have higher and more variable CD_{CMP}. Brooks and Farquhar (1985) formulated the CD_{CMP} of C_3 species as a function of temperature:

$$CD_{CMP} = CD_{CMP0}\left[1 + \delta_1(TG - 20) + \delta_2(TG - 20)^2\right] \tag{5.14}$$

where CD_{CMP0} is the control value at 20 °C, and δ_1 and δ_2 are parameters of temperature sensitivity. Apparently, F_{PC} (CD_{ICL}) represents the stomatal limitation of water stress on photosynthesis, because CD_{ICL} is strongly regulated by stomatal conductance, which responds to air humidity. On the other hand, F_{PC} (MS_{LW}) indicates the non-stomatal limitation of water stress, that is, the direct effect of soil-water availability on photosynthetic capacity:

$$F_{PC}(MS_{LW}) = \frac{MS_{LW}}{KM_{SW} + MS_{LW}} \tag{5.15}$$

where KM_{SW} is a parameter for soil-water availability. Since the components of single-leaf gas exchange, i.e. GS, CD_{ICL}, PC, and QE, change interactively, a stationary state is numerically found by iterative calculations of Eqs. (5.5)–(5.9), (5.10a), (5.10b), (5.11)–(5.15).

5.2.1.2. Ecosystem-scale processes

1. Photosynthesis

GPP is the ultimate origin of all organic car-bon, through which atmospheric CO_2 is fixed into dry matter. Indeed, the scaling procedure in terms of *GPP* is one of the characteristics of Sim-CYCLE, such that *GPP* is estimated by the dry-matter production theory established by Monsi and Saeki (1953). In our parameterization, it was assumed that environmental factors, such as temperature, CO_2, and water, were similar among all leaves. Monsi and Saeki (1953)

first formulated the downward attenuation of *PAR* irradiance due to mutual shading of leaves in a canopy with accumulating leaf area, as follows:

$$PPFD_{IN} = PPFD_{TOP} \exp(-KA \cdot LAI_{CMI}) \tag{5.16}$$

where $PPFD_{TOP}$ denotes the photosynthetic photon flux density at a canopy top. It is apparent that *PAR* irradiance attenuates exponentially with the biome-specific coefficient *KA*, such that a leaf underlying the cumulative leaf area index (LAI_{CML}) receives light equivalent to $PPFD_{IN}$. If a spherical distribution of leaf inclination is assumed, then *KA* is a function of solar height:

$$KA = \frac{KA_0}{\sin(SE_{MD})} \tag{5.17}$$

where KA_0 is the value for vertical incident radiation (biome-specific value), and SE_{MD} is the solar elevation at midday. In Sim-CYCLE, the single-sided leaf area index *LAI* is a prognostic variable, given by the following:

$$LAI = 0.5SLAW_F \tag{5.18}$$

where *SLA* is the specific leaf area. Based on the above assumption with respect to light attenuation, $PPFD_{IN}$ in Eq. (5.5) can be substituted with Eq. (5.16), and integrate for the total leaf area index (*LAI*), in order to obtain the instantaneous GPP_{INS} rate.

$$GPP_{INS} = \int_0^{LAI} PCdLAI$$

$$= \frac{PC_{SAT}}{KA}\left[\ln(QE + KA \cdot PPFD_{TOP}) - \ln(QE + KA \cdot PPFD_{TOP}) \times \exp(-KA \cdot LAI)\right] \tag{5.19}$$

According to Kuroiwa (1966), the diurnal change in $PPFD_{TOP}$ is approximated well by a sine-square curve with the peak at midday, as follows:

$$PPFD_{TOP} = PPFD_{MD} \sin^2\left(\frac{360 \cdot t}{DL}\right) \tag{5.20}$$

where t is time since sunrise, DL is day length, and $PPFD_{MD}$ is the irradiance of $PPFD_{TOP}$ at midday. After substituting $PPFD_{TOP}$ with Eq. (5.20), Eq. (5.19) is integrated for DL to obtain the daily GPP_{DAY} rate:

$$GPP_{DAY} = \varepsilon \int_0^{DL} \int_0^{LAI} PCdLAIdt$$

$$= \frac{2\varepsilon PC_{SAT} DL}{KA}\left[\ln\left\{1+\sqrt{1+\frac{KA \cdot QE \cdot PPFD_{MD}}{PC_{SAT}}}\right\} - \ln\left\{1+\sqrt{1+\frac{KA \cdot QE \cdot PPFD_{MD}\exp(-KA \cdot LAI)}{PC_{SAT}}}\right\}\right] \tag{5.21}$$

The units is converted from μmol CO_2 m^{-2} per day to Mg C ha^{-1} per day by multiplying a unit conversion factor ε (= 4.32 x 10^{-4}) and the number of days in a month.

2. Respiration

Although autotrophic plant respiration (*AR*) is a major CO_2 flux comparable to *GPP* and *NPP* in magnitude, our ability to model *AR* is insufficient, especially at an ecosystem scale. However, physiological studies (e.g. Amthor, 1989) suggest that *AR* is composed of two components that have distinct functional meanings (i.e. for maintenance and for growth), and that different plant organs respire at different rates. *AR* is calculated as a sum of six respiration rates, thus:

$$AR = ARM + ARG$$

$$AR = \sum_{X=organ}^{F,C,R}(ARM_X) + \sum_{X=organ}^{F,C,R}(ARG_X) \tag{5.22}$$

where *ARM* denotes the maintenance respiration of the whole plant, foliage, stem, and root, and similarly *ARG* denotes growth respiration. *ARM* is a function of the amount of existing carbon (*WP*) and temperature (*TG*):

$$ARM_X = SARM_X \exp\left[\frac{\ln(QT)}{10}(TG - 15)\right] WP_X \tag{5.23}$$

where *SARM* is the specific respiration rate, and *TG* is the temperature (control temperature, 15 °C). *QT* represents the sensitivity to temperature change. A typical value for *QT* is 2.0, and it ranges from 1.0 to 3.0 (Ryan, 1991) for various biomes and plant organs. However, as implied by Paembonan et al. (1992), Yokota and Hagihara (1996), *QT* may vary seasonally in temperate and boreal ecosystems that experience a large temperature change between summer and winter. Based on their findings, *QT* is formulated as a function of temperature:

$$QT = 2.0 \exp[-0.009(TG - 15)] \tag{5.24}$$

This modification results in a reduced sensitivity of *ARM* at higher temperatures, but very limited data are available to characterize biome specificity. In forest ecosystems, the maintenance respiration rate per unit biomass (*SARM*) for stem WP_C and root WP_R would decrease as passive woody tissues, or heartwood, accumulate (Yokota et al., 1994). The size-dependence of *SARM* can be approximated by a function of standing biomass, given as:

$$SARM = \phi_1 + \frac{\phi_2}{\phi_3 + \exp[\phi_4(WP - \phi_5)]} \tag{5.25}$$

where ϕ_1 to ϕ_5 are parameters for size-dependence. On the other hand, *ARG* is not an explicit function of environmental factors but of plant growth rate, because *ARG* represents the cost to produce new biomass (Amthor, 1989). Thus, *ARG* is calculated only when biomass has a net gain (i.e. $\Delta WP > 0$), as follows:

$$ARG_X = SARG_X \Delta WP_X \cong SARG_X \frac{PT_X}{1 + SARG_X} \tag{5.26}$$

where *SARG* is the specific growth respiration rate (foliage has a higher value than stem or root) and *PT* is the photosynthate translocation to each organ (cf. Eq. (5.33)). Consequently, *ARG* is indirectly regulated by environmental factors, via the *GPP* and *ARM* rates.

3. Decomposition

Soil organic carbon was divided into two compartments, because the decomposition rate differs greatly between them. The labile part of litter (*WSL*) circulates once every few months or years, while the passive part in mineral soil (*WSH*) lingers for decades or centuries. Heterotrophic soil respiration (*HR*) is composed of two constituents from each compartment:

$$HR = HR_L + HR_H \tag{5.27}$$

Both HR_L and HR_H are affected by temperature and soil moisture conditions:

$$HR_L = SHR_L \cdot WS_L \cdot F_{HR_L}(TS_{10}) \cdot F_{HR_L}(MS_{UP}) \tag{5.28a}$$

$$HR_H = SHR_H \cdot WS_H \cdot F_{HR_L}(TS_{200}) \cdot F_{HR_L}(MS_{LW}) \tag{5.28b}$$

where SHR_L and SHR_H are the specific respiration rates and F_{HRL} and F_{HRH} are the coefficient functions for temperature and soil-moisture conditions, respectively. For temperature dependence, an exponential function similar to Eq. (5.23) has been frequently used, but Lloyd and Taylor (1994) showed that it is not the best model, and they alternatively proposed an Arrhenius-type model:

$$F_{HR}(TS) = \exp\left[308.56\left(\frac{1}{56.02} - \frac{1}{TS + 46.02}\right)\right] \tag{5.29}$$

where TS is soil temperature (TS_{10} for WS_L and TS_{200} for WS_H). Eq. (5.29) resulted in a lower responsiveness at higher temperatures than does the exponential equation (Lloyd and Taylor, 1994). Although this process does not explicitly include the effect of soil freezing, it would have a negligible effect on HR estimation. The coefficient function with respect to soil moisture $F_{HR}(MS)$ is the minimum of two contrasting components:

$$F_{HR}(MS) = \min\{F_{HR}(WA), F_{HR}(EA)\} \tag{5.30}$$

$F_{HR}(WA)$ represents the effect of soil moisture on microbial activity, while $F_{HR}(AE)$ represents the effect of soil air space (i.e. aerobic or anaerobic conditions):

$$F_{HR}(WA) = WA_0 + \frac{MS/WHC}{KM_{WA} + MS/WHC} \tag{5.31a}$$

$$F_{HR}(AE) = AE_0 + \frac{MS/WHC}{KM_{AE} + MS/WHC} \tag{5.31b}$$

where WA_0 and AE_0 are minimum values of, KM_{WA} and KM_{AE} are parameters related to responsiveness, and WHC is water-holding capacity. In sum, a larger MS increases HR under dry conditions, whereas a larger MS reduces HR near the water-saturation point.

4. Litterfall

In the equilibrium state, the amount of annual *LF* must be identical to annual *NPP*, so plant biomass becomes stable. However, the shedding of dead biomass is one of the most difficult processes for mechanistic models to simulate. Consequently, a constant mortality or turnover rate irrespective of environmental conditions is assumed for evergreen biomes:

$$LF = \sum_{X=organ}^{F,C,R} (SLF_X WP_X) \tag{5.32}$$

where *SLF* is the specific litter-fall rate, or mortality. In grasslands, plants shed most of their shoots (WP_F and WP_c) during the winter (C_3, $TG > 5$ °C; C_4, $TG > 8$ °C) or the dry season ($MS > 0.1 \times WHC$), while the roots have a constant mortality.

5. Photosynthate translocation

Although a mechanistic model of photosynthate allocation (*PT*) is far from sufficient, the dry-matter production theory provides keys for addressing the problem. First, Monsi (1960) created a schematic diagram of plant growth, from CO_2 assimilation to biomass incrementation. This scheme suggests that assimilated carbon should be partitioned among plant organs, after subtracting the maintenance cost of the organs (*ARM*):

$$EP = GPP - ARM = \sum_{X=organ}^{F,C,R} (PT_X) \tag{5.33}$$

where *EP* is effective photosynthate for growth. If *EP* is negative, translocation and vegetative growth cannot be expected. Accordingly, a positive *EP* is partitioned among WP_F, WP_C, and WP_R, such that the fixed carbon is utilized by the plants most profitably to survive. Second,

Kuroiwa (1966) derived the optimal leaf area index (LAI_{OPT}) to maximize daily net carbon uptake from the daily *GPP* estimate using Eq. (5.21), as follows:

$$LAI_{OPT} = \frac{1}{KA} \ln \left[\frac{KA \cdot QE \cdot PAR_{MD}}{PC_{SAT} \left\{ PC_{SAT} \cdot DL / \left(PC_{SAT} - DCST \right) - 1 \right\}} \right] \tag{5.34}$$

where *DCST* is the daily cost of maintaining a unit amount of foliage:

$$DCST = \frac{\left[SARM_F + SLF_F \left(1 + SARG_F \right) \right]}{2SLA} \tag{5.35}$$

When the community *LAI* is identical to the LAI_{OPT}, almost all leaves, even those at the bottom of the canopy, may perform as a carbon source. In other words, this model prohibits the existence of heterotrophic leaves. Many empirical studies support shoot independence in terms of carbon economy; therefore, the theoretical prediction of LAI_{OPT} will be a valid indicator of carbon allocation to WP_F. Thus, if *EP* is positive, photosynthate is allocated first to WP_F so that *LAI* becomes close to LAI_{OPT}. Note that to avoid overshooting, an excessive amount of carbon should not be allocated to WP_F, and that the LAI_{OPT} can be enlarged by stimulating the photosynthetic properties, i.e. *QE* and PC_{SAT}. Residual carbon is allocated to WP_C and WP_R with a constant ratio, in order to realize the biome-specific growth form; woody biomes invest a considerable fraction to stem WP_C, while in herbaceous biomes mostly is allocated to root WP_R.

5.2.2. Soil thermal profile

When the soil water was freezing, the decline of the rate of thermal change induced by the latent heat (334.7 J g^{-1}), and the changes of the specific heat and thermal conductivity induced by the phase change of soil water vary the heat transfer in the soil layer. Especially at the temperature of near 0 °C, the former affects strongly. The vertical thermal profile of frozen

soil is calculated by changing the specific heat at the temperature of near 0 °C (Fukuda et al., 1980; Fig. 5.4).

The heat conduction equations in the frozen and unfrozen soil layer are described as follows:

$$\Delta TS/\Delta t = K_f / C_f \rho \cdot \Delta^2 TS/\Delta Z^2 \quad (5.36a)$$

$$\Delta TS/\Delta t = K_u / C_u \rho \cdot \Delta^2 TS/\Delta Z^2 \quad (5.36b)$$

where TS is the soil temperature (°C), Z is the depth (m), $C_f\rho$, and $C_u\rho$ are the specific heat of frozen and unfrozen soil (J m^{-3} K^{-1}), K_f, and K_u are the thermal conductivities of frozen and unfrozen soil (W m^{-1} K^{-1}). The latent heat generation induced by soil water freezing reflects on increasing the specific heat near the freezing point, and the heat conductivity equation is rewritten as follows;

$$\Delta TS/\Delta t = K_u / \left[MS \cdot L + 1/2\left(C_u \rho + C_u \rho\right)\right] \cdot \Delta^2 TS/\Delta Z^2 \quad (5.37)$$

where MS is the volumetric soil water content (m^3 m^{-3}), L is the latent heat of freezing and thawing (344.7 J g^{-1}).

The three heat conduction equations described above are solved by the boundary condition, initial condition and the "Pure Implicit"-type difference equation as follows (Fig. 5.4):

$$T(p+1,n) = \theta\left(T(p+1,n+1) + T(p+1,n-1) - 2t(p+1,n)\right) + T(p,n) \quad (5.38)$$

$$\theta = A \cdot \Delta t / (\Delta x)^2 \quad (5.39)$$

where A is:

$$K_f / C_f \rho \qquad \text{(T<=-1)} \quad (5.40a)$$

$$K_u/(MS \cdot L + 1/2(C_u\rho + C_f\rho)) \qquad (-1<=T<0) \qquad (5.40b)$$

$$K_u/C_f\rho \qquad (0<=T) \qquad (5.40c)$$

where $T(p,n)$ is the temperature at the time of Δt (sec) x p and the location of Δx x n (m). The boundary condition is given for the top and bottom soil layer temperature, and the calculation is repeated to be at a steady state.

5.2.2.1. Thermal parameter

1. Specific heat

The volumetric specific heat C of soil is defined as a sum of the specific heat of all soil components.

$$C = C_m\phi_m + C_w\theta + C_a\phi_a + C_o\phi_o \qquad (5.41)$$

where C is the volumetric specific heat (J m^{-3} K^{-1}), θ is the volumetric soil water content (cm^3cm^{-3}), ϕ is volumetric fraction of each phase, subscripts m, w, a, and o indicate mineral soil, water, air, and organic matter, respectively. C_a is very small, and C_o is similar to C_m. So the C could be simplified as follows:

$$C = C_m(1-\phi_f) + C_w\theta \qquad (5.42)$$

where ϕ_f is the porosity, C_m is adopted for 2.01, and C_w is adopted for 4.18 (water) and 1.88 (ice) (de Vries, 1963).

2. Thermal conductivity

The thermal conductivity of soil K depends on the solid density, water content, quartz density and organic matter content. Their qualitative relationship was examined in many

experimental studies. However, there is no universal equation to apply for various soil textures. This study adopted the experimental equation derived by Kersten (1963):

- for unfrozen sandy soil:

$$K_u = 0.1442(0.7 \cdot \log(\vartheta) + 0.4) \cdot 10^{0.6243} \cdot \rho_s \quad (5.43a)$$

- for frozen sandy soil:

$$K_f = 0.01096 \cdot 10^{0.8116} \cdot \rho_s + 0.00461 \cdot \vartheta \cdot 10^{0.9115} \cdot \rho_s \quad (5.43b)$$

where ρ_s is the bulk density of soil (Mg m^{-3}).

5.2.3. Water budget

The water cycle in terrestrial ecosystems is simulated by a subscheme (Fig. 5.1) simply. The water storage is divided into three compartments, upper layer (*MSUP*, from 0 to 30 cm depth), lower layer (*MSLW*, from 30 cm to rooting depth), and snow accumulation (*SNA*). For each water compartment, net balance of water content (Δ) during a given period is represented as follows:

$$\Delta MS_{up} = PR_{rain} + TW - (EV + TR_{up}) - PN \quad (5.44)$$

$$\Delta MS_{lw} = PN - TR_{lw} - RO \quad (5.45)$$

$$\Delta SNA = PR_{snow} - TW \quad (5.46)$$

where *MS* is the soil water content (mm), *SNA* is the amount of snow cover (mm), *PRrain/snow* are the rainfall and snowfall (mm), *TW* is thawing snow (mm), *EV* and *TR* are evaporation and transpiration (mm), *PN* is the penetration from upper storage to lower storage (mm), *RO* is the runoff (mm), subscript *up* and *lw* indicate the upper and lower storage, respectively. The calculations of each water budget component are explained in the following subsections.

5.2.3.1. Rainfall, snow and thawing

The amounts of the rainfall and snowfall in the total precipitation are estimated in the following equation:

$$PR_{rain} = PR - PR_{snow} \tag{5.47}$$

$$PR_{snown} = PR/(1 + \exp(0.75 \cdot TA - 2.0)) \tag{5.48}$$

where PR is the total precipitation (mm), TA is air temperature at a height of 2.0 m (°C). The snow thawing is estimated as a function of the soil temperature as follows:

$$TW = SNA/(1 + \exp(-0.375 \cdot TG)) \tag{5.49}$$

where TG is the soil surface temperature (°C).

5.2.3.2. Evaporation and transpiration

The S-W model also uses an electrical analogy to treat vertical water vapor movement in the SPAC circulation (Fig. 5.5), similar to the P-M model. The S-W model combines a one-dimensional model of crop transpiration and a one-dimensional model of soil evaporation. Surface resistances regulate the heat and mass transfer at the plant and soil surfaces, and aerodynamic resistances regulate those between the surfaces and the atmospheric boundary layer.

$$\lambda ET = \lambda T + \lambda E = \lambda C_c T_o + \lambda C_s E_o \tag{5.50}$$

where λET is the sum of the latent heat flux from the crop (λT) and soil (λE) (W m^{-2}), λT_o and λE_o are terms similar to those in the Penman-Monteith model (Montieth, 1965) that would apply to transpiration from the canopy and evaporation from the soil, respectively. C_c and C_s are the

canopy resistance coefficient and soil surface resistance coefficient, respectively. They are obtained as follows:

$$\lambda T_o = \frac{\Delta R + (\rho(_p D - \Delta r_{ac} R_s)/(r_{aa} + r_{ac})}{\Delta + \gamma(1 + r_{sc}/(r_{aa} + r_{ac}))} \tag{5.51}$$

$$\lambda E_o = \frac{\Delta R + (\rho(_p D - \Delta r_{as}(R - R_s))/(r_{aa} + r_{as})}{\Delta + \gamma(1 + r_{ss}/(r_{aa} + r_{as}))} \tag{5.52}$$

$$C_c = \frac{1}{1 + \rho_c \rho_a / \rho_s (\rho_c + \rho_a)} \tag{5.53}$$

$$C_s = \frac{1}{1 + \rho_s \rho_a / \rho_c (\rho_s + \rho_a)} \tag{5.54}$$

$$\rho_a = (\Delta + \gamma) r_{aa} \tag{5.55}$$

$$\rho_c = (\Delta + \gamma) r_{ac} + \gamma r_{sc} \tag{5.56}$$

$$\rho_s = (\Delta + \gamma) r_{as} + \gamma r_{ss} \tag{5.57}$$

where r_{sc} is the canopy resistance, and r_{ac} is the aerodynamic resistance of the canopy to in-canopy flow, and r_{ss} is the soil surface resistance. r_a and r_{as} are eddy diffusion resistances from the reference height to in-canopy heat exchange plane height and from there to the soil surface, respectively. R and R_s are the active radiation at the top of the canopy and the soil surface, respectively, and are defined as follows:

$$R = R_n - G \tag{5.58}$$

$$R_s = R_{ns} - G \tag{5.59}$$

where *Rn* and *Rns* are net radiation fluxes into the complete canopy and the substrate (W m^{-2}), respectively, and G is soil heat flux (W m^{-2}).

The radiation reaching the soil surface can be calculated using Beer's law as follows (e.g. Ross, 1981).

$$R_{ns} = R_n \exp(-CLAI) \tag{5.60}$$

where C is the extinction coefficient of light attenuation, for which 0.7 was adopted (Monteith, 1973).

1. Stomatal and leaf boundary resistances

The canopy resistance r_{sc}, and the aerodynamic resistance r_{ac} are defined as values dividing the bulk stomatal resistance r_{st}, and the mean boundary layer resistance r_b, of the canopy, respectively, by the sum of the abaxial and adaxial leaf areas.

$$r_{sc} = r_{st} / 2LAI \tag{5.61}$$

$$r_{ac} = r_b / 2LAI \tag{5.62}$$

where r_{st} was taken as an inverse number of stomatal conductance GS. r_b was taken as a typical value of 25 s m^{-1} (Denmead, 1976; Uchijima, 1976).

2. Soil Surface Resistance

The soil surface resistance, r_{ss}, is the resistance to water vapor movement from the interior to the surface of the soil, and was calculated using Kondo's model (Kondo et al., 1990).

$$r_{ss} = F(\theta)/D_{atm} \tag{5.63}$$

$$F(\theta) = F_1(\theta_{sat} - \theta)^{F_2} \tag{5.64}$$

where θ is the volumetric soil water content (cm^3 cm^{-3}), T_s is the soil surface temperature (K). $F(\theta)$ is the water vapor diffusion distance (m) as a function of θ introduced by Kondo et

al.(1990) that developed the simple model of evaporation from the bare soil surface in laboratory experiments. In loamy soil, F_1 is 2.16×10^2 (m) and F_2 is 10.0. θ_{sat} is the saturated volumetric soil water content, and was taken as 0.54 m^3 m^{-3} of the Mat Cry-gelic soil value at the experimental site (Cao et al., 1998). The molecular vapor diffusivity for movement from the interior to the surface of the soil, D_{atm} has been given by Camillo et al. (1983)

$$D_{atm} = D_0(T_s/273.16)^{1.75} \tag{5.65}$$

where D_o = 0.229×10^{-4} (m^2 s^{-1}) is the diffusivity of water vapor in soil air at the standard state; (Camillo et al., 1983).

3. Eddy Diffusion Resistance

The aerodynamic resistance of the mean canopy flow, r_{aa}, and the aerodynamic resistance of the soil surface to in-canopy flow, r_{as}, were calculated from the vertical wind profile at the field and the eddy diffusion coefficient. In this paper, the scheme is referred to as Shuttleworth and Gurney (1990). This empirically and simply simulates the more important results of a second-order closure theory of in-canopy turbulence and, for this reason, is arguably superior to the earlier submodel in Shuttleworth and Wallace (1985), in both diagnostic and predictive applications of its theory. Above the canopy height, the eddy diffusion coefficient, K, is given by

$$K = ku_*(z-d) \tag{5.66}$$

where u_*, for neutral atmospheric stability, is given as follows:

$$u_* = ku/\ln[(z-d)/z_0] \tag{5.67}$$

where u is the wind speed at the reference height z. d, z_0 is the zero plane displacement and the roughness length (m), and are given by the relational expression as a fixed fraction of crop height h as presented by Monteith (1973):

$$d = 0.63h \tag{5.68}$$

$$z_0 = 0.13h \tag{5.69}$$

Beneath the canopy height, the exponential decrease of the eddy diffusion coefficient, K, through the canopy, is given as follows:

$$K = K_h \exp\left[-n(1 - Z/h)\right] \tag{5.70}$$

where K_h is the eddy diffusion coefficient at the top of canopy, and n is the extinction coefficient of the eddy diffusion, chosen as a typical value for crops (wheat, rice, clover and corn), 2.5 (Monteith, 1973). K_h is determined as follows:

$$K_h = ku_*(h - d) \tag{5.71}$$

r_{as} and r_{aa} are assumed as integrations of Eqs. (5.66) and (5.70), respectively, over the height ranges 0 to (z_0+d) and (z_0+d) to z; thus

$$r_{as} = \frac{h\exp(n)}{nK_h}\left[\exp(-nz_0'/h) - \exp\left[-n(z_0 + d)/h\right]\right] \tag{5.72}$$

$$r_{aa} = \frac{1}{ku_*}\left[\ln\left(\frac{z-d}{h-d}\right)\right] + \frac{h}{nK_h}\left[\exp\left\{n(1-(z_0+d)/h)\right\} - 1\right] \tag{5.73}$$

where z_0'= 0.01 m (van Bavel and Hillel, 1976) is the roughness length of the substrate.

5.2.3.3. Runoff and Infiltration

Two buckets are settled for runoff and infiltration calculations (Fig. 5.6). The overflow from the upper bucket comes into the lower bucket as an infiltration. The overflow from the lower bucket outflows from the ecosystem as a runoff. In a new bucket model (Kondo, 1993), the soil water content *MS*, the inflow water into the ground *RI*, and the runoff *RO* are expressed in the following equations.

(a) in the upper bucket

$$\Delta MS_{up} = \left(MS_{up\max} - MS_{up}\right) \cdot \tanh\left(X_{up}\right) \tag{5.74}$$

where MS_{upmax} is the maximum water storage (mm), and MS_{up} is the water storage in the previous time step (mm). X_{up} and $\tanh(X_{up})$ are described as follows:

$$X_{up} = RI / \left(MS_{up\max} - MS_{up}\right) \tag{5.75}$$

$$RI = PR_{rain} + TW - \left(EV + TR_{up}\right) \tag{5.76}$$

$$\tanh\left(X_{up}\right) = \left(1 - \exp\left(-2X_{up}\right)\right) / \left(1 + \exp\left(-2X_{up}\right)\right) \tag{5.77}$$

From these equations above, the penetration from the upper bucket to the lower bucket *PN* is defined as follows:

$$PN = RI - \Delta MS_{up} \qquad (PN > 0) \tag{5.78}$$

(b) in the lower bucket

$$\Delta MS_{lw} = \left(MS_{lw\max} - MS_{lw}\right) \cdot \tanh\left(X_{lw}\right) \tag{5.79}$$

where MS_{lwmax} is the maximum water storage (mm), MS_{lw} is the water storage in the previous time step (mm). X_{lw} is described as follows:

$$X_{lw} = PN/\left(MS_{lw\max} - MS_{lw}\right) \tag{5.80}$$

From these equations above, the runoff from the lower bucket RO is defined as follows:

$$RO = PN - \Delta MS_{lw} \qquad (RO > 0) \tag{5.81}$$

In the frozen soil, the moisture movement induced by unfrozen soil water should be taken into account. However, its hydraulic conductivity is as very small as in the order of 10^{-8} (m s^{-1}) at the temperature of 0 °C, in the order of 10^{-13} (m s^{-1}) at the temperature of -1 °C and extremely smaller at the lower temperature. Consequently, the moisture movement in the frozen soil is assumed to be negligible in this study.

5.3. Model experiment designs

Three model experiments were made in this study: a steady state simulation, a transient simulation and a sensitivity analysis. All experiments used the monthly climate data measured at the meteorological observation filed of the Haibei station, the Chinese Academy of the Sciences for twenty years from 1981 to 2000 as the input climate data, and adopted the ecophysiological parameters (Fig. 5.3, Table 5.1) equipped as a Tibetan meadow ecosystem (No. 20 biome) in the Sim-CYCLE.

In a steady state simulation, calculation is launched from the juvenile stage, where initial carbon content is 0.1 Mg C ha^{-1} for each compartment, and repeated for a sufficiently long period to attain the equilibrium state under a stationary environmental condition using 20 years averaged monthly climate condition for 1981-2000 (Fig. 5.7). Annual *NEP* is used as the criteria to determine whether the ecosystem carbon dynamics is sufficiently equilibrated (i.e. climax

stage): *NEP* < 0.0001 Mg C ha^{-1} yr^{-1}. The resulting equilibrated carbon dynamics was compared to observed values for examination of the model estimation accuracy.

In a transient simulation, calculation is started from an equilibrium state, where annual *NEP* is less than 0.0001 Mg C ha^{-1} yr^{-1} after the steady state simulation. The carbon dynamics was simulated for 1981-2000 using the 20 years transient monthly climate data, and compared with the climate perturbations and global climatic events, e.g. volcanic eruptions and *ENSO*.

In a sensitivity analysis, calculation is also started from the equilibrium state where annual *NEP* is less than 0.0001 Mg C ha^{-1} yr^{-1} after the steady state simulation. The carbon dynamics was simulated for the equilibrium state using the 20 years averaged monthly climate data including the prescribed climate shifts, e.g. ±10 °C in air temperature, ±50 % in precipitation and 200-1000 ppm in CO2 concentration.

5.4. Results

5.4.1. Steady state experiment

In the steady state experiment using 20 years, 1981-2000, averaged monthly climate data, 1003 years are necessary to equilibrate the annual *NEP*. Figure 5.8 shows the growth of ecosystem carbon fluxes and storages for the first 200 years. *GPP*, *AR* and *NPP* increased in the beginning of calculations rapidly, and were re-equilibrated in the 50 years. On the other hand, the *HR* increased slowly, and *NEP* (=*NPP-HR*) decreased slowly toward zero. The plant biomass W_{plant} and *LAI*, gas exchange area in the photosynthesis, increased in the beginning of calculations rapidly, and were re-equilibrated in the 50 years. The soil microbes and litter biomass W_{soil}, determined by the input of plant litterfall, increased slowly.

The annual carbon fluxes, equilibrated by Sim-CYCLE, were compared with the observed and estimated values around the Haibei station derived from the literatures (Fig. 5.9; Table. 5.2). Although the *GPP*s are 1.5 times larger than the observed values (Sim-CYCLE, 847.8; Observation, 575.1-527.4), the other fluxes are as much as the observed values (*NPP*; Sim-CYCLE, 427.8; Observation, 124.2-823.0; *SR*; Sim-CYCLE, 602.3; Observation, 578.0-2721.0).

In the seasonal changes of the carbon fluxes, the *GPP*, *AR* and *NPP* are positive from May to September, and zero during other months (Fig. 5.10). The *HR* is positive from May to November, and zero during other months (Fig. 5.10). The *NEP* reached maximum state in July and August, and decreased to be negative in October. In the seasonal changes of the carbon storages, the leaf, and stem biomass and *LAI* are positive from May to September (Fig. 5.11). The root biomass increases from May to October gradually, and the litter biomass increases rapidly in October induced by the plant litterfall. The mineral soil biomass does not change during whole year.

The soil thermal profiles show a good agreement with the measured data except for June and July (Fig. 5.12). The soil freezing depths are also estimated successfully. The heat budgets are shown in Fig. 5.13. The *Rn* reached its maximum in June and the *G* reached its maximum in April and minimum in November. The *H* reached its maximum in May and the λE reached maximum in July. The water budgets are shown in Fig. 5.14. The *TR* reached its maximum status in summer (July and August), when the *LAI* reached the maximum status (Fig. 5.11). The *EV* was large in spring (April and May) and the end of autumn (October), when the *LAI* was low (Fig. 5.11). The *RO* existed during the growing season. The *TW* reached its maximum in the spring (April). The SWC_{up} started to increase from May and reached its maximum in September, and the SWC_{lw} did not change significantly.

5.4.2. Transient experiment

In the transient state experiment using the 20 years, transient climate data, the averaged annual carbon fluxes were similar to the observed and estimated values around the Haibei station derived from the literatures (Table 5.2). Aboveground *NPP*s were slightly larger than the observed values for 1981-1993 (Fig. 5.16).

In the interannual changes of the carbon fluxes and storages (Fig. 5.16), the *GPP*s ranged from 7.66 to 9.11, the *AR*s from 3.95 to 4.64, the *NPP*s from 3.71 to 4.47, the *HR*s from 3.61 to 4.41 and the *NEP*s from –0.65 to +0.65 (Mg C ha^{-2} yr^{-1}). The W_{plant} ranged from 6.63 to

6.75. The W_{soil} reached a maximum of 207.25 (Mg C ha^{-2}) in 1984 and decreased to 205.82 (Mg C ha^{-2}) in 2000 (Table 5.3).

In the comparisons of the climate and carbon flux anomalies, the variation from their 20 years averaged values (Fig. 5.17; Table 5.4), the *GPP*, *AR*, *NPP*, *NEP* anomalies are synchronized with each other. The *GPP* and *NEP* anomalies ranged in ±0.76 and ±0.68 Mg C ha^{-2}, respectively. The *HR* anomaly changed along with the surface temperature variations.

Carbon flux anomalies plotted against the climate (annual average temperature, annual precipitation and annual averaged solar radiation) anomalies are shown in Figs. 5.18, 19, and 20. The increment of annual averaged temperature increased *ΔGPP*, *ΔAR* and *ΔNPP* slightly, but increased *ΔHR* largely with relatively higher determinant coefficient, and decreased the resulting *ΔNEP* (Fig. 5.18). The increment of annual precipitation and annual averaged solar radiation increased or decreased the carbon fluxes so slightly with relatively lower determinant coefficient (Figs. 5.19 and 5.20).

Figure 5.22 shows the seasonal changes in the slope of regression lines between temperature, precipitation, solar radiation and carbon flux anomalies. The increment of temperature in June to August increased the *HR* and decreased the *NEP*, and the increment of temperature in September increased the *GPP*, *AR* and *NPP*. The fluctuations of precipitation seemed not to affect the carbon fluxes. The increment of solar radiation from June to August increased the *GPP*, *AR* and *NPP*.

5.4.3. Model sensitivity analysis

In the model sensitivity analysis, the time courses of carbon fluxes and storage variation, calculated using 20 years averaged climate data with the increment of temperature of 5 °C, solar radiation of 10 % and precipitation of 30 % and the CO2 concentration of 700 ppm, were shown in Figs. 5.23 and 5.24. These results show the potential responses of the carbon dynamics to climate changes. The *GPP*, *AR* and *NPP* increased rapidly in the beginning of the experiment, and were equilibrated after 20 years elapsed. In contrast, The *HR* increased slowly, and the *NEP* decreased slowly toward zero. The plant biomass W_{plant} increased in the beginning of

calculations rapidly, and were re-equilibrated in the 20 years. The soil microbes and litter biomass W_{soil} increased slowly.

Next, the equilibrated carbon, water and heat fluxes and storages calculated using 20 years averaged climate data with the temperature data of ± 10 °C, the solar radiation data of $\pm$ 30 % and the precipitation data of ± 50 % and the CO2 concentration data of 200-1000 ppm respectively, were plotted against the prescribed climate fluctuations in Fig. 5.25 and 5.26. The increment of temperature by the 5°C increased the carbon fluxes and storages larger than the present values, and the increment over 7.5 °C decreased them reversely. The magnitude of photosynthesis (*GPP*) links to the magnitude of the transpiration (*TR*). The increment of temperature by the 3°C increased the latent heat flux larger than the present values, and the increment over 5 °C did not increase them moreover. The increment of solar radiation and precipitation did not affect the carbon dynamics largely. The increment of solar radiation leads to increase the *TR* and decrease the soil water content significantly. The decrescent of precipitation leads to decrease the soil water content significantly. The increment of CO2 concentration by the 700 ppm increased the carbon fluxes and storages, but that at the concentration of 1000 ppm did not change the carbon dynamics significantly.

5.5. Discussion

5.5.1. Model accuracy

In the validation of the simulated annual carbon dynamics (Fig. 5.9; Table 5.2), the model estimated values coincided with the observed values, and this confirms the successful model simulation.

In the seasonal changes, the *GPP* and R_e (*AR+HR*) coincided with the measured data by the eddy covariance method in 2002 (Fig. 5.10; Table 4.2). But, the *NEP* did not synchronized in the maximum and minimum timings with the measured data. However, it is not enough to judge whether this results are reasonable or not from the current limited measurement. Furthermore multi-year data acquisitions of the CO2 exchanges are therefore required.

In the transient state experiment (Fig. 5.16), the simulated aboveground *NPP*s were slightly larger than the observed values for 1981-1993 (RMSE = 0.089 MgC ha^{-2}; Fig. 5.15). Because the observed values may contain the sampling error, these relatively high agreements confirm the high model accuracy.

5.5.2. The Relationship between climate perturbations and ecosystem CO2 exchanges

The increment of temperature increased the *HR*, and decreased the *NEP* reversely in the transient state experiment. This was caused by the microbial decomposition rate increasing in the mineral soil and litter biomass. On the other hand, there was no clear relationship between the precipitation fluctuations and carbon fluxes. This indicated that the water is not a limiting factor in this ecosystem in the contrast to other relatively dry grassland, e.g. steppes, savannas. There was also no clear relationship between the solar radiation fluctuations and carbon fluxes. This may be caused by the seasonality of plant response to solar radiation increment; the increment of solar radiation only from June to August increased the *GPP*, *AR* and *NPP* (Fig. 5.22).

The global climate events affected the ecosystem carbon dynamics. Mt. *El Chichon* eruption in 1982 lead to lower temperature and the decrements of *GPP* and R_e (*AR*+*HR*) in the next year 1983. The *ENSO* (*El-Nino* and Southern Oscillation) event in 1997 winter to 1998 summer lead to higher temperature and the increments of *GPP* and R_e (*AR*+*HR*) in 1998. Thus, the increments of temperature increased the ecosystem carbon fluxes. In contrast, Mt. *Pinatsubo* eruption in 1991 lead to lower temperature and the increments of *GPP* and R_e (*AR*+*HR*) in the next year 1992. This increment may be caused by the increments of solar radiation in the summer of 1998 (Figs. 5.21 and 5.22). The anomalies in the *NEP*s did not synchronize with those in a global scale as presented by Ito and Oikawa (2000a). Resultingly, the *NEP*s tended to be negative and the W_{soil} decreased gradually for 20 years period. However it cannot be concluded that study site was a source of atmospheric CO_2, because the transient calculation in the carbon dynamics started from the neutral condition (i.e. $NEP \sim 0$) and have the possibility to

balance out the long-term effects on ecosystem carbon uptake by global warming and CO_2 fertilization.

5.5.3. The potential response of the ecosystem CO_2 exchanges against global warming

The model sensitivity analysis showed that the *GPP*, *AR*, *NPP* and W_{plant} responded quickly and the *HR* and W_{soil} responded very slowly against the climate change. Consequently, the *NEP* was positive in the beginning of the model simulation. These may indicate that the long-term global warming will increase the ecosystem carbon uptake, and now the alpine meadow ecosystems maybe in this situation.

The increments of temperature by 5 °C increased the *GPP* and that over 7.5 °C decreased the *GPP* (Fig. 5.25). Zhang and Welker (1996) showed that while the peak community biomass showed no significant change, the duration of peak biomass was extended in the warming experiment by 5 °C of air temperature at the Haibei alpine meadow. Thus, the warming by 5 °C advances the ecosystem photosynthetic activity and increases the duration of growing season, and thus, the *GPP*. But, the warming over 7.5 °C may go beyond the optimum temperature of photosynthesis and decrease the *GPP*. In this extreme warming, this ecosystem may shift to another biome type that can survive the new climate.

The increments of CO_2 concentration by 700 ppm increased the *GPP*, but that at the concentration of 1000 ppm carbon dynamics showed no significant change (Fig. 5.25). One possibility is that such high CO_2 concentration as 1000 ppm induced the stomatal conductance.

Table 5.1. Site-specific parameters used in Sim-CYCLE running at the Haibei study site.

Parameter	Value	Unit	Explanation	Remarks
albcv	0.2	dimensionless	reflectivity or albedo	field experiment
alloc_assv	0.22		allocation ratio for assimilation organ, fraction	
alloc_abgv	0.05		allocation ratio for aboveground non-assimilation organ, fraction	
slav	240.0	cm^2 g dm^{-1}	specific leaf area	field experiment
eK0v	0.7	dimensionless	light attenuation coefficient, no dimension	
luev	0.06	mol CO2 mol $photon^{-1}$	control light dependence coefficient	
pmaxv	20	micro mol CO2 m^{-2} s^{-1}	potential maximum rate	
topt0v	18	deg C	optimum temperature	
tminv	-1	deg C	minimum temperature	
tmaxv	40	deg C	maximum temperature	
gs_b0v	10	mmol H_2O m^{-2} s^{-1}	parameters of stomatal conductance	
gs_b1v	170000	mmol H_2O m^{-2} s^{-1}	parameters of stomatal conductance	
gs_b2v	4.8	mmol H_2O m^{-2} s^{-1}	parameters of stomatal conductance	
km_nstlv	0.32		maximum stomatal conductance	
kmciv	40	ppmv	dependence of photosynthesis on intercellular CO2 concentration	
cmpcdv	50		CO2 compensation point, ppmv	
rgfv	0.57	g C g C^{-1} alloc	specific growth respiration rate	
rgcv	0.31	g C g C^{-1} alloc	specific growth respiration rate	
rgrv	0.39	g C g C^{-1} alloc	specific growth respiration rate	
rmf0v	1.61	mg C g C^{-1} day^{-1}	specific maintenance respiration rate at 15 degC	
rmc_sv	0.095	mg C g C^{-1} day^{-1}	specific maintenance respiration rate at 15 degC	
rmr_sv	0.51	mg C g C^{-1} day^{-1}	specific maintenance respiration rate at 15 degC	
rmc_hv	0.009	mg C g C^{-1} day^{-1}	specific maintenance respiration rate at 15 degC	
rmr_hv	0.037	mg C g C^{-1} day^{-1}	specific maintenance respiration rate at 15 degC	
qTfv	3.0	dimensionless	temperature dependence	field experiment
qTcv	3.0	dimensionless	temperature dependence	field experiment
qTrv	3.0	dimensionless	temperature dependence	field experiment
lfv	0.0017		specific litter fall rate, fraction	
lcv	0.000128		specific litter fall rate, fraction	
lrv	0.00093		specific litter fall rate, fraction	
dcdv	1	dimensionless	deciduous leaf fraction	
root_stratv	0.8833	dimensionless	root profile parameter	field experiment
topo	3250	m	topography, orology, and altitude, m above MSL	
whc30	15	cm	soil water holding capacity at the depth of 0-30 cm	
whc	42	cm	soil water holding capacity at the depth of 30-100 cm	
sd	42	cm	soil rooting depth	
hyd_cond	0.005757		hydraulic conductivity	

1

Table 5.2. Comparisons of ecosystem carbon dynamics between Sim-CYCLE estimates and those from other studies

Term	Method	Value	Unit	Year	Remarks	Reference
GPP	Sim-CYCLE	847.8	gC m^{-2} yr^{-1}	1981-2000	steady state	this study
	Sim-CYCLE	834.4 ± 45.7	gC m^{-2} yr^{-1}	1981-2000	transient state	this study
	Eddy covariance	575.1	gC m^{-2} yr^{-1}	2002	gap-filled by the non-linear regression method with u*-correction	Kato et al. (submitted, 2003)
	Eddy covariance	527.4	gC m^{-2} yr^{-1}	2002	gap-filled by the non-linear regression method without u*-correction	Kato et al. (submitted, 2003)
NPP	Sim-CYCLE	412.7	gC m^{-2} yr^{-1}	1981-2000	steady state	this study
	Sim-CYCLE	406.1 ± 23.3	gC m^{-2} yr^{-1}	1981-2000	transient state	this study
	Miami model	248.4	gC m^{-2} yr^{-1}	1981-2000	steady state	Lieth (1975)
	Miami model	248.2 ± 12.4	gC m^{-2} yr^{-1}	1981-2000	transient state	Lieth (1975)
	Montreal model	501.8	gC m^{-2} yr^{-1}	1981-2000	steady state	Lieth (1975)
	Montreal model	454.8 ± 24.1	gC m^{-2} yr^{-1}	1981-2000	transient state	Lieth (1975)
	Rosenzweig model	282.6	gC m^{-2} yr^{-1}	1981-2000	steady state	Rosenzweig (1968)
	Rosenzweig model	242.8 ± 24.9	gC m^{-2} yr^{-1}	1981-2000	transient state	Rosenzweig (1968)
	Chikugo model	823.0	gC m^{-2} yr^{-1}	1981-2000	steady state	Uchijima and Seino (1985)
	Chikugo model	822.6 ± 20.7	gC m^{-2} yr^{-1}	1981-2000	transient state	Uchijima and Seino (1985)
	QingZhang NPP model	124.2	gC m^{-2} yr^{-1}	1981-2000	steady state	Li and Zhou (1998)
	QingZhang NPP model	124.2 ± 10.6	gC m^{-2} yr^{-1}	1981-2000	transient state	Li and Zhou (1998)
	CASA model	176.0 ± 99.0	gC m^{-2} yr^{-1}	1982-1999	average value for alpine meadow on the Qinghai-Tibetan Plateau	Piao and Fang (2002)
Aboveground *NPP*	Sim-CYCLE	197.6 (92.0*)	gC m^{-2} yr^{-1}	1981-2000	steady state	this study
	Sim-CYCLE	194.4 ± 10.4 (90.5 ± 3.5*)	gC m^{-2} yr^{-1}	1981-2000	transient state	this study
	Observation	155.5 ± 2.4*	gC m^{-2} yr^{-1}	1981-1993	mowed at the same observation site	Shi et al. (1991)
	Regression model	163.3 ± 2.4*	gC m^{-2} yr^{-1}	1981-2000	modeled at the same observation site	Li and Zhang (1998)
	Estimated from literature	125.9	gC m^{-2} yr^{-1}	---		Luo et al. (2002)

Table 5.2. *Continued*

Belowground *NPP*	Sim-CYCLE	215.1 (140.7**)	gC m^{-2} yr^{-1}	1981-2000	steady state	this study
	Sim-CYCLE	210.9 ± 3.6 (139.0 ± 8.2**)	gC m^{-2} yr^{-1}	1981-2000	transient state	this study
	Estimated from literature	274.3	gC m^{-2} yr^{-1}	---		Luo et al. (2002)
NEP	Sim-CYCLE	0.0	gC m^{-2} yr^{-1}	1981-2000	steady state	this study
	Sim-CYCLE	-3.6 ± 32.2	gC m^{-2} yr^{-1}	1981-2000	transient state	this study
	Eddy covariance	78.5	gC m^{-2} yr^{-1}	2002	gap-filled by the non-linear regression method with u*-correction	Kato et al. (submitted, 2003)
	Eddy covariance	113.9	gC m^{-2} yr^{-1}	2002	gap-filled by the non-linear regression method without u*-correction	Kato et al. (submitted, 2003)
	Eddy covariance	145.9 ± 3.3	gC m^{-2} yr^{-1}	2002	gap-filled by the MDV method	Kato et al. (submitted, 2003)
	Eddy covariance	118.8 ± 18.9	gC m^{-2} yr^{-1}	2002	gap-filled by the LookUp method	Kato et al. (submitted, 2003)
Soil Respiration	Sim-CYCLE	602.3	gC m^{-2} yr^{-1}	1981-2000	steady state	this study
	Sim-CYCLE	596.3 ± 23.0	gC m^{-2} yr^{-1}	1981-2000	transient state	this study
	Observation	2721.0	gC m^{-2} yr^{-1}	1981-1993	alkali absorption method?	Wang et al. (1982)
	Observation	578.0	gC m^{-2} yr^{-1}	1998-1999	closed chamber method	Zhao et al. (2001)
	Observation	707.2	gC m^{-2} yr^{-1}	1998-1999	closed chamber method	Liu et al. (2001)

* Aboveground *NPP* as a maximum aboveground biomass, ** Belowground *NPP* as a maximum belowground biomass

Table 5.3. Comparisons of carbon pools and *LAI* between Sim-CYCLE estimates and those from other studies.

Term	Method	Value	Unit	Year	Remarks	Reference
Maximum aboveground biomass (foliage + stem)	Sim-CYCLE	92.0 (85.3*)	$gC\ m^{-2}$	1981-2000	steady state	this study
	Sim-CYCLE	90.5 ± 3.5 (83.9 ± 3.2*)	$gC\ m^{-2}$	1981-2000	transient state	this study
	Observation	165.5	$gC\ m^{-2}$	2001	mowed on 20 Aug.	Kato et al. (in press, 2004b)
	Observation	127.3**	$gC\ m^{-2}$	2002	Mowing	Kato et al. (in press, 2004b)
	Estimated from literature	114.1	$gC\ m^{-2}$	---		Luo et al. (2002)
Belowground biomass (root)	Sim-CYCLE	635.6 ± 45.4	$gC\ m^{-2}$	1981-2000	steady state	this study
	Sim-CYCLE	623.2 ± 44.6	$gC\ m^{-2}$	1981-2000	transient state	this study
	Observation	738.8	$gC\ m^{-2}$	2001	mowed on 20 Aug.	Kato et al. (in press, 2004b)
	Estimated from literature	903.5	$gC\ m^{-2}$	---		Luo et al. (2002)
Litter biomass	Sim-CYCLE	1075.9 ± 26.3	$gC\ m^{-2}$	1981-2000	steady state	this study
	Sim-CYCLE	1074.1 ± 35.3	$gC\ m^{-2}$	1981-2000	transient state	this study
Mineral soil	Sim-CYCLE	19586.9 ± 6.1	$gC\ m^{-2}$	1981-2000	steady state	this study
	Sim-CYCLE	19578.9 ± 34.3	$gC\ m^{-2}$	1981-2000	transient state	this study
	Estimated from literature	18200	$gC\ m^{-2}$	---	assigned to alpine meadow grassland type	Ni, J. (2002)
	Estimated from literature	36500	$gC\ m^{-2}$	---	assigned to alpine meadow soil type	Fang et al. (1996)
Maximum Leaf Area Index	Sim-CYCLE	2.25	$cm^3\ cm^{-3}$	1981-2000	steady state	this study
	Sim-CYCLE	2.21 ± 0.08	$cm^3\ cm^{-3}$	1981-2000	transient state	this study
	Observation	3.08	$cm^3\ cm^{-3}$	2001	mowed on 20 Aug.	Kato et al. (in press, 2004b)
	Observation	2.70**	$cm^3\ cm^{-3}$	2002	Mowing	Kato et al. (in press, 2004b)

Data shows annual values for single year estimations and measurements, annual averages and standard deviation for multiple years estimations and measurements (average ± s.d.). * maximum foliage biomass, ** monthly averaged value from Kato et al. (in press, 2004b)

Table 5.4. Climate and carbon fluxes annual anomalies in the Haibei alpine meadow.

Year	$\Delta T_{surface}$	ΔPR	ΔSWR	ΔGPP	ΔAR	ΔNPP	ΔHR	ΔNEP
	°C	mm	W m^{-2}	Mg C ha^{-1}	Mg C ha^{-1}	Mg C ha^{-1}	Mg C ha^{-1}	Mg C ha^{-1}
1981	-0.43	-61.32	0.36	-0.30	-0.14	-0.17	0.09	-0.25
1982	-0.41	-105.62	1.75	0.35	0.16	0.19	-0.49	0.68
1983	-0.98	-31.52	1.73	-0.29	-0.16	-0.12	-0.30	0.17
1984	-0.72	-75.02	0.97	-0.28	-0.16	-0.11	-0.13	0.01
1985	-0.23	263.18	0.36	-0.69	-0.34	-0.35	0.12	-0.47
1986	-0.18	112.88	0.39	0.02	-0.01	0.03	-0.17	0.20
1987	0.47	57.98	-1.15	-0.16	-0.07	-0.08	0.02	-0.10
1988	0.43	211.78	-2.27	-0.18	-0.08	-0.10	-0.09	-0.01
1989	0.38	289.08	-1.27	-0.23	-0.10	-0.12	0.03	-0.15
1990	0.44	-39.62	4.75	0.36	0.17	0.19	0.02	0.17
1991	-0.47	-136.02	23.34	-0.41	-0.19	-0.21	0.02	-0.23
1992	-0.82	1.38	44.96	0.12	0.03	0.09	-0.13	0.21
1993	0.04	-53.72	49.65	-0.07	-0.04	-0.03	0.11	-0.14
1994	0.85	-39.02	39.02	-0.55	-0.25	-0.31	0.31	-0.62
1995	-0.16	-8.42	39.02	0.76	0.35	0.41	-0.17	0.58
1996	-0.60	-55.92	-16.86	0.50	0.22	0.28	0.03	0.25
1997	0.12	-97.32	-47.27	-0.72	-0.34	-0.37	0.01	-0.38
1998	0.92	-19.92	-37.51	0.46	0.26	0.21	0.28	-0.08
1999	0.83	-153.62	-35.36	0.69	0.38	0.32	0.12	0.20
2000	0.51	-59.22	-37.07	0.59	0.32	0.27	0.32	-0.04
s.d.	0.58	125.65	26.43	0.46	0.23	0.23	0.20	0.32

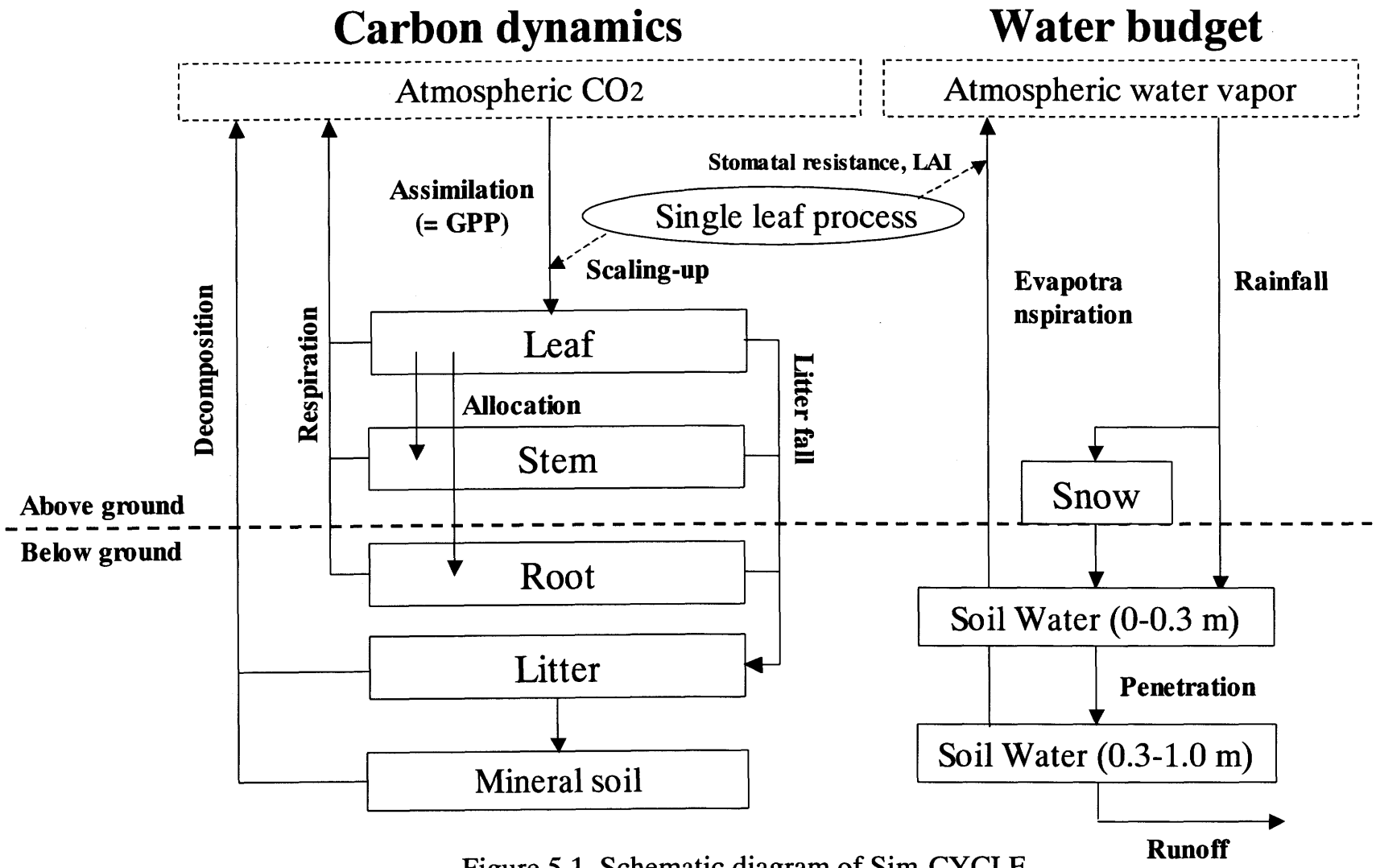

Figure 5.1. Schematic diagram of Sim-CYCLE.

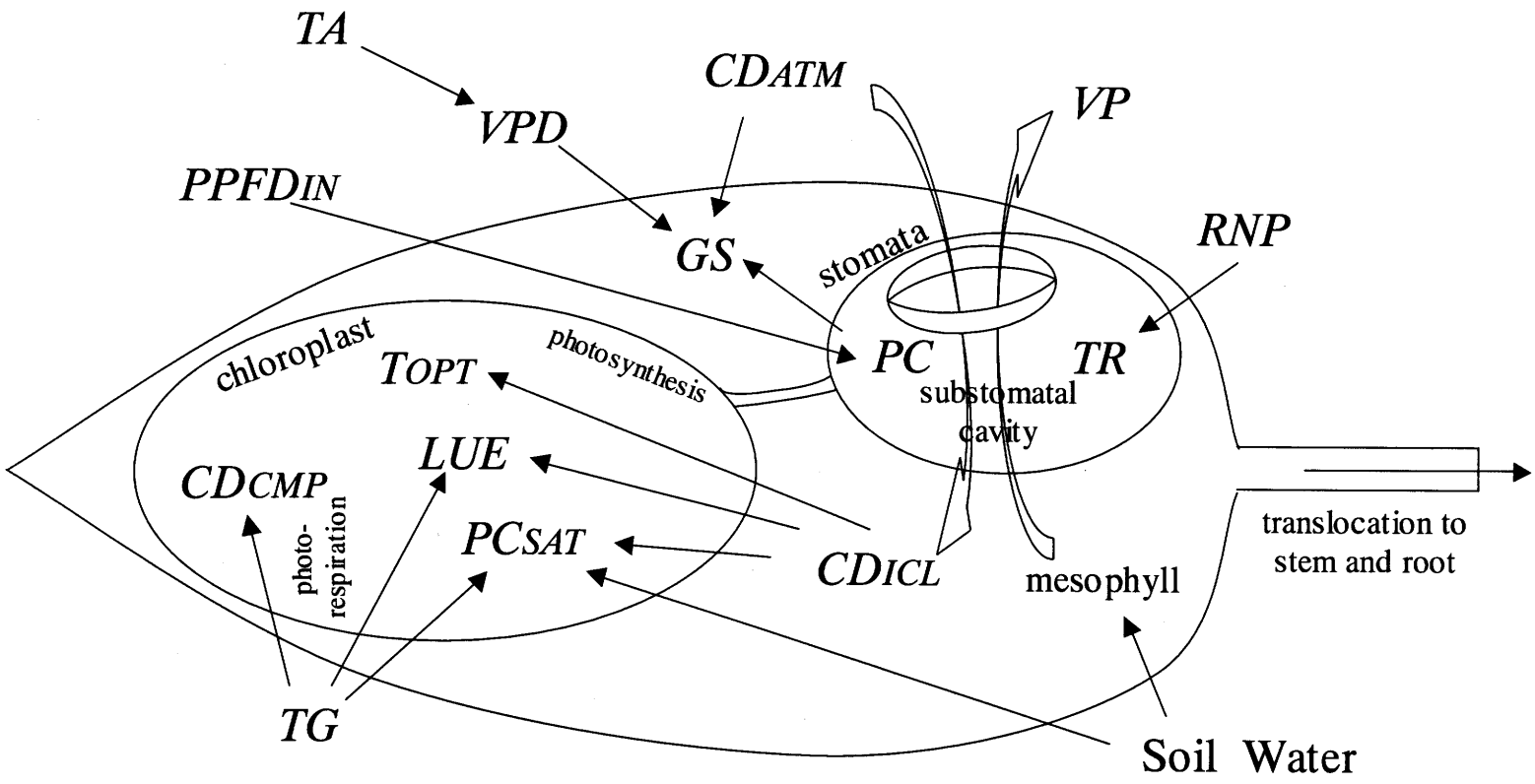

Figure 5.2. Schematic diagram of single leaf processes in Sim-CYCLE (Adopted from Ito, 2000). CO_2 and H_2O (vapor) are exchanged through stomata, i.e. photosynthesis *PC* and transpiration *TR*, respectively. The conductance of stomata *GS* is regulated by atmospheric CO_2 concentration CD_{ATM}, vapor pressure deficit *VPD*, and photosynthetic rate *PC*. The term *PC* is a function of irradiance of photosynthetically active radiation *PPFDIN* , intercellular CO_2 concentration CD_{ICL} , surface temperature *TG*, and soil moisture content *MS*. In the calculation, photosynthetic properties, i.e. light use efficiency *LUE*, CO_2 compensation point CD_{CMP}, and optimum temperature T_{OPT} , are also estimated. The term *TR* is affected by net radiation *RNP* and *VPD* (a function of air vapor pressure *VP* and air temperature *TA*).

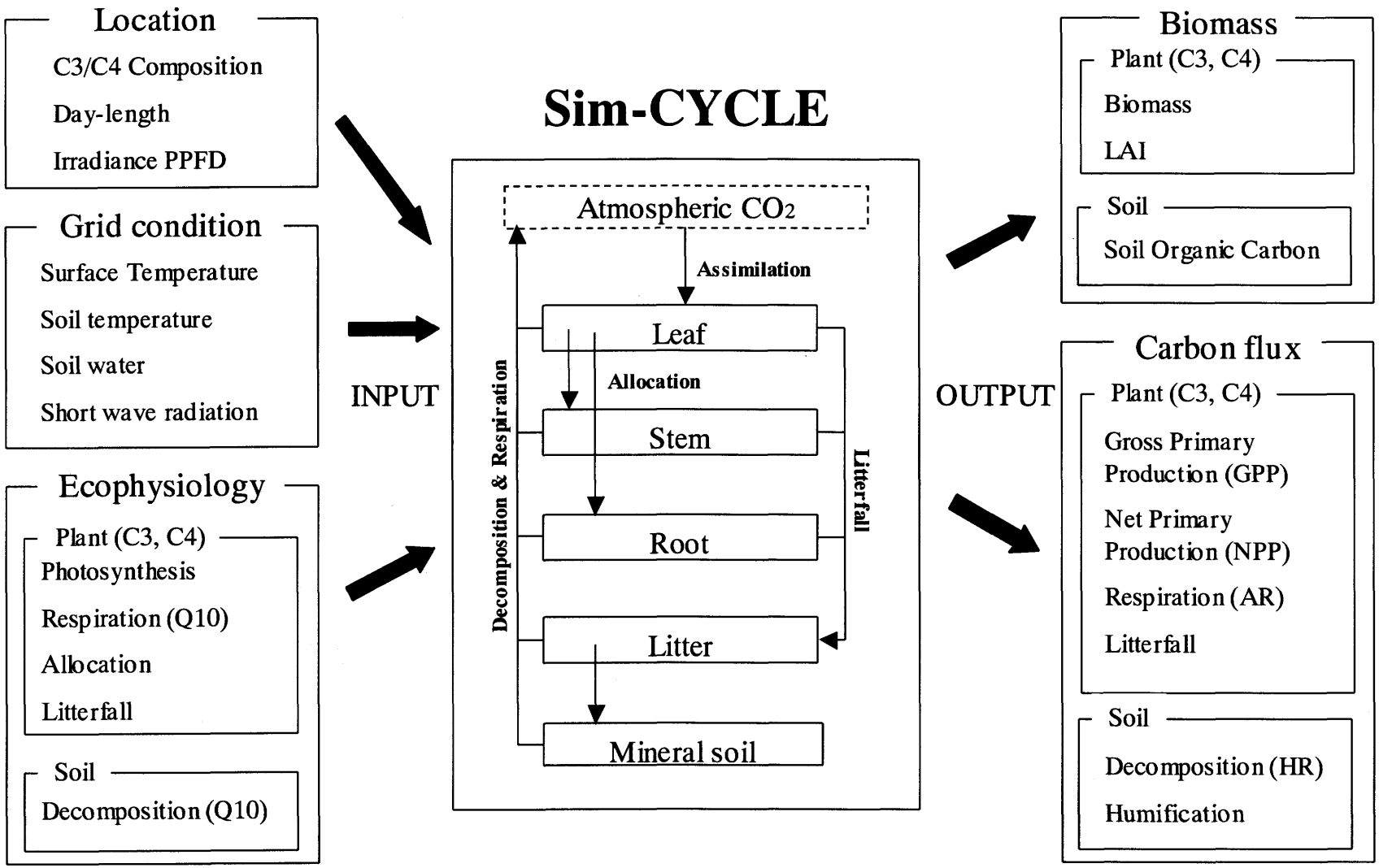

Figure 5.3. Schematic diagram of the Sim-CYCLE calculation processes.

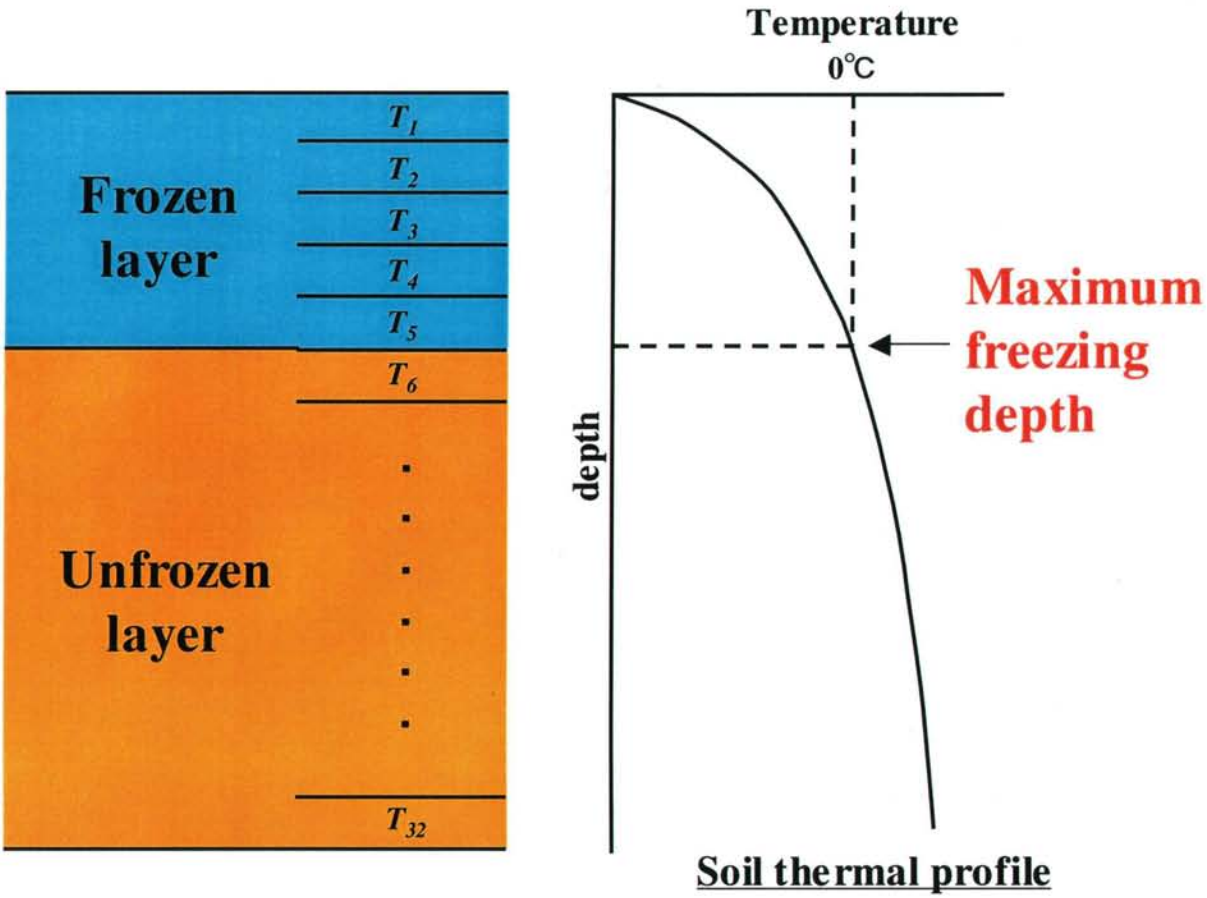

$$T_{y,i+1}=rT_{y-1,i}+(1-2r)T_{y,i}+rT_{y+1,i}$$

$T_{y,i}$, temperature at the horizon y in the time step i (y=1～32)

r, coefficient

Figure 5.4. Schematic diagram of soil thermal profile processes in Sim-CYCLE.

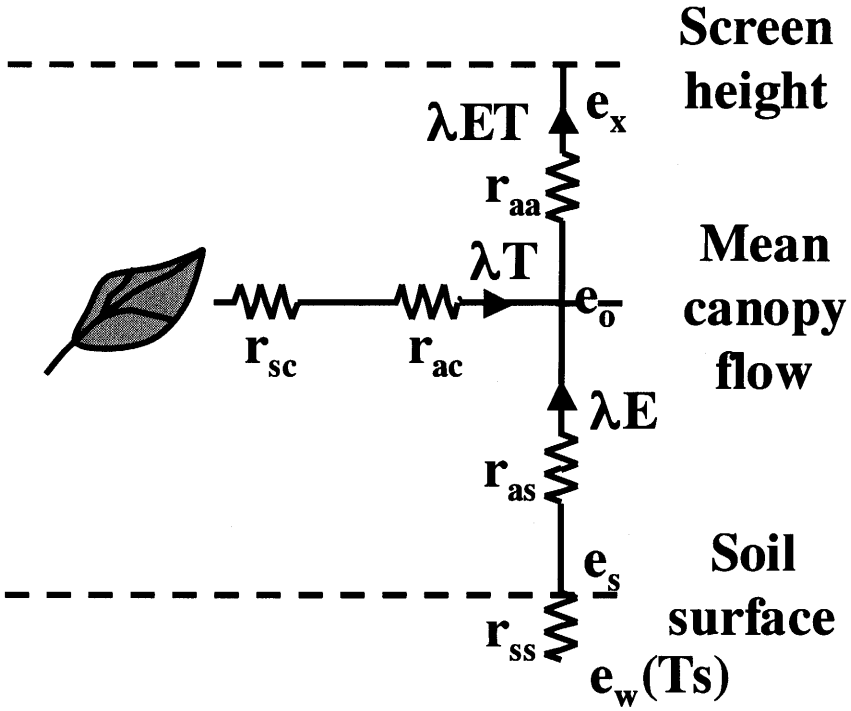

Figure 5.5. Schematic diagram of a one-dimensional description of energy partitioning for a canopy. Illustration shows the S-W model description (Shuttleworth and Wallace, 1985). λET is the evapotranspiration from the crop (λT) and soil (λE). $r_{c,}$ and r_{sc} are the canopy resistances, and r_{ss} is the soil surface resistance. r_a is the aerodynamic resistance of the canopy, r_{ac} is that of the canopy to in-canopy flow, r_{aa} and r_{as} are those of the reference height to in-canopy heat exchange plane height and there to the soil surface, respectively. e_x, e_l, e_o and e_s are the vapor pressures at the reference height, the leaf surface, the mean flow height, and the soil surface, respectively. e_w (Ts) is the saturated vapor pressure at temperature T_s.

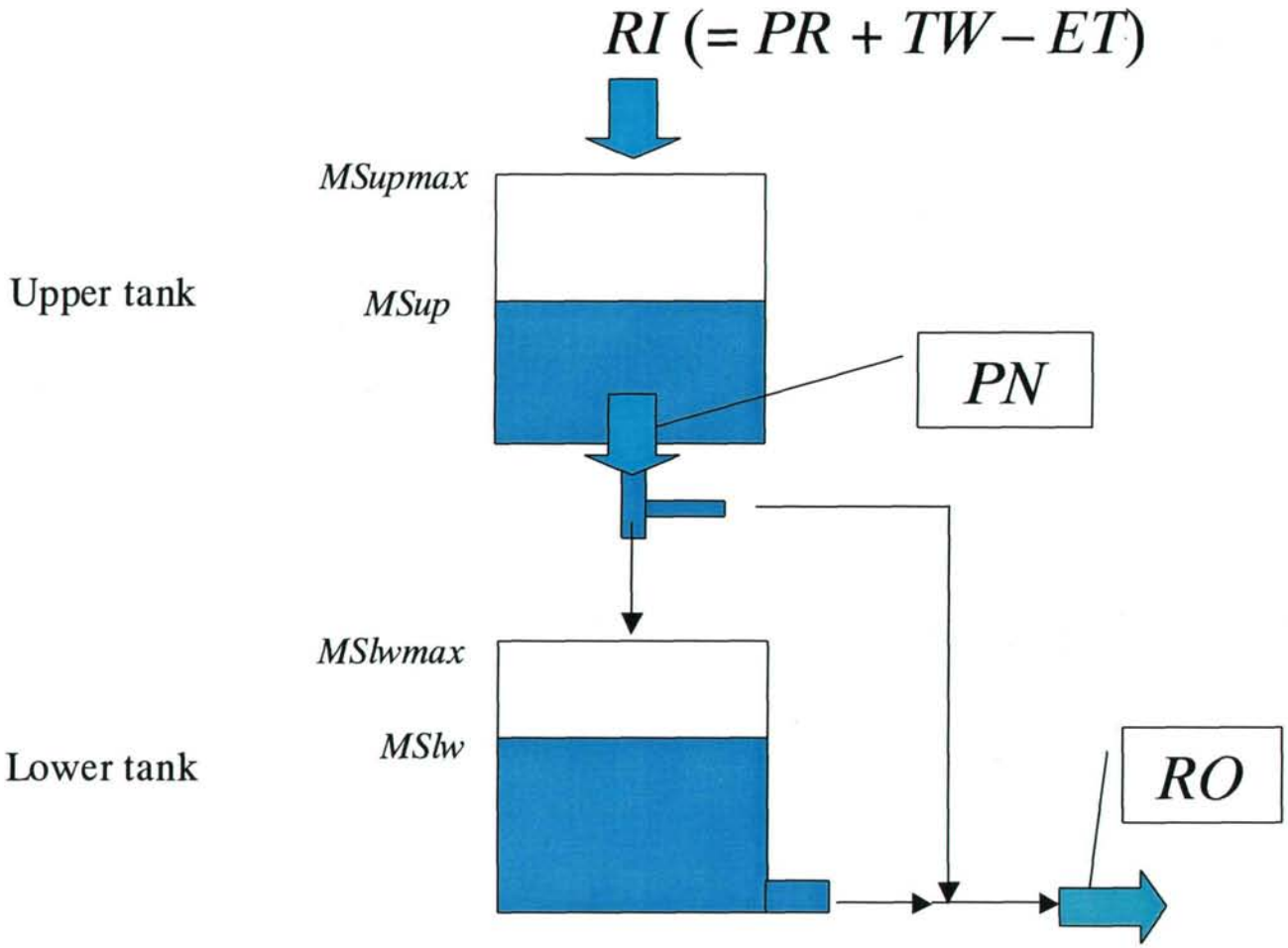

$$
\begin{aligned}
PN &= RI - \Delta MSup \quad (RI - \Delta MSup > 0) \\
&= 0 \quad (RI - \Delta MSup =< 0) \\
RO &= PN - \Delta MSlw \quad (RI - \Delta MSlw > 0) \\
&= 0 \quad (RI - \Delta MSlw =< 0)
\end{aligned}
$$

Figure 5.6. Schematic diagram of runoff and infiltration processes in Sim-CYCLE. *RI* is the inflow derived from precipitation *PR*, thawing snow *TW* and evapotranspiration *ET*. *PN* and *RO* are the penetration and runoff, respectively. *MS* is the soil moisture in the tank. MS_{max} is the storage capacity in the tank. ΔMS is the increment of water storage in the unit time. *up* and *lw* indicate the upper and lower tank, respectively.

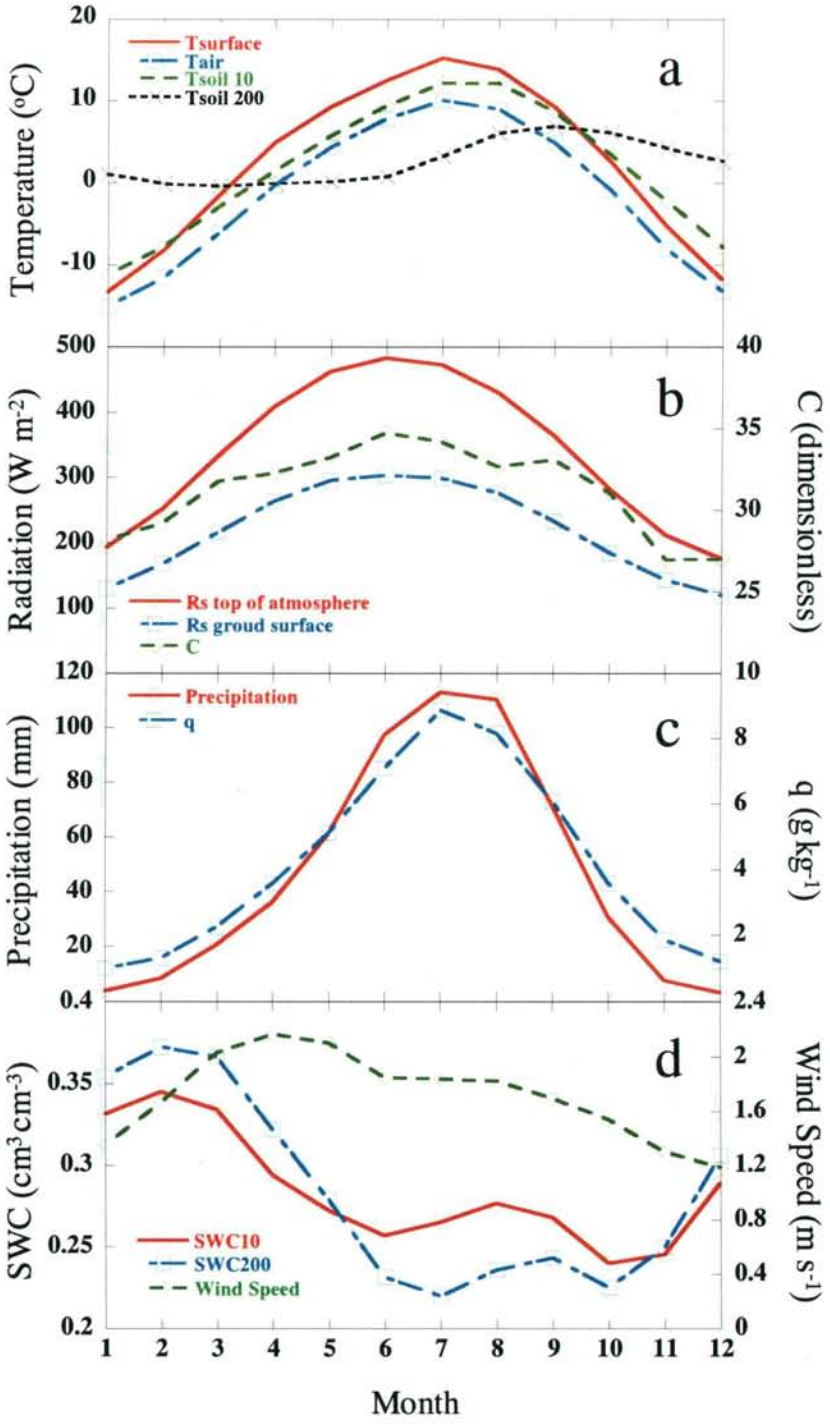

Figure 5.7. Seasonal changes of input climate data in the steady state experiment in (a) ground surface temp. ($T_{surface}$), 2m air temp. (T_{air}) and 10, and 200 cm soil temperature (T_{soil} 10, T_{soil} 200); (b) solar radiation at the top of atmosphere (R_s top of atmosphere) and the ground surface (R_s ground surface), cloudiness (C); (c) precipitation and specific humidity (q); and (d) soil water content at the depth of 10 cm (T_{soil} 10) and 200cm (T_{soil} 200), wind speed.

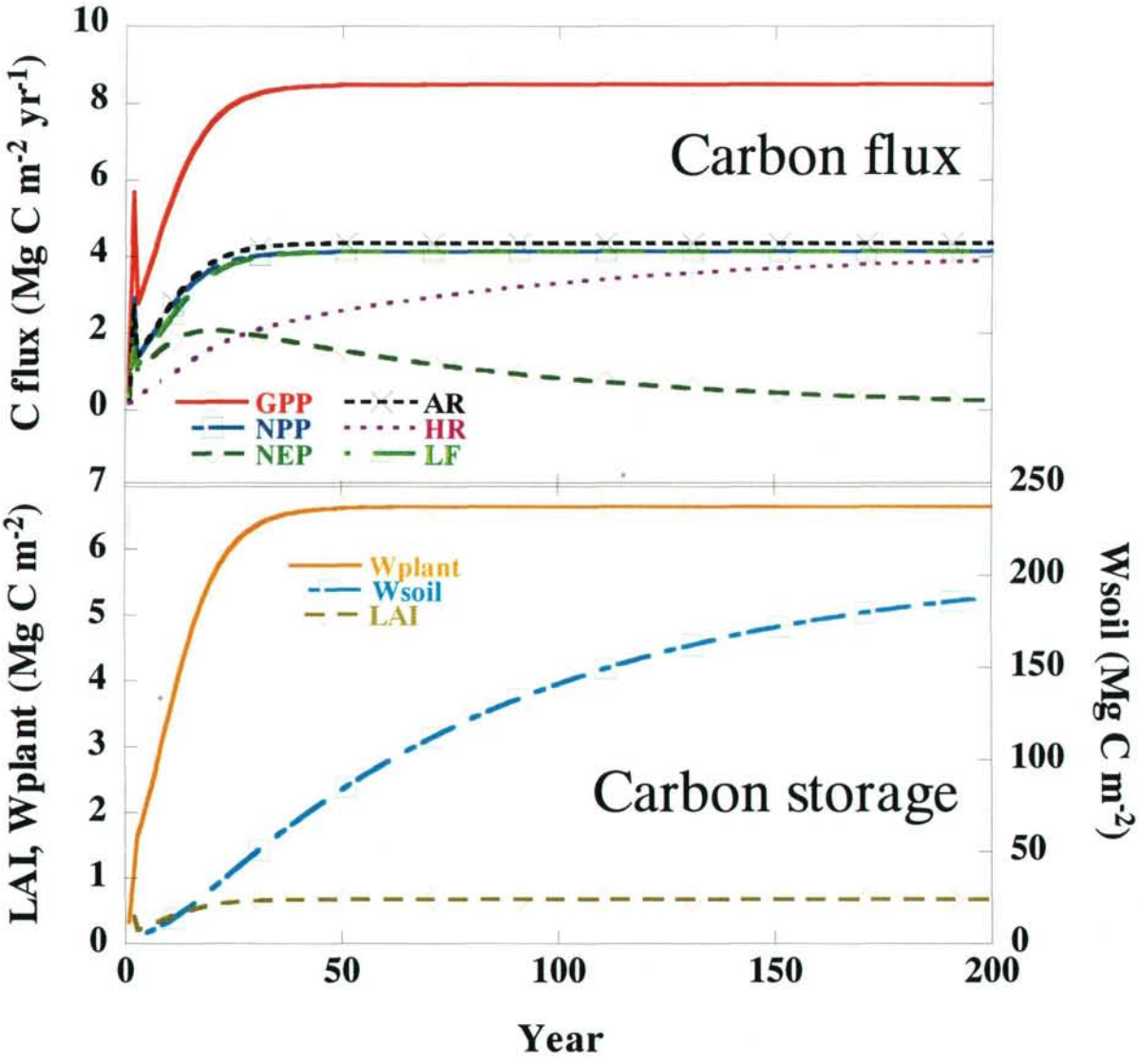

Figure 5.8. Growth of ecosystem carbon fluxes and storages, estimated by Sim-CYCLE equilibrium run. Results for the first 200 years. 1003 yrs are necessary for equilibrium.

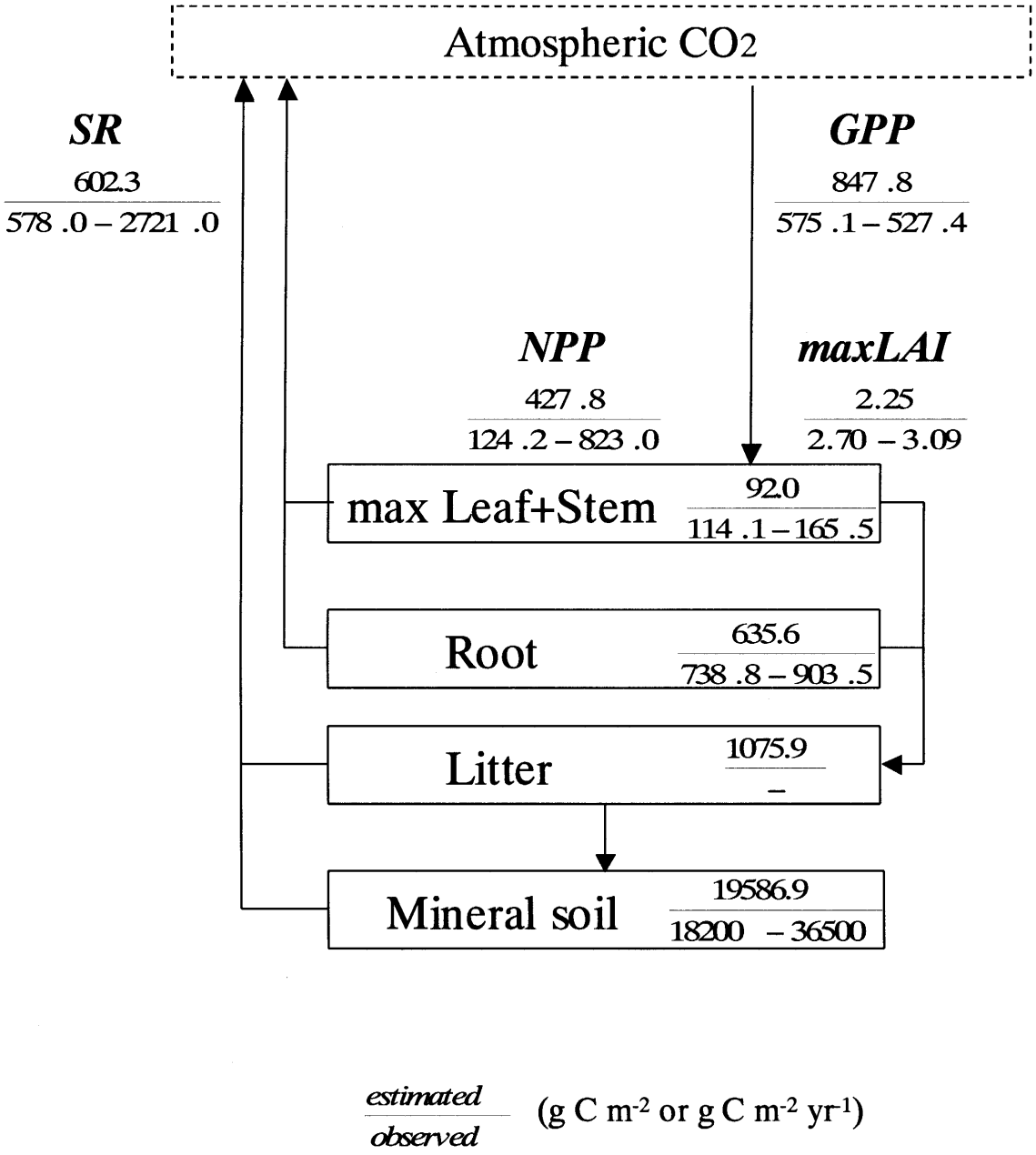

Figure 5.9. Schematic diagram of carbon dynamics in the Haibei alpine meadow ecosystem, estimated by Sim-CYCLE equilibrium run.

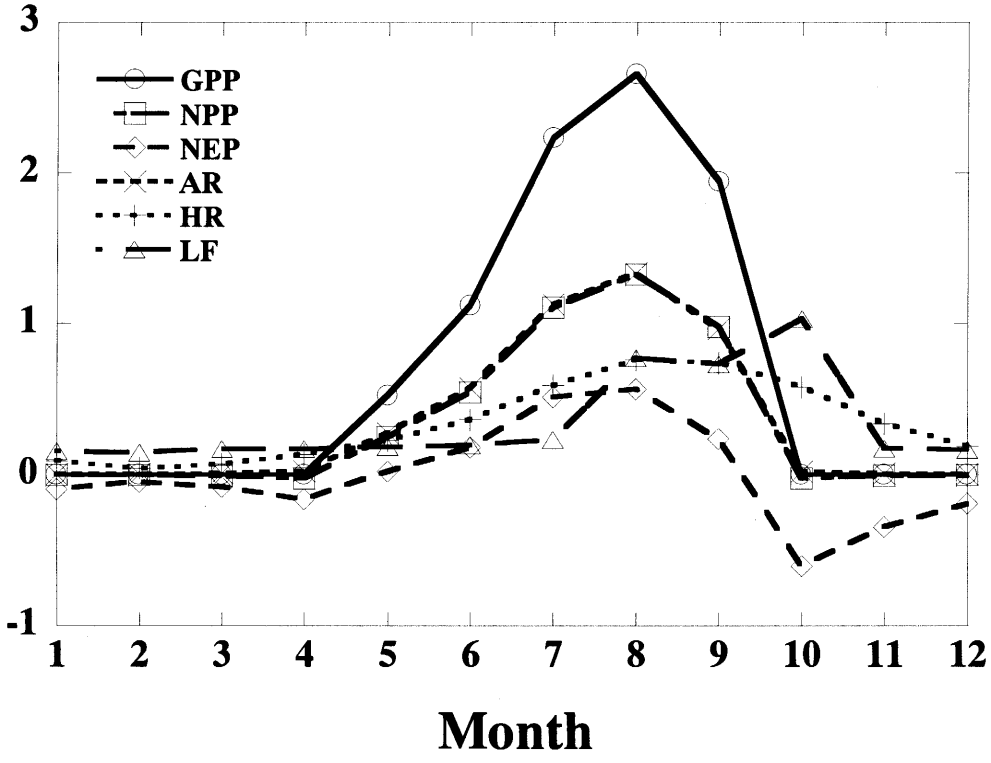

Figure 5.10. Seasonal patterns of carbon fluxes, estimated by Sim-CYCLE equilibrium run

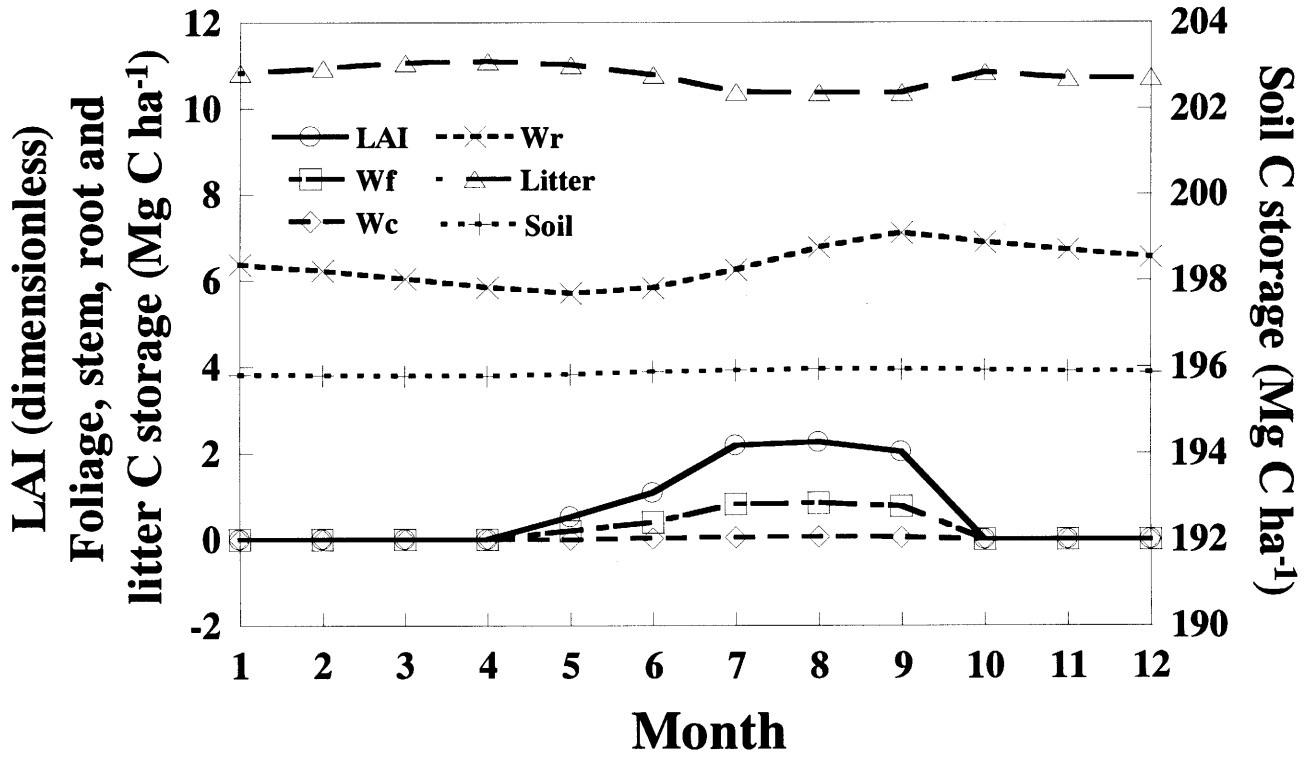

Figure 5.11. Seasonal patterns of carbon storages, estimated by Sim-CYCLE equilibrium run

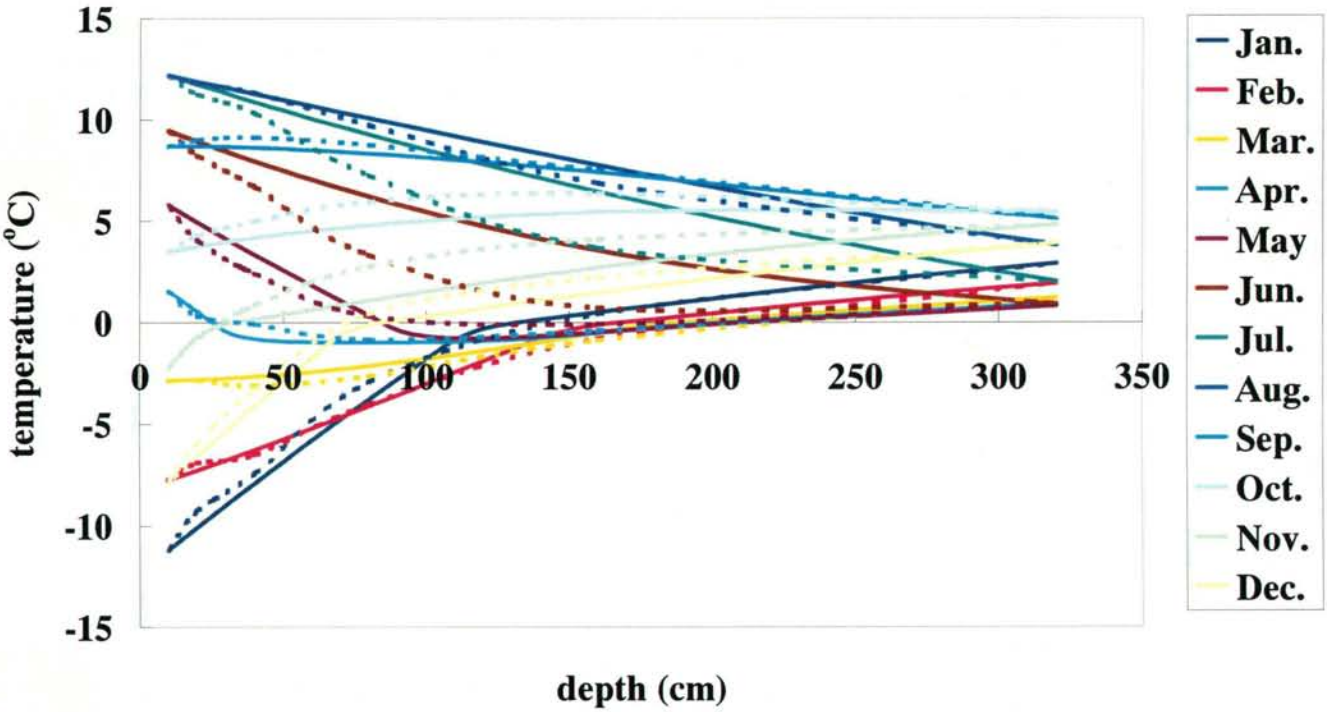

Figure 5.12. Seasonal patterns of soil thermal profiles, estimated by Sim-CYCLE equilibrium run. Solid lines show the estimated profiles and broken lines show the measured profiles.

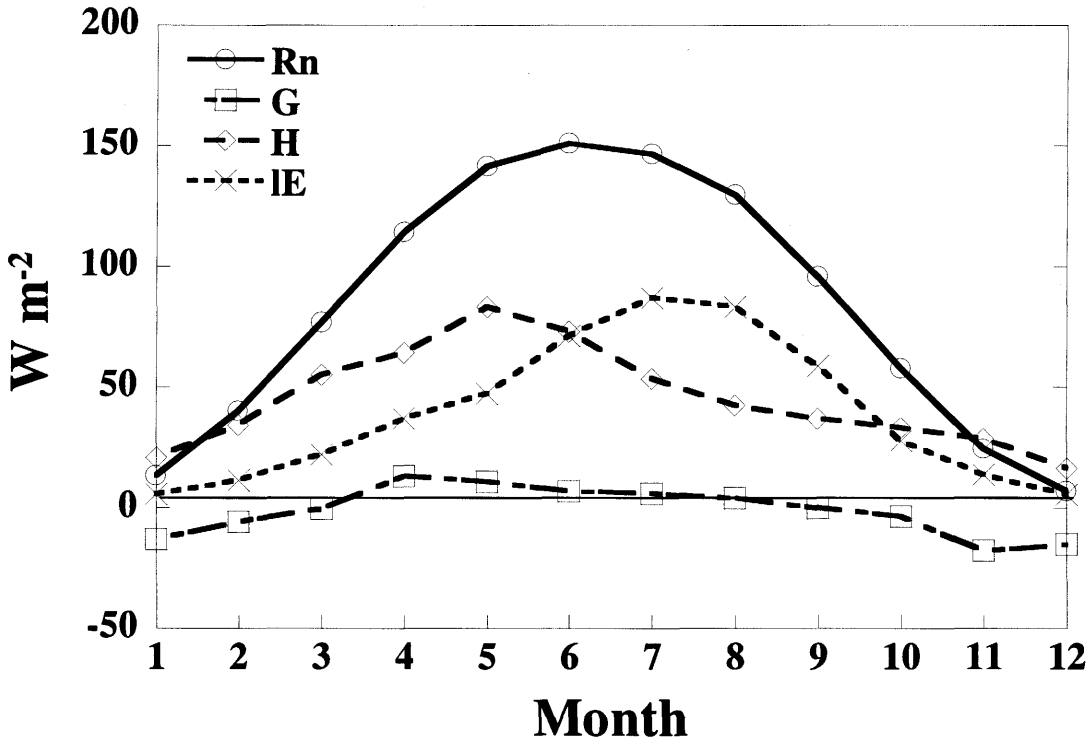

Figure 5.13. Seasonal patterns of heat budgets, estimated by Sim-CYCLE equilibrium run

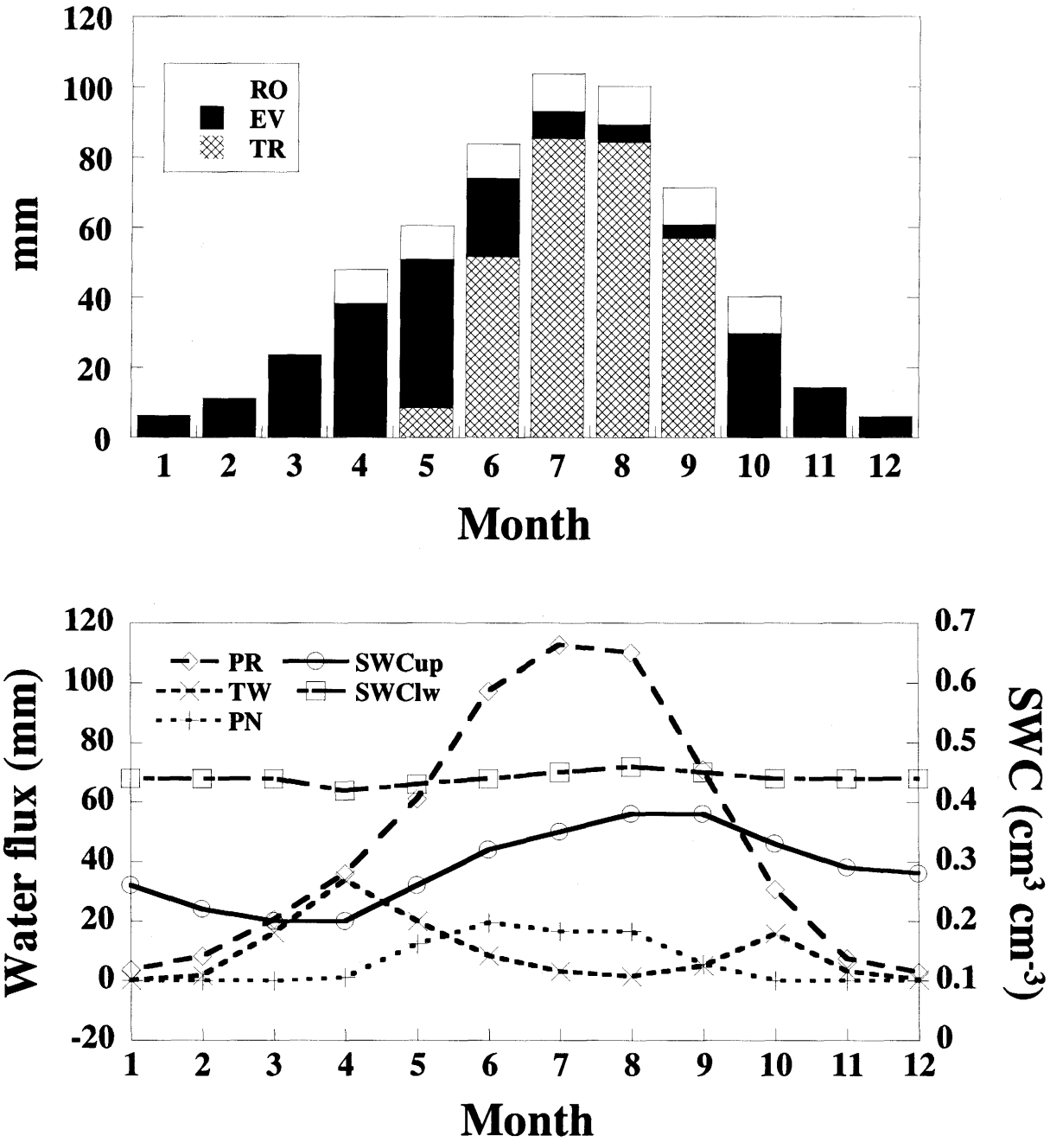

Figure 5.14. Seasonal patterns of water budgets, estimated by Sim-CYCLE equilibrium run

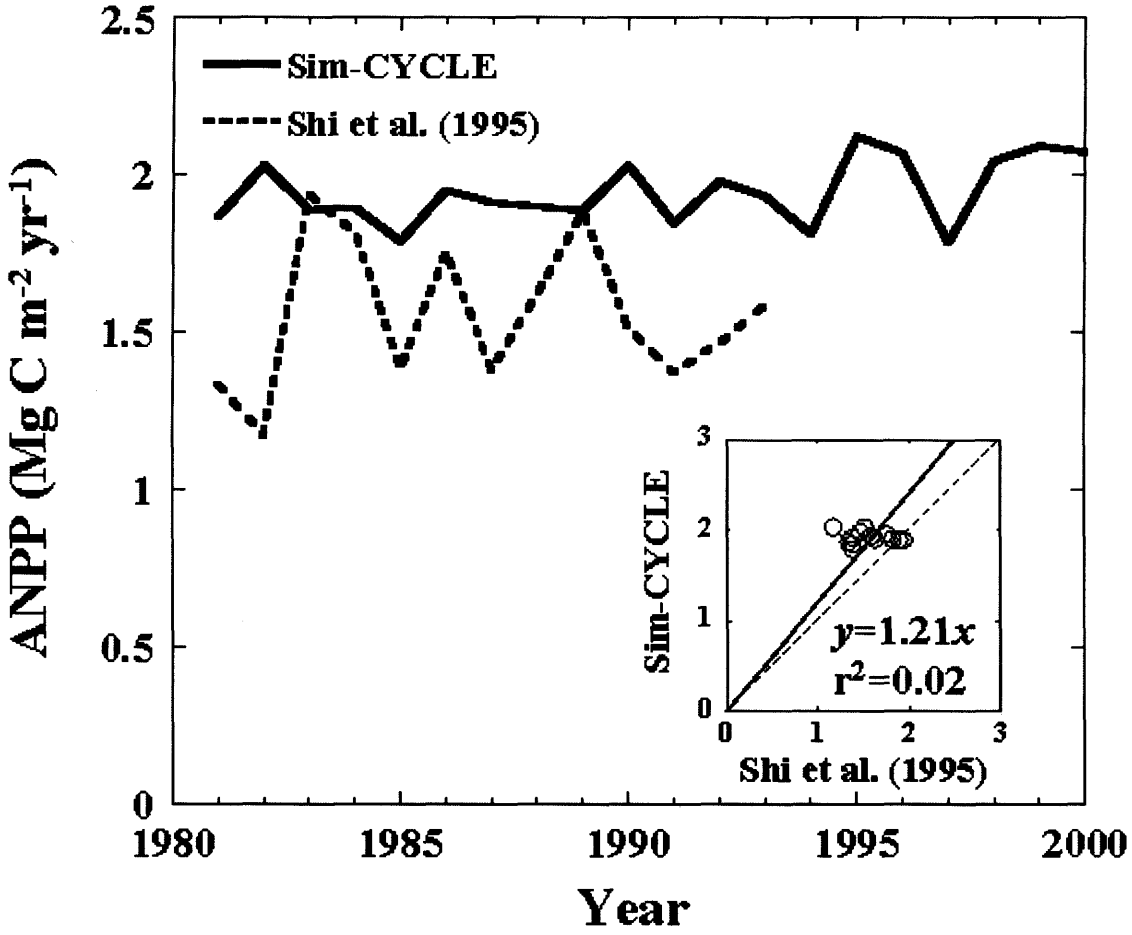

Figure 5.15. Comparisons of the simulated above ground *NPP* (*ANPP*) of Sim-CYCLE transient run and observed values of other studies in the Haibei alpine meadow. RMSE = 0.089 MgC m^{-2} yr^{-1}.

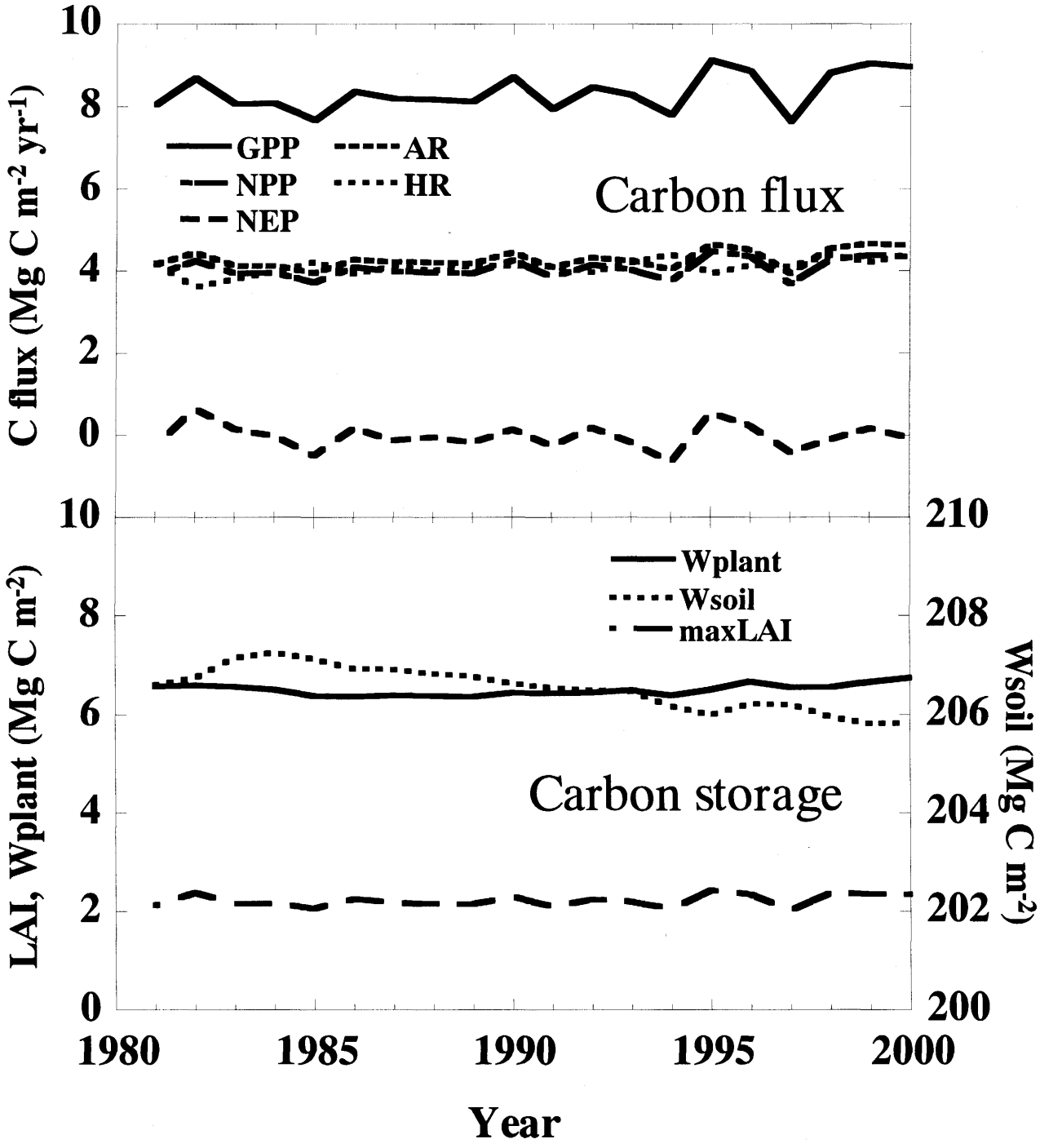

Figure 5. 16. Yearly changes of ecosystem carbon fluxes and storages, estimated by Sim-CYCLE transient run.

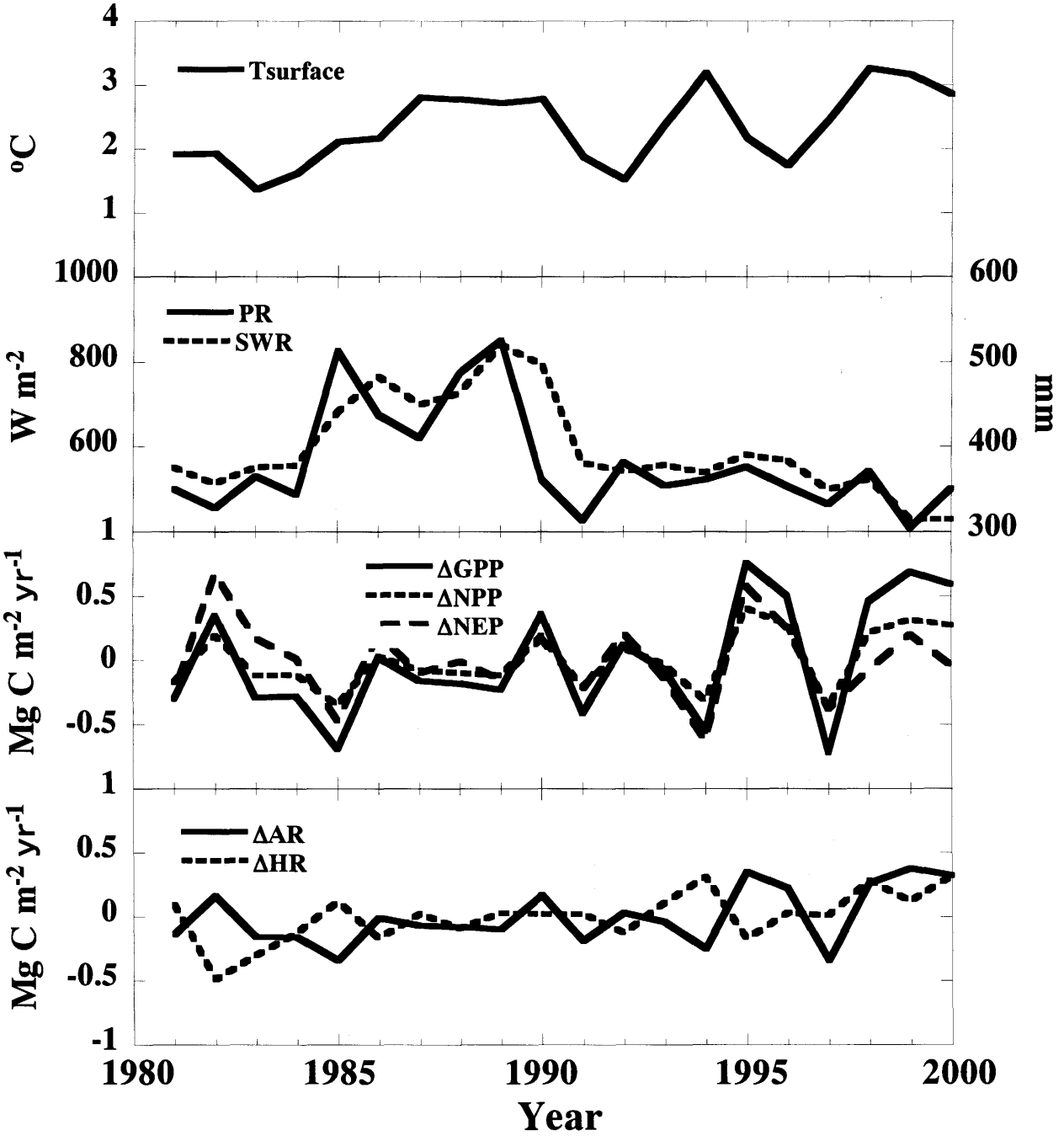

Figure 5.17. Annual climate and anomalies in carbon fluxes.

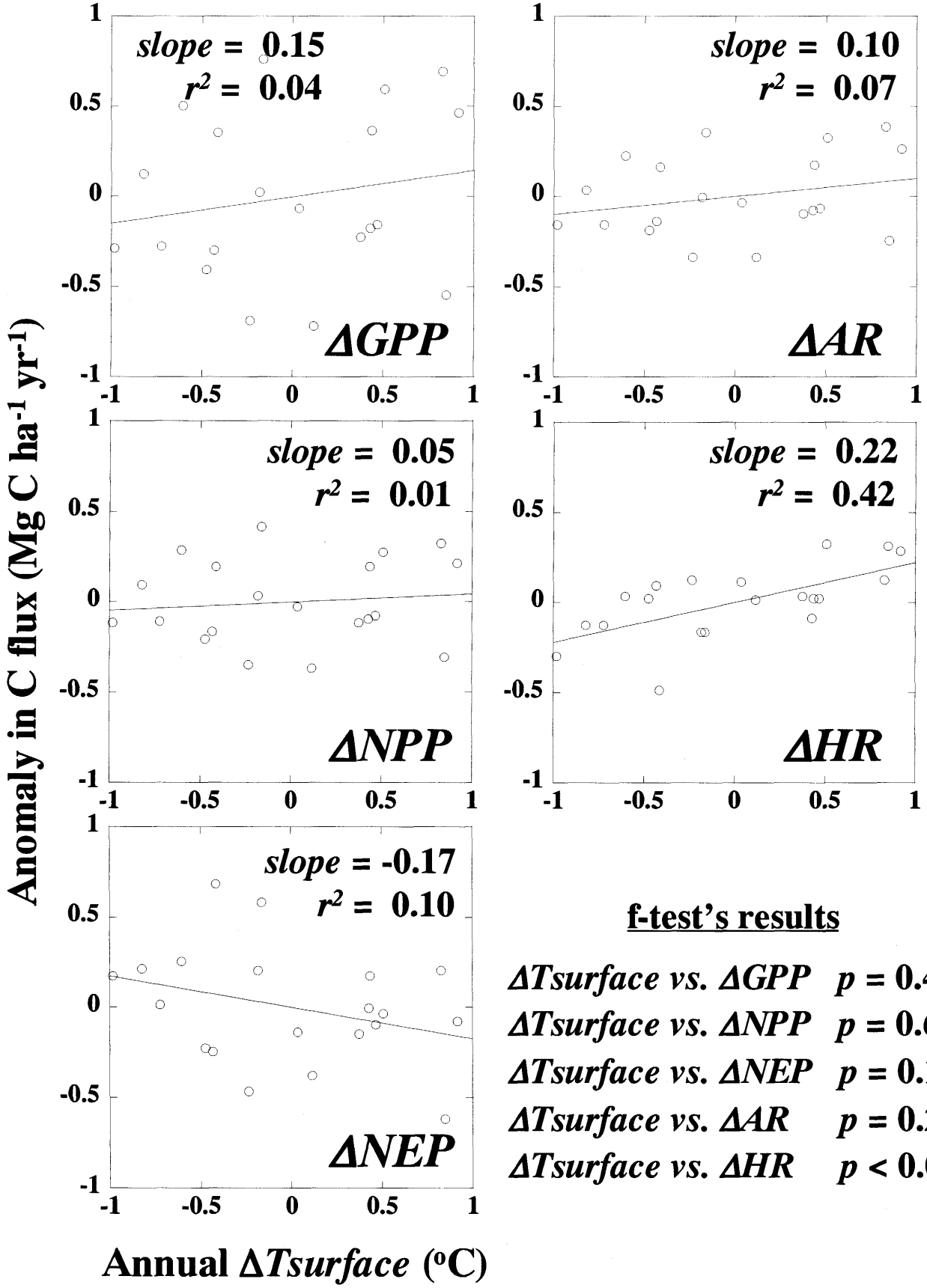

f-test's results

ΔTsurface vs. ΔGPP	$p = 0.4285$
ΔTsurface vs. ΔNPP	$p = 0.6205$
ΔTsurface vs. ΔNEP	$p = 0.1737$
ΔTsurface vs. ΔAR	$p = 0.2716$
ΔTsurface vs. ΔHR	$p < 0.001$

Figure 5.18. Relationships between temperature and carbon fluxes anomalies.

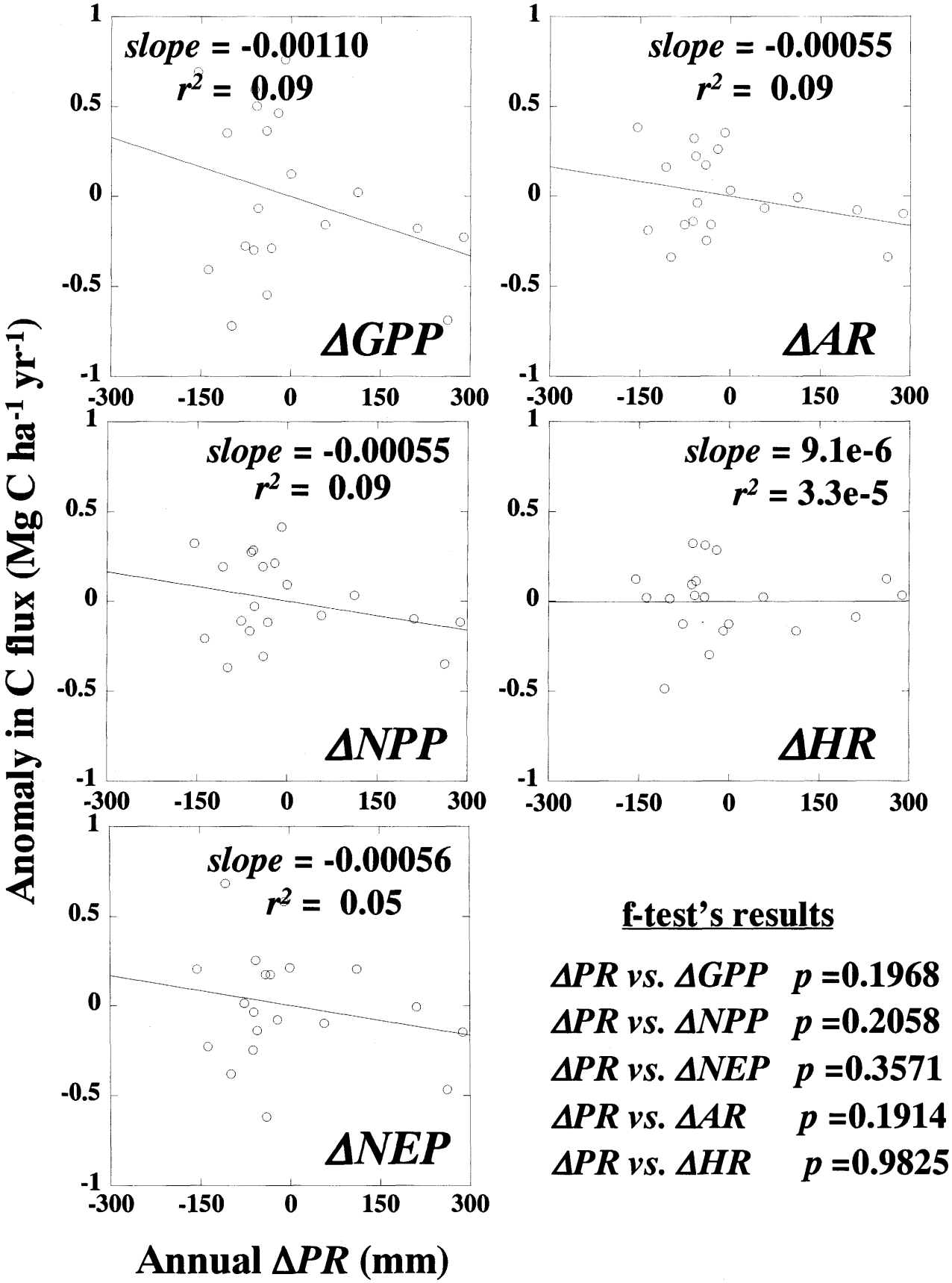

f-test's results

ΔPR vs. ΔGPP	*p* =0.1968
ΔPR vs. ΔNPP	*p* =0.2058
ΔPR vs. ΔNEP	*p* =0.3571
ΔPR vs. ΔAR	*p* =0.1914
ΔPR vs. ΔHR	*p* =0.9825

Figure 5.19. Relationships between precipitation and carbon fluxes anomalies.

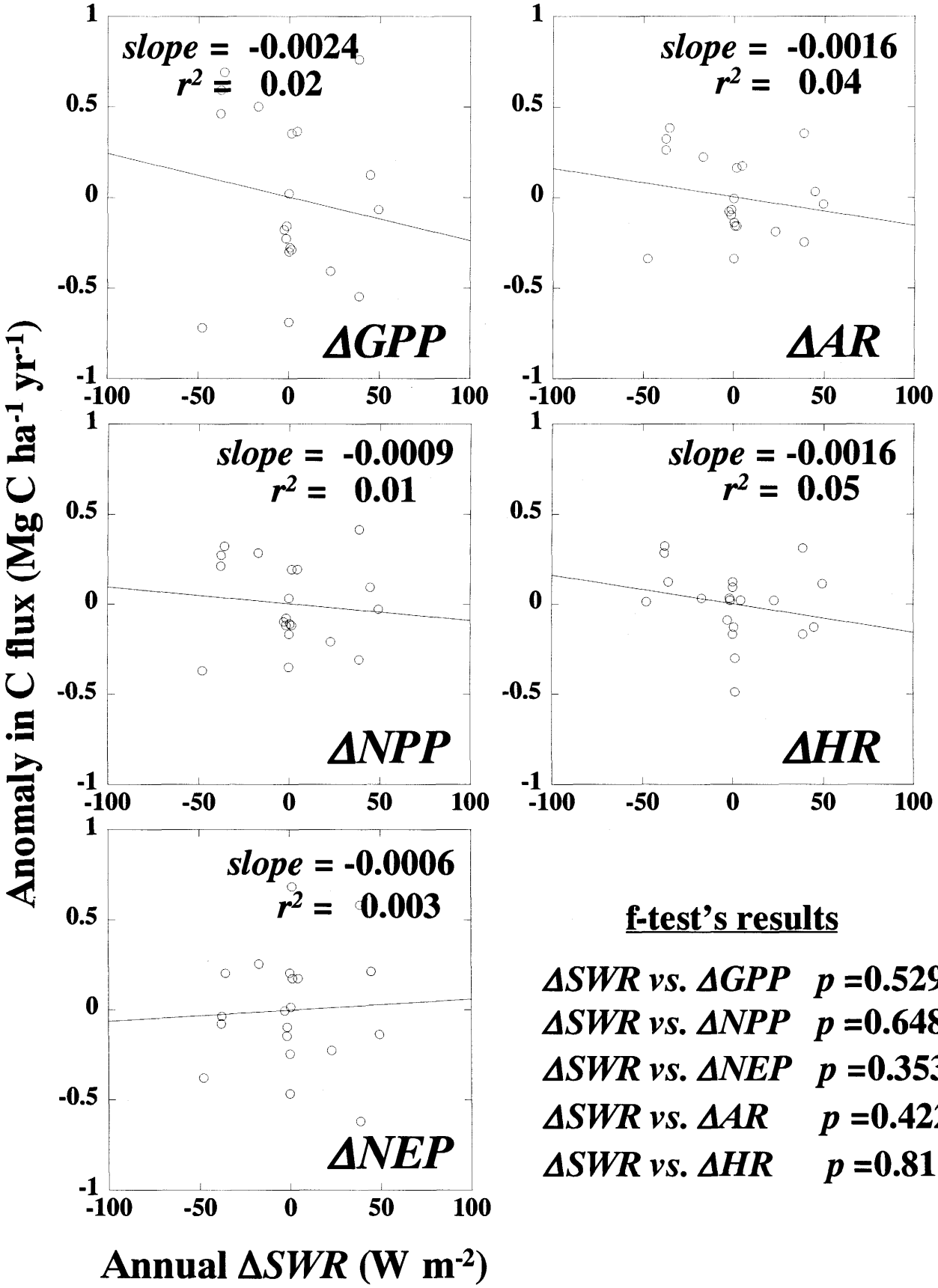

Figure 5.20. Relationships between radiation and carbon fluxes anomalies.

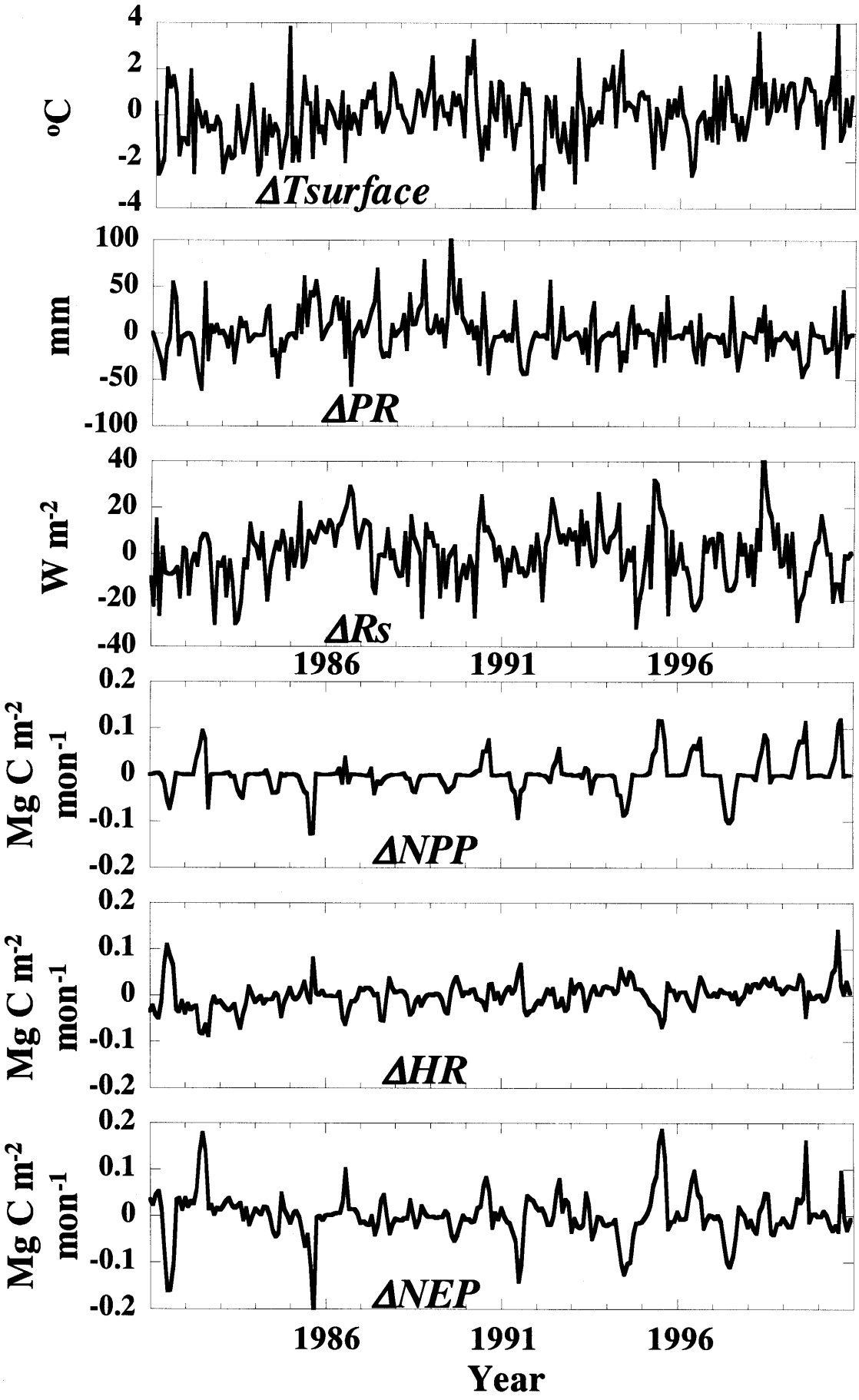

Figure 5.21. Anomalies in monthly climate and carbon flux.

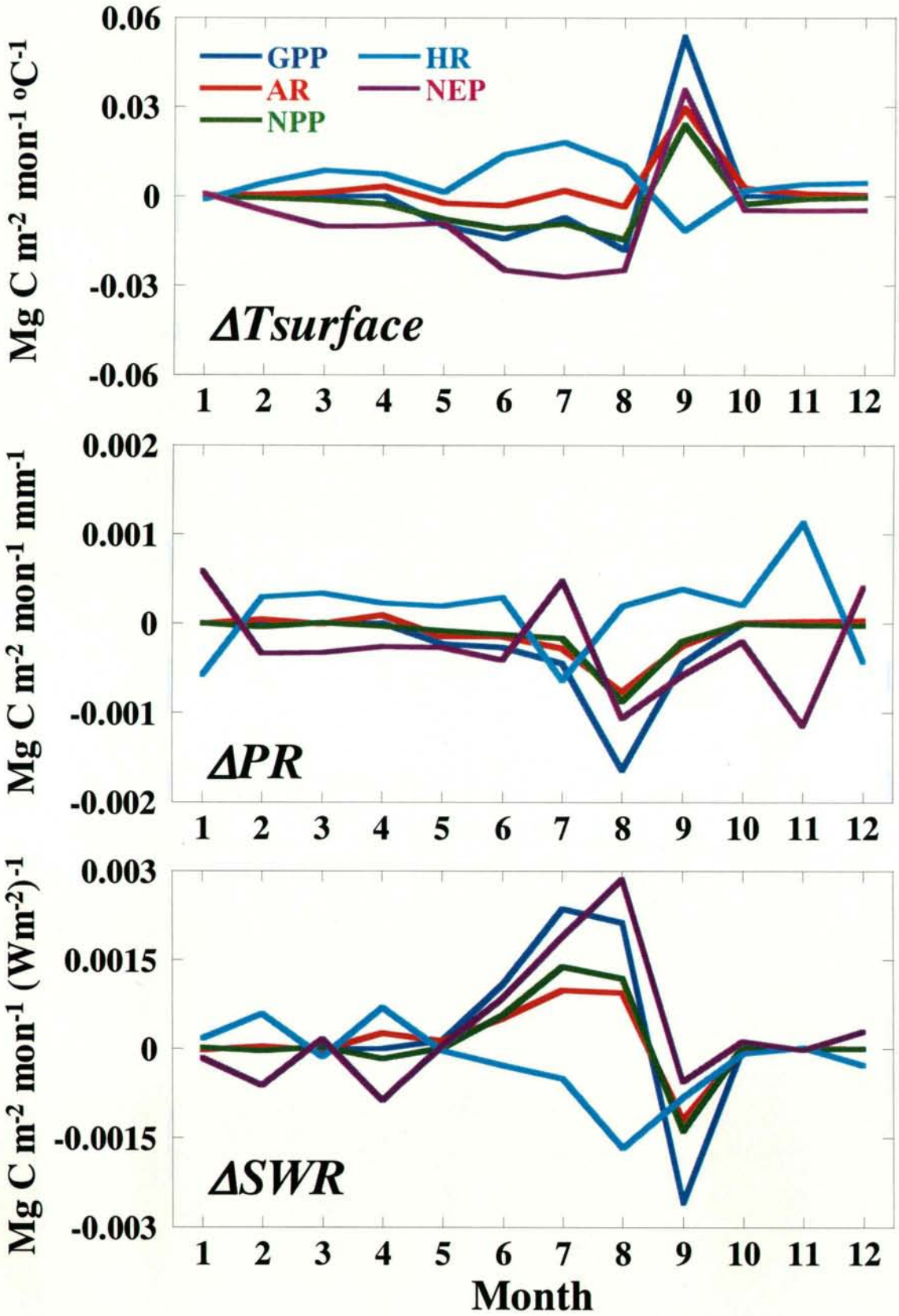

Figure 5.22. Seasonal changes in the slope of regression between temperature, precipitation, short wave radiation and carbon flux anomalies.

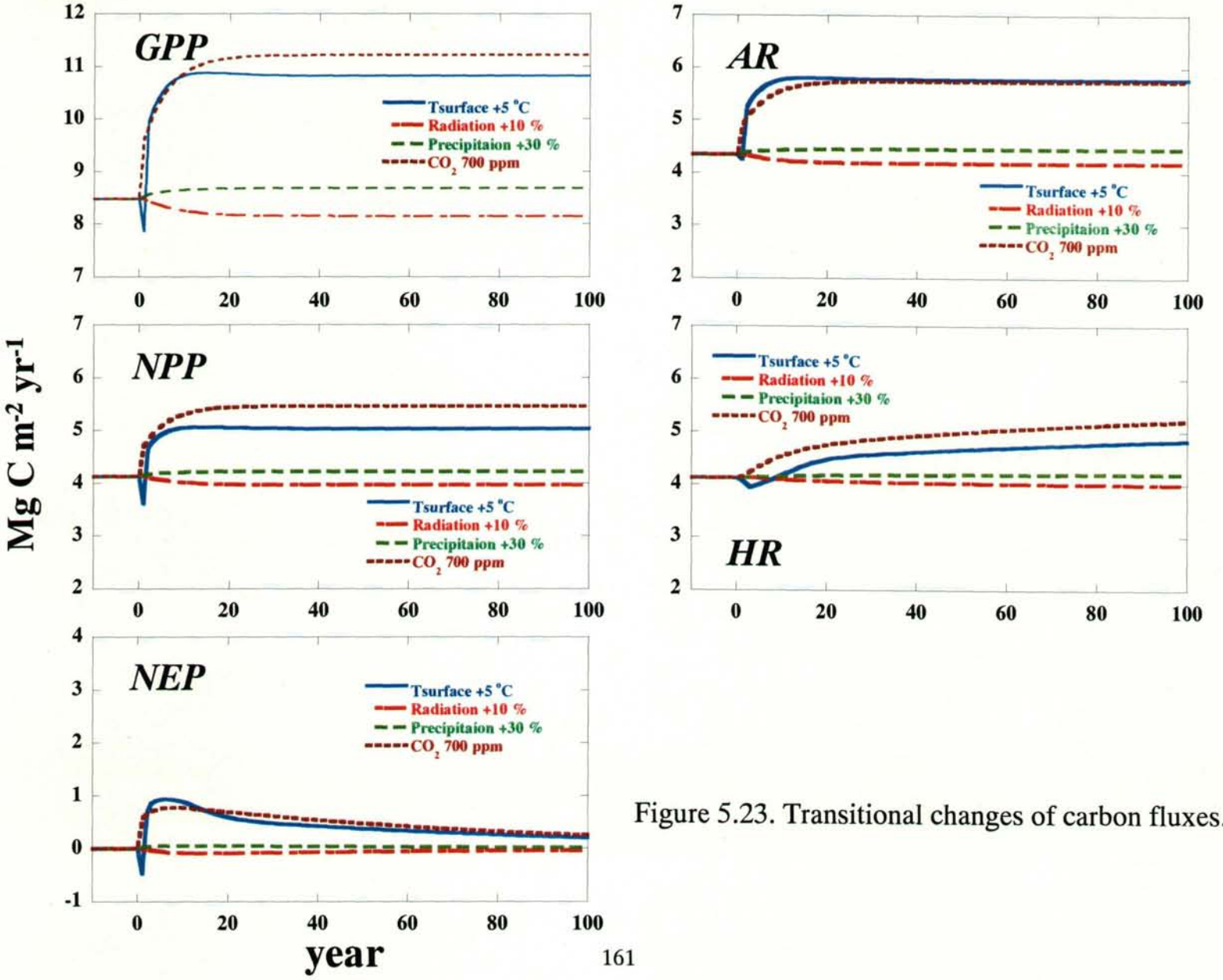

Figure 5.23. Transitional changes of carbon fluxes.

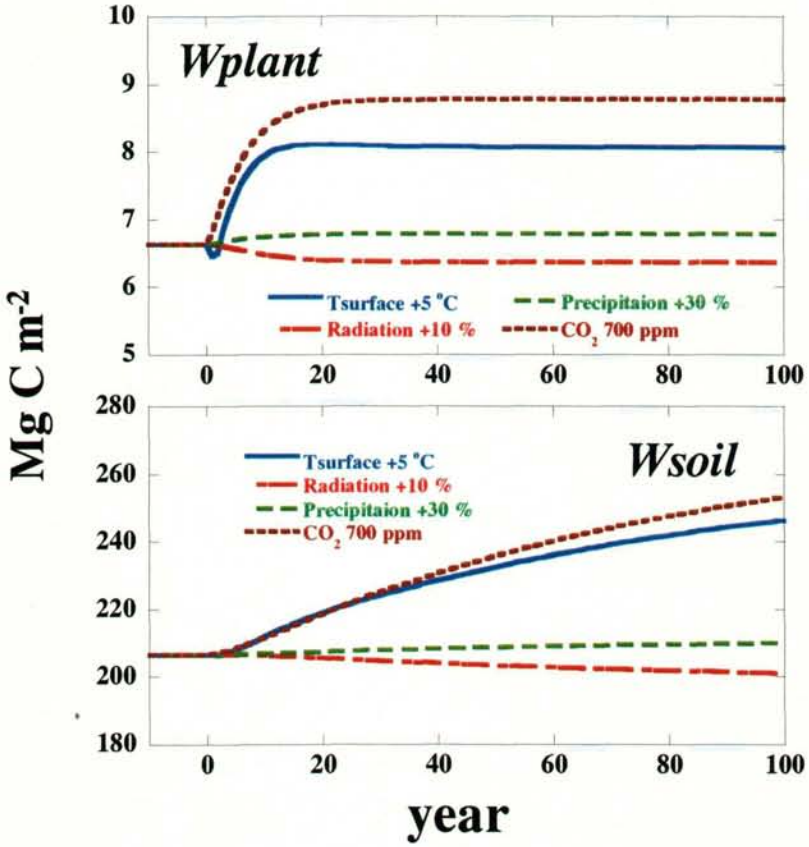

Figure 5.24. Transitional changes of carbon storages.

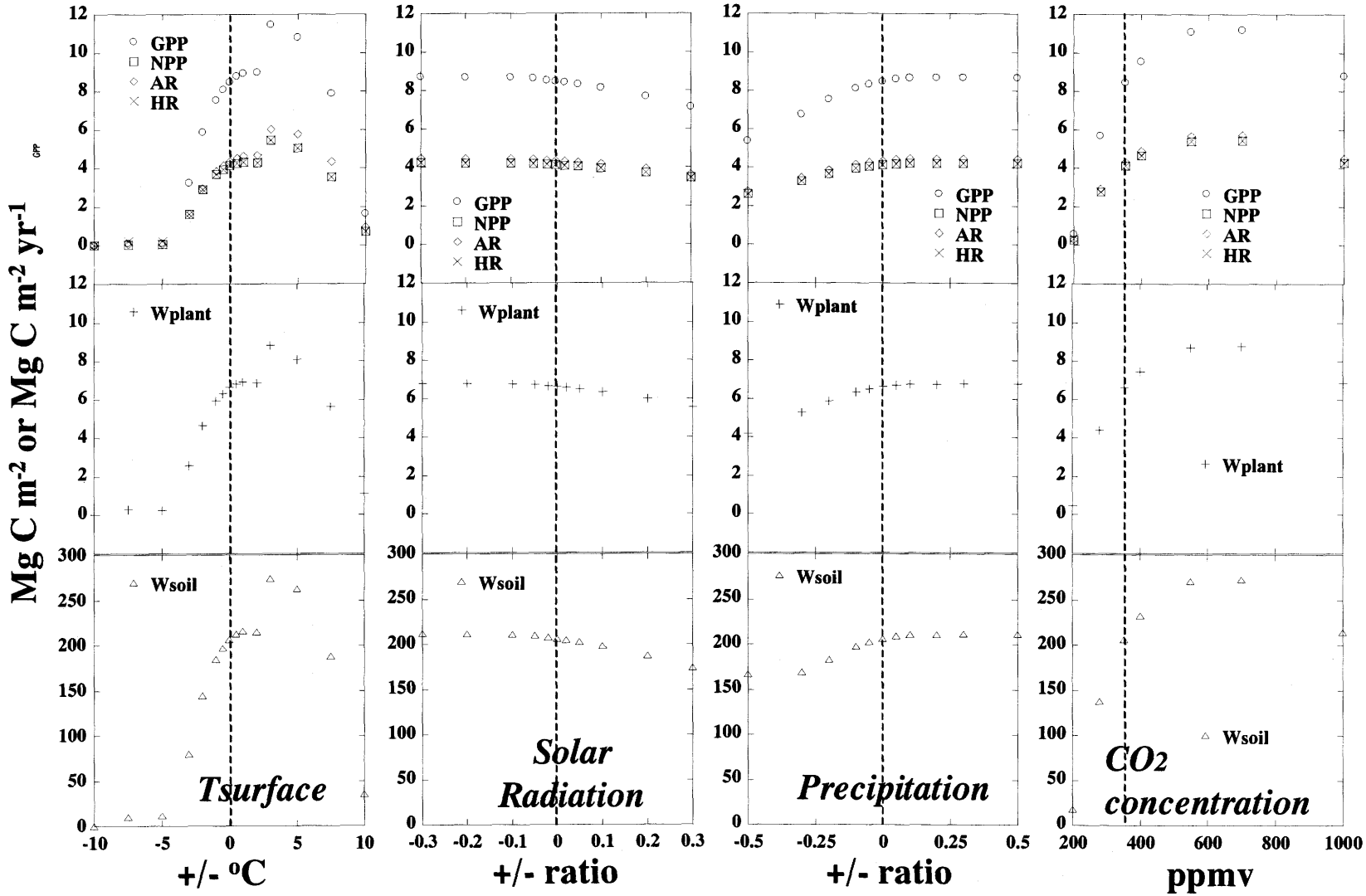

Figure 5.25. Relationship between prescribed environmental changes and equilibrium carbon fluxes

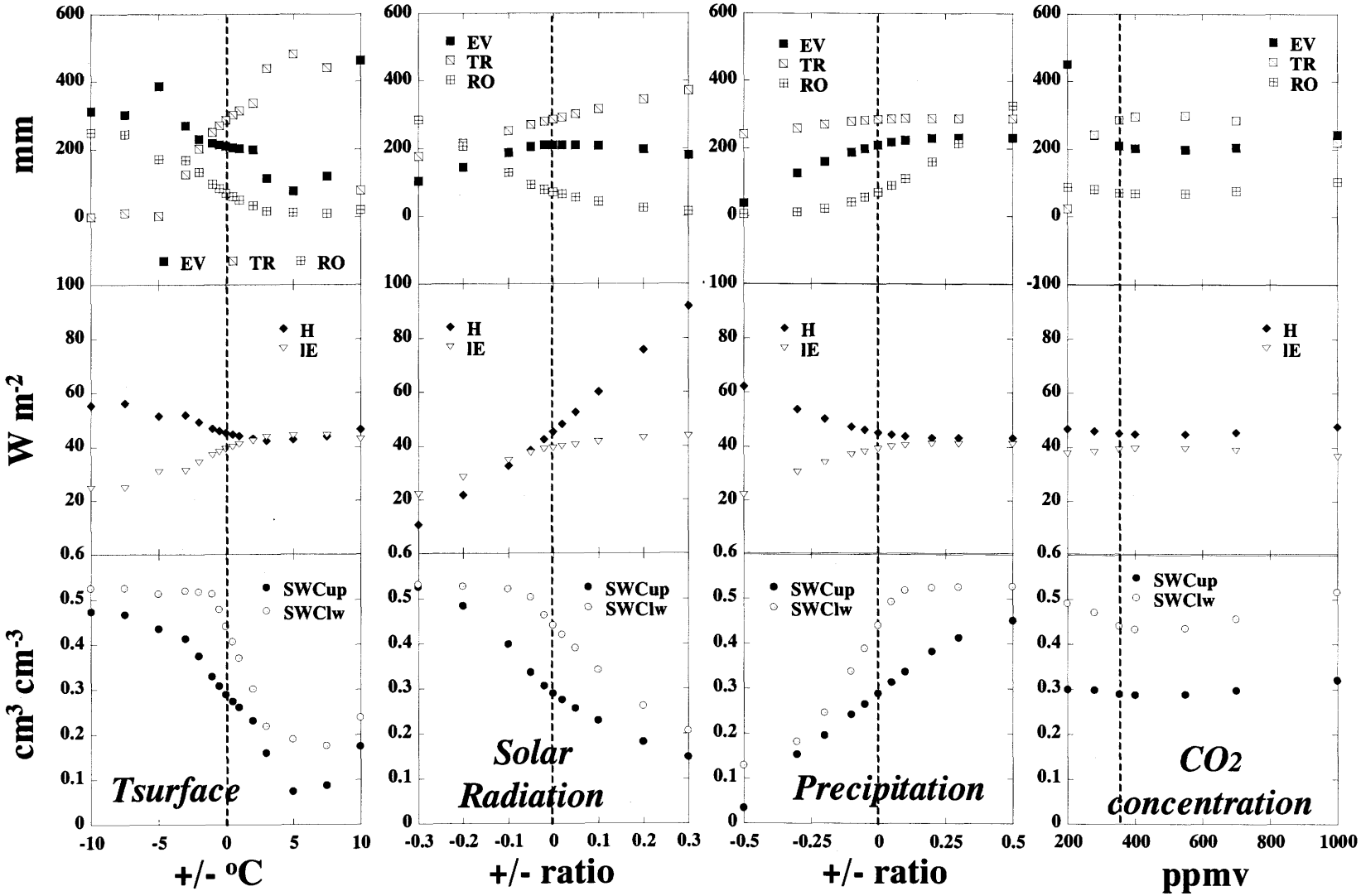

Figure 5.26. Relationship between prescribed environmental changes and equilibrium water, heat fluxes and soil water content.

Chapter 6 General Discussion

6.1. Carbon dioxide assimilation capacity of alpine meadow ecosystem on the Qinghai-Tibetan Plateau

The daily changes of CO_2 exchanges showed the CO_2 uptake in the daytime and CO_2 release in the nighttime in summer and small CO_2 release during all the days in winter in an alpine ecosystem (Fig. 3.30). The seasonal changes of CO_2 exchanges showed the growing season that the ecosystem absorbed CO_2 from May to September (Fig. 4.3). In 2002, the CO_2 uptake during those five months was amounted to 138.4 g C m^{-2}. The CO_2 release during the other seven months was amounted to 59.9 g C m^{-2}. The measurement provided very important information to estimate the annual carbon dynamics.

The maximum daily CO_2 uptake (3.9 g C m^{-2} day^{-1}) was smaller than other grassland ecosystem at a similar latitude, although the maximum *LAI* was larger than those reported for these ecosystems (Sec. 4.4.3). The low temperature seemed limit the photosynthetic activity and thus the net CO_2 uptake of the alpine ecosystem. The annual CO_2 uptake (78.5 g C m^{-2} yr^{-1}) in 2002 was lower than those reported from other warmer ecosystems, e.g. temperate and tropical ecosystems, but was similar to those for other cool ecosystem, e.g. alpine and boreal forest ecosystems (Sec. 4.4.3). The low temperature shortened the growing season and thus may decrease the net CO_2 uptake of the alpine meadow ecosystem.

The eddy covariance measurement indicated that this ecosystem was a CO_2 sink, amounted to 78.5 g C m^{-2} yr^{-1} in 2002. On the other hand, the transition experiment for 1981-2000 using Sim-CYCLE showed that the annual *NEP* ranged from -70 to +70 g C m^{-2} yr^{-1} in the 20 years widely (Fig. 5.16). The measured annual CO_2 uptake is close to the fluctuating range derived from model analysis, although this may contain the estimation errors caused by the energy imbalance and the gap-filling methods. However it is not enough to judge whether this ecosystem is a CO_2 sink or source in average from the current measurement and model analysis. This is mainly due to the limited observation data. Furthermore multi-year data acquisitions of the CO_2 exchanges are therefore required.

6.2. The response of the CO_2 exchanges in alpine meadow ecosystem to the characteristic environments on the Qinghai-Tibetan Plateau

The Qinghai-Tibetan Plateau is characterized by extremely intensive sunlight, low temperature, little precipitation and limited plant growth. How do they affect the carbon dioxide uptake in this ecosystem? Which do they have a good influence or bad influence on it? In this chapter, the site-specific responses of CO_2 exchange to four environmental factors, light, temperature, water and biology, were summarized and discussed in the followings.

Light: In the diurnal changes, the light responses of the afternoon CO_2 uptake are lower than those of the beforenoon (Fig. 3.31 and 3.33). In the grassland ecosystems with low *LAI*, because of the low interception of intensive sunlight by vegetation, the soil surface temperature could be very high, which will further result in the increase of soil CO_2 efflux as estimated in Fig. 3.35. In addition, the high *VPD* might cause the closure of stomata and thus suppress CO_2 uptake. Such stomatal response to increased *VPD* has been observed in grassland (Verma et al., 1992) and forest ecosystems (Jarvis et al., 1997; Baldocchi and Vogel, 1997). In the alpine meadow, the increase of R_{canopy} is correlated with the decrease of λE but with the increase of *VPD* (Fig. 3.32). The amplitude of the diurnal *SWC* change was small and may play a very limited role in ecosystem respiration (Fig. 3.32b). The photosynthesis (i.e. *GPP*) in response to high *PPFD* did not differ between the beforenoon and the afternoon in this study (Fig. 3.35). It was concluded that the increasing air and soil temperatures accelerate plant respiration and soil organic matter decomposition, and as a result suppress the net CO_2 uptake flux in this study.

Extremely intensive sunlight may induce down-regulation of photosynthesis in plants living in this alpine ecosystem. The depression of photosynthesis (i.e. *GPP*) increment in response to *PPFD* increasing was founded both in the beforenoon and the afternoon in this study (Fig. 3.35). Cui et al. (2003) investigated the leaf gas exchange and fluorescence emission in response to the changes in *PPFD* and leaf surface temperature for two Asteraceae herbaceous

species at same alpine meadow. They showed that under natural environmental conditions, apparent photoinhibition, indicated by reduced electron transport (*ETR*), was evident at high *PPFD* for both species. They also showed that the thermal dissipation, indicated by enhanced non-photochemical quenching (*NPQ*), which is associated with the xanthophylls cycle (Deming-Adams et al., 1996), played an essential role in photoprotection at low leaf temperature in the morning. At higher leaf temperatures, photorespiration was reported to play a more prominent role (Park et al., 1996; Streb et al., 1998; Manuel et al., 1999). Cui et al. (2003) showed the significant reduction of *ETR* in *S. katochaete* in the afternoon with high leaf temperature and expected that more than two-thirds of the photochemical energy was flown through the photorespiration pathway at a *PPFD* above 1800 μmol m^{-2} s^{-1} if there were no other significant electron acceptors. Thus, the photoinhibition and photoprotection was evident at the high *PPFD* for two Asteraceae herbaceous species, which is non-dominant species. Further research about the photoinhibition and photoprotection in dominant species is necessary to clarify the representative response to intensive sunlight.

In the seasonal changes, the daily *NEP* was correlated to daily *PPFD* positively in the growing season (Fig. 4.4), however, those linear relationships were slight weak. Gu et al. (in press, 2003) showed that for the same *PPFD*, the *NEP* was significantly higher on cloudy days than on clear days at the same site. Law et al. (2002) also founded that the *NEP* is more positive for cloudy condition than for clear sky condition in boreal aspen and Scots pine forests. Gu et al. (2002) suggested that diffuse radiation result in higher light use efficiency in plant canopies and has much less tendency to cause canopy photosynthesis. It is possible that the light quality caused the weakness of the linear relationship between daily *NEP* and *PPFD*. These findings call for different treatments of diffuse and direct radiation in models of ecosystem carbon cycle.

Temperature:

Respiration by autotrophs and heterotrophs was correlated positively with temperature in the seasonal changes (Fig. 4.5) and interannual changes (Fig. 5.18). The exponential coefficient

for the relation corresponds to a Q_{10} of 3.21 (Fig. 4.5), higher than the value of 2.0 that is typically used as a default in modeling respiration (Law et al., 2002).

The annual *GPP* of 575 g C m^{-2} (Table 4.5) was lower than those of boreal coniferous forest (723–959 g C m^{-2} y^{-1}) and Colorado subalpine coniferous forest (831 g C m^{-2} y^{-1}; 3050 m) at similar elevations, and much lower than that of tropical forest (3249 g C m^{-2} y^{-1}), but within the range for temperate ecosystems, including forests and grasslands (542–1924 g C m^{-2} y^{-1}; average, 1262 g C m^{-2} y^{-1}; Falge et al., 2002). The daily *GPP* of the study site (3.59 g C m^{-2} d^{-1}, Table 4.5) was similar to those of boreal evergreen forest and Colorado subalpine coniferous forest (4.6, 4.4 g C m^{-2} d^{-1}, respectively), although slightly lower than those of temperate coniferous forest and C_3 crops and grassland (5.7–6.9 g C m^{-2} d^{-1}). Thus, although our alpine meadow ecosystem has a daily CO_2 assimilation equal to that of a Colorado subalpine forest ecosystem, it has a lower annual *GPP* because of the restricted growing period, which was caused by low temperature.

The annual sum of *NEP* (78.5 g C m^{-2} y^{-1}, Table 4.5) was close to that of the Colorado subalpine coniferous forest (71 g C m^{-2} y^{-1}), although substantially lower than that of grassland (231.3 g C m^{-2} y^{-1}) and boreal ecosystems (121.4 g C m^{-2} y^{-1}). The daily *NEP* of the study site (0.49 g C m^{-2} d^{-1}, Table 4.5) was similar to that of the Colorado subalpine forest (0.38 g C m^{-2} d^{-1}). Although our alpine meadow ecosystem has a lower annual *GPP* than that of the subalpine forest ecosystem, it has a comparable annual *NEP*. It is assumed that not only low temperature but also small biomass suppresses the ecosystem respiration; as a result, this ecosystem may sequester substantial amount of C. Thus, much of the dynamic response of processes to temperature is lost in annual estimates, because of factors such as phonological influences.

Moisture:

In the seasonal changes, the CO_2 efflux increased as *SWC* decreased, and a CO_2 release of 0.94 μmol m^{-2} s^{-1} was maintained even in saturated conditions. This response to *SWC* has been observed in tundra under near-saturation (Oechel et al., 1998). Figure 4.6 might partly show the effect of increasing temperature. However, it is considered that the temperature

increment is not enough to increase respiration, and the depression of *SWC* from saturation to adequate contributes significantly to CO_2 efflux. This is an opposite response to that in relatively dry grassland (Hunt et al., 2002). It is assumed that the transition from aerobic condition (adequate moisture) to anaerobic condition (saturation) contributes to the rise in plant root and microbial activity. It suggests that ecosystem respiration in this meadow has an optimal *SWC* of approximately 0.3. Many respiration models mostly neglect the decline in microbial activity at high soil water content (Paul, 2001). So this result suggests that respiration depends on *SWC*.

In the diurnal changes and interannual changes, the apparent relationships between moisture factor and carbon dynamics were not founded. This suggested that alpine meadow ecosystem was advantaged in available water, although annual precipitation is not plentiful, because of low temperature.

Biology:

The linear regression slopes of $NEP_{daytime}$ against *PPFD* changed with the changes in the *LAI* (Fig. 4.4). GPP_{max} is positively related to *LAI* (Fig. 4.10a). RUE_{GPP} and WUE_{GPP} also tended to increase as *LAI* increased (Figs. 4.10b, c). These results suggest that *LAI* determines the ecosystem capacity for assimilation and resource requirements in the seasonal changes. The *LAI* also seems the major factor causing the increase of ecosystem CO_2 uptake in interannual changes. The linear regression slopes of $NEP_{daytime}$ against *PPFD* were higher for August 2001 than August 2002 (Fig. 4.4), probably due to higher CO_2 uptake rate and/or lower rate of ecosystem respiration. The *LAI* was 3.1 in August 2001 and 2.6 in August 2002.

In general, seasonal changes in respiratory processes are controlled by climate more strongly than by biological factors (Falge et al., 2002). However, at this study site, R_{emax}, which reached the maximum in autumn (Fig. 4.8), may be associated with above- and below-ground biomass, which reached the maximum at the same time (Fig. 3.24).

The maximum CO_2 uptake (–10.8 μmol m^{-2} s^{-1}) at our site has lower potential of CO_2 uptake and release than C_4 grasslands, but similar potential of net CO_2 uptake to alpine conifer

forest because of its equivalent uptake potential with lower release potential. The *Kobresia humilis* meadow had relatively high *LAI* (~3.1) with low aboveground biomass (ca. 300 g m^{-2}). With a similar *LAI* to our study site, the aboveground biomass in a grassland in Oklahoma was reported to be as high as 800 g m^{-2}. The lower ratio of aboveground biomass to *LAI* in the *K. humilis* meadow might have been due to the low shoot system in the alpine meadow, which resulted from the relatively greater abundance of broad-leaved species and the low canopy height. The high *LAI*, on the other hand, suggests a likely contribution to the high belowground biomass in the alpine meadow. The belowground biomass was 6-7 times higher than the aboveground biomass (e.g. 1892 g d.w. m^{-2} on 11 August 2001; unpublished data). This particular allocation pattern of plants may favor high soil carbon storage in the alpine ecosystem. Although the CO_2 uptake was not high, the daily net ecosystem carbon gain reached a fairly high value under clear weather conditions in August 2001. One of the reasons could be the low nighttime temperature (e.g. near freezing air temperature 2.2 °C) that limited ecosystem respiration. It also could be the low maintenance respiration due to low aboveground biomass in the alpine meadow (Table 3.2).

The maximum NEP_{total} of our site (3.9 g C m^{-2} d^{-1}; Table 3.2) was 20-55% less than those of tallgrass prairies in Kansas and Oklahoma, USA (4.9-8.4 g C m^{-2} d^{-1}, Kim et al., 1992; Ham and Knapp, 1998; Suyker and Verma, 2001). However, seasonal maximum was almost four times larger than that of a subalpine conifer forest in Colorado (1.0 g C m^{-2} d^{-1}; Monson et al., 2002) at similar altitude (~ 3050 m). As pointed out earlier, not only low temperature but also small biomass significantly suppressed plant respiration at our site.

6.3. The global warming effects on the ecosystem carbon sequestration

The model sensitivity analysis showed that the *GPP*, *AR*, *NPP* and W_{plant} responded quickly, while the *HR* and W_{soil} responded very slowly against the climate change. These may indicate that the long-term global warming will increase the ecosystem carbon uptake. Cao and Woodward (1998) used a terrestrial biogeochemical model, forced by simulations of transient

climate change with a general circulation model to quantify the dynamics variations in ecosystem carbon fluxes induced by transient changes in atmospheric CO_2 and climate from 1861 to 2070. They predicted that these changes increased global net ecosystem production significantly, but that will decline as the CO_2 fertilization effect becomes saturated and is diminished by changes in climate factors. Cox et al. (2000) presented results from a fully coupled, three-dimensional carbon-cycle model, indicating that carbon-cycle feedbacks could significantly accelerate climate change over twenty-first century. They found that under a business as usual scenario, the terrestrial biosphere acted as an over all carbon sink until about 2050, but turn into a source thereafter. Thus, both in alpine meadow and in global scales, the long-term global warming seems to make the terrestrial ecosystems as a carbon sink at least in its initial period (i.e. ~ 2050), but that seems decline as the CO_2 fertilization effect is saturated.

The increments of temperature by 5 °C increased the *GPP* but the increase over 7.5 °C decreased the *GPP*. Zhang and Welker (1996) showed that while the peak community biomass showed no significant change, the duration of peak biomass was extended in the warming experiment by 5 °C of air temperature at the Haibei alpine meadow. Thus, the warming by 5 °C advances the ecosystem photosynthetic activity and increases the duration of growing season, and thus, the *GPP*. However, the temperature increase over 7.5 °C may go beyond the optimum temperature of photosynthesis for the objective ecosystem and decreases the *GPP*. This suggests that the ecosystem may shift to another biome type that would survive the high temperature environment. In this analysis, the optimum temperature of photosynthesis plays an important role to determine the threshold temperature to change the warming effects on the ecosystem canopy growth from positive to negative.

To obtain the ecosystem response to the climate change qualitatively and quantitatively, shorter- and longer-term measurement about the ecosystem carbon dynamics are necessary.

6.4. Recommendations for future research

1) The validation of hypothesis in the several environmental controls on the CO_2 exchanges.

To clarify the mechanism involved in the environmental controls on CO_2 dynamics in the alpine ecosystem, for examples, the CO_2 uptake depression in the afternoon at the same light intensity, the smaller scale measurements on single leaf are necessary.

2) The long-term eddy covariance measurement of the CO_2 exchanges

To assess the average and fluctuation of the CO_2 exchange in this ecosystem, the CO_2 flux measurement using the eddy covariance method is necessary to continue for several years.

3) The model construction using the measured ecophysiological parameters

To construct the representative model to simulate the ecosystem carbon dynamics, the ecophysiological parameters are necessary to be measured at the experimental sites. In this study, Sim-CYCLE used the ecophysiological parameter provided for global scale simulation.

4) The longer-term model simulation to investigate the effect of global warming

In general, there are three experimental styles in the model simulation studies; the spin-up experiment, the historical experiment and the future experiment.

The spin-up experiment is conducted to equilibrate the carbon dynamics using the climate data before 1850s, in which the ecosystem reached the climatic climax. The historical experiment is conducted to investigate the past climate perturbation effect, containing the global warming, and the ecosystem carbon dynamics using the re-analyzed climate data. The future experiment is conducted to predict the climate change effect on the ecosystem carbon dynamics using the future modeled climate data induced by the global warming scenarios.

In this ecosystem, these three experiments are necessary to represent the more real ecosystem response to climate changes in the long-term scale.

Chapter 7 Conclusions

Considering the vast area of about 2.5 x 10^6 km^2 of the Qinghai-Tibetan Plateau with the large variation in topography, it seems difficult to determine a 'representative' site for CO2 flux observation. The alpine meadow is located at either the horizontal extreme of the plateau, or at a low altitude within the plateau with averaged elevation of above 4000m. However, the alpine *Kobresia* meadow ecosystem is one of the most widely distributed vegetation on the Qinghai-Tibetan Plateau (Zhou, 2001). The alpine meadow occurs in the areas with a large elevation ranging from 3200 to 5200 m with variable climatic conditions. If it can be assumed that carbon budget depend on more on vegetation types than on any particular geological conditions, it is thus conclusive that the knowledge obtained from the current ecosystem should provide an important insight into our understanding on the carbon dynamics for the grassland ecosystems on the Qinghai-Tibetan Plateau. It should be noticed here that various grassland ecosystems occupy more than 60% of the plateau (Wang et al., 2002).

The CO_2 flux measurement was conducted for two years by the eddy covariance method in an alpine *Kobresia* meadow on the Qinghai-Tibetan Plateau. Such the measurement provided the first example of CO_2 exchange in the blank area of global flux network in an extreme environment from China. The evidence from the observation led to the conclusion that the alpine meadow was a CO_2 sink at least in 2002. The current CO_2 sink strength seems not too high (78.5 g C m^{-2} yr^{-1}), but is comparable with many sub-alpine ecosystems reported so far. Moreover, it is also concluded that temperature was the major environmental control on CO_2 exchange and the low temperature limited evidently the ecosystem respiration. Soil water availability was high in the alpine meadow. The high soil water might reduce the ecosystem respiration. This conclusion seems subjected to the argument that it is difficult to separate the effects of the temperature and soil water contents on the ecosystem carbon budget. However, it is evident that the soil water content showed very sharp temporal variations during a short period such as one week or so, while temperature exhibited much gentle and small variation at the similar temporal scale. Therefore, it is concluded that a high soil water content is correlated

with a low ecosystem respiration at nighttime for the alpine ecosystem.

The CO_2 flux was modeled by the ecosystem carbon dynamics model, Sim-CYCLE, for 20 years at the same site. The modeling provided the reasonable interannual changes of CO_2 exchange. The results of modeling led to conclude that annual carbon budgets were fluctuated ranging from +70 to -70 g C m^{-2} yr^{-1} and it was unclear whether this ecosystem was a carbon sink or source for long-term periods qualitatively. It is also concluded that temperature was the major environmental control on annual CO_2 exchange similarly to the measurement results. The model sensitivity analysis suggested that the long-term global warming by 5 °C in annual average temperature would increase the ecosystem carbon uptake due to the extension of the ecosystem photosynthetic activity and the duration of growing season. However, the long-term global warming over 7.5 °C may go beyond the optimum temperature of photosynthesis for the objective ecosystem. This suggests that the ecosystem may shift to another biome type that would survive the high temperature environment.

The alpine meadow exhibited a relatively low ecosystem CO_2 uptake when taken into account of the fairly high leaf area index of about 3. From this study, it is further concluded that the alpine meadow has the potential to sequester carbon, but the potential appears to be small possibly because of the limitation of low temperature. Further studies are needed to clarify the environmental controls on the carbon dynamics of the alpine meadow ecosystem from in short-term to in long-term periods.

Acknowledgement

I am most grateful to my supervisor, Prof. Takehisa OIKAWA, Institute of Biological Sciences, University of Tsukuba for his patient guidance and continued encouragement. I owe gratitude to Dr. Yanhong TANG, National Institute for Environmental Sciences for his many suggestions and helps on my research and the paper editing.

I also wish to express special thanks to Professors Shigeru MARIKO, Takeo HAMA, and Fujio KIMURA, University of Tsukuba, for their valuable comments of the former manuscript of the thesis.

I thank Dr. Wenhong MO of the Institute of Biological Science, University of Tsukuba, for her comments on the manuscript, and Dr. Jun ASANUMA of the Terrestrial Environmental Research Center, University of Tsukuba, for his advice on the eddy covariance method.

I am grateful to Dr. Song GU, Dr. Xiaoyong CUI, National Institute for Environmental Sciences, and my colleague, Mr. Mitsuru HIROTA, Doctoral Program in Biological Sciences, University of Tsukuba, and Dr. Mingyuan DU, National Institute for Agro-Environmental Sciences for their suggestions and assistance on the field observations. I acknowledge greatly help from Dr. Yingnian LI, Dr. Xingquan ZHOU and the staff of the Haibei station, the Northwest Plateau Institute of Biology, Chinese Academy of Sciences, China for the field observations.

Thanks are extended to the staff and students of Terrestrial Ecosystem Laboratory, Institute of Biological Sciences, University of Tsukuba. Thanks are also due to Prof. Richard, WEISBURD of the Institute of Biological Science, University of Tsukuba for his paper editing.

Finally, I would like to express my acknowledgement to my parents for their financial continuing support and encouragement.

This research was a part of the joint research projects between the National Institute for Environmental Studies, Japan, and the Northwest Plateau Institute of Biology, China (Grand No: 13575035 and B13), which are supported by the Global Environmental Research Program

of the Ministry of Environment, Japan and by the Ministry of Education, Culture, Sports, Science and Technology, Japan.

References

Aber, J. D., Reich, P. B., Goulden, M. L., 1996. Extrapolating leaf CO_2 exchange to the canopy: a generalized model of forest photosynthesis compared with measurements by eddy correlation. *Oecologia* **106**, 257-265.

Adams, J.M., Faure, H., Faure-Denard, L., McGlade, J.M., Woodward, F.I., 1990. Increases in terrestrial carbon storage from the Last Glacial Maximun to the present. *Nature* **348**, 711-714.

Alexandrov, G.A., Oikawa, T., 1995. Net ecosystem produc-tion resulted from CO_2 enrichment: evaluation of potential response of a Savannah ecosystem to global changes in atmospheric composition, *Proceedings of the Tsukuba Global Carbon Cycle Workshop -Global Environment Tsukuba'95-*, Environmental Agency of Japan, Tsukuba, pp. 161–168.

Amiro, B.D, 2001. Paired-tower measurements of carbon and energy fluxes following disturbance in the boreal forest. *Global Change Biol.* **7**, 253–268.

Amthor, J.S., 1989. *Respiration and Crop Productivity*. Springer, New York, p. 215.

Amthor, J.S., Goulden, M.L., Mungeer, J.W., Wofsy, S.C., 1994. Testing a mechanistic model of forest-canopy mass and energy exchange using eddy correlationo: Carbon dioxide and ozone uptake by a mixed oak-maple stand. *Australian Journal of Plant Physiology* **21**, 623-651.

Arora, V., 2002. Modeling vegetation as a dynamic component in soil-vegetation-atmosphere transfer schemes and hydrological models. *Rev. Geophys.* **40(2)**, 1006.

Aubinet, M., Grelle, A., Ibrom, A., Rannik, Ü., Moncrieff, J., Foken, T., Kowalski, A.S., Martin, P.H., Berbigier, P., Bernhofer, Ch., Clement, R., Elbers, J., Granier, A., Grünwald, T., Morgenstern, K., Pilegaard, K., Rebmann, C., Snijders, W., Valentini, R., Vesala, T., 2000. Estimates of the annual net carbon and water vapor exchange of forests: the EUROFLUX methodology. *Adv. Ecol. Res.* **30**, 113–175.

Baldocchi, D.D. and Vogel, C.A., 1997. Seasonal variation of energy and water vapor exchange rates above and below a boreal jack pine forest canopy. *J. Geophys. Res.* **102 (D24)**, 28939-28951.

Baldocchi D., Falge, E., Olson, R., Hollinger, D., Running, S., Anthoni, R., Berhofer, C., Davis, K., Fuentes, J.D., Goldstein, A., Katul, G., Law, B., Lee, X., Malhi, Y., Meyers, T., Munger, W., Oechel, W., Paw, K.T., Pilgaard, U.K., Schmidt, H.P., Valentini, R., Verma, S., Vessala, T., Wilson, K., Wofsy, S., 2001. FLUXNET: A new tool to study the temporal and spatial variability of ecosystem-scale carbon dioxide, water vapor and energy flux densities. *Bulletin of the American Meteorological Society* **82,** 2415-2434.

Ball, J.T., Woodrow, I.E., Berry, J.A., 1987. A model predicting stomatal conductance and its contribution to the control of photosynthesis under different environmental conditions. In: Biggens, J. (Ed.), *Progress in Photosynthesis Research*. Martinus Nijhoff, Dordrecht, pp. 221–224.

Brooks, A., Farquhar, G.D., 1985. Effect of temperature on the CO_2/O_2 specificity of ribulose 1,5-bisphosphate car-boxylase/ oxygenase and the rate of respiration in the light. *Planta* **165**, 397–406.

Brutsaert, W.H., 1982. *Evaporation into the atomosphere*. D.Reidel Publishing Company, Boston, U. S. A.

Camillo, P.J., Gurney, R.J. and Schumugge,T.J., 1983. A soil and atmospheric boundary layer model for evapotranspiration and soil moisture studies. *Water Resour. Res.* **19**, 371-380.

Cao, G., Li, Y., Bao, X., 1998. Characteristics of water-holding capacity in Mat-Cryic Cambisoil in alpine region (in Chinese). *Soils*. 27-30.

Cao, M., Woodward, F.I., 1998. Dynamic responses of terrestrial ecossytem carbon cycling to global climate change. *Nature* **393**, 249-252.

Cox, P., Betts, R.A., Jones, C.D., Spall, S.A., Totterdell, I.J., 2000. Acceleration of global warming due to carbon-cycle feedbacks in a coupled climate model. *Nature* **408**, 184-187.

Cramer W., Kicklighter, D.W., Bondeau, A., Moore, III, B., Churkina, G., Nemry, B., Ruimy, A., Schloss, A.L., 1999. The Participants of the Potsdam NPP Model Intercomparison, Comparing global models of terrestrial net primary productivity (NPP): overview and key results. *Global Change Biol.* **5** (Suppl.), 1–15.

Cui, X., Tang, Y., Gu, S., Nishimura, S., Shi, S., Zhao, X., 2003. Photosynthetic depression in relation to plant architecture in two alpine herbaceous species. *Environ. Exper. Botany* **50(2)**, 125-135.

Davidson, E.A., Belk, E., Boone, R.D., 1998. Soil water content and temperature as independent or confounded factors controlling soil respiration in a temperate mixed hardwood forest. *Global Change Biol.* **4**, 217–227.

Deming-Adams, B., Adams III W.W., 1996. The role of xanthophyll cycle carotenoids in the protection of photosysnthesis. *Trends Plant Sci.* **1**, 21-26.

Denmead, O.T., 1976. 'Temperate Cereals', in *Vegetation and the Atomosphere*, Vol2. (Ed. J.L.Montieth) Academic Press, London pp.1-31.

de Vries DA, 1963. *Thermal properties of soils*, ed. by van Wijk WR, Physics of Plant Environment. North-Holland Publishing Co., Amsterdam. p210-235.

Ehleringer, J.R., Cerling, T.E., Helliker, B.R., 1997. C4 photosynthesis, atmospheric CO2, and climate. *Oecologia* 112, 285-299.

Ehleringer, J., Björkman, O., 1977. Quantum yields for CO_2 uptake in C_3 and C_4 plants. *Plant Physiol.* **59**, 86–90.

Falge, E., Baldocchi, D., Tenhunen, J., Aubinet, M., Bakwin, P., Berbigier, P., Bernhofer, C., Burba, G., Clement, R., Davis, K.J., Elbers, J.A., Goldstein, A.H., Grelle, A., Granier, A., Guðmundsson, J., Hollinger, D., Kowalski, A.S., Katul, G., Law, B.E., Malhi, Y., Meyers, T., Monson, R.K., Munger, J.W., Oechel, W., Paw U, K.T. Pilegaard, K., Rannik, Ü., Rebmann, C., Suyker, A., Valentini, R., Wilson, K., Wofsy, S., 2002. Seasonality of

ecosystem respiration and gross primary production as derived from FLUXNET measurements. *Agric. For. Meteorol.* **113**, 53–74.

Falge, E., Tenhunen, J.D., Baldocchi, D.D., Aubinet, M., Bakwin, P., Berbigier, P., Bernhofer, C., Bonnefond, J.-M., Burba, G., Clement, R., Davis, K.J., Elbers, J.A., Falk, M., Goldstein, A.H., Grelle, A., Granier, A., Grünwald, T., Guðmundsson, J., Hollinger, D., Janssens, I.A., Keronen, P., Kowalski, A.S., Katul, G., Law, B.E., Malhi, Y., Meyers, T., Monson, R.K., Moors, E., Munger, J.W., Oechel, W., Paw U, K.T., Pilegaard, K., Rannik, U., Rebmann, C., Suyker, A., Thorgeirsson, H., Tirone, G., Turnipseed, A., Wilson, K., Wofsy, S., 2002. Phase and amplitude of ecosystem carbon release and uptake potentials as derived from FLUXNET measurements. *Agric. For. Meteorol.* **113**, 75–95.

Fang, J.Y., Liu, G.H., Xu, S.L., 1996. Soil carbon pool in China and its global significance. *J. Environ. Sci.* **8(2)**, 249-254.

Field, C.B., Jackson, R.B., Mooney, H.A., 1995. Stomatal responses to increases CO_2: implications from the plant to global scale. *Plant Cell Environ.* **18**, 1214–1225.

Flanagan, L.B., Wever, L.A., Carlson, P.J., 2002. Seasonal and interannual variation in carbon dioxide exchange and carbon balance in a northern temperate grassland. *Global Change Biol.* **8**, 599–615.

Friend, A.D., Stevens, A.K., Knox, R.G., Cannell, M.G.R., 1997. A process-based, terrestrial biosphere model of ecosystem dynamics (Hybrid v3.0). *Ecological Modelling* **95**, 29-287.

Fukuda, M., Ishizaki, T., 1980. A simulation model of frost penetration beneath the ground on the basis of equilibrium surface temperature (in Japanese with English summary). *Seppyo* **42(2)**, 71-80.

Goetz, S.J., Prince, S.D., Small, J., Gleason, A.C.R., 2000. Interannual variability of global terrestrial primary production: Results of a model driven with satellite observations. *J. Geophys. Res.* **105(D15)**, 20077-20091.

Gu, L., Baldocchi, D., Verma, S.B., Black, T.A., Falge, E.M., Dowty, P.R., 2002. Advantages of diffuse radiation foro terestrial ecosystem productivity. *J. Geophys. Res.* **107(D6)**, ACL 2, 1-23.

Gu, S., Du, M., Kato, T., Li, Y., Cui, X., Zhao, X., Tang, Y. 2003. Short-term variation oFCO_2 flux in relation to environmental controls in an alpine meadow on the Qinghai-Tibetan Plateau. *J. Geophys. Res. Atmos.* in press.

Ham, J.M., Knapp, A.K., 1998. Fluxes of CO_2, water vapor, and energy from a prairie ecosystem during the seasonal transition from carbon sink to carbon source. *Agric. Forest Meteorol.* **89**, 1-14.

Haxeltine, A., Prentice, I. C., 1996. BIOME3: An equilibrium terrestrial biosphere model based on ecophysiological constraints, resource availability, and competition among plant functional types, *Global Biogeochemical Cycles* **10(4)**, 693-709.

Haxeltine, A., Prentice, I. C., Creswell, I. D., 1996. A coupled carbon and water flux model to predict vegetation structure (BIOME2), *J. Veg. Sci.* **7**, 651-666.

Hollinger, D.Y., kelliher, F.M., Byers, J.N., Hunt, J.E., McSeveney, T.M., Weir, P.L., 1994. Carbon dioxide exchange between an undisturbed old-growth temperate forest and the atmosphere. *Ecology* **75**, 134-150.

Houghton, R.A., 2003. Revised estimates of the annual net flux of carbon to the atmosphere from changes in land use and land management. *Tellus* **55B**, 378-390.

Hunt J.E, Kelloher, F.M., McSeveny, T.M., Byers, J.N., 2002. Evaporation and carbon dioxide exchange between the atmosphere and a tussock grassland during a summer drought. *Agric. Forest Meteorol.* **111**, 65-82.

Institute of Soil Science and the Chinese Academy of Sciences, 2001. *Chinese Soil Taxonomy*. Science Press, Beijing.

IPCC, 1990: Climate Change, The IPCC Scientific Assessment. J.T. Houghton, G.J. Jenkins and J.J. Ephraums (eds.), Cambridge University Press, Cambridge, UK, 365 pp.

IPCC, 1996: Climate change 1995 : the Science of Climate Change. Contribution of Working Group I to the Second Assessment of the Intergovernmental Panel on Climate Change. J.T. Houghton, L.G. Meira Filho, B.A. Callender, N. Harris, A. Kattenberg and K. Maskell (Eds). Cambridge University Press, UK. pp 572

IPCC, 2001. Climate Change 2001: The scientific basis. Contribution of working group I to the Third Assessment Report of the Intergovernmental Panel on Climate Change. (eds. J. T. Houghton, Y. Ding, D. J. Griggs, M. Noguer, P. J. van der Linden, X. Dai, K. Maskell and C. A. Johnson). Cambridge University Press, Cambridge, United Kingdom and New York, USA, 881pp.

Ito, A, 2000. The Relationship between Atmospheric Change and Carbon Dynamics in Terrestrial Ecosystems: A Global Study Using a Mechanistic Model, Sim-CYCLE. *Ph.D thesis, Doctoral Program in Biological Sciences, the University of Tsukuba.*

Ito, A, Oikawa, T., 2000. A model analysis of the relationship between climate perturbations and carbon budget anomalies in global terrestrial ecosystems: 1970-1997. *Climate Research* **15**: 161-183.

Ito A., Oikawa, T., 2002. A simulation model of the carbon cycle in land ecosystems (Sim-CYCLE): a description based on dry-matter production theory and plot-scale validation, *Ecol. Modelling* **151**, 143–176.

Jarvis, P.G., McNaughton, K.G., 1986. Stomatal control of transpiration: Scaling up from leaf to region. *Adv. Ecol. Res.* **15**, 1-49.

Jarvis, P.G., Massheder, J.M., Hale, S.E., Moncrieff, J.B., Rayment, M., Scott, S.L., 1997. Seasonal variation of carbon dioxide, water vapor, and energy exchanges of a boreal black spruce forest. *J. Geophys. Res.* **102 (D24)**, 28953-28966.

Jones, H.G., 1992. *Plants and microclimate*. Second edition. Cambridge Univ. Press, 428 pp.

Kader, B. A., Yaglom, A. M., 1990. Mean fields and fluctuation moments in unstably stratified turbulent boundary layers. *J. Fluid Mech.* **212**, 637--662.

Kaimal. J.C., 1988. *The atmospheric boundary layer -Its structure and measurement* (in Japanese), translated by Mitsuta, Y. and Yamada, M., Gijyutudo Syuppan, 116pp.

Kaimal, J.C., Finnigan, J.J., 1994. *Atmospheric Boundary Layer Flows: Their Structure and Measurement*. Oxford University Press, New York, 289 pp.

Kato, T., Kimura, R., Kamichika, M., 2004a. Estimation of Evapotranspiration, Transpiration Ratio and Water-Use Efficiency from Sparsely Vegetated Sorghum Fields using the Compartment Model. *Agric. Water Manage.* in press.

Kato, T., Tang, Y., Gu, S., Cui, X., Hirota, M., Du, M., Li, Y., Zhao, X., Oikawa, T., 2004b. Carbon dioxide exchange between the atmosphere and an alpine meadow ecosystem on the Qinghai-Tibetan Plateau, China. *Agric. For. Meteorol.* in press.

Kato, T., Hirota, M., Gu, S., Cui, X., Tang, Y., Du, M., Li, Y., Zhao, X., Oikawa, T., 2003. Seasonal patterns of gross primary productivity and ecosystem respiration in an alpine meadow ecosystem on the Qinghai–Tibetan Plateau, China. *J. Geophys. Res. Atmos.* submitted.

Kersten, 1963. Thermal properties of frozen ground. *Proceedings 1st International Conference of Permafrost*, 301-304.

Kim, J., Verma, S.B., Clement, R.J, 1992. Carbon dioxide budget in a temperate grassland ecosystem. *J. Geophys. Res.* **97** (D5), 6057-6063.

Kondo, J., 1993. A new bucket model for predicting water content in the surface soil layer. *J. Japan Soc. Hydro & Water Resour.* **6(4)**, 344.

Kondo, J., Saigusa, N. and Sato, T., 1990. A parameterization of evaporation from bare soil surface. *J. Appl. Meteorol.* **29**, 383-387.

Kuroiwa, 1966. Kuroiwa, S., 1966. *Dry matter production of plants, Ecology and Evolution*. A Series of Modern Biology, Iwanami Shoten, Tokyo, pp. 71–100, (in Japanese)

Larcher W., 1995. Physiological Plant Ecology (3rd Edition) Springer-Verlag Berlin Heidelberg PP.149.

Law, B.E., Falge, E., Gu, L., Baldocchi, D.D., Bakwin, P., Berbigier, P., Davis, K., Dolman, A.J., Falk, M., Fuentes, J.D., Goldstein, A., Granier, A., Grelle, A., Hollinger, D., Janssens, I.A., Jarvis, P., Jensen, N.O., Katul, G., Malhi, Y., Matteucci., G., Meyers, T., Monson, R., Munger, W., Oechel, W., Olson, R., Pilegaard, K., Paw U, K.T., Thorgeirsson, H., Valentini, R., Verma, S., Vesala, T., Wilson, K., Wofsy, S., 2002. Environmental controls over carbon dioxide and water vapor exchange of terrestrial vegetation. *Agric. For. Meteorol.* **113**, 97-120.

Leuning, 1990. Leuning, R., 1990. Modelling stomatal behavior and photo-synthesis of *Eucalyptus grandis*. *Aust. J. Plant Physiol.* **17**, 159–175.

Leuning, R., 1995. A critical appraisal of a combined stomatal-photosynthesis model. *Plant Cell Env.* **18**, 339-357.

Li, S.G, Oikawa, T., 2001. Energy budget and canopy carbon dioxide flux over a humid C3 and C4 co-existing grassland. International Workshop for Advanced Flux Network and Flux Evaluation - Proceedings -. CGER-REPORT. CGER-M011-2001, 23-28.

Li, W., Zhou, X. (Chief Editors), 1998. Ecosystems of Qinghai-Xizang(Tibetan) Plateau and Approach for Their Sustainable Management, The Series of Studies on Qinghai-Xizang(Tibetan) Plateau, Guangdong Science & Technology Press, Guangzhou, China.

Li, Y.N., Zhang, J.H., 1998. The influences of winter – spring's air temperature change on grassland productivity in haibei at qilian monutain (in chinese with english abstract). *Plateau Meteorol.* **17(4)**, 443-446.

Lieth, H., 1975. Modeling the primary productivity of the world. In *Primary productivity of the biosphere* (ed. H. Lieth and R. H. Whittaker), pp. 237-263. Springer, Berlin.

Liu, Y.F., Ouyang, H., Cao, G.M., Luo, J., Zhao, X.Q., Zhang, X.Z., Yang, Z., 2001. The diurnal and seasonal characteristic of soil CO_2 efflux from eastern ecosystems of

Qinghai-Tibet Plateau. *Proceedings of workshop on impact of global change on terrestrial ecosystems* (IGCTE-2001), 77-88.

Lloyd, J., Taylor, J.A., 1994. On the temperature dependence of soil respiration, *Funct. Ecol.* **8**, 315–323.

Long, S.P., 1991. Modification of the response of photosynthetic productivity to rising temperature by atmospheric CO_2 concentrations. Has its importance been underestimated? - Opinion. *Plant Cell and Environment* **14**: 729-739.

Luedeke, M. K. B., Badeck, F.-W., Otto, R. D., Haeger, Ch., Doenges, S., Kindermann, J., Wuerth, G., Lang, T., Jaekel, U., Klaudius, A., Ramge, P., Habermehl, St., Kohlmaier, G. H., 1994. The Frankfurt Biosphere Model: a global process oriented model of seasonal and long-term CO_2 exchange between terrestrial ecosystems and the atmosphere. I. Model description and illustrative results for cold deciduous and boreal forests. *Climate Research* **4**, 143-166.

Luo, T.X., Li, W.H., Zhu, H.Z., 2002. Estimated biomass and productivity of natural vegetation on the tibetan plateau. *Ecol. Appl.* **12(4)**, 980-997.

Manabe, 1969. The atmospheric circulation and the hydrology of the earth's surface. *Mon. Wea. Rev.* **97**, 739-774.

Manuel, N., Cornic, G., Aubert, S., Cholder, P., Bligny, R., Heber, U., 1999. Protection against photoinhibition in the alpine plant *Geum montanum*. *Oeclogia* **119**, 149-158.

McGuire, A.D., Melillo, J.M., Joyce, L.A., Kicklighter, D.W., Grace, A.L., Moore, III B., Vorosmarty, C.J., 1992. Interactions between carbon and nitrogen dynamics in estimating net primary productivity for potential vegetation in North America. *Global Biogeochemical Cycles* **6(2)**, 101-124.

Monin, A., Obukhov, A., 1954. Basic laws of turbulent mixing in the atmosphere near the ground, *Tr. Akad. Nauk.* **24**, 1963-1987

Monsi, M., 1960. Dry-matter reproduction in plants. I. Sche-mata of dry-matter reproduction. *Bot. Mag.* **73**, 81–90.

Monsi M., Saeki T., 1953. Über den Lichtfaktor in den Pfanzengesellschaften und seine Bedeutung für die Stoffproduktion. *Japanese Journal of Botany* **14**, 22-52.

Monson, R.K., Turnipseed, A.A., Sparks, J.P., Harley, P.C., Scott-Denton, L.E., Sparks, K. and Huxman, T.E., 2002. Carbon sequestration in a high-elevation, subalpine forest. *Global Change Biol.* **8**, 459-478.

Monteith, J.L., 1965. Evaporation and the environtment. Symp. Soc. Expl. Biol. **19**, 205-234.

Montieth, J.L. (ed.), 1972. *Vegetation and the atmosphere*, vol. 1, Principles. London. Academic Press, 278pp.

Monteith, J.L., 1973. *Principles of Environtmental Physics*, Edward Arnold, London.

Morison, J.L., Gifford, R.M., 1983. Stomatal sensitivity to carbon dioxide and humidity: a comparison of two C_3 and two C_4 grass species. *Plant Physiol.* **71**, 789–796.

Ni, J., 2002. Carbon storage in grasslands of China. *J. Arid Environ.* **50**, 205-218.

Nichols, W.D., 1992. Energy budgets and resistances to energy transport in sparsely vegetated rangeland. *Agric. For. Meteorol.* **60**, 221-247.

Nieveen J.P., Jacobs, C.J., Jacobs, A.F., 1998. Diurnal and seasonal variation of carbon dioxide exchange from a former true raised bog. *Global Change Biol.* **4**, 823-833.

Oechel W.C., Hastings, S.J., Vourlitis, G.L., Jenkins, M., Riechers, G., Grulke, N., 1993. Recent change of Arctic tundra ecosystems from a net carbon dioxide sink to a source. *Nature* **361**, 520-523.

Oechel, W.C., Vourlitis, G.L., Hastings, S.J., ULT,Jr., R.P., Bryant, P., 1998. The effects of water table manipulation and elevated temperature on the net CO_2 flux of wet sedge tundra ecosystems. *Global Change Biol.* **4**, 77-90.

Ohtaki, E., 1985. On the similarity in atmospheric fluctuations of carbon dioxide, water vapor and temperature over vegetated fields. *Boundary layer Meteorol.* **32**, 32-37.

Oikawa, T., 1985. Simulation of forest carbon dynamics based on dry-matter production model: 1. Fundamental model structure of a tropical rainforest ecosystem. *Bot. Mag.* **98**, 225–238.

Oikawa, T., 1986. Simulation of forest carbon dynamics based on dry-matter production model: 3. Effects of increasing CO_2 upon a tropical rainforest ecosystem. *Bot. Mag.* **99**, 419–430.

Oikawa, T., 1993. Comparison of ecological characteristics between forest and grassland ecosystems based on a dry-matter production model. *J. Environ. Sci.* **7**, 67–78.

Oikawa, T., 1998. Modeling carbon dynamics of a lucidophyll forest under monsoon climates. *Global Environ. Res.* **1**, 25–33.

Parton, W.J., Ssurlock, J.M.O., Ojima, D.S., Gilmanov, T.G., Scholes, R.J., Sshimel, D.S., Kirchner, T., Menaut, J.C., Seastedt, T., Moya, E.G., Kamnalrut, A., Kinyamario, J.I., 1993. Observations and modeling of biomass and soil organic matter dynamics for the grassland biome worldwide. *Global Biogeochemical Cycles* **7(4)**, 785-809.

Paembonan, S.A., Hagihara, A., Hozumi, K., 1992. Long-term respiration in relation to growth and maintenance processes of the aboveground parts of a hinoki forest tree. *Tree Physiol.* **10**, 101–110.

Park, Y.I, Chow, W.S., Anderson, J.M., Hurry, V.M., 1996. Differential susceptibility of photosystem II to light stress in light-acclimated pea leaves depends on the capability for photochemical nad non-radiative dissipation of light. *Plant Sci.* **115**, 137-149.

Pasquille, F., 1974. *Atmospheric Diffusion*, John Wiley and Sons Inc., pp 74-84.

Paul, K., 2001. Temperature and moisture effects on decomposition. Net Ecosystem Exchange. *Workshop proceedings CRC for greenhouse accounting*. 95-102.

Pearcy, R. W., Ehleringer, J. R., 1984. Comparative ecophysiology of C3 and C4 plants. *Plant Cell and Environment* **7**, 1-13.

Penman, H.L., 1948. Natural evaporation from open water, bare soil, and grass. *Proc. Roy. Soc. London A* **193**, 120-146.

Piao, S.L., Fang, J.Y., 2002. Terrestrial net primary production and its spatio-temporal patterns in Qinghai-Xizang Plateau, China during 1982-1999. *J. Natural Resources* **17 (3)**, 234-380.

Phelps, G.T., Pond, S., 1971. Spectra of the temperature and humidity fluctuations and of the fluxes of moisture and sensible heat in the marine boundary layer. *J. Atmos. Sci.* **28**, 918-928.

Potter, C.S., Randerson, J.T., Field, C.B., Matson, P.A., Vitousek, P.M., Mooney, H.A., Klooster, S.A., 1993. Terrestrial ecosystem production: A process model based on global satellite and surface data (CASA), *Global Biogeochemical Cycles* **7(4)**, 811-841.

Raich J.W., Rastetter E.B., Melillo J.M., Kicklighter D.W., Steudler, P.A., Peterson, B.J., Grace, A.L., Moore III B., Vorosmarty, C.J., 1991. Potential net primary productivity in South America: application of a global model. *Ecological Applications* **1**, 399-429.

Randerson, J.T., Field, C.B., Fung, I.Y., Tans, P.P., 1999. Increases in early season ecosystem uptake explain recent changes in the seasonal cycle of atmospheric CO_2 at high northern latitudes. *Geophys. Res. Lett.* **26**, 2765–2768.

Ryan, M.G., 1991. Effects of climate change on plant respi-ration. *Ecol. Appl.* **1**, 157–167.

Ross, J., 1981. *The radiation regime and architecture of plant stands.* (Tasks for vegetation sciences,3;ed.Helmut Lieth) Dr W. Junk Publishers. The Hague.

Roy, J., Saugier, B., Mooney, H.A., 2001. *Global Terrestrial Productivity: Past, present and future*. Academic Press, San Diego, pp 572.

Rosenzweig, M. L., 1968. Net primary productivity of terrestrial communities: prediction from climatological data. *American Naturalist* **102(923)**, 67-72.

Running, S. W., Coughlan, J. C., 1988. A general model of forest ecosystem processes for regional applications I. Hydrologic balance, canopy gas exchange, and primary production processes. *Ecological Modelling* **42**, 125-154.

Running, S. W., Hunt, E. R., 1993. Generalization of a forest ecosystem process model for other biomes, BIOME-BGC, and an application for global scale models, in *Scaling Physiological Processes: Leaf to Globe*, editors J. R. Ehleringer and C. B. Field, pp. 141-158.

Saigusa, N., Yamamoto, S., Murayama, S., Kondo, H., Nishimura, N., 2002. Gross primary production and net ecosystem exchange of a cool-temperature deciduous forest estimated by the eddy covariance method. *Agric. Forest Meteorol.* **112**, 203-215.

Scurlock, J.M.O., Hall, D.O., 1998. The global carbon sink: a grassland perspective. *Global Change Biol.* **4**, 229-233.

Shi, S.B., Ben, G.Y., Han, F., 1991. Analysis of plant growth in *Kobresia Humilis* meadow (in chinese with english abstract). *Alpine Meadow Ecosystem* **3**, 69-74.

Shuttleworth, W.J., Wallace, J.S., 1985. Evaporation from sparse crops-an energy combination theory. *Q. J. R. Meteorol. Soc.* **111**, 839-855.

Shuttleworth, W.J., Gurney, R.J., 1990. The theoretical relationship between foliage temperature and canopy resistance in sparce crops. *Q. J. R. Meteorol. Soc.* **116**, 497-519.

Shulze, E.-D., Lloyd, J., Keilliher, F.M., Wirth, C., Rebmann, C., Luhker, B., Mund, M., Knohl, A., Miyukova, I.M., Schulze, W., Ziegler, W., Varlagin, A.B., Sogachev, A.F., Valentini, R., Dore, S., Grigoriev, S., Kolle, O., Panfyorov, M.I., Tchebakova, N., Vygodskaya, N.N., 1999. Productivity of forests in the Eurosiberian boreal region and their potential to act as a carbon sink - a synthesis. *Global Change Biol.* **5**, 703–722.

Sims, P., Bradford, J.A., 2001. Carbon dioxide fluxes in a southern plains prairie. *Agric. Forest Meteorol.* **109**, 117-134.

Streb, P., Shang, W., Feierabend, J., Bligny, R., 1998. Divergent strategies if photoprotection in high-mountain plants. *Planta* **207**, 313-324.

Sugawara, M., Maruyama, T., 1952. Statistical method of predicting the runoff from rainfall. *Proceedings of the 2nd Japan National Con. for Appl. Mech.*, 213-216.

Sugawara, M., 1961. On the analysis of runoff structure about several Japanese rivers. *Japan J. Geophys.* **2(4)**, 1-76.

Suyker A.E., Verma, S.B., 2001. Year-round observations of the net ecosystem exchange of carbon dioxide in a native tallgrass prairie. *Global Change Biol.* **7**, 279-289.

Takata, K., Kimoto, M., 2000. A numerical study on the impact of soil freezing on the continental-scale seasonal cycle. *J. Meteorol. Soc. Japan* **78**, 199-221.

Tissue, D.T., Oechel, W.C., 1987. Response of *Eriophorum vaginatum* to elevated CO_2 and temperature in the Alaskan tussock tundra. *Ecology* **68**, 401–410.

Tsukamoto, O., Monji, N., Ito, Y., 2001. Flux measurements of momentum, sensible and latent heat (water vapor) using eddy covariance method. In: *O. Tsukamoto and N. Monji (eds.) Methods for measuring surface fluxes. Kisho Kenkyu Note, Meteorological Research Note* (in Japanese), Meteorological Society of Japan. **199**, 19-55.

Uchijima, Z., 1976. 'Maize and Rice', in *Vegetation and the Atomosphere*, Vol2. (Ed.J.L.Montieth) Academic Press, London pp.33-64.

Uchijima, Z., Seino, H., 1985. Agroclimatic evaluation of net primary productivity of natural vegetations (1) Chikugo model for evaluating net primary productivity. *J. Agricultural Meteorology* **40**, 353-352.

Valentini, R., Matteucci, G., Dolman, A.J., Schulze, E.D., Rebmann, C., Moors, E.J., Granier, A., Gross, P., Jensen, N.O., Pilegaard, K., Lindroth, A., Grelle, A., Bernhofer, C., Grünward, T., Aubinet, M., Geulemans, R., Kowalski, A.S., Vasala, T., Rannik, Ü., Berbigier, P., Loustau, D., Guðmundsson, J., Thorgeirsson, H., Ibrom, A., Morgenstern, K.,

Clement, R., Moncriff, J., Montagnani, L., minerbi, S., Jarvis, P.G., 2000. Respiration as the main determinant of carbon balance in European forests. *Nature* **404**, 861-865.

van Bavel, C.H.M., Hillel, D.I., 1976. Calculating potential and actual evaporation from a bare soil surface by simulation of concurrent flow of water and heat. *Agric. Meteorol.* **17**, 453-476.

Verma, S.B., Kim, J., Clement, J., 1992. Momentum, Water Vapor, and Carbon Dioxide Exchange at a Centrally Located Prairie Site During FIFE. *J. Geophys. Res.* **97 (D17)**, 18629-18639.

Wang G. X., Qian J., Cheng G. D. & Lai Y. M., 2002. Soil organic carbon pool of grassland soils on the Qinghai-Tibetan Plateau and its global implication. *Science of the Total Environment* **291**, 207-217.

Wang, Z., Le, Y., Zhang, J., 1982. Preliminaly study of the respiratory intensity of alpine soils. In: Xia WA, editor (in chinese). *Alpine Meadow Ecosystem* **1**, 174-183.

Waring, R.H., Landsberg, J.J., Williams M., 1998. Net primary production of forests: a constant fraction of gross primary production?. *Tree Phys.* **18**, 129-134.

Warnant, P., Francois, L., Gerard, J.-C., 1994. CARAIB: A global model of terrestrial biological productivity. *Global Biogeochemical Cycles* **8(3)**, 255-270.

Webb, E.K., Pearman, G.I., Leuning, R., 1980. Correction of flux measurements for density effects due to heat and water vapor transport. *Quart. J. Roy. Met. Soc.* **106**, 85-100.

White, M.A., Running, S.W., Thornton, P.E., 1999. The impact of growing-season length variability on carbon assimilation and evapotranspiration over 88 years in the eastern US deciduous forest. *Int. J. Biometeorol.* **42**, 139–145.

Wilson, K.B., Baldocchi, D.D., Aubinet, M., Berbiger, P., Bernhofer, C., Dolman, H., Falge, E., Field, C., Goldstein, A., Granier, A., Grelle, A., Halldor, T., Hollinger, D., Katul, G., Law, B.E., Lindroth, A., Meyer, T., Moncrieff, J., Monson, R., Oechel, W., Tenhunen, J., Valentini, R., Verma, S., Vesala, T., Wofsy, S., 2002. Energy partitioning between latent

and sensible heat flux during the warm season at FLUXNET sites. *Water Resour. Res.* **38(12)**, 1294.

Woodward, F. I., Smith, T. M., Emanuel, W. R., 1995. A global land primary productivity and phytogeography model. *Global Biogeochemical Cycles* **9(4)**, 471-490.

Wyngaard, J.C., Cote, O.R., 1972. Cospectral similarity in the atmospheric surfave layer. *Quart. J. Roy. Meteorol. Soc.* **98**, 590-603.

Xu, M., Y. Qi, 2001. Soil surface CO_2 efflux and its spatial and temporal variations in a young ponderosa pine plantation in northern California, *Global Change Biol.* **7**, 667–677.

Yaglom, A.M., 1977. Comments on wind and temperatures flux-profile relationships. *Boundary Layer meteorol.* **11**, 89-102.

Yamamoto, S., Saigusa, N., Harazono, Y., Fujinuma, Y., Inoue, G., Hirano, T., Fukushima, Y., 2001. Present status of AsiaFlux Network and a view toward the future. *Extended Abstract, Sixth International Carbon Dioxide Conference*, Sendai, 404-407.

Yasunari, T. ed., 2001. Special issue, GEWEX Asian Monsoon Experiment (GAME). *J. Meteor. Soc. Japan* **79B**, 241-605.

Yokota, T., Hagihara, A., 1996. Seasonal change in the tem-perature coefficient Q10 for respiration of field-grown hinoki cypress *(Chamaecyparis obtus*a) trees. *J. Forest Res.* **1**, 165–168.

Yokota, T., Ogawa, K., Hagihara, A., 1994. Dependence of the aboveground respiration of hinoki cypress (*Chameacy-paris obtusa*) on tree size. *Tree Physiol.* **14**, 467–479.

Zhao, X.Q., Cao, G.M., Zhou, H.K., 2001. Carbon balance in the alpine meadow (*Kobresia Humilis*) ecosystem and its impacts of human activities. *Proceedings of workshop on impact of global change on terrestrial ecosystems* (IGCTE-2001), 4-11.

Zhang, Y., Welker, J.M., 1996. Tibetan alpine tundra rensponses to simulated changes in climate: aboveground biomaqss and community responses. *Arc. Alp. Res.* **28(2)**, 203-209.

Zheng D., Zhang, Q. S., Wu, S. H., 2000. *Mountain geoecology and sustainable development of the Tibetan plateau*. Kluwer Academic Press, Dordrecht, Boston, London. P. 393.

Zhou, X., 2001. *Kobresia Meadow in China*. Science Publisher, China, Beijing.